Novel pathomechanisms and disease associations of the voltage-gated sodium channel $Na_V1.4$

Michael Gunnar Thor

A thesis submitted to UCL

for the degree of Doctor of Philosophy

Department of Molecular Neuroscience

UCL Institute of Neurology

Queen Square

London WC1N 3BG

Declaration

I, Michael Gunnar Thor, confirm that the work presented in this thesis is my own. Where information has been derived from other sources, I confirm that this has been indicated in the thesis.

_____

Acknowledgements

First I would like to thank Roope Männikkö, whose input and help was invaluable to the progression of this thesis, the papers published as a result, and my career as a whole. I would like to thank Stephanie Schorge, for her input throughout my PhD. Also thank you to Michael G. Hanna and Dimitri M. Kullmann for accepting me into their labs with welcome arms, providing a fantastic platform for fruitful collaborations and development. Thank you also to Emma Matthews. I would warmly like to thank all the collaborators (too many to list here), without whom none of the projects detailed in this thesis would have been possible. Equally, and more importantly, thank you to the individuals and families who consented to these studies being carried out. They are the cornerstones of translational research.

I would also like to thank everyone in the Department of Molecular Neuroscience, Queen Square Centre for Neuromuscular Diseases (CNMD), and Department of Clinical and Experimental Epilepsy for their continued support throughout my stay at the ION. I would like to thank Gareth Morris, for the daily support – both in life and in science – throughout the PhD and beyond. Thank you to Jenna for trading battle stories.

I can't thank enough the support of Phillip Kia, Demis Smethurst, Sarah Chou, and Michael Morgan for their daily (and nightly!) help throughout my thesis. They helped me through some very tough times, and made me last till the end (certainly with the odd eggscapade on the town here and there).

A very special thank you to Susan Zhuang. Thank you for everything.

Abstract

Voltage-gated sodium channels initiate and shape the upstroke of the action potential, allowing fast electrical signaling between cells. Mutations in the genes encoding these channels are associated with a group of disorders known as channelopathies. This project aimed to characterize mutations in *SCN4A* encoding $Na_V1.4$ associated with traditional skeletal muscle channelopathies as well as novel conditions using functional expression in *Xenopus* oocytes or HEK293T cells.

Mutations of gating charges in the voltage sensor domain in the fourth transmembrane segment (S4), such as p.R222W or p.R222G, were found in patients with hypokalemic periodic paralysis. Another mutation, p.R222Q, was found in an individual with myotonia. I found that unlike hypoPP S4 arginine mutations causing gating pore currents, p.R222Q results in gain of function typically associated with sodium-channel myotonia.

In another project, novel homozygous or compound heterozygous *SCN4A* mutations were found in eleven families with congenital myopathy. Each affected individual carried at least one mutation causing full loss of function. In all but one case the mutation in the opposite allele caused full or partial loss of function. The genetic and functional data are consistent with heteroallelic loss of function mutations—one of which confers full loss of function—underlying the clinical presentation by reducing the action potential amplitude in the muscle to a level insufficient to sustain normal muscle function.

Some *SCN4A* mutations are lethal in infants when affecting muscle regulating respiration. Whole-exome sequencing of 434 cases of sudden infant death syndrome (SIDS) identified in six novel and five very rare *SCN4A* variants. Channel defects were found in four variants, two of which were gain of function and the other two loss of function. Dysfunctional *SCN4A* variants were also overrepresented in the SIDS cohort compared to controls. These results suggest pathogenic variations in *SCN4A* may be a genetic risk factor for SIDS.

Table of Contents

Declaration 1

Acknowledgements 2

Abstract 3

Table of Contents 4

List of tables 12

List of figures 13

List of abbreviations 16

List of publications arising from this thesis 17

1. Introduction *18*

1.1. Ion channels 18

1.2. Voltage-gated sodium channels 18

1.2.1. Genetics 19

1.2.2. Tissue-specific expression of Na_V isoforms 20

1.2.3. Structure 24

1.2.4. Molecular physiology and channel modulation 27

1.2.4.1. Trafficking 27

1.2.4.2. Voltage sensing 28

1.2.4.3. Activation, inactivation, and slow inactivation 31

1.2.4.4. Channel modulation 35

1.2.5. Pharmacology 36

1.2.6. Beta subunits 39

1.3. The neuromuscular junction and skeletal muscle physiology 43

1.4. Disorders of skeletal muscle 50

1.4.1. Congenital myopathies 51

1.4.2. Neuromuscular junction disorders 54

1.4.3. Muscle dystrophy 55

1.4.4. Skeletal muscle channelopathies 57

1.4.4.1. Myotonia congenita 57

1.4.4.2. Andersen-Tawil syndrome 58

1.4.5. $Na_V1.4$ channelopathies 59

1.4.5.1. Sodium-channel myotonia, paramyotonia congenita, and hyperkalemic periodic paralysis 59

1.4.5.3. Hypokalemic periodic paralysis 64

1.4.6. *SCN4A* mutations in other clinical phenotypes 69

1.4.6.1. Congenital myasthenic syndrome 69

1.4.6.2. Sudden infant death syndrome 70

1.5. Overall experimental aims 72

2. Materials and methods 74

2.1. Ethical approval 74

2.2. Molecular biology, cell culture, and DNA transfection 75

2.2.1. DNA and RNA constructs used 75

2.2.2. Molecular biology 75

2.2.2.1. LB agar and LB broth 75

2.2.3. Site-directed mutagenesis 76

2.2.4. Design of primers used for site-directed mutagenesis 76

2.2.5. Heat-shock transformation of *Escherichia coli* 76

2.2.6. Plasmid DNA purification 77

2.2.6.1. Spin method protocol 77

2.2.6.2. DNA quantification and sequencing 77

2.2.7. mRNA transcription for *X. laevis* expression of *rSCN4A*/*rSCN1B* 78

2.2.7.1. Agarose gel electrophoresis 78

2.2.8. HEK293T cell culture and transfection 79

2.2.9. Preparation of *Xenopus laevis* oocytes 80

2.2.10. Oocyte microinjection 80

2.3. Electrophysiology 80

2.3.1. HEK293T whole-cell voltage patch clamp 80

2.3.2. Two-electrode voltage clamp (TEVC) in *Xenopus laevis* oocytes 82

2.4. Analysis of HEK293T whole-cell patch clamp data 84

2.4.1. Voltage protocols of HEK293T whole-cell electrophysiology 84

2.4.1.1. Voltage dependence of activation 84

2.4.1.2. Voltage dependence of fast inactivation 84

2.4.1.3. Voltage dependence of slow inactivation 84

2.4.1.4. Time course of recovery from fast inactivation 85

2.4.1.5. Time course of onset of open state fast inactivation 85

2.4.1.6. Fitting of Boltzmann and exponential functions to data 85

2.5. Analysis of *X. laevis* oocyte TEVC data 86

2.5.1. Voltage protocols for *Xenopus laevis* oocyte TEVC 86

2.5.2. Offline leak subtraction of gating pore current data after *X. laevis* oocytes TEVC recording 86

2.5.3. *Heriaeus melloteei* (Hm-3) toxin description and Hm-3 block 87

2.6. Statistical Analysis 88

3. Differing pathomechanisms and clinical presentations of mutations affecting the same S4 arginine in domain I of $Na_V1.4$ 89

3.1. Background, aims, and hypothesis 90

3.2. Results 91

3.2.1. Note on Results 91

3.2.2. Clinical details and genetic diagnosis 91

3.2.3. Main pore current properties of VSD-I R2 mutants 93

3.2.3.1. Fast steady-state properties and current density 93

3.2.3.2. Slow inactivation, rate of recovery from fast inactivation, and onset of open-state inactivation 96

3.2.4. Gating pore current properties of VSD-I R2 mutants 101

3.3. Discussion 105

3.3.1. Implications of main pore currents to clinical phenotype 105

3.3.2. Implications of gating pore currents to clinical phenotype 107

3.3.3. Implications of gating pore currents to channel function 109

3.3.4. Implications of the silent *CLCN1* mutation for the clinical presentation of the p.R222Q patient 113

3.4. Summary 116

4. Gating pore currents caused by hypoPP mutations p.R222G and p.R222W are blocked by the Heriaeus melloteei crab spider gating modifier toxin Hm-3 117

4.1. Background, aims, and hypothesis 118

4.2. Results 119

4.2.1. Note on results 119

4.2.2. Gating pore currents in VSD-I R2 mutants p.R222W and p.R222G 120

4.2.3. Gating pore currents in p.R222W and p.R222G are blocked by the *Heriaeus melloteei* crab spider toxin Hm-3 120

4.2.4. Gating pore currents in arginine mutants of domain II and III 122

4.2.5. Functional data show a VSD-I specific block by Hm-3 125

4.3. Discussion 126

4.3.1. Hm-3 specifically binds the first voltage sensor domain (VSD-I) 126

4.3.2. Implications for developing pharmacological therapy targeting the gating pore current directly 130

4.3.3. The mechanism of Hm-3 block of main pore current and gating pore currents 132

4.4. Summary 133

5. Heteroallelic loss of function in the skeletal muscle sodium channel gene SCN4A cause congenital myopathy or fetal hypokinesia *134*

5.1. Background, aims, and hypothesis 135

5.2. Results 136

5.2.1. Note on results 136

5.2.2. Identification of bi-allelic *SCN4A* mutations in patients with congenital myopathy or fetal akinesia 137

5.2.3. Genetics of the myopathy cohort 138

5.2.4. Major clinical findings 141

5.2.5. Functional characterization of *SCN4A* variants 141

5.2.5.1. Main pore current properties in HEK293T cells 141

5.2.5.2. Gating pore current properties in *Xenopus* oocytes 151

5.3. Discussion 153

5.3.1. A new molecular pathomechanism associated with *SCN4A* 153

5.3.2. Intra- and interfamilial phenotype severity 156

5.3.3. Correlating channel defect with clinical presentation 157

5.3.4. Implications for understanding $Na_V1.4$ structure-function relationships 160

5.3.5. Limitations to the study 161

5.4. Summary 161

6. Identification of additional heteroallelic SCN4A loss of function mutations in fetal akinesia deformation sequence *162*

6.1. Aims and hypothesis 163

6.2. Results 163

6.2.1. Note on results 163

6.2.2. Genetics and major clinical findings 164

6.2.1.1. Clinical and genetic findings of Family 1 165

6.2.1.2. Family 2 166

6.2.1.3. Family 3 167

6.2.1.4. Family 4 168

6.3. Discussion 169

6.3.1. Severe *SCN4A* loss of function is incompatible with life 169

6.2.2. Implications for genetic counseling and therapeutic options 171

6.3.3. Implications for correlating function and structure of voltage-gated sodium channels 172

6.4. Summary 173

7. Bi-allelic SCN4A loss of function in congenital "corona" myopathy 174

7.1. Aims and hypothesis 175

7.2. Results 175

7.2.1. Note on results 175

7.2.2. Genetics and major clinical findings 175

7.2.3. Functional characterization 177

7.3. Discussion 181

7.3.1. Molecular pathomechanism and correlation with clinical phenotype 181

7.3.2. Structure-function elucidation 182

7.4. Summary 183

8. SCN4A mutations associated with sudden infant death syndrome 184

8.1. Background, aims, and hypothesis 185

8.2. Results 186

8.2.1. A note on results 186

8.2.2. Genetics 186

8.2.3. Clinical details of individuals in the SIDS cohort 187

8.2.4. Functional expression of *SCN4A* variants in HEK293T cells 188

8.2.4.1. Voltage-dependent properties of activation and fast inactivation 189

8.2.4.2. Recovery from fast inactivation and time-course of onset of open state inactivation. 195

8.2.5. *SCN4A* variants causing channel dysfunction are over-represented in the SIDS cohort compared to controls 196

8.3. Discussion 197

8.3.1. Summary of effects of *SCN4A* variants from the SIDS cohort on channel function 197

8.3.2. $Na_V1.4$ loss of function as a risk factor in sudden infant death syndrome 198

8.3.3. Gain of function mutations in *SCN4A* and SIDS risk 199

8.3.4. Changes in skeletal muscle channel expression profile during development may define a critical period 201

8.3.5. Genetic analysis and implications for global SIDS risk 203

8.3.6. $Na_V1.4$ dysfunction and triple risk hypothesis of SIDS 204

8.3.7. Correlating the biophysical impact of amino acid-residue specific variants with sodium channel structure and function 205

8.3.8. Outlook on genetic counseling and prevention options 206

8.3.9. Limitations to the study 207

8.4. Summary 208

9. Outlook 209

9.1. Functional genetics of ion channels 209

9.2. $Na_V1.4$ loss of function variants raising their ugly head 210

9.2.1. Limitations to the studies of full loss of function mutations 213

9.3. Implications for other channels and channelopathies 214

10. Conclusions 215

11. References 216

List of tables

Table 1.1. Brief overview of the NaV1.x sodium channels.

Table 1.2. Summary of disorders affecting skeletal muscle

Table 3.1. Activation and fast inactivation.

Table 3.2. Recovery tau and slow inactivation

Table 5.1. Overview of family genetics.

Table 5.2. Properties of channel activation.

Table 5.3. Voltage dependence of channel fast inactivation.

Table 5.4. Summary of biophysical effects and clinical effects

Table 6.1. Newly identified cases with identical clinical presentation.

Table 7.1. Tau of onset of open-state inactivation

Table 8.1. Genetic and clinical overview of carriers of*SCN4A* variants in the SIDS cohort.

Table 8.2. Summary of all biophysical properties of $Na_V1.4$ variants in SIDS and control cohorts with European ancestry.

Table 8.3. Summary of biophysical effects in *SCN4A* variants in SIDS cohort with channel dysfunction

List of figures

Figure 1.1. Sequence similarity and phylogenetic tree of the nine rat NaV1.x channel isoforms.

Figure 1.2. Schematic diagram of the sodium channel alpha subunit structure.

Figure 1.3. Superimposition of NaVAb and KV1.2 shows striking VSD similarity.

Figure 1.4. The three principal channel functional states depend on the voltage across the cell membrane.

Figure 1.5. Schematic diagram outlining the basic features of the beta subunit.

Figure 1.6. Mechanisms of synaptic release.

Figure 1.7. Skeletal muscle fiber structure and the insides of the myofibrils.

Figure 1.8. Sequence of skeletal muscle contraction within the sarcomere

Figure 1.9. Simplified schematic diagram of the neuromuscular junction.

Figure 1.10. Models of myotonia and myotonia transitioning into an episode of paralysis in hyperPP muscle.

Figure 1.11. Gain of function mutations increase the probability of the channel to enter and stabilize the open state while loss of function mutations may stabilize the inactivated conformation.

Figure 1.12. The bistable resting membrane potential in skeletal muscle in healthy and hypoPP fibers.

Figure 1.13. The direction of the gating pore current depends on which arginine is affected.

Figure 2.1. Current-voltage plot of leak-subtraction reveals the inwardly conducted gating pore current.

Figure 3.1. Location of R2-VSD I mutations p.R222G/Q/W mapped onto a schematic diagram of the NaV1.4 alpha subunit.

Figure 3.2. Current density of mutant R2 VSD-I channels.

Figure 3.3. Voltage-dependence of activation and fast inactivation

Figure 3.4. Onset of open-state inactivation, tau of recovery from inactivation, and slow inactivation properties in R2 VSD-I variants in HEK293T cells.

Figure 3.5. Gating pore currents in p.R222Q, p.R222W, and p.R222G mutant channels.

Figure 3.6. Differential behavior of gating pore currents induced by mutant VSD-I R1, R2, and R3.

Figure 4.1. Hm-3 blocks gating pore currents of variants p.R222G and p.R222W

Figure 4.2. Position of gating charge arginines in the $Na_V1.4$ alpha pore subunit

Figure 4.3. Gating pore currents induced by arginine substitution in VSD-II

Figure 4.4. Hm-3 does not block gating pore currents caused by arginine mutations in domains II and III, or domain I R1, R3.

Figure 4.5. Hm-3 right-shifts the wild-type peak current and the fraction of main pore current block by Hm-3 is dependent on the channel genotype.

Figure 4.6. Specific binding of Hm-3 to VSD-I by NMR and functional experiments.

Figure 5.1. Location of mutations in the index case with congenital myopathy.

Figure 5.2. Functional expression of index case missense variant p.R104H reveals complete loss of function.

Figure 5.3. Location of all congenital myopathy variants.

Figure 5.4. Family pedigrees of the six initial kindreds.

Figure 5.5. Family 2: Functional properties of variants p.R225W and p.C1209F.

Figure 5.6. Family 3: Functional properties of H1782Qfs65 channels.

Figure 5.7. Family 4: Functional properties of p.D1069N mutant channels.

Figure 5.8. Family 5: Functional characterization of p.P382T mutant channels.

Figure 5.9. Family 6: Functional properties of p.M203K $Na_V1.4$ channels.

Figure 5.10. Slow inactivation properties.

Figure 5.11.Recovery from fast inactivation.

Figure 5.12. Onset of open-state inactivation.

Figure 5.13. Gating pore currents in p.R225G, but not p.R225W channels.

Figure 6.1. Location of FADS variants.

Figure 6.2. Family pedigrees of the four follow-up kindreds with FADS.

Figure 6.3. Family 2: functional characterization of missense variants by patch clamp.

Figure 6.4. Functional characterization missense in family 3 variants by patch clamp.

Figure 7.1. Pedigree and distinguishing muscle pathology of the mild congenital myopathy kindred.

Figure 7.2. Location of mutations in both siblings with mild congenital myopathy.

Figure 7.3. Functional properties of mutants p.C375R and p.R1142Q in HEK293T cells.

Figure 7.4. Inactivation properties for p.R1142Q vs. wild-type.

Figure 8.1. Location of *SCN4A* variants.

Figure 8.2. Current density and voltage-dependence of activation in SIDS and control variants.

Figure 8.3. The voltage-dependence of fast inactivation in SIDS and control variants.

Figure 8.4. Recovery and time-course of open-state inactivation.

Figure 9.1. Increasing channel dysfunction severity correlates with increased clinical severity.

Figure 9.2. Summary of SCN4A variants and their functional effects.

List of abbreviations

ACh – acetylcholine, neurotransmitter
A gate – activation gate
Ca_V – voltage-gated calcium channel
ClC-1 – chloride channel 1
CMS – congenital myasthenic syndrome
CTD – c-terminal domain
DI-IV domains I to IV , homologous domains of sodium and calcium channels made up of six transmembrane segments
E. coli – bacterial cells Escherichia coli
EM – electron microscopy / electron micrograph
FADS – fetal akinesia deformation sequence
GEFS+ - generalized epilepsy with febrile seizures plus
HEK293T – human embryonic kidney cells expressing the SV40 T antigen
hERG – gene encoding human Ether-à-go-go-Related Gene (hERG) potassium channels
Hypo-/hyperPP – hypo-/hyperkalemic periodic paralysis
IC50; half maximal inhibitory concentration
I gate – inactivation gate
IQ motif - isoleucine-glutamine (IQ)-like motif IQXXXRGXXXR located in the C-terminus of calcium and sodium channels
K_{ir} – inward rectifying potassium channel
K_V – voltage-gated potassium channel
LB – *lucia bertani*
mRNA – messenger RNA
nAChR – [postsynaptic] nicotinic acetylcholine receptors
Na_V – voltage-gated sodium channel
NHNN – National Hospital for Neurology and Neurosurgery
PMC – Paramyotonia congenita
RCF – Relative centrifugal force (rw2/g)
RPM – revolutions per minute
RYR1 – ryanodine receptor 1
S1-S6, transmembrane segments 1-6
SCM – Sodium channel myotonia
SCNxA – Human voltage-gated sodium channel gene (where x=1-9)
SIDS – sudden infant death syndrome
SNEL – severe neonatal episodic laryngospasm
T-tubules - transverse tubules
TTX – tetrodotoxin
VSD – Voltage sensing domain
WES – Whole-exome sequencing
X. laevis – *Xenopus laevis,* African clawed frog

List of publications arising from this thesis

Original Research

1. Spider toxin inhibits gating pore currents underlying periodic paralysis. Roope Männikkö*, Zakhar O. Shenkarev*, **Michael G. Thor**, … , Dimitri M. Kullmann, Alexander A. Vassilevski ***PNAS.*** **2018.** *Accepted.* Second author. (*Joint first author)

2. Loss-of-function mutations in *SCN4A* cause severe foetal hypokinesia or 'classical' congenital myopathy. Zaharieva IT*, **Thor MG***, Oates EC*, … , Männikkö R, Muntoni F. ***Brain.*** **2016** Mar;139(Pt 3):674-91. PMID: 26700687; doi: 10.1093/brain/awv352.

3. Congenital myopathy with "corona" fibres, selective muscle atrophy, and craniosynostosis associated with novel recessive mutations in *SCN4A*. Gonorazky HD, Marshall CR, Al-Murshed M, Hazrati LN, **Thor MG**, Hanna MG, Männikkö R, Ray PN, Yoon G. ***Neuromuscular Disorders.*** **2017.** http://dx.doi.org/10.1016/j.nmd.2017.02.001

4. Dysfunction of the skeletal muscle voltage gated sodium channel in sudden infant death syndrome. (2018) R. Männikkö*, L. Wong*, D. J. Tester, **M.G. Thor**, …, E.R. Behr and E. Matthews. ***Lancet.*** **2018.** *In press.* Third author. (*Joint first author)

Published during PhD; unrelated to project

5. Contrasting roles of the h-current (Ih) and the persistent sodium current (INaP) at subthreshold voltages during naturalistic stimuli. **Thor MG**, Morris G. ***J Neurophysiol.*** 2016 Feb 24 (epub) PMID: 26912587; doi: 10.1152/jn.00031.2016.

1. Introduction

1.1. Ion channels

Alan Hodgkin, Andrew Huxley, and Bernard Katz published in 1952 a series of five articles in *The Journal of Physiology*, comprehensively describing the nature of electric current across the membrane of nerve fibers. With this they laid the foundations of the following six and a half decades to come: the study of cell membrane excitability and the emergence of *ion channels*. Ion channels are pore-forming membrane proteins that allow selective permeation of ions across the cell membrane, down the electrochemical gradient, enabling generation and propagation of electrical signals.

Ion channels can be classified by the type of ion they conduct (e.g. sodium, potassium, calcium or chloride) or by the type of stimuli controlling channel activity. Voltage-gated ion channels are characterized by their sensitivity to changes in the voltage across the membrane – the membrane potential. Ion flux through channels alters the membrane potential, feeding back to control the activity of the channel.

1.2. Voltage-gated sodium channels

Voltage-gated sodium channels are highly expressed in most excitable cells in the human body. The rapid sodium ion influx through voltage-gated sodium channels rapidly changes the membrane potential, giving rise to the rising phase of the action potential, a short-lasting change in the membrane potential of a cell in a rapidly rising and falling fashion. Action potentials carry electrical signals throughout the nervous system. When the cell membrane is depolarized, voltage gated sodium channels activate, sodium ions enter through open channels, further depolarizing the membrane and leading to further activation of sodium channels, resulting in a rapid increase in sodium conductance into the cell. These channels inactivate rapidly (within 1-2 ms), which stops depolarizing sodium current, ensuring the signal is transient.

1.2.1. Genetics

Ten voltage-gated sodium channels are found in the human genome, *SCN1A-SCN5A*, and *SCN7A-SCN11A* or $Na_V1.1$-$Na_V1.9$ and NaX (Catterall et al., 2005). Catterall and colleagues established the phylogenetic relationship of the nine major alpha subunit isoforms by aligning the amino acid sequences and comparing sequence relatedness (Figure 1.1). The voltage-gated sodium channels share 50-85 % amino acid sequence identity.

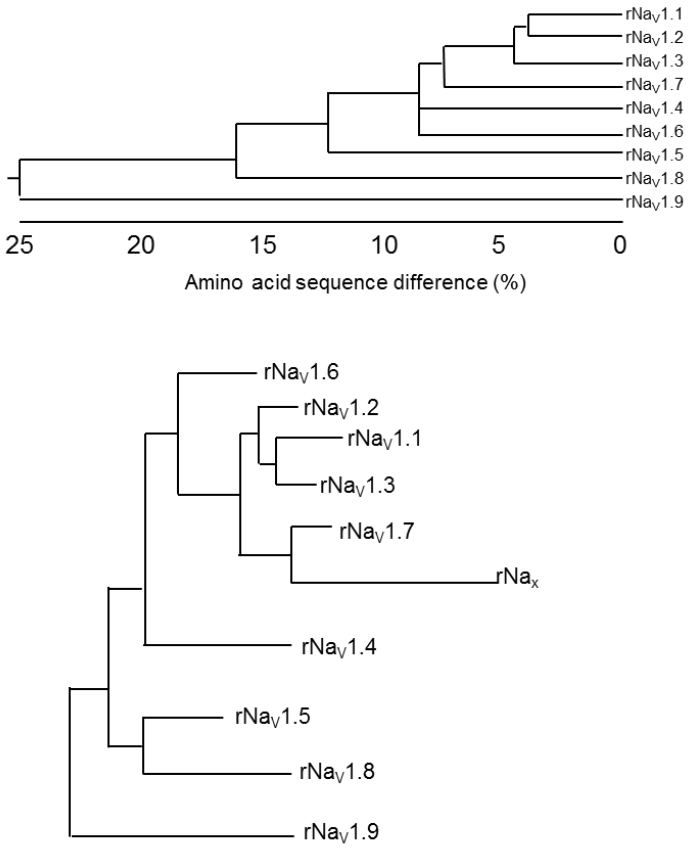

Figure 1.1. Sequence similarity and phylogenetic tree of the nine rat NaV1.x channel isoforms.
Top: $Na_V1.x$ rat clones in order of amino acid sequence differences in percent. **Bottom:** phylogenetic relationship of $Na_V1.x$ and Na_Vx channels analyzed using maximum parsimony analysis. Figure from Catterall et al., (2005), derived from (Goldin et al., 2000). Figure re-illustrated based on the figure by Catterall et al., 2005, derived from Goldin et al., 2000). For detailed information regarding analysis see Catterall et al., (2005).

1.2.2. Tissue-specific expression of Na_V isoforms

Expression of a Na_V isoform may not be confined to specific tissue; more than one subtype may be expressed in a cell; and the channel expression often depends on the developmental stage of the cell or tissue.

In the brain, isoforms $Na_V1.1$-1.3 and $Na_V1.6$ are widely expressed (Trimmer and Rhodes, 2004). Within neurons, certain subcellular localization patterns have been found. For instance, at the axon initial segment, the base of the axon where action potentials are believed to be initiated, have in certain neurons high density of $Na_V1.6$ expression (Boiko et al., 2003). Further, $Na_V1.6$ expression is also high at the proximal dendrites. $Na_V1.6$ density is also high at the nodes of Ranvier, the gaps in the myelin sheaths of axons. During development however, $Na_V1.2$ expression dominates (Boiko et al., 2001; Leterrier, 2018). As developmental stages progress, the $Na_V1.2$ is progressively exchanged for $Na_V1.6$, but a portion of $Na_V1.2$ remain. $Na_V1.2$ channels are expressed in excitatory glutamatergic neurons of the cerebral cortex in adult mice, with more expression at distal axons compared to proximally (Ogiwara et al., 2018)

$Na_V1.1$ and $Na_V1.2$ expression can be seen in the brain from as early as seven days after birth, with progressively increasing expression until adulthood (Gong et al., 1999). Duflocq and colleagues found that $Na_V1.1$ expression is dense at the nodes of Ranvier, and at the axon initial segments of several brain regions (Duflocq et al., 2008). $Na_V1.1$ was also found in the spinal cord at the nodes of Ranvier. Further, in 80 % of motor neurons, $Na_V1.1$ isoform predominated at the AIS. Another study found that in four percent of hippocampal cells (CA3) $Na_V1.1$ is localized to the AIS at high density (Van Wart et al., 2007). High expression of $Na_V1.1$ has been found in GABAergic interneurons of the hippocampus and cerebral cortex (Cheah et al., 2012). $Na_V1.1$ channels are also found in neurons projecting from the thalamus to the cortex, and a small population of excitatory neurons in the fifth layer of the neocortex (Ogiwara et al., 2013).

The $Na_V1.7$, $Na_V1.8$, and $Na_V1.9$ are expressed in the peripheral nervous system, and have all been implicated in facilitating nociceptive signaling. Their expression in cells such as sensory neurons of the dorsal root ganglion in the spinal cord (Cummins et al., 2007). $Na_V1.7$ channels are expressed at the somata of all-diameter dorsal root ganglion cells, from C-fibers to A-delta fibers (Djouhri et al., 2003; Harper and Lawson, 1985), and have been to be expressed at the skin level, the distal processes, as well as the central processes (Black et al., 2012). $Na_V1.7$ is also expressed in sympathetic neurons and are together with sensory neurons important for pain sensation (Minett et al., 2012)

In turn, $Na_V1.8$ expression has been described in both small and large diameter sensory neurons (Ramachandra et al., 2013). Interestingly, in the neurodegenerative disease multiple sclerosis, $Na_V1.8$ channel upregulation is also found in Purkinje cells of the cerebellum, where they alter the physiological properties of the cells (Renganathan et al., 2003). In the mouse, $Na_V1.8$ channels have also been found in vagal neuron afferents (Gautron et al., 2011). These cranial nerves innervate organs of the abdomen and thorax. $Na_V1.9$ channels are found in nociceptive small-diameter non-myelinated C-fibers of dorsal root ganglion neurons and trigeminal ganglion neurons (Liu et al., 2001; Priest et al., 2005). Through this they play an integral role in nociceptive signaling.

$Na_V1.3$ is normally expressed only during development in fetal dorsal root ganglion cells, however, upregulation of $Na_V1.3$ has been described during peripheral nerve damage (Wood et al., 2004). Because $Na_V1.3$ channels recover quickly from inactivation, this causes increased firing of sensory neurons in the dorsal horn. This has an important role for understanding neuropathic pain. $Na_V1.3$ channels are also found expressed in vomeronasal sensory axons and olfactory neuron axons of adult mice (Bolz et al., 2017). Subcellular localization is however different during development, and subsequent to inducing a lesion in the olfactory system, where expression in the cell bodies increase.

$Na_V1.4$ and $Na_V1.5$ are primarily expressed in the sarcolemma of skeletal muscle and cardiac myocytes, respectively. Although $Na_V1.5$ is believed to be the major sodium current carrier in cardiac myocytes, where it initiates and propagates action potentials (Rook et al., 2012), $Na_V1.1$, $Na_V1.2$, $Na_V1.3$, $Na_V1.4$, and $Na_V1.6$ expression has been detected in the human myocardium by immunohistochemistry (Kaufmann et al., 2013). Whole-cell patch clamp of human atrial cells found that up to 27 % of the total sodium current was carried by channels other than $Na_V1.5$. Equally intriguingly, $Na_V1.5$ has also been found in the various brain regions such as the basal ganglia, hypothalamus, brain stem, cerebral cortex, and the cerebellum (Wu et al., 2002).

In smooth muscle cells, different sodium channel isoforms have been discovered. For instance, Lee-Kwon and colleagues show expression of $Na_V1.3$ in vasa recta (the blood supply to the kidney) (Lee-Kwon et al., 2007). The $Na_V1.6$ isoform has been found in myocytes of the vas deferens (Teramoto et al., 2012), as well as portal vein, which supplies blood to the liver from the intestines, stomach, pancreas, and spleen (Saleh et al., 2005). The isoform $Na_V1.8$ was also found in the portal vein.

Both $Na_V1.4$ and $Na_V1.5$ isoforms are expressed in skeletal muscle during development. Early in development $Na_V1.5$ expression dominates, and is subsequently replaced by a rapidly increasing expression of adult skeletal sodium channel–namely $Na_V1.4$ (Kallen et al., 1990; Zhou and Hoffman, 1994). Myoblasts (Weiss and Horn, 1986) and myofibers of newborn rats express TTX resistant Na_V channels (Harris and Marshall, 1973), most likely $Na_V1.5$. Very few studies delineating $Na_V1.4$ and $Na_V1.5$ expression in skeletal muscle during development exist. One study employed multiplex fluorescent PCR (QMF-PCR) to study the expression levels of the fetal/cardiac isoform $Na_V1.5$ and the adult/skeletal isoform $Na_V1.4$ in human fetal, neonatal, young child, and adult muscle tissue (Zhou and Hoffman, 1994).

Zhou and Hoffman (1994) extracted muscle from mice and human post-mortem tissue the diaphragm and skeletal muscle. Throughout development (embryonic and postnatal) *SCN4A* expression is higher than *SCN5A*. Expression of *SCN5A* is reduced over time in a similar fashion in both mice and humans of both tissues, with *SCN4A* increasing exponentially. At 5 years of age in humans (and approximately P7-P14 in mice), *SCN4A* expression reaches 40 % of that of adults. In mice, *SCN5A* expression is negligible at P14. In humans after 5 years *SCN4A* expression increases until maximum expression is achieved in healthy adults. It is estimated adult *SCN4A* expression level is reached after the age of 10 (Zhou and Hoffman 1994). Interestingly, expression of the TTX-resistant isoform has been shown to increase in skeletal muscle after denervation (Kallen et al., 1990).

Table 1.1. Brief overview of the $Na_V1.x$ sodium channels.

Listed are gene name, UniProt number, [TTX?] sensitivity (S) or resistance (R) to tetrodotoxin (TTX), typical functional characteristics in respect to activation and fast inactivation (V1/2 or activation and fast inactivation, in mV), and location of expression.

Channel isoform	Gene	TTX?	V1/2 activation (mV)	V1/2 inactivation (mV)	Location	UniProt number
$Na_V1.1$	*SCN1A*	S	-22	-65	CNS	P35498
$Na_V1.2$	*SCN2A*	S	-24	-56	CNS	Q99250
$Na_V1.3$	*SCN3A*	S	-25	-65	CNS	Q9NY46
$Na_V1.4$	*SCN4A*	S	-20	-65	Muscle	P35499
$Na_V1.5$	*SCN5A*	R	-45	-84	fetal/neonatal skeletal muscle, and heart	Q14524
$Na_V1.6$	*SCN8A*	S	-35	-70	DRG, CNS	Q8WWN3
$Na_V1.7$	*SCN9A*	S	-30	-78	PNS	Q15858
$Na_V1.8$	*SCN10A*	R	-12	-40	DRG	Q9Y5Y9
$Na_V1.9$	*SCN11A*	R	-54	-56	DRG	Q9UI33

1.2.3. Structure

The voltage-gated sodium channels comprise of a main pore-forming alpha subunit, usually associated with one or two beta subunits (Alexander et al., 2013). The alpha subunit consists of four homologous domains (DI-DIV), each containing six helical transmembrane segments (S1-S6; Figure 1.2). Helices S5 and S6 are connected by the pore loop, and together S5 and S6 of all four domains form the ion-conducting pore. The pore contains a selectivity filter and the channel gates (Doyle et al., 1998). Helices S1-S4 of each subunit form a voltage sensing domain (VSD). Positively charged arginine residues in S4 are sensitive to changes in transmembrane voltage, and serve as gating charges (Larsson et al., 1996; Seoh et al., 1996). The positive charges are stabilized in the hydrophobic transmembrane region by negatively charged amino acid residues located in segments S2-S3 that may also function as gating charges. Beta subunits are not required from functional expression of the alpha subunit, but modify its function (Lee et al., 2014).

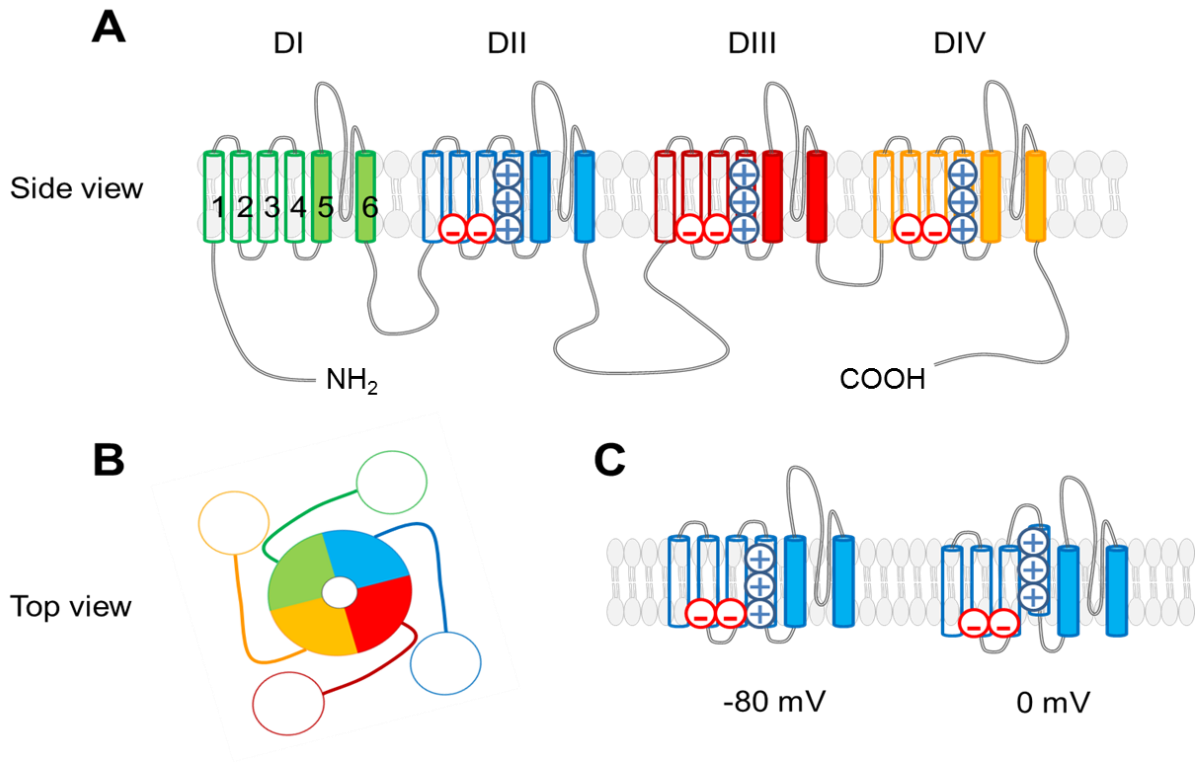

Figure 1.2. Schematic diagram of the sodium channel alpha subunit structure.

A. alpha subunit viewed in membrane plane. Domains I-IV color coded. Each domain made up of six transmembrane segments (1-6). NH_3 signifies the N-terminal domain, and COOH denotes the carboxyl C-terminal domain. Pore forming S5-S6 helices are filled; S1-S4 helices of the VSD are open. **B.** Alpha subunit view from above the membrane plane. Segments S5-S6 of each domain form the pore module (solid) and surround the central aqueous pore. The four VSDs (open) are peripheral to the pore. **C.** One VSD displaying gating charges in S4 and negative countercharges in S2/S3. At rest (and holding voltage; -80 mV) S4 helix containing the positively charged arginine residues, is attracted toward intracellular direction (down). The S4 segment is positioned outward (up) during depolarization (0 mV).

Structure-function studies, crystallography, and nuclear magnetic resonance analysis of related potassium channels have laid foundations into to understanding the structure of voltage-gated ion channels. A key step in the understanding of channel structure was discovery of the structure of the KcsA channel from *Streptomyces lividans* using x-ray crystallography (Doyle et al., 1998). X-ray crystallography is an elegant technique that

allows determination of the molecular structure of e.g. a protein in crystal form. X-rays diffract into different directions when it hits the structure. From the diffracted waveforms intensities and angles are measured, and a 3D structure of electron densities is extrapolated, allowing calculation of atom positions. Doyle found that the KcsA potassium channel is shaped like a cone, with the wide end facing outward. At the extracellular end is a selectivity filter with three key hydrophobic amino acids GYG (G: glycine; Y: tyrosine). The pore is geometrically shaped so that the sodium ion is too small for the selectivity filter to strip its hydration shell. At the center of the pore is wide water filled cavity lined with hydrophobic amino acid residues. By means of molecular cloning and site-directed mutagenesis, Doyle and colleagues probed the molecular underpinnings of selective permeation through the pore (the selectivity filter) and confirmed the main gate location to the intracellularly positioned S6 segments. The main activation gate resides in the intracellular tip of the cone.

In 2011 the crystal structure of a prokaryotic voltage-gated sodium channel (Na_VAb) from *Arcobacter butzleri* was described (Payandeh et al., 2011a). It constitutes a useful tool to understanding the structural basis underlying channel gating and ion selectivity. Payandeh and colleagues crystallized Na_VAb in the closed conformation. For the closed conformation to open, all VSDs need to be activated (S4 in the up state). Since the S4 segments are in the up state, but the channel pore is not yet open, the channel conformation in this study is proposed to be in the pre-open state, the stage just prior to S4 movement translating into the opening of the central pore. Similar to previous literature, modeling of Na_VAb shows that outward S4 movement moves together with the S4-S5 linker, this pulls the S5-S6 segments (that are strongly associated with each other). When one S5-S6 pair moves, the physical force also moves the other S5-S6 segments, so that together they open a translocation pathway for ions. The sequence of activation has previously been proposed to be in the order of: DIII, DII, DI, and lastly DIV (Gosselin-badaroudine et al., 2012).

Another bacterial channel was cloned from *Magnetococcus* sp. (strain MC-1) by a group at Birkbeck College, London – but this time instead in the open conformation – where it appeared the activation gate was disconnected from the selectivity filter (McCusker et al., 2012). In its open state the activation gate was more than 8 A in diameter, sufficiently large to allow hydrated sodium ions to conduct through the pore.

Recently, cryo-EM structure of electric eel $Na_V1.4$ channel was published (Yan et al., 2017). Although across crystal structures there is some variability in the channel structure, the VSD is in the up state due to the absence of voltage (0 mV) when the structural snapshots are taken. Thus no structure of the down state VSDs exists currently.

1.2.4. Molecular physiology and channel modulation

1.2.4.1. Trafficking

Motifs controlling the trafficking of the voltage-gated ion channels have been identified in the intracellular N- and C-termini. The N-terminus of voltage-gated sodium channels is an approximately 100 residues long cytoplasmic domain. Disease-associated mutations in various channel subtype have shed light on its role in channel trafficking. For example, a p.S21P (where p. is the mutant protein resultant from a substitution of S (serine) to P (proline) at amino acid position 21) $Na_V1.6$ channel in mouse dorsal root ganglion neuroblastoma hybrid ND7/23 cells produced no functional currents at 37 °C (Sharkey et al., 2009). Immunocytochemistry of cerebellar granule cells of mutant mice revealed channels were retained in the Golgi complex, implicating this N-terminus residue in the transport of sodium channels to the cell membrane. Similarly, two $Na_V1.5$ N-terminal mutant channels associated with Brugada syndrome, p.R104W and p.R121W, were mostly retained in the endoplasmic reticulum in rat neonatal cardiomyocytes (Clatot et al., 2012).

Disrupting specific C-terminus residues may also interrupt ion channel trafficking. Similar to Clatot and Sharkey papers p.M1841T, a C-terminal $Na_V1.1$ missense mutation associated with generalized epilepsy with febrile seizures plus (GEFS+) (Rusconi et al., 2007) also revealed a near complete loss of channel function by reducing the current density ten-fold compared to wild-type (I_{mutant}: 12.9±1.4 pA/pF vs. I_{WT}: 121.1±12.2 pA/pF). This residue has been shown to interact with accessory subunits (Rusconi et al., 2007). Co-expression with beta-1 subunit increased the expression of the mutant $Na_V1.1$ to approximately 50 % of wild-type currents; strikingly, no effect was seen on wild-type current density after beta-1 co-expression. Beta subunits are described in detail in 1.2.5.

1.2.4.2. Voltage sensing

Different ion channel types are activated by different stimuli. Voltage-gated ion channels are activated by changes in the electrical field across the membrane. A component integral to the channel's voltage-dependent properties is the voltage sensor, which in response to changes in the membrane potential undergoes conformational changes. The positively charged amino acids of S4 act as gating charges that when mutated reduce the total gating charge of the channel (Seoh et al., 1996). Depolarization causes the S4 segment to move in an extracellular direction through a structure called the gating pore formed by the S1-S3 helices, while hyperpolarization moves S4 inwards (Larsson et al., 1996; Männikkö et al., 2002; Yang et al., 1996). At hyperpolarized voltages, positive S4 charges are attracted inward (Catterall, 1986), forming ion pairs with negative countercharges in S1-S3 to stabilize the closed state (Catterall, 2010). Conformational changes in the VSD control opening and closing of the central channel pore. The up state of S4 stabilizes the open channel state, while the down state stabilizes the closed state.

The voltage sensor of Na_V and $K_V1.2$ are strikingly similar as is illustrated in Figure 1.3. There are three key positions in the voltage-sensing module. At the extracellular side is an extracellular negative charge cluster (ENC) where amino acids with negatively charged

sidechains interact closely with gating charges of S4. In the middle there is the hydrophobic constriction site (HCS), situated in the middle of the voltage sensor, which is a plug or seal, preventing movement of ions and water through the voltage sensor from the extracellular space to the intracellular space through the voltage sensor (Figure 1.3.). Lastly, the intracellular negative cluster (INC) is made up of negatively charged amino acid residues, also interacting with positive S4 gating charges. As the electrostatic forces change across the membrane during depolarization, the gating charges move out and back in. In so doing, ion pair partners are exchanged from the INC, through the HCS to the ENC. Through this, positively charged arginines are neutralized by negative countercharges (Payandeh et al., 2011). In this particular model R4 interacts with the INC, while R2/R3 interact with the ENC, indicating that the Na_VAb structure was captured in the activated state of S4 (S4 position in the up state), as stated previously (Figure 1.3.).

Hydrophobic residues which are highly conserved are localized to the HCS (e.g. [NaVAb numbering]: Ile 22, Phe 56 and Val 84, which during the movement of S4 in the gating pore prevents leakage of ions (Payandeh 2011).

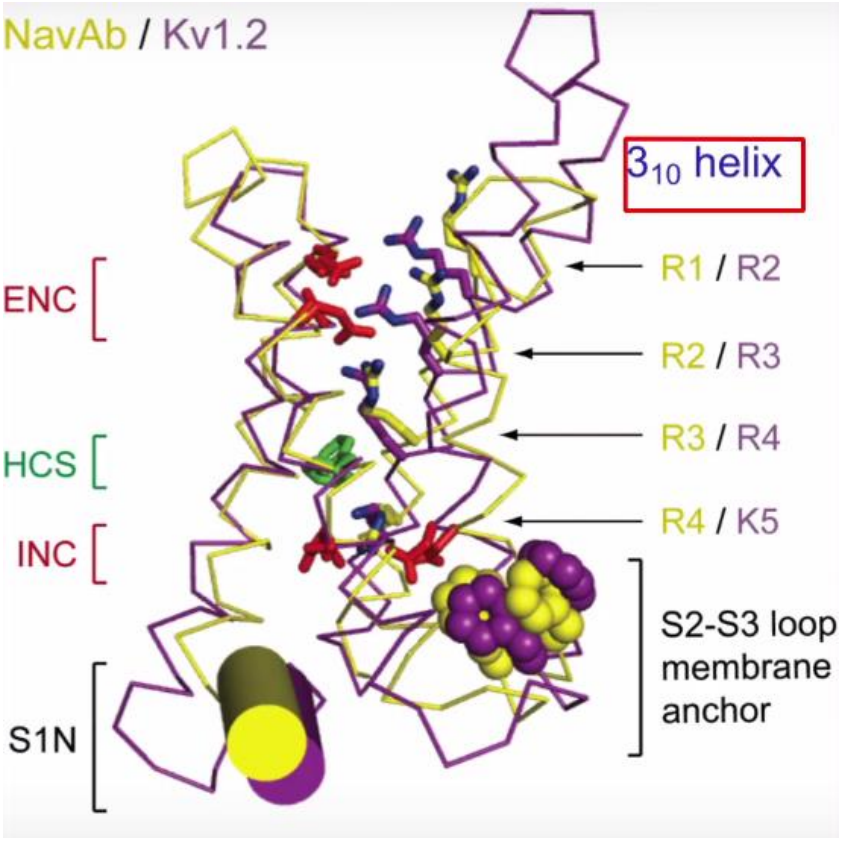

Figure 1.3. Superimposition of Na_VAb and $K_V1.2$ shows striking VSD similarity.

Na_VAb is in green/yellow while $K_V1.2$ is in purple. ENC: extracellular negative cluster with negatively charged amino acid side chains in red; HCS: hydrophobic constriction site, with hydrophobic side chains in green; INC: intracellular negative cluster (negative amino acid side chains in red). Note how $K_V1.2$ R2 corresponds to Na_VAb R1 […]; K5 corresponds to R4. Figure from Payandeh (2011), re-adapted to lecture at iBiology.org

The S4 segment moves through a structure called the *gating pore* shaped by segments S1-S3 (Catterall, 2014). Mutations of S4 arginine residues can introduce a leak current through the gating pore (Sokolov et al., 2007) suggesting that the S4 arginines normally occlude the gating pore from ion leak. Neutralization of the outermost S4 arginine residues introduces hyperpolarization-activated gating pore currents (Starace and Bezanilla, 2001; Tombola et al., 2005), while lower-arginine neutralization create gating pore currents active during depolarization (Moreau et al., 2014). These currents can be studied in isolation by blocking the main pore currents, for example by tetrodotoxin in the case of $Na_V1.4$.

When a S4 arginine gating charge is mutated guanidinium ion conductance through the gating pore is often higher than that of inorganic ions (Sokolov et al., 2010). The charge-carrying ability of guanidinium strongly suggests that this region is the pathway through which S4 arginines permeate as it is a moiety of an arginine side chain. Its selective permeation through the VSD renders guanidine sulfate a useful tool to identify and characterize gating pore currents, as the presence of guanidinium will increase the current measured. If indeed a gating pore is present, an increased current will be measured with guanidinium in the extracellular solution due to the relatively higher influx of guanidinium compared to sodium.

1.2.4.3. Activation, inactivation, and slow inactivation

The pore of the voltage-gated sodium channel has three principal states: closed (deactivated), open, and inactivated. Closed and inactivated channels do not conduct ions, but represent different channel conformations. During an action potential, sodium channels activate in response to membrane depolarization which leads to activation of VSDs, which leads to opening of the channel pore, allowing sodium influx. Influx of sodium further depolarizes the plasma membrane, acting as a positive feedback system. Following activation, Na_V channels inactivate to prevent excess depolarization of the membrane. During repolarization sodium channels deactivate and recover from inactivation (Kuo and Bean, 1994). During prolonged depolarization the channels may enter a slow inactivated state. This state is non-conducting, structurally distinct from fast inactivated state, and recovery from this inactivated state is also slow.

To allow conduction of ions through the channel pore, the channel's two gates – the activation (*a*) and inactivation (*I*) gates must be open (Armstrong, 2006). Activation- and inactivation gating are coupled processes. Ion channels can inactivate in both the open and closed state. Channels inactivate when the *a* gate is open (open-state inactivation) but also before the *a* gate is open (closed-state inactivation). Open-state inactivation follows activation, prevents excess depolarization and keeps the action potential short.

Closed-state inactivation is the principal mechanism during small depolarizing inputs, thereby controlling channel availability at voltages negative to action potential thresholds.

The activation gate is located inside the pore-forming module of the channel, in intracellular facing amino acid residues (Payandeh and Minor, 2015). One key residue in the pore-lining S6 segments of bacterial Na_V channels Na_VSp1 and Na_VAe1p is p.Met241, which when in Na_VAe1p was mutated to p.M241A displayed a 50 mV hyperpolarizing shift in the voltage-dependence of activation. Mutating residues directly above p.M241 however had no effect on activation kinetics. In Na_VAb, a key residue is p.M221, which occludes the pathway through which ions permeate in the open state (Payandeh et al., 2011a). It is thought that during pore opening the activation gate opens like the iris of a camera, large enough to fit sodium ions through the cavity.

Ion permeation through the channel pore is selective for sodium due to the ion selectivity filter made up by the four P-loops. Residues in these loops together form outer ring made up of amino acids glutamic acid and aspartic acid (EEDD) and inner rings (DEKA; aspartic acid, glutamic acid, lysine, alanine) within the channel (Catterall, 2000) that confer ion selectivity. Site-specific substitution of the inner ring residues to glutamate renders the pore selective to calcium ions (Heinemann et al., 1992).

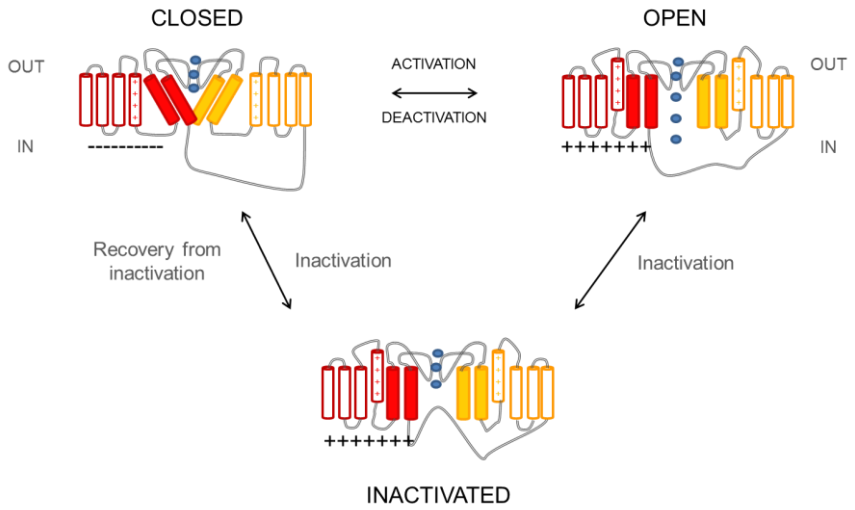

Figure 1.4. The three principal channel functional states depend on the voltage across the cell membrane. The voltage-gated sodium channel can sustain one of three functional states: closed, open or inactivated. Channel activation in response to depolarizing stimuli causes the S4 segment of the VSD (red/yellow square with + charges) to move outward due to electrostatic repulsion. This movement pulls S5 and S6 to open the intracellular gate via S4-S5 loop. Channels may inactivate from either the closed or the open channel state. Only two domains are shown for clarity.

The inactivation gate was initially identified using site-directed mutagenesis studies of the DIII-DIV intracellular loop, a peptide segment, implicated this region in fast inactivation (Vassilev et al., 1988). Entry into the inactivated state was slowed by binding a peptide to this segment, thereby obstructing the fast inactivation gate, which was believed to occlude the central pore with a *hinged lid* mechanism (Figure 1.4) (Vassilev et al., 1989). Cleaving the DIII-DIV loop also slowed the rate of fast inactivation (Stühmer et al., 1989). The key region underlying this hinged lid mechanism of fast inactivation is the hydrophobic isoleucine-phenylalanine-methionine (IFM) motif (Goldin, 2003). The lid binds to the intracellular end of S6 of various domains, thus mediating the closing of the inactivation gate. These residues are critical for the inactivation gate to remain closed, while mutations in this region disrupt its closure and thus inactivation. Domain IV VSD has a particular role

in controlling fast inactivation. Conformational changes of DIV VSD are slower than those for DI-DIII (Capes et al., 2013; Lacroix et al., 2013), and consequently fast inactivation has a slower time course than channel activation (Armstrong, 2006). Fast inactivation in the $Na_V1.4$-Beta-1 channel complex cloned from the electric eel *Electrophorus electricus* also acts through a hinged-lid mechanism with an LFM motif (equivalent of IFM) (Yan et al., 2017). Its binding is slightly different in that it does not physically occlude permeation, but rather LFM positions itself in the corner of DIII/DIV S4-S5 and the intracellular ends of S6 DIII/DIV.

A more detailed (3.8 A) eukaryotic sodium channel structure called Na_VPaS from the American cockroach was described recently (Shen et al., 2017). In contrast to Na_VAb, it contained the DIII-DIV intracellular linker important for fast inactivation. The Na_VPaS channel does not have the DIII-DIV linker IFM motif per se, but rather equivalent residues ATD (alanine-threonine-aspartate) (Shen 2017). Because the channel could not be functionally studied using heterologous expression, it is not verified (though predicted) whether fast inactivation is a property of Na_VPaS. The authors found the CTD of Na_VPaS to be structurally similar to the CTD of NaV1.5. The III-IV linker interacted with the CTD, as well as the domain IV VSD and S5-S6 linker and S6 (of DIV). The linker binds intracellularly facing S6 of DIII and DIV, as well as VSD-IV, providing structural evidence of VSD-IV involvement in fast inactivation. In agreement with these data, the $Na_V1.5$ VSD-IV regulates the onset of fast inactivation in $Na_V1.5$ (Hsu et al., 2017). The VSD-IV is believed to interact directly with the DIII-DIV IFM motif and the S4-S5 linker of DIV, consistent with the structural data by Shen and colleagues (2017).

Slow inactivation is independent from DIII-DIV loop associated with fast inactivation. In fact, bacterial channels do not have fast inactivation – only slow inactivation, and so eukaryotic channel studies are integral to understanding the structural underpinnings of fast inactivation. Site-specific mutagenesis has implicated residues in the pore loop and in the S6 in modulating slow inactivation (Mitrovic et al., 2000). Using the bacterial sodium

channel Na_VAb, El-Din and colleagues identified the Asn49 residue located in the ENC of the S2 segment as critical for late slow inactivation (Gamal El-Din et al., 2013). Na_VAb does not have the DIII-DIV linker responsible for fast inactivation, but has three modes of slow inactivation: two early phases (occur through single depolarization) and later phase that is use-dependent. Studies in human Ether-à-go-go-Related Gene (hERG) potassium channels have implicated some form of collapse of the selectivity filter region, thereby obstructing ion influx (Smith et al., 1996), suggesting that the selectivity filter can act as a permeation gate. Detailed understanding of the molecular mechanism of slow inactivation is currently lacking.

1.2.4.4. Channel modulation

Sodium channel expression and function is modulated by extracellular and intracellular signaling cues. Recent evidence has emphasized the role of calmodulin in sodium channels due to high C-terminus homology across sodium and calcium channels (Ben-Johny et al., 2014). Calmodulin (CaM) is an omnipresent calcium sensor and interacts with the isoleucine-glutamine (IQ)-like motif IQXXXRGXXXR located in the C-terminus of calcium and sodium channels (Van Petegem et al., 2012). Deletion at the C-terminal domain that removes the IQ domain reduces the current density by 99 % and 62 % in $Na_V1.4$ and $Na_V1.6$, respectively, while deletion of the C-terminus after the IQ motif retained fully functional currents comparable to those of wild-type constructs (Herzog et al., 2003). Calmodulin overexpression increased the current density of both isoforms without altering voltage-dependent properties.

The C-terminal domain also contributes to inactivation gating. Mantegazza and colleagues investigated the C-terminal domain (CTD) properties of cardiac $Na_V1.5$ and brain $Na_V1.2$ channels (Mantegazza et al., 2001). By swapping the CTD of each channel into the other channel, inactivation gating properties changed drastically. $Na_V1.2$ channels expressing a $Na_V1.5$ CTD shifted the voltage-dependence of inactivation by 14 mV, and $Na_V1.5$

expressing a $Na_V1.2$ CTD enhanced inactivation by 12 mV, comparable to that of wild-type $Na_V1.2$ channels. Previously it has been shown that swapping only the inactivation gate did not affect the inactivation properties. Although the exact mechanism is unclear, it could be concluded that the distal portion of the c-terminal domain plays an important role in determining inactivation properties in sodium channels. The activation properties of either channel were unaffected.

1.2.5. Pharmacology

The function of voltage-gated sodium channels can be modulated by various pharmacological agents. Two important toxins are saxitoxin and tetrodotoxin, who with diverse affinity bind and block the various Na_V isoforms (Hille, 1975; Narahashi, 1974). Tetrodotoxin divides the Na_V channels into two groups: the TTX-resistant and the TTX-sensitive, depending on their affinity of block (mM-μM range vs. nM range) (Catterall et al., 2005). Tetrodotoxin is primarily associated with puffer fish and has been found in 40 species (Catterall et al., 2007). Saxitoxin is found in a family of plankton called the dinoflagellates (Schantz, 1986).

Both tetrodotoxin and saxitoxin bind a group of primarily negatively charged amino acid residues at the outer portion of the S6 segment of all domains (Noda et al., 1989; Terlau et al., 1991). This site is made up of two “rings”. In $Na_V1.2$ outer ring consists of DI: E387; DII: E945: DIII: D1426; and DIV: D1717, while ring two consists of DI: D384; DII: E942; DIII: K1422; and DIV: A1717 (Terlau et al., 1991). Homologous residues in other channels are thought to confer the same properties. However, in $Na_V1.5$, a TTX-resistant channel, a single amino acid change from tyrosine to cytosine markedly reduces TTX affinity. When in $Na_V1.5$ the cysteine residue was mutated to tyrosine its TTX sensitivity was restored (Backx et al., 1992; Satin et al., 1992).

Other toxins do not occlude the pore directly, but rather modify the channel’s gating. These toxins are known as gating modifiers, which stabilize one of the voltage sensing

domain states. One such modifier is batrachotoxin, a steroidal alkaloid found for instance in *Ifrita Rowaldi* birds of Papua New Guinea (Dumbacher et al., 2000). By binding several S6 segments at the inside of the pore, it causes a hyperpolarizing shift in the voltage-dependence of activation as well as inhibition of inactivation. This causes channel open probability to increase and hyperexcitability ensues (Linford et al., 1998; Wang and Wang, 1998; Wang et al., 2000). Batrachotoxin does not fully block the main pore and thus a part of the sodium current still enter through the pore (Wang and Wang, 1998). In contrast, derived from plants of the *Liliacae* family is veratridine, an opener of some sodium channels (Ulbricht, 1998). It achieves a persistent opening of channels by binding residues of S6 during sustained depolarization by inhibiting inactivation.

Local anesthetics are another group of important pharmacological agents, a group that abort pain perception by interrupting neuronal excitation in sensory nerves. These drugs bind Na_V's state-dependently, preferably in the inactivated or open state of the channel. One important agent is lidocaine, which blocks Na_V pores by interacting with pore-forming S6 of DIV in $Na_V1.2$ (Ragsdale et al., 1994, 1996). The binding site of lidocaine and the related agent etidocaine was tested by mutagenesis of IV S6 residues F1764A and Y1771A. Mutagenesis strongly reduced the affinity for block, implicating this region in the mechanism of block by local anesthetics,

Equally, lidocaine which favors binding of channels in the inactivated state had a 25-fold reduced affinity for block in F1764A mutant channels. Another channel blocker, flecainide, which favors open-state binding had a 2-3 fold reduced affinity when this residue was mutated. Taken together, these results point to a similar receptor binding site for local anesthetics in inner residues of S6 in residing in the pore domain. Further studies showed binding sites of local anesthetics in S6 segments of DI and DIII as well (Qu et al., 1995; Yarov-Yarovoy et al., 2001). Together they form a receptor site constituting S6 segments that form the inner vestibule of the pore. In order for drugs to fit inside the pore, the activation gate must be open (Payandeh et al., 2011b).

Na_V channels are also blocked by other agents such as the anti-anginal ranolazine. In a study of the inhibitory effect of ranolazine on $Na_V1.5$ channels, both the main pore and the late/persistent current was blocked by ranolazine; however, the block of the persistent current was ten-fold higher compared to the main current. The affinity for block was markedly reduced by DIV S6 F1760A mutant $Na_V1.5$ channels (Fredj et al., 2009). Ranolazine has also been found to block the open state of isoforms $Na_V1.4$ and $Na_V1.7$ (El-Bizri et al., 2011; Wang et al., 2008). Wang and colleagues found ranolazine-mediated inhibition to be modest in the closed or inactivated channel state of $Na_V1.4$ and $Na_V1.7$, but blocked currents in the open state during repetitive pulses in a use-dependent manner. To determine the binding site, S6 DIV F1576K mutant $Na_V1.4$ channels were generated. These channels had markedly reduced affinity for ranolazine block. Taken together, these results suggest the receptor binding site for ranolazine is similar to that of local anesthetics.

The problem with many pharmacological agents targeting sodium channels is that they act on several Na_V isoforms at the same time. In a clinical setting this is unfavorable due to its off-target effects. Recently an $Na_V1.7$ antagonist was described (Ahuja et al., 2015), which upon binding locks VSD-IV in the activated configuration. This is thought to perturb the channel's recovery from fast inactivation, thereby maintaining a non-conducting channel state. This compound is unusually isoform-selective. Targeting voltage-sensing domains might be a good strategy to find isoform specific blockers.

Another selective blocker is the $Na_V1.8$ isoform specific PF-01247324, which blocked TTX-resistant sodium currents in human sensory neurons of the dorsal root ganglion at an IC_{50} of 331 nM (Payne et al., 2015). PF-01247324 block selectivity for $Na_V1.8$ was compared to $Na_V1.5$, $Na_V1.2$, and $Na_V1.7$ 50-fold, 65-fold, and 100-fold more selective. Equally, rat C-fiber sensory neurons TTX-resistant sodium currents were blocked at IC_{50} = 448 nM. At 100 mg/kg of PF-01247324 was also found to reduce persistent pain in a rat formalin model.

In another study, Shields and colleagues describe reduce motor deficits of the cerebellum in a mouse model of multiple sclerosis (Shields et al., 2015). Cerebellar deficits include ataxia, tremors, and nystagmus. In animal models of, and in humans with multiple sclerosis (MS), the expression of $Na_V1.8$ in Purkinje cells of the cerebellum may increase (Renganathan et al., 2003). To tackle these symptoms, other sodium blockers such as anti-convulsants carbamazepine and lamotrigine have been used previously; however, due to their non-specificity have had adverse effects. To test motor coordination Shields and colleagues placed a mouse over-expressing $Na_V1.8$ in Purkinje cells (called L7-1.8TG mice) on a wire grid and inverted it, and measured the latency to fall. In wild-type mice the latency was approximately 75 seconds, while in muscle from L7-1.8TG mice the latency was approximately 15 seconds. After treatment with PF-01247324 a modest improvement was seen to approximately 45 seconds (Shields et al., 2015). Although no ex vivo or *in vitro* physiology experiments were performed, it is intriguing to speculate this may be due to $Na_V1.8$ channel isoform-specific block in the cerebellum. More experiments are warranted to test this hypothesis.

1.2.6. Beta subunits

The alpha subunit is the principal pore-forming channel that can form heterotrimeric or heterodimeric complexes with beta subunits (Isom et al., 1992, 1995). Growing evidence shows that beta subunits play an important role in fine tuning channel behavior (Namadurai et al., 2015; Patino and Isom, 2010). They've been shown to affect brain development by modulating cell migration, neural process growth, and help guide axons to find their path (Brackenbury and Isom, 2011; Calhoun and Isom, 2014).

There are five sodium channel beta subunits: β_1 and its splice variant beta β_{1B} (both encoded by *SCN1B*) and β_2-β_4 (encoded by *SCN2B* - *SCN4B*) (O'Malley and Isom, 2015). Beta subunits are single transmembrane segment proteins with a long extracellular N-

terminal domain and a short intracellular C-terminal domain (Yu and Catterall, 2004). The beta subunit has an immunoglobulin fold, making it a molecule capable of cell adhesion. The immunoglobulin fold (or Ig loop) is made up of two beta sheets linked together with a disulfide bond as well as hydrophobic interactions, and is a homolog of the family of cell adhesion molecules Ig (Isom and Catterall, 1996). It also has three hypervariable loops located at the N-terminal. A schematic diagram of a generic beta subunit can be found in Figure 1.5.

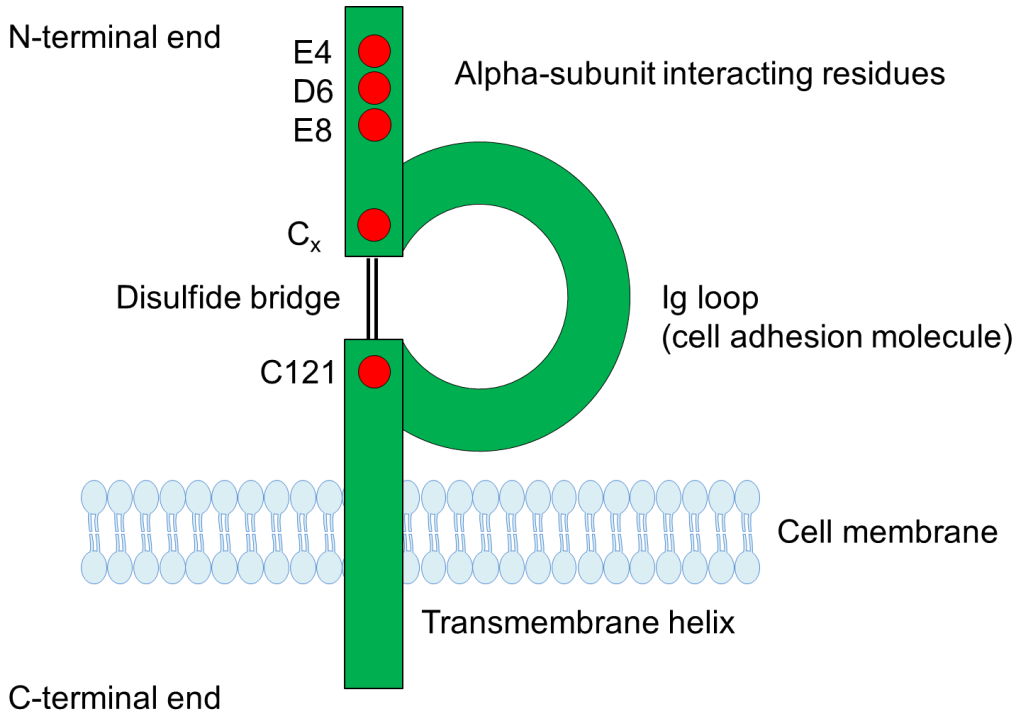

Figure 1.5. Schematic diagram outlining the basic features of the beta subunit.

E4, D6, and E8 denote alpha subunit interacting residues. C_x signifies cysteine residue combining with p.C121 a disulfide bridge. For instance in beta-1 this is p.C40 (Islas et al., 2013). p.C121W in *SCN1B* has been linked to generalized epilepsy with febrile seizures plus (GEFS+; (Wallace et al., 1998)). The Ig loop, a cell-adhesion molecule, is situated on the extracellular side. This domain is similar to other cell-adhesion molecules such as cadherins, integrins, and spectrins.

Crystal structures of β_1 and β_3 show that they are the most structurally homologous to myelin protein zero, a cell adhesion molecule integral to the myelin sheath structure of the peripheral nervous system (Gilchrist et al., 2013; Namadurai et al., 2014). From this homology, functions of beta subunits have been deduced. Later crystal structures of β2 and β4 confirmed these findings. Beta-1 and beta-3 isoforms bind non-covalently with alpha subunits through their N- and C-terminal domains. Meanwhile, β_2 and β_4 interact in a covalent manner through a disulfide bonds with cysteine residue located in the Ig loop (β_2 through residue p.C26; β_4:p.C58) (Chen et al., 2012)

Recently a cryo-EM structure of the Na_V channel of the electric eel was described in complex with beta-1, called $EeNa_V1.4$-β_1, at a 4.0 A resolution (Yan et al., 2017). It was found that transmembrane segment of β_1 complexed with S2 of VSD-III within the membrane, while the Ig motif binds the extracellular loops of DIV most adjacent to S6 and the extracellular loop adjacent to DI S5

Expression of beta subunits varies throughout the body, and beta subunits exist in various orthologs across vertebrates, invertebrates, and bacteria. During brain development of mammals, β_{1B} and β_3 are most common, but as the animal reaches adulthood, β_1 and β_2 are most ubiquitous. Subcellular localization of beta subunits is also diverse. For instance, beta subunits have been found at sites of high alpha subunit density, such as the axon initial segment (AIS) and nodes of Ranvier (Brackenbury et al., 2010). To this end, ankyrin-G has been hypothesized to complex with the c-terminal end of beta subunits at the AIS and nodes of Ranvier. Ankyrin G is believed through this to allow close contact with spectrin beta-IV (cytoskeletal protein) previously found to co-localize with alpha subunits of the sodium channel, through which it guides molecular assembly (Malhotra et al., 2002).

Beta subunits modulate alpha subunit expression and trafficking. If the two are co-expressed in vitro, expression of the cell membrane is increased. In fact, beta subunits

are so important for alpha subunit expression that *Scn2b null/null* mice halve the main pore current measured in pyramidal neurons of the hippocampus (Chen et al., 2002). This mechanism is dependent on which alpha subunit the beta subunit modulates. Knocking down beta-1 in granule cells of the cerebellum leads to a reduction in $Na_V1.6$ expression at the AIS, but vis-à-vis increases expression of $Na_V1.1$ and $Na_V1.2$ (Brackenbury et al., 2010).

In addition to trafficking and expression, beta subunits also directly modulate the function of alpha subunits. Changes in beta co-expression alter alpha function for instance by modulating rate of inactivation, activation/fast inactivation voltage-dependencies, and the peak current (Calhoun and Isom, 2014). In skeletal muscle, beta-1 subunits complex with $Na_V1.4$ and modulate their function. HEK293T cells expressing rat *SCN4A* when co-transfected with β_1 increased the current density and accelerated recovery from inactivation (Tammaro et al., 2002). Co-expression of the alpha subunit with β_1 subunit been found to shift the voltage-dependence of steady-state fast inactivation of $Na_V1.4$ by 10 mV in the hyperpolarizing direction (McClatchey et al., 1993). Co-expression of the human alpha (*SCN4A)* and beta-1 (*SCN1B)* subunits in HEK293T has previously been found to shift the voltage-dependence of slow inactivation in the depolarizing direction (Webb et al., 2009).

Lastly, beta subunits are also important for cell adhesion. Their conformation is similar to cadherins, spectrins, and integrins, and the Ig loop motif allows insertion into the membrane without the need for alpha subunit co-expression. In order to promote expression of Na_V channels however, adhesion is required (Kazarinova-Noyes et al., 2001; McEwen et al., 2004). For instance, beta-1 interacts with N-cadherin, sodium beta-2 subunits, Contactin-1, Neurofascin-186 (extracellular matrix assembly, neurite outgrowth), and Neurofascin-155. These adhesion properties are important for instance for axon guidance during development (O'Malley and Isom, 2015).

Knocking down *Scn1b* in mice was found to cause defective axonal extension and incorrect guidance of somata and axons of hippocampal interneurons of the CA1 and dentate gyrus. In the cerebellum, beta-1 deficiency put molecular cell layer axons in disarray, and reduced the number of cells in the granule cell layer of the dentate gyrus (Brackenbury et al., 2008, 2013).

1.3. The neuromuscular junction and skeletal muscle physiology

Descending motor pathways travel from upper motor neurons of the cerebral cortex via the corticospinal tract and synapse on interneurons and motor neurons in the ventral horn of the spinal cord, which in turn innervate skeletal muscle. In brief, as the action potential reaches the motor endplate, calcium influx through voltage-gated calcium channels into the terminal triggers vesicle fusion with the plasma membrane. The neurotransmitter acetylcholine is released in the cleft, binds acetylcholine receptors in the muscle endplate, allowing sodium and potassium influx into the postsynaptic cell membrane, resulting in depolarization of the muscle endplate. The entire process of how excitation through neurotransmission at the neuromuscular junction leads to muscle contraction is a complex process. This part will outline this in more detail in a stepwise manner.

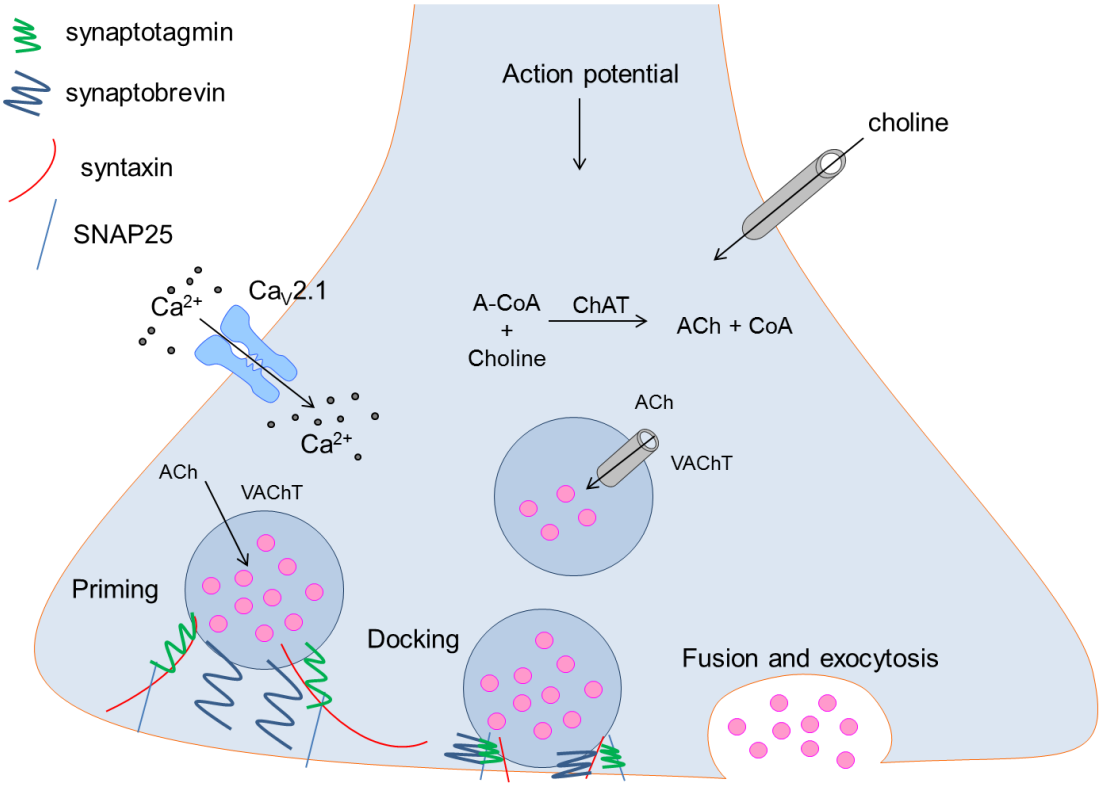

Figure 1.6. Mechanisms of synaptic release.

Action potential depolarizes the membrane, activating P/Q-type calcium channels. Acetylcholine is produced through the combination of acetyl-coenzyme A (A-CoA) and choline by ChAT (choline acetyltransferase), which is taken up into synaptic vesicles through VAChT (vesicular acetylcholine transporter). Calcium influx initiates the exocytosis process. Using a host of SNARE-s at the vesicle and membrane level, synaptic vesicles are primed for release, pulled towards the membrane, docked, fused with the membrane, and the contents of the vesicle released into the synaptic cleft.

Acetylcholine is synthesized in the motor neuron by taking up choline from the extracellular space through a process known as sodium-dependent-high-affinity-choline-uptake (SDHACU) (Amenta and Tayebati, 2008). When taken up by the presynaptic cell, choline acetyltransferase (ChAT) transfers an acetyl group from acetyl-coenzyme A (acetyl-CoA) to choline, producing acetylcholine and coenzyme A (byproduct). Because choline must be transferred from the extracellular medium this is considered a rate-limiting step in acetylcholine synthesis. Acetylcholine is taken up into synaptic vesicles through

the vesicular ACh transporter VAChT using a proton gradient set up by a vacuolar H^+-ATPase.

The release of acetylcholine into the synaptic cleft is triggered by the arrival of an action potential, which depolarizes the membrane, causing voltage-gated calcium channels to open, allowing calcium influx. A very rapid process of fusing the synaptic vesicle membrane with the presynaptic cell membrane occurs, expelling acetylcholine into the synaptic cleft, a process known as exocytosis (Südhof, 2013). This swift operation is mediated by SNARE proteins, found associated with the plasma membrane (target membrane; t-SNAREs) and docked to the vesicle membrane (vesicular; v-SNAREs) (Südhof and Rizo, 2011). SNARE stands for soluble N-Ethylmaleimide-sensitive factor attachment receptor. There are more than 60 types of SNAREs in mammalian cells, including: synaptotagmin and synaptobrevin (v-SNAREs) as well as SNAP25 and syntaxin (t-SNAREs). Synaptotagmin acts as a calcium sensor, binding calcium ions as they enter the cell, which changes its structure, allowing t-SNAREs to interact with the v-SNAREs (Brose et al., 1992; Li et al., 1995). This interaction pulls the vesicle close to the plasma membrane. The two membranes fuse and acetylcholine is exocytosed.

Acetylcholine binds ligand-gated nicotinic acetylcholine receptors (nAChRs) in the muscle endplate causing a conformational change which opens the receptor pore (Albuquerque et al., 2009). The pore is permeable to sodium and potassium, but the net current is inward due to the relative permeability of the channel and to their different electrochemical gradients. nAChRs are pentaheteromeric structure made up of different subunits: alpha, beta, delta, epsilon, and gamma, encoded respectively by the genes *CHRNA, CHRNB, CHRND, CHRNE,* and *CHRNG.* At the neuromuscular junction they are made up (in the adult) of two alpha, one beta, one delta, and one epsilon subunit. During development the gamma subunit is exchanged for an epsilon subunit, together forming a pore with increased conductance and reduced channel opening (Bouzat et al., 1994). This allows for more efficient transmission at the neuromuscular junction.

Net inward current (carried By Na^+) causes the membrane potential to depolarize, which is referred to as the endplate potential. If the depolarization of the endplate potential exceeds the $Na_V1.4$ channel activation threshold, a sarcolemmal action potential is triggered by activation of $Na_V1.4$ channels. The depolarization activates voltage-gated sodium channels, which in turn depolarize the membrane further, which allows even more sodium into the cell, which furthermore depolarizes the membrane. This cascade effect causes the upstroke and overshoot phase of the action potential.

To ensure neurotransmission at the neuromuscular junction is brief, acetylcholine diffuses away from the site, and acetylcholine is broken down to choline and acetate by acetylcholinesterase (Böhm et al., 1997). The latter is found either in the synaptic cleft, or bound to the postsynaptic membrane through collagen Q which in turn is bound to MuSK (Cartaud et al., 2004; Kawakami et al., 2011). Acetate is recycled into the presynaptic cell for the synthesis of acetyl-CoA. Choline can also be recycled and taken up into the presynaptic neuron through the choline transporter. If the rapid recycling of acetylcholine is disrupted, e.g. due to the impaired function of acetylcholinesterase, acetylcholine may build up in the synaptic cleft, such that stimulation of the endplate continues and muscle contraction persists.

The action potential is rapidly transduced along the sarcolemmal muscle fiber membrane and move in an inward, radial direction to the transverse (T)-tubules. In T-tubules the action potential activates and induces a conformational change in voltage-gated L-type $Ca_V1.1$ channels, located in the terminal cisternae. $Ca_V1.1$ channels are physically coupled to ryanodine type 1 receptors (RYR1) located in the sarcoplasmic reticulum. This physical coupling is what combines excitation of the muscle sarcolemma with contraction of the muscle, termed *excitation-contraction coupling.* Calcium influx through $Ca_V1.1$ is not required for RYR1-mediated calcium release, but rather the $Ca_V1.1$ channels act as voltage sensors for RyR1 channels activation (Flucher and Tuluc, 2017). RYR1 activation allows calcium release from the sarcoplasmic reticulum into the cytoplasm, which in turn

causes sarcomere shortening and muscle contraction by affecting myosin-actin interaction (Lee et al., 2015). This process is explained in detail below.

Skeletal muscle cells are long multinucleated cells running parallel to each other, with striations that run across (Figure 1.7.). Not much unlike a rope, muscle is made by many smaller strings. Many myofibrils together (small strings) form a muscle fiber (big string) containing nuclei, a sarcolemma, and energy-producing mitochondria. In turn the muscle fibers form bundles of big strings – fascicles. Many fascicles combined make up an entire muscle such as the brachioradialis of the forearm.

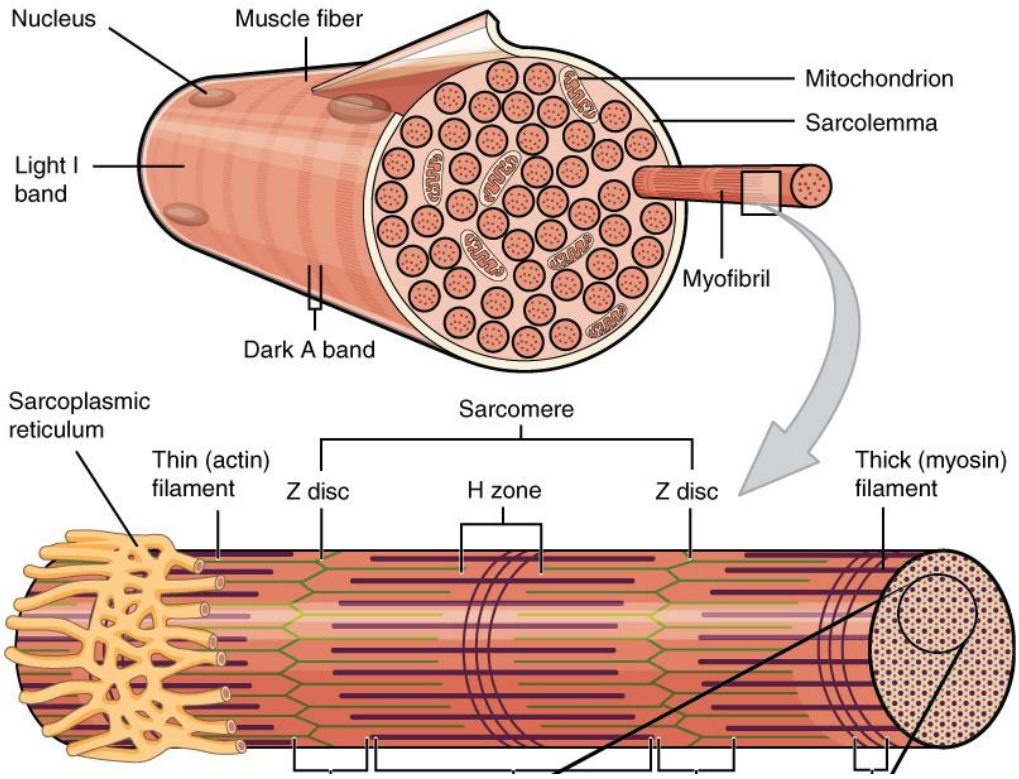

Figure 1.7. Skeletal muscle fiber structure and the insides of the myofibrils.

Reproduced from OpenStax College under a Creative Commons 4.0 license.

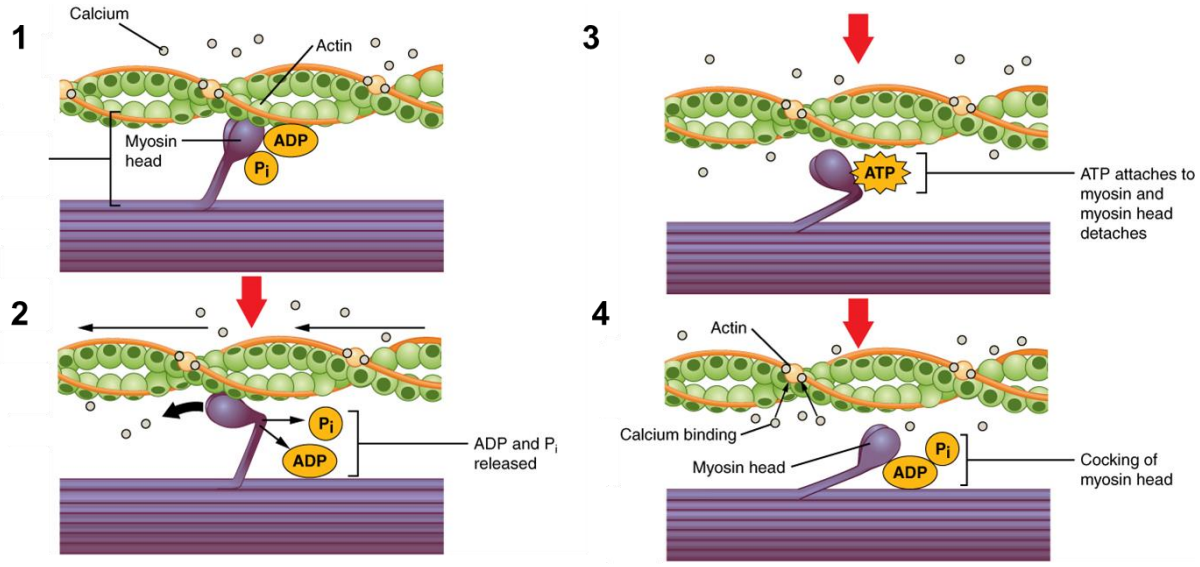

Figure 1.8. Sequence of skeletal muscle contraction within the sarcomere

Stepwise from 1 to 4 myosin heads bound with ADP+Pi adhere to actin filaments, the sarcomere moves, ADP and Pi is released making room for ATP attachment to myosin, causing the myosin head to detach. Calcium binds troponin and tropomyosin resumes its relaxed position. In 2: Black arrows indicate the direction of actin movement causing sarcomere shortening. Tropomyosin: orange lines; actin: green balls; troponin: orange balls; dark green circles: binding site for myosin. From OpenStax Anatomy and Physiology (Version 8.25; Creative Commons 4.0 International)

The muscle contracts and relaxes. The myofibrils are in a lengthwise manner divided into sarcomeres, which contain filaments actin and myosin (Figure 1.8). Their interaction forms the basis of muscle contraction. Actin is a thinner, while myosin filaments are thick. Bordering the ends of the sarcomere are the Z lines (or Z discs), which during contraction of the sarcomere move closer to each other (McKillop and Geeves, 1993). At rest myosin and actin do not interact. Attached to actin are two proteins called troponin and tropomyosin, which together prevent myosin binding.

When calcium is released from the sarcoplasmic reticulum, troponin binds calcium, pulling tropomyosin from actin binding sites thereby exposing these to myosin (Squire and Morris, 1998). Only myosin heads carrying adenosine diphosphate and phosphate are bound to

the thin actin filament and upon binding releases its stored energy, thereby pulling on the actin strand, shrinking the sarcomere. Adenosine diphosphate and phosphate unbind from the myosin heads, allowing ATP to bind, which in turn causes the myosin to release from actin (Lehman et al., 2000). Calcium pumps in turn refuel calcium stores, so that calcium unbinds troponin, and tropomyosin returns to its original state. The muscle returns to its relaxed state.

Sodium channels inactivate after prolonged depolarization and voltage-gated potassium channels activate causing potassium efflux. But unlike neurons, potassium accumulation in the T-tubules reduces the role of the potassium gradient in membrane repolarization. For instance during muscle contraction, potassium extrusion leads to accumulation of potassium in the T-tubules that cannot be cleared rapidly enough. This activity diminished the concentration gradient of potassium ions leading, to depolarization of the potassium reversal potential and consequently a reduction in the driving force of potassium. Instead, in the muscle, Cl^- influx through the depolarization activated ClC-1 chloride channel plays a key role in the membrane repolarization (Steinmeyer et al., 1994). Voltage-gated potassium channels such as $K_V3.4$ have been suggested to help set the resting membrane potential in the muscle (Abbott et al., 2001). Inward rectifier potassium channels e.g. $K_{ir}2.1$ also play a role in maintaining resting membrane potential by allowing transient low-amplitude potassium efflux as the membrane potential exceeds the potassium reversal potential. They also contribute to potassium influx during hyperpolarization, thus clearing accumulated potassium from the T-tubules.

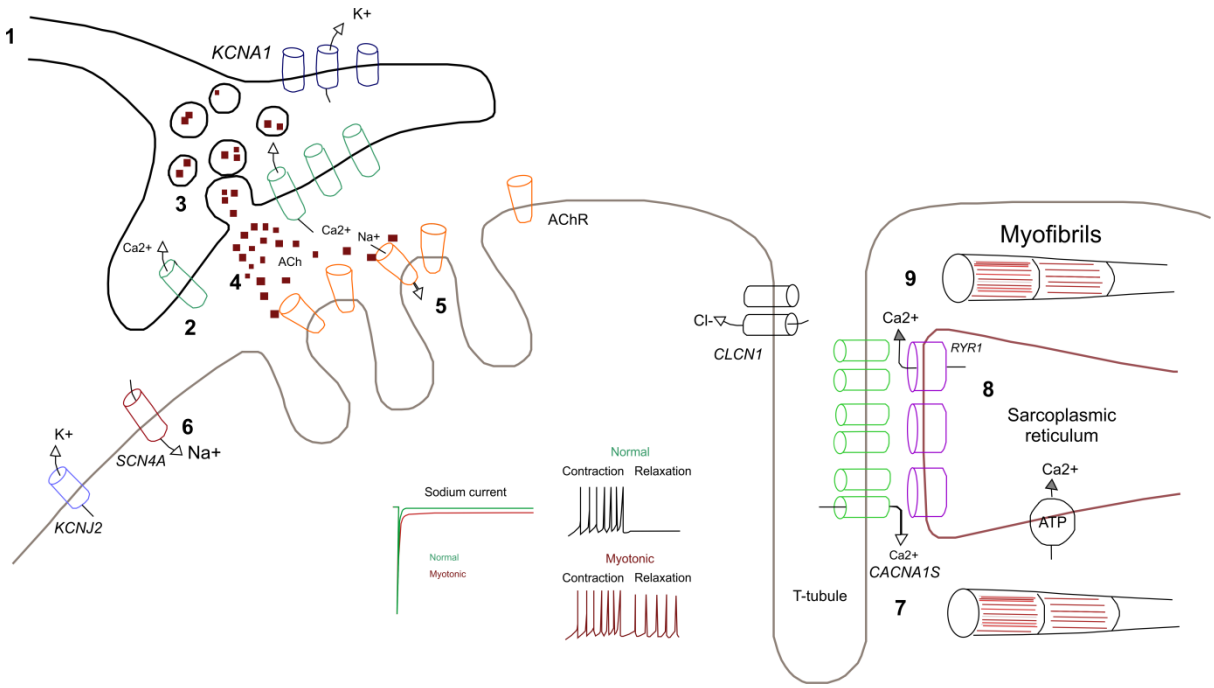

Figure 1.9. Simplified schematic diagram of the neuromuscular junction. 1. Action potential arrives at presynaptic terminal **2.** Depolarization of membrane allows calcium channel activation and calcium influx **3.** Calcium influx triggers vesicle membrane fusion **4.** Vesicle contents (ACh) released into synaptic cleft **5.** ACh binding of ACh receptors allows cation influx **6.** Depolarization of membrane allows sodium channel activation and sodium influx **7.** Transduction into T-tubules activates *CACNA1S* and *RYR1* **8.** Calcium release from sarcoplasmic reticulum into cytoplasm **9.** Myofibril contraction *Insert left:* Sodium current in normal (green) and myotonic (red) muscle. *Insert right:* Action potential firing measured during contraction and subsequent relaxation in normal and myotonic. Re-drawn from (Ashcroft, 2006).

1.4. Disorders of skeletal muscle

There are several groups of skeletal muscle disorders, including myotonias, periodic paralyses, congenital metabolic, muscular and endocrine myopathies, as well as drug-induced myopathies, inflammatory muscle disorders, and neurogenic disorders. This section will discuss briefly skeletal muscle disorders that are the most common and most related to the experimental aims and results of this thesis. As the focus of this project is

the inherited skeletal muscle channelopathies of voltage gated sodium channel $Na_V1.4$, a more detailed description of channelopathies of skeletal muscle, and in particular due to mutations in *SCN4A* will follow.

1.4.1. Congenital myopathies

The congenital myopathies are a group of clinically and genetically heterogeneous muscle disorders characterized by hypotonia and weakness, with typical presentation at birth (North *et al.*, 2014). Disease severity varies widely from profound muscle weakness leading to lethality *in utero* or shortly after term, to less severe muscle weakness presenting in infancy or in childhood. Clinical features include prominent facial muscle weakness with or without ptosis and predominant proximal limb muscle weakness. The classical pathological features include: the presence of nemaline rods; core areas devoid of oxidative enzyme; increased number of centrally located nuclei; and predominance of smaller type 1 fibers (North et al., 2014). Most genes associated with congenital myopathy encode proteins involved in excitation-contraction coupling, myofibrillar force generation, or regulation of membrane trafficking and signaling (Ravenscroft et al., 2014).

When excitation-contraction coupling mechanism is disturbed, disease may arise. Disorders of skeletal muscle contraction include those due to mutations in *RYR1* and *CACNA1S*, which encode ryanodine receptor 1 and $Ca_V1.1$, respectively. These channels are responsible for mediating calcium release from the muscle sarcolemma into the cytoplasm. Mutations in RYR1 can cause malignant hyperthermia, and congenital myopathies such as central core disease (a form of myopathy) and multiminicore disease (Wu et al., 2006). These diseases affect calcium release in the muscle and consequently excitation-contraction coupling. Central core disease is primarily autosomal dominant form of congenital myopathy due to RYR1 mutations (Wu et al., 2006). Patients present with muscle weakness first from early childhood, with delayed motor development milestones. Pathology examination shows cores at the center of type 1 muscle fibers.

Table 1.2. Summary of disorders affecting skeletal muscle

CNBP: the cellular nucleic acid binding protein, DMPK: myotonin-protein kinase, SMN: survival motor neuron; NM2: dynamin 2; DOK7: Adaptor protein crucial for synapse formation, Rapsyn: associates with MuSK important for acetylcholine clustering, RYR1: ryanodine receptor 1, MuSK: receptor tyrosine kinase aiding clustering of nAChR, agrin: proteoglycan that activates MuSK; LRP4: low-density lipoprotein receptor-related protein 4, interacts with agrin/MuSK

1	Neurogenic	Demyelinating disorders e.g. multiple sclerosis	Loss of myelinating sheaths of axons leads to progressive nerve degeneration causing muscle weakness
		Amyotrophic lateral sclerosis	Motor neuron disease (upper and lower) causing muscle weakness and progressive degeneration; lethal
		Spinal muscular atrophy	Loss of motor neurons causing progressive muscle weakness and progressive loss of muscle mass; autosomal recessive; *SMN* gene
2	Muscular dystrophy	Duchenne (more severe)	Muscle weakness, progressive muscle atrophy; lethal; *dystrophin*
		Becker's (milder)	Milder form of Duchenne, muscle weakness, progressive muscle atrophy; lethal; *dystrophin*
		Myotonic dystrophy 1	Weakness and gradual loss of muscle mass caused by CTG repeats in *CNBP*
		Myotonic dystrophy 2	Weakness and gradual loss of muscle mass due to CCTG repeats in *DMPK*
3	Congenital myopathies	Central core disease	Autosomal dominant form of congenital myopathy due to RYR1 mutations
		Nemaline rod myopathy	Mutations in *NEB* (nebulin, an actin-binding protein) and *ACTA1* (alpha-actin) predominate, causing difficulties in muscle contraction at the sarcomere level
		Centronuclear myopathy	Reduced muscle tone, muscle weakness; autosomal dominant mutations in *DNM2*
4	Metabolic myopathies	McArdle disease	Glycogen storage disease type V characterized by muscle pain, and progressively worsening weakness and atrophy due to defective myophosphorylase
5	Inflammatory myopathies	Inclusion body myositis	Slow progressive weakness, both proximal and distal muscles, protein deposits in muscle; either sporadic or inherited
		Dermatomyositis	Skin rash, muscle weakness, and inflammatory myopathy
6	Toxic myopathies	State-induced necrotizing myopathy	Complication from statin use (lipid-lowering medication), proximal muscle weakness
		Colchicine-induced vacuolar myopathy	Complication from colchicine use in patients with compromised renal function; proximal muscle weakness, distal sensory loss
7	Neuromuscular junction disorders	Myasthenia gravis	Autoimmune disease attacking neuromuscular junction proteins e.g. acetylcholine receptors, MuSK, agrin, LRP4; muscle weakness
		Lambert-Eaton	Autoimmune, antibodies against P/Q-type calcium

			channels of presynaptic cell
		Congenital myasthenia	Weakness, often with problems swallowing or breathing; due to mutations in synaptic, presynaptic, or postsynaptic proteins e.g. DOK7, Rapsyn,
8	Channelopathies	Andersen-Tawil syndrome	Kir2.1 dysfunction due to mutations in *KCNJ2* mutations causing a multi-system disorder with periodic paralysis, dysmorphic features of the bone (e.g. scoliosis), and ventricular ectopy
		Thyrotoxic hypoPP	Episodes of muscle weakness amidst hyperthyroidism and often with hypokalemia; mutations in Kir2.6 (*KCNJ18*) and *CACNA1S*
		Myotonia congenita	Dominant or recessive due to *CLCN1* mutations causing myotonia due to muscle membrane hyperexcitability Mutations in *CLCN1* causing loss of function of CLC-1, e.g. due to compromised chloride conductance or reduced surface expression
		Hyperkalemic periodic paralysis	Dominantly inherited *SCN4A* mutations resulting in gain of function; sodium channel overactivity may lead to inactivation of the voltage gated sodium channels, inexcitability of the muscle and can develop into episodes of paralysis.
		Hypokalemic paralysis type 1	*CACNA1S* mutations cause $Ca_V1.1$ dysfunction, an aberrant leak current causing sodium channel inactivation, which leads to episodes of flaccid paralysis in the presence of low serum potassium (Wu et al., 2018)
		Hypokalemic paralysis type 2	*SCN4A* mutations causing an aberrant leak current leading to sodium channel inactivation, which results inepisodes of muscle weakness in the presence of low serum potassium
		Sodium-channel myotonia	$Na_V1.4$ gain of function e.g. enhanced voltage-dependence of activation causing hyperexcitability of the sarcolemma
		Paramyotonia congenita	$Na_V1.4$ gain of function causing hyperexcitability of the sarcolemma, with at times sustained depolarization

When defective ryanodine receptors cause a leak of calcium ions into the cytoplasm the cytoplasmic calcium concentration increases and stores of calcium in the sarcoplasmic reticulum are exhausted (Wu et al., 2006). This is due to mutations outside the C-terminal region of the RYR1 protein. If mutations are instead in the pore region channel gating may instead be affected, which might uncouple the excitation contraction coupling.

Malignant hyperthermia is caused by mutations in *CACNA1S* or *RYR1*, and is primarily an autosomal dominant disorder. As one of the most prevalent causes of death during anesthesia, malignant hyperthermia patients are particularly susceptible to adverse effects of inhalant anesthetics such as halothane. In addition to hyperthermia, patients may present with muscle rigidity, arrhythmia, rhabdomyolysis, tachycardia, respiratory distress, and death.

1.4.2. Neuromuscular junction disorders

Myasthenia gravis is a disease where the body's own immune system attacks the body (autoimmune). Antibodies attack postsynaptic receptors AChR or muscle-specific receptor tyrosine kinase (MuSK) (Sivak, 2016). MuSK forms a complex with agrin and LRP4 (low density lipoprotein receptor related protein 4), which help AChR's cluster at the postsynaptic cell membrane (Ohno et al., 2017). Mutations in MuSK destabilize clustering of acetylcholine receptors (Ohno et al., 2017; Zong and Jin, 2013). Antibodies against AChR either inhibit or destroy them, consequently the neuromuscular junction collapses. Damage to the neuromuscular junction ensues, causing $Na_V1.4$ channel downregulation and consequently the input required to elicit an action potential to allow muscle contraction is raised. As a result, muscle weakness ensues.

Lambert-Eaton myasthenic syndrome is another form of autoimmune disorder where antibodies are thought to bind presynaptic P/Q-type calcium channels ($Ca_V2.1$), thereby reducing the amount of calcium taken up in the presynaptic neuron. In turn this reduces

the amount of acetylcholine exocytosed; the probability of endplate potential generation is drastically reduced. As sarcolemmal excitation is reduced muscle weakness ensues.

Mutations in other neuromuscular junction proteins, such as DOK7, choline acetyltransferase (CHAT) (Ohno et al., 2001), as well as *SCN4A* can give rise to congenital myasthenic syndrome. This heterogeneous group of conditions is associated with neuromuscular junction defects either in the pre- or postsynaptic terminal or the synaptic basal lamina (Engel et al., 2003). Some patients present with generalized fatigable weakness and recurring episodes of bulbar and respiratory paralysis from birth. Some also develop apnea.

1.4.3. Muscle dystrophy

Myotonic dystrophy is characterized by muscle weakness and gradual loss of muscle mass. It is divided into two types: DM1 and DM2 (Cho and Tapscott, 2007). DM1 is caused by trinucleotide repeats in intron 1 of the gene encoding the cellular nucleic acid binding protein CNBP (Fu et al., 1992), while DM2 is caused by tetranucleotide repeats in DMPK encoding the myotonin-protein kinase (Liquori et al., 2001). Both disorders are autosomal dominant. Although the nucleotide repeats disrupt different genes, they act through a similar mechanism. CUG (DM1) and CCUG (DM2) RNA repeats are expanded, generating ribonuclear inclusions, which perturb the function of RNA binding proteins. One such example is the muscleblind-like proteins MBNL1-3. Knocking down Mbnl3 in mice disrupts muscle regeneration, indicating dysfunctional function of MBNL proteins downstream are part of the disease pathomechanism (Poulos et al., 2013).

Duchenne's muscular dystrophy is a progressively worsening disease characterized by muscle weakness and atrophy. Generally individuals die from cardiac arrest or respiratory insufficiency before the end of the third decade. Duchenne's milder counterpart is Becker's muscular dystrophy. Both diseases are caused by mutations in the *dystrophin*

gene, often due to duplications, frameshifts, or long deletions. Dystrophin is part of the dystrophic associated protein complex, which is important for cytoskeleton properties at the cell membrane (Salmaninejad et al., 2018). This complex together anchors the cell membrane with the extracellular matrix. As muscles in individuals with Duchenne's and Becker's contract and relax, the muscle becomes damaged, degrades, and wastes away.

1.4.4. Skeletal muscle channelopathies

The skeletal muscle channelopathies are a group of rare neuromuscular disorders caused by mutations disrupting the function of ion channels controlling skeletal muscle excitability, including $Na_V1.4$, $Ca_V1.1$, ClC-1, and $K_{ir}2.1$ (Ptáček, 2015). Two main presentations characterize these disorders: myotonia and periodic paralysis (Figure 1.6.). Myotonia is caused by muscle overactivity, while periodic paralysis is due to depolarization block. The same condition can be caused by mutations in different genes, and mutations in the same gene can result in disparate presentations.

Myotonia is divided into two groups: either dystrophic myotonia (e.g. myotonic dystrophy) or the non-dystrophic myotonias, which include myotonia congenita, sodium-channel myotonia, and paramyotonia congenita. Although they have different etiology and disease presentation, they all have the characteristic muscle stiffness – myotonia. Muscular dystrophy is present only in the former group, characterized by muscle weakness and successive skeletal muscle breakdown.

1.4.4.1. Myotonia congenita

Myotonia congenita (MC) is the most common type of non-dystrophic myotonias with an estimated prevalence of 0.52 per 100,000 in the English population (Horga et al., 2013). Myotonia is the inability to relax muscle after contraction, due to repetitive firing of action potentials in an aberrantly hyperexcitable membrane due to mutations in the *CLCN1* gene encoding the ClC-1 chloride channel (Pusch, 2002). These mutations cause loss of function by reducing the repolarizing chloride current, thus increasing cell excitability.

This persistent muscle contraction is a result of the diminished chloride conductance, which in normal conditions amounts to 85 % of the membrane conductance at rest (Bryant and Morales-Aguilera, 1971). In the T-tubule system of skeletal muscle potassium builds up extracellularly after persistent muscle contraction, such that in ClC-1 deficient muscle

repolarization by chloride is defective, thus resulting in depolarization of the muscle. Myotonia congenita can be inherited either in a dominant and recessive manner. Mutations in *CLCN1* have not been associated with periodic paralysis, but as movement is initiated may experience a brief episode of muscle weakness.

Chloride ClC-1 expression is upregulated during development, and symptoms typically develop later (Pierno et al., 1999). In the autosomal dominant form, symptoms arise during early childhood or infancy, while recessive patients develop symptoms later in the third or fourth decade (Colding-Jørgensen, 2005; Pusch, 2002).

In dystrophic myotonia ClC-1 function is affected also affected. Nucleotide repeat expansions result in erroneous *CLCN1* spicing and consequently in reduction on ClC-1 currents in the muscle (Ursu et al., 2012).

1.4.4.2. Andersen-Tawil syndrome

Loss of function mutations $K_{ir}2.1$ can predispose to abnormal depolarization. Andersen-Tawil syndrome is a rare multi-system disorder with periodic paralysis, dysmorphic features of the bone (e.g. scoliosis), and ventricular ectopy (Tawil *et al.*, 1994). It is caused by mutations in *KCNJ2*, the gene encoding the inward rectifier potassium channel $K_{ir}2.1$ (Plaster et al., 2001). Mutations cause loss of function and often dominant-negative effects on co-expressed wild-type *KCNJ2* constructs (Davies et al., 2005; Plaster et al., 2001; Tristani-Firouzi et al., 2002). Reduction in the hyperpolarizing potassium current results in depolarization of the membrane, sodium channel inactivation and episodes of paralysis. Periodic paralysis in these patients is often but not always associated with hypokaleemia. $K_{ir}2.1$ is also expressed in heart and bone, explaining the extramuscular symptoms.

1.4.5. $Na_V1.4$ channelopathies

1.4.5.1. Sodium-channel myotonia, paramyotonia congenita, and hyperkalemic periodic paralysis

Sodium-channel myotonia, paramyotonia congenita (PMC), and hyperkalemic periodic paralysis are rare disorders with a point prevalence of approximately 0.06, 0.17, and 0.13 in 100,000 in England, respectively, due to mutations in *SCN4A* (Horga et al., 2013; Ptácek et al., 1992).

Patients with sodium-channel myotonia present with myotonia only. Paramyotonia congenita and hyperPP patients present with both myotonia and periodic paralysis. In hyperPP patients paralysis is the predominant clinical presentation, while in PMC patients myotonia is the primary symptom. Patients with sodium-channel myotonia are often sensitive to changes in serum potassium. In paramyotonia congenita, attacks are exacerbated by cold temperatures or exertion and can last from minutes to hours or days. During paralytic episodes in hyperPP, an increased level of serum potassium, which may depolarize the muscle, is often found (Ptácek et al., 1991).

Sodium-channel myotonia, PMC, and hyperPP are typically caused by dominantly inherited *SCN4A* mutations resulting in gain of function by enhancing channel activation or attenuating fast inactivation (Matthews et al., 2010). In case of myotonia, increased sodium currents cause sarcolemmal hyperexcitability. However, the increased depolarization due to sodium channel overactivity may lead to inactivation of the voltage gated sodium channels, inexcitability of the muscle and can develop into episodes of paralysis. Mutations in *SCN4A* associated with myotonia are often localized to regions important for regulating fast inactivation (DIII-DIV loop, C-termini of S6 helices)(Jurkat-Rott and Lehmann-Horn, 2006) or activation. It has been suggested that mutations with larger gating defects result in paralytic episodes while mutations with mild defects result in myotonia only, though direct correlation has not been established. In addition, it has been

suggested that variants that develop hyperPP require compromised slow inactivation (Hayward et al., 1997, 1999).

With increased activity, potassium may accumulate in the narrow T-tubules. If an *SCN4A* variant attenuates fast inactivation properties of the channel, a large sodium current can be triggered by the extracellular potassium accumulation, which consequently triggers the characteristic rapid action potential firing in the muscle with myotonia (i.e. failure to relax the muscle).

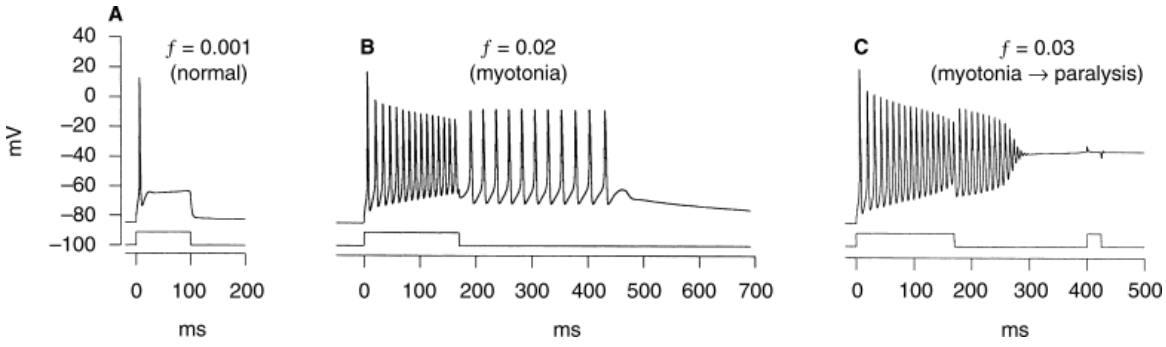

Figure 1.10. Models of myotonia and myotonia transitioning into an episode of paralysis in hyperPP muscle. Computational model of a muscle cell in a normal, myotonic, and myotonic transitioning to paralysis state. f represents the fraction of Na_V channels that did not inactivate. This value is low in A, eliciting a single action potential with a subsequent refractory period. In (B) the failure fraction is 2 % of Na_V channels, resulting in the persistent discharge after the end of the (square-shaped) current pulse. In (C), 3 % of channels fail to inactivate, leading again to a myotonic burst after end of current pulse, but with reduced amplitude compared to (B). These discharges end before t=300 ms, and at t=400 ms a new pulse is generated, which fails to elicit an action potential, i.e. the muscle has now entered a state of paralysis. Figure from (Cannon, 2000).

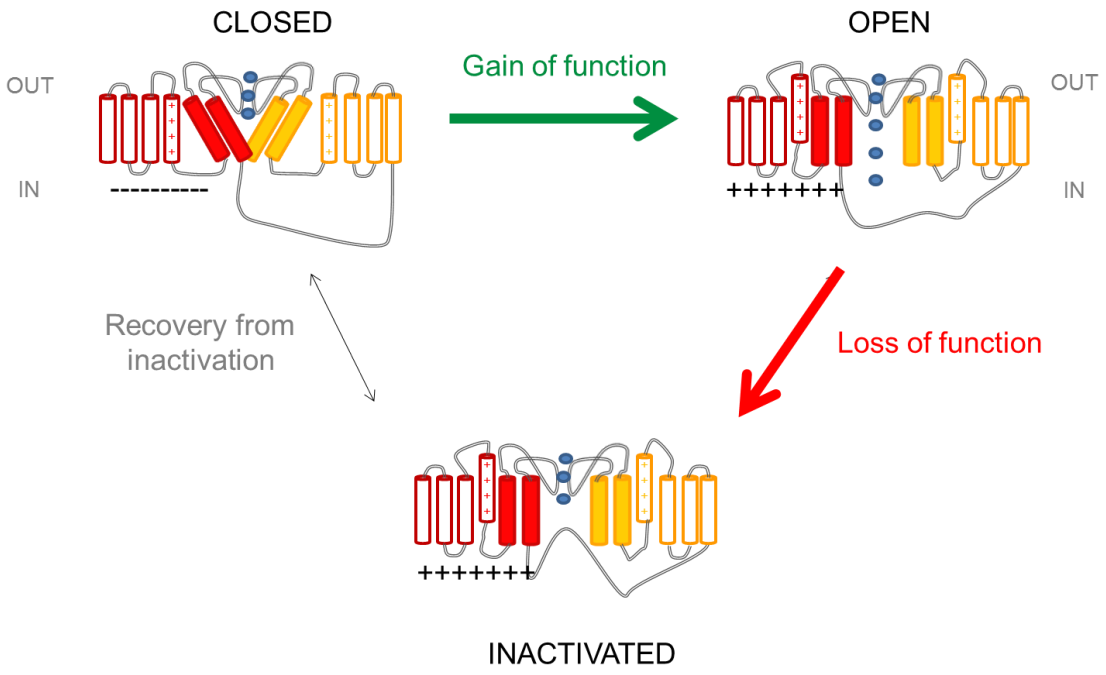

Figure 1.11. Gain of function mutations increase the probability of the channel to enter and stabilize the open state while loss of function mutations may stabilize the inactivated conformation.

NaV channels have three functional states: closed, open or inactivated. Channel activation moves S4 outward due to electrostatic repulsion. This movement pulls S5 and S6 to open the intracellular gate via the S4-S5 loop. Channels may inactivate from either the closed or the open channel state. Specific missense mutations ablate one or several of these processes, for instance by altering the channel's response to voltage changes across the membrane, leading to either gain or loss of channel function effects. In green is illustrated a gain of function mutation, which stabilizes the channel's open state, e.g. in sodium-channel myotonia. In red is a loss of function mutation, which may stabilize the inactivated state, e.g. in myasthenia. Only two domains are shown for clarity.

When myotonia is present, the sodium channel blocker mexiletine is currently first line treatment. A double-blind placebo-controlled trial found mexiletine to be efficacious in 70 % of 59 adult participants with a non-dystrophic myotonia (Statland et al., 2012). Other sodium channel blockers are also in clinical use.

Myotonia caused by mutations in *SCN4A* is associated with other presentations, including severe neonatal episodic laryngospasm in infants. Although $Na_V1.4$ is expressed in all skeletal muscle, respiratory compromise, stridor, or dysphagia rarely occur in adults (Lerche et al., 1993; McClatchey et al., 1992). Myotonia typically presents in the first decade of life, but is also found in neonates. A severe infantile *SCN4A* myotonic phenotype has recently been described (Lee and Chahin, 2013). The affected infants display brief, recurrent episodes respiratory muscle myotonia with apnea or hypoxia and cyanosis. The episodes can be life threatening and require intensive care support. The majority of these events are associated with severe neonatal episodic laryngospasm (SNEL) caused by laryngeal muscle myotonia (Lion-François et al., 2010). Disease severity is variable; however, some infants display stridor but with minimal respiratory compromise (Matthews et al., 2011a).

To date, only 15 cases have been described. A p.G1306E is the most commonly found mutation in SNEL. This residue is located to the intracellular DIII-DIV linker. This region is important for fast inactivation, where the hinged lid mechanism is located. Mutations in this region often disrupt fast inactivation. This glycine-to-glutamic acid substitution inserts a negative charge in place of a small glycine residue, and consequently attenuated the rate of fast inactivation, and the voltage-dependence of fast inactivation (Mitrović et al., 1995).

Despite spontaneously improved laryngeal and respiratory function in mildly affected patients, myotonia of the face and limb muscles often develops later in life (Singh et al., 2014; Yoshinaga et al., 2012). In these studies, most infants were efficaciously treated with a sodium channel blocker after genetic diagnosis. The more severely affected infants were treated earlier. All but one child had improved respiratory function (Caietta et al., 2013; Lion-François et al., 2010). Two deaths occurred: one in a child who was diagnosed posthumously, and the other in an infant with an initially good mexiletine response – which

ultimately was incomplete – leading to respiratory arrest (Gay et al., 2008; Lion-François et al., 2010).

Replacing mexiletine with flecainide helped respiratory insufficiency in one patient who did not respond to mexiletine (Desaphy et al., 2013). In a study by the same group in 2016, they determined the differential block sensitivity of mexiletine compared to flecainide in vitro. They expressed the mutation of a patient (P1158L located to the S4-S5 linker of DIII) in tsA201 cells and found that the sensitivity of mexiletine was reduced compared to flecainide, which was more efficacious (Desaphy et al., 2016).

1.4.5.2. Treatment in non-dystrophic myotonia

In sodium-channel myotonia, the first line of treatment is mexiletine, a class Ib anti-arrhythmic agent, which by blocking $Na_V1.4$ reduces channel open probability thus repolarizing the cell membrane. In 2012 a randomized clinical trial found that the patient-reported muscle stiffness improves in a 4-week treatment process (Statland 2012). This was an important study, as previously only anecdotal evidence or individual case reports had been presented. In the Statland (2012) study, primary focus was muscle stiffness – a crucial symptom in any form of NDM. *CLCN1*-associated myotonia had a higher improvement of hand-grip myotonia compared to sodium channel myotonia patients.

At present there are no drugs that act directly on ClC-1 channels. In myotonia congenita, carbonic anhydrase inhibitor acetazolamide has also been found efficacious in some cases. Overall, sodium channel blockers such as local anesthetics, anti-convulsants, and anti-arrhythmic agents have been reported to be efficacious but not tested systematically in clinical trials. One ongoing trial is ranolazine, in PMC, MC, and myotonic dystrophy type 1 (ClinicalTrials.gov identifier: NCT02251457). Ranolazine has been found to inhibit *SCN4A* gain of function mutations associated with PMC such as p.R1448C/H/P (El-Bizri et al., 2011)

Another trial in 2015 of mexiletine long-term efficacy and safety in non-dystrophic myotonia established that if tolerated, mexiletine should be used as a symptom control, with the dosage titrated slowly to avoid adverse effects (Suetterlin et al., 2015). In myotonia due to *CLCN1* mutations, patients often require a higher dose (not directly acting) thus increasing the risk of adverse effects.

1.4.5.3. Hypokalemic periodic paralysis

Hypokalemic periodic paralysis is characterized by episodes of paralysis concurrent with low serum potassium levels, with a prevalence rate of 0.17 in 100,000 in England (Horga et al., 2013; Simkin and Bendahhou, 2011). This disorder can be caused by mutations in *CACNA1S* encoding the L-type $Ca_V1.1$ calcium channel or the skeletal muscle sodium channel $Na_V1.4$ encoded by *SCN4A*. Most mutations associated with hypoPP affect the voltage sensing arginines in VSDs I-III of both channels (Matthews et al., 2009); however 10-20 % remain undiagnosed.

Mutations in *SCN4A* have been more extensively studied. The clinical presentation of $Ca_V1.1$ and $Na_V1.4$ hypoPP is similar, with recurrent attacks of paralysis in serum hypokalemia (<3.5 mM). Carbohydrate rich meals raise glucose and consequently insulin, which trigger potassium uptake. Equally this may occur after vigorous exercise, where the long exercise test can be used as a clinical measure to diagnose periodic paralysis. Episodes of weakness often occur as the individual wakes up (especially if a carbohydrate rich meal was consumed the night before).

Neutralization of $Na_V1.4$ S4 gating charges in DI-DIII, but not in DIV, introduce gating pore currents (Francis et al., 2011a; Sokolov et al., 2007; Struyk and Cannon, 2007a).The resultant intracellular accumulation of cations results in paradoxical membrane depolarization and $Na_V1.4$ channel inactivation, such that the muscle is unable to contract, resulting in episodic paralysis (Sokolov et al., 2008). The gating pore currents associated

with gating charge neutralization in $Ca_V1.1$ were not experimentally verified in muscle cells until recently (Fan et al., 2013).

Gating pore current is often a non-selective cation leak (Moreau et al., 2014). For instance, gating pores have been found to conduct various ions, including K^+, Li^+, or Cs^+ (Moreau et al., 2014), while other divalent cations may block the pore (Ba^{2+}, Zn^{2+}) in certain mutant channels, e.g. p.R663G (Sokolov et al., 2007). However, if the arginine is mutated to a histidine, a proton leak ensues which is dependent on the pH gradient across the membrane. If the pH is higher in the intracellular medium, the chemical potential drives protons inward, given the presence of a downward concentration gradient for protons. For example, increasing the intracellular pH to 9 increased the gating pore currents in p.R663H $Na_V1.4$ mutant channels (Struyk and Cannon, 2007b).

The small amplitude inward gating pore current per se is unlikely to have a deleterious effect in healthy muscle at physiological conditions. In typical physiological conditions the extracellular potassium concentration is 4.5 mM. Modeling the gating pore current shows that this results in a 3 mV depolarization of the membrane (Struyk and Cannon, 2008). But if the extracellular potassium is lowered (approximately 2.5 – 3.5 mM), the reversal potential of potassium is left-shifted and the muscle fiber correspondingly hyperpolarizes. However, this hyperpolarization in potassium reversal reduces the outward component of inward rectifying potassium currents, likely due to increased block by intracellular Mg^{2+} and polyamines at resting muscle membrane potential. Thus, rather than hyperpolarizing the muscle, hypokalemia leads to depolarization of the muscle, in particular in presence of gating pore currents. The inward rectifying potassium channel K_{ir} balances the inward gating pore current at normokalemia, but at hypokalemia is unable to compensate for the gating pore current. This (paradoxically) depolarizes the muscle membrane. It is not fully established how muscle membrane potential recovers but this may involve the action of delayed rectifying channel called K_{DR}, which discharges potassium to repolarize the membrane. This is the physiological mechanism underlying periodic paralysis. Reduced

potassium efflux through K_{ir} during low extracellular potassium conditions is also possible in healthy muscle in absence of gating pore currents, but only at extreme conditions (<1 mM).

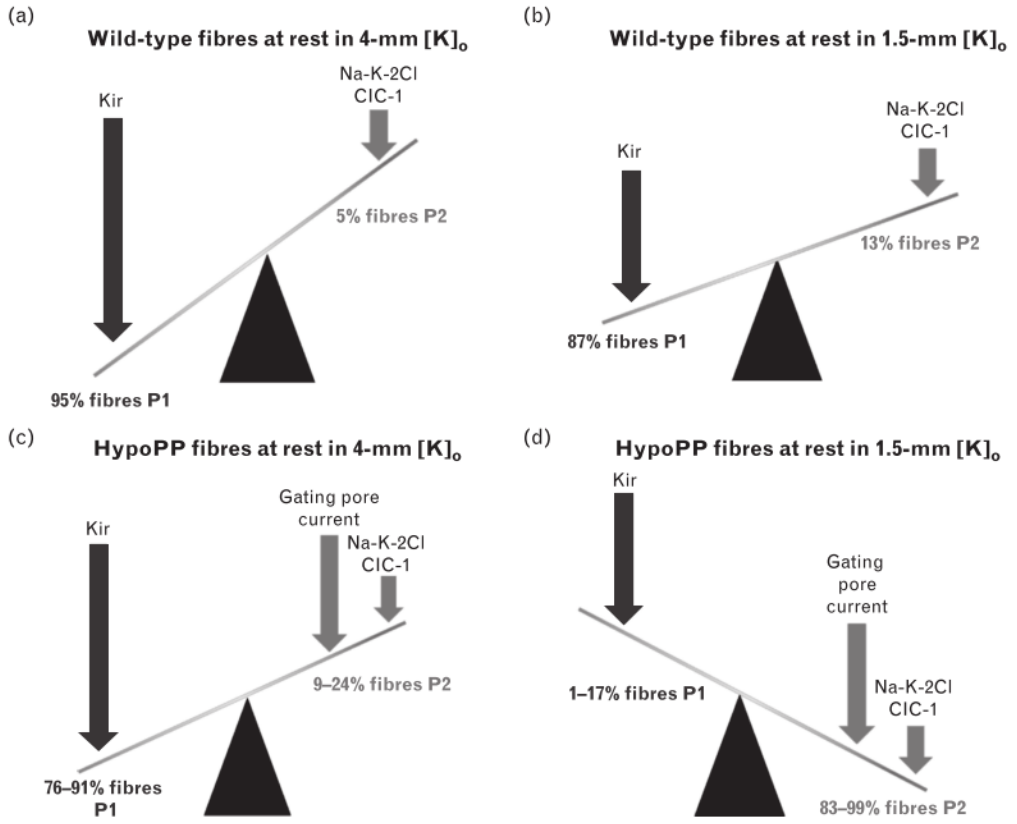

Figure 1.12. The bistable resting membrane potential in skeletal muscle in healthy and hypoPP fibers.

The skeletal muscle membrane is bistable, i.e. with two resting membrane potential levels, known as P1 (-90 mV) and P2 (-60 mV). At normal serum K^+ (4 mM), 95 % of the muscle is in P1, which is sustained by Kir channels. When the extracellular K+= concentration drops to hypokalemic levels (e.g. 1.5 mM), the number of P2 fibers increases to 13 %, i.e. more muscle membranes are depolarized. This may be reversed by addition of bumetanide, which antagonizes the Na-K-2Cl (NKCC) transporter, and thereby preventing Cl^- accumulation inside the muscle. When chloride accumulates intracellularly, its reversal potential is depolarized, which leads to depolarization of the membrane. In the fibers of patients with hypoPP (C), 76-91 % of fibers are in P1 at 4 mM potassium, but when hypokalemia ensues (1.5 mM), most (83-99 %) of fibers are in the P2 state. This is a combination of the influx of the depolarizing gating pore current, and ClC-1 and NKCC activity. Again, bumetanide may reverse this effect by minimizing the intracellular chloride accumulation by inhibiting the

NKCC transporter, which would otherwise depolarize the muscle. Adapted with permission from Suetterlin et al. (2014)

Figure 1.10. describes the gating pore current in a model of the S4 (Moreau et al 2014). The positively charged S4 arginine residues normally occlude the gating pore where the S4 helix is situated (top panel). There are at least two states of the S4 segment: up or down. At hyperpolarized voltages the positive charges are attracted inward, while in the active state it is attracted to the negative extracellular space.

If R1, the outermost arginine, is neutralized, the occlusion of the gating pore is ablated, and ions may permeate the gating pore, generating a small leak current inward. This occurs in the down state of the S4 when the voltage is hyperpolarized. In the up state, R1 neutralization of DI/DII does not appear to cause a leak current. If a deeper arginine is neutralized the mutation does not lead to gating pore currents in the down state, but rather in the up state of S4. However, in the up state, the mutation leads to leak currents.

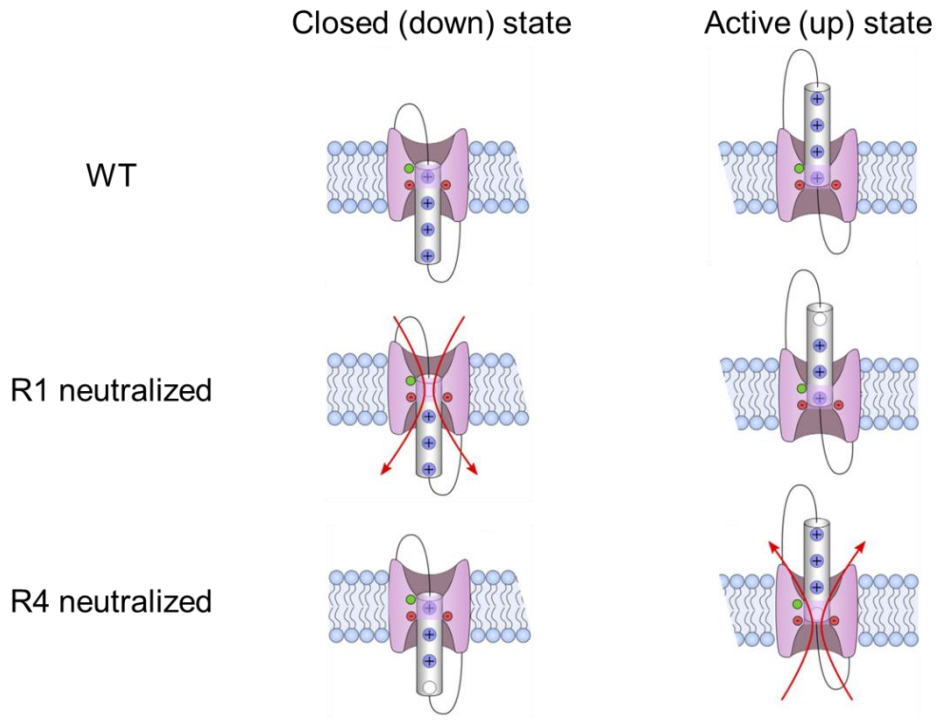

Figure 1.13. The direction of the gating pore current depends on which arginine is affected.

Adapted from Moreau et al (2014)

1.4.5.4. HypoPP treatment

Acetazolamide, a carbonic anhydrase inhibitor has been the go-to drug for hypoPP. Despite this, its efficacy and mechanism of action is not wholly understood. If considering both type 1 and type 2 hypoPP, 60 % of patients were efficaciously treated with acetazolamide (Matthews et al., 2011b). However, in hypoPP type 2 alone acetazolamide was efficacious only in half of patients. This opens up new avenues to explore for efficacious treatment. For instance, bumetanide, a Na-K-2Cl (NKCC) co-transporter inhibitor was found to prevent paradoxical depolarization during conditions mimicking hypokalemia in skeletal muscle cells isolated from mice (van Mil et al., 1997).

The healthy skeletal muscle resting membrane potential is slightly more depolarized than the equilibrium potential of potassium due to a high chloride resting conductance (Cannon, 2015). This is due to the action of the NKCC, which transport Na^+, K^+, and $2Cl^-$ into the muscle. Although the net charge is unaltered, myoplasmic chloride may increase. As a consequence efflux of chloride ions through ClC-1 depolarize the membrane potential. Bumetanide which blocks the NKCC transporter in turn reverses this action, consequently hyperpolarizing reversal voltage of Cl^-. Bumetanide has shown positive results in both type 1 and type 2 hypoPP mouse models (Wu et al., 2013a, 2013b). A randomized, double-blind clinical trial of bumetanide in hypoPP is currently ongoing at the MRC CNMD in London, United Kingdom.

Diclofenamide, another carbonic anhydrase inhibitor was shown in a phase III randomized, double-blind placebo-controlled to be efficacious in hypoPP patients by reducing the rate of paralytic attacks (Sansone et al., 2016).

1.4.6. *SCN4A* mutations in other clinical phenotypes

An increase in whole-exome sequencing (WES) data has led to a surge of *SCN4A* variants in conditions not previously associated with disease. Of particular interest for this work were congenital myopathy and sudden infant death syndrome. Determining pathogenicity of WES data involves filtering of putative structural effects, population frequency (in disease and control population), and effect on gene function. However, to be able confirm the pathogenicity and the pathomechanism of the novel *SCN4A* variants, the functional properties of the mutant $Na_V1.4$ channels need to be analyzed.

1.4.6.1. Congenital myasthenic syndrome

Mutations in *SCN4A* have been associated with three cases of CMS. Tsujino et al. (2003) described the first *SCN4A* loss of function in a patient with CMS. They described a young woman with respiratory and bulbar paralysis, apnea, limited speech, and swallowing difficulties (Tsujino et al., 2003). The patient required respiratory support during apneic episodes. Two heteroallelic *SCN4A* mutations: p.S246L and p.V1442E were characterized by patch clamp revealing strongly enhanced fast inactivation in p.V1442E channels (DIV S3-S4 linker), resulting in muscle action potential failure. The p.S246L variant (DI S4-S5 cytoplasmic linker) displayed a -7 mV hyperpolarizing shift in the voltage dependence of fast inactivation and a large (-20 mV) shift in slow inactivation. Enhanced fast inactivation reduces channel availability at the normal resting membrane potential (≈-80 mV).

A second study identified a homozygous p.R1457H (R4 of S4, DIV) (Arnold et al., 2015) in a patient who at age 12 presented with hour-long episodes of generalized weakness. The parents were heterozygous carriers and displayed no symptoms. Functional characterization of mutants revealed a -14 mV shift in the voltage dependence of fast inactivation. A third study described a patient with CMS and paralysis carrying a homozygous *SCN4A* mutation located to the third arginine (R3) of domain IV, p.R1454W (Habbout et al., 2016). The resultant substitution enhanced fast and slow inactivation, and

slowed recovery from the channel's non-conducting inactivated state. The authors hypothesized that because at the T-tubules there is such a high density of $Na_V1.4$ channels that in the heterozygous state wild-type channels would compensate. But, in the homozygous state there is a markedly reduced action potential initiation at the neuromuscular junction (consistent with CMS) as well as reduced propagation of action potentials (periodic paralysis). In the Habbout study respiratory intervention was also required.

In all three CMS cases described mutant channels displayed enhanced fast inactivation. This reduces the amount of channels available at normal resting membrane potential, enhances the inactivation upon activity and slows down recovery from inactivation. These lead to accumulation of channels in the inactivated state upon repetitive firing (Arnold et al., 2015; Habbout et al., 2016; Tsujino et al., 2003). When the muscle is activated, in addition to muscle weakness, a fatigable weakness is described due to reduced channel availability.

1.4.6.2. Sudden infant death syndrome

Sudden infant death syndrome (SIDS) is the leading cause of death of infants aged 1-12 months in developed countries, with death generally occurring between 2-4 months after birth (Hakeem et al., 2015; Moon et al., 2007). Despite a dramatic incidence decline since the early 1990s, in 2009 there were 279 unexplained infant deaths in England and Wales combined (Wong and Behr, 2014). Although the pathophysiological mechanisms underlying SIDS are incompletely understood, recent evidence has implicated neurodevelopmental delay and abnormal cardiorespiratory reflexes – with emphasis on aberrant response to life-threatening respiratory compromise (Kinney and Thach, 2009; Leiter and Böhm, 2007). A number of epidemiological risk factors are associated with SIDS, including: male sex, prematurity, lower socio-economic status, exposure to smoke, prone sleeping position, and co-sleeping (Moon et al., 2007). At present one important risk

factor in SIDS is the exposure to smoke, further implicating a crucial respiratory involvement (Zhang and Wang, 2013).

Mutations in the cardiac sodium channel gene *SCN5A* (encoding $Na_V1.5$) have been associated with sudden infant death syndrome in two studies. In one study, 2/96 individuals in a SIDS cohort had an *SCN5A* variant that caused channel dysfunction, corresponding to 2.1 % of the cohort (Ackerman et al., 2001). In a larger study of a Norwegian SIDS cohort, eight variants causing dysfunction were found in a total of 201 SIDS cases, i.e. 4.0 % of the cohort (Wang et al., 2007).

1.5. Overall experimental aims

Understanding the physiology and pharmacology of voltage-gated sodium channels has been integral to physiology research for the past 60 years. Given their ubiquitous expression and involvement in a wide range of pathophysiological channelopathies, their molecular and cellular mechanisms need to be understood.

The overarching aim of my project is to characterize pathogenicity and pathomechanism of *SCN4A* mutations, either within the classical skeletal muscle channelopathies, or with novel clinical associations. This was achieved by analyzing the functional properties of different $Na_V1.4$ channel variants and correlating them with disease manifestation.

Chapter 3 deals with the classical skeletal muscle channelopathies, trying to delineate what are the underlying biophysical differences between three mutations in R2 of VSD-I causing two disparate clinical syndromes: myotonia and hypoPP. To study this, channel variants identified in patients were reconstructed using DNA cloning techniques. Channels were heterologously expressed in either *Xenopus laevis* oocytes and studied using two-electrode voltage clamp or in HEK293T cells and studied using whole-cell voltage patch clamp. The same techniques were used in the following chapter, which aimed to investigate a novel spider toxin and its ability to block gating pore currents associated with hypoPP.

Chapter 5-8 deals with novel disease associations with variants identified in *SCN4A*. Through these chapters I sought to understand the differences in the biophysical properties of sodium channel variants, and attempt to try and correlate the genotype (and consequently changes in channel function) with clinical manifestations. Similar to Chapters 3 and 4, these chapters used functional expression of sodium channel clones in HEK293 cells and studied using electrophysiological techniques such as voltage patch clamp. Chapter 5 identifies recessive *SCN4A* variants associated with congenital myopathy that align on a spectrum of disease severity. Chapter 6 aimed to recapitulate

the findings of Chapter 5, with recessive variants found in the most severe form, leading to all individuals dying prematurely, either in utero or shortly after birth. Chapter 7 identified a mild form of congenital myopathy with unusual muscle pathology. As in previous chapters, the goal was to study the variants using recombinant technology and electrophysiological techniques.

In Chapter 8 I sought to understand whether *SCN4A* variants identified in a cohort of infants who died from sudden infant death syndrome (SIDS) may be constitute a risk factor in the pathogenesis. Variants identified in the SIDS cohort as well as a healthy control group were studied using patch clamp.

2. Materials and methods

2.1. Ethical approval

Informed consent was obtained from all individuals included in this study or from their parents or legal guardians. This consent was not obtained by me, but from clinicians and geneticists at the respective centers individuals were identified.

For chapter 3, patients gave written informed consent for the DNA analysis, which had ethics committee approval from the National Hospital for Neurology and Neurosurgery & Institute of Neurology Joint Research Ethics Committee.

For studies performed by collaborating groups in chapter 5 (Zaharieva et al.), the study was approved by the Health Research Authority, NRES Committee East of England – Hatfield (REC 13/EE/0398), the institutional review boards of BC Children's Hospital and the University of British Columbia Canada (CW12-0019; H12-00067), the medical ethics committee of the Radboud University Medical Center (2011/188), Human Research Ethics Committee of the University of Western Australia (RA/4/1/4403).

For chapter 8 (SIDS project), genetic studies were undertaken on anonymized samples. This was approved by the National Research Ethics Service in Wandsworth (REC reference 10-H0803-73) as well as the May Clinic Institutional Review Board, United States.

For chapter 3-5, oocytes were isolated from adult female *Xenopus laevis* following procedures that have been approved by UCL's Biological Services Management Group and the UK Home Office.

2.2. Molecular biology, cell culture, and DNA transfection

This work was conducted in collaboration with Dr Roope Mannikko.

2.2.1. DNA and RNA constructs used

All clones used (rat *SCN1B* and *SCN4A* mRNA) and human *SCN4A* are a gift from Professor Steve Cannon, at the Department of Physiology, David Geffen School of Medicine at UCLA, Los Angeles, CA, USA. For mutagenesis and in vitro transcription, human *SCN4A* expression clone was used, pRc/CMVhSkM (Chahine et al., 1994; Wu et al., 2005), based on accession M81758.1, previously used for functional expression by (Corrochano et al., 2014; Gonorazky et al., 2017; Zaharieva et al., 2016). All three DNA and mRNA constructs used contain the ampicillin resistance gene amp^R.

2.2.2. Molecular biology

For all bacterial work, ampicillin was used for antibiotic selection. A stock concentration at 100 mg/ml of ampicillin (Sigma-Aldrich) was stored at -20 °C and diluted to 100 µg/ml working concentration was used.

2.2.2.1. LB agar and LB broth

Luria bertani (LB, Sigma-Aldrich) broth was dissolved in ddH_2O (20 g/l), autoclaved and stored at room temperature. Each 20 g of broth contains: 10 g tryptone, 5 g yeast extract, and 5 g NaCl. Luria bertani agar (Sigma-Aldrich) was dissolved in ddH_2O (35 g/l; 15g/l agar, 10g/l tryptone, 10 g/l NaCl, 5 g/l yeast extract), autoclaved, and cooled before addition of ampicillin. Agar plates were made by pouring agar into 10 cm diameter plates (VWR International), and either used on the day or stored at 4 °C for maximum two weeks.

2.2.3. Site-directed mutagenesis

Mutagenesis was performed using a QuikChange® site-directed mutagenesis kit (Agilent Technologies) according to the manufacturer's instructions. Briefly, 1 µl template DNA (10 ng), forward and reverse primers (125 ng), 5 µl 10X reaction buffer, 1 µl (2.5 U/µl) Pfu Ultra high-fidelity (HF) DNA polymerase (Agilent Technologies), 1 µl dNTPs (10 mM), double-distilled (PCR-grade) water was added up to a final volume of 50 µl. Contents were mixed and placed in PCR cycler: denaturation step (95 °C, 1 min), followed by 18 cycles of denaturation (95 °C, 50 s), annealing (60 °C, 50 s), extension (68 °C, 15 min [~1 min/kb]), and subsequently an extension step (60 °C, 7 min). DpnI was added and mixed, and placed at 37 °C for 2 hours. DpnI is a restriction enzyme that cleaves only methylated DNA i.e. cleaves the methylated template plasmid so that this is not transformed later.

2.2.4. Design of primers used for site-directed mutagenesis

Design of primers is based on the guide provided by Agilent Technologies. Primers for mutagenesis would have the mutated nucleotide base in the middle, with approximately 14 base pairs on each side (generating approximately 29-mer primers). GC content is approximately 40-60 %. Melting temperature was calculated and adjusted by altering the primer length according to the equation given in the mutagenesis manual.

2.2.5. Heat-shock transformation of *Escherichia coli*

Ultracompetent *Escherichia coli* (*E. coli*) cells XL10-Gold® cell (Agilent Technologies) were kept at -80 °C. According to the manufacturer's manual, 14 ml round-bottom Falcon tubes were pre-chilled. Ultracompetent cells were aliquoted into the Falcon tubes after being thawed on ice, and 1-5 µl mutagenesis PCR product was added to 30-50 µl ultracompetent cells. As positive control, 1 µl of template DNA was often used. Negative control (H_2O) was always included.

2.2.6. Plasmid DNA purification

Single colonies from plates described above were picked using a pipette tip, and added to a round-bottom 14 ml Falcon tube containing 2-5 ml LB broth, and shaken at 225 rpm in a 37 °C shaker overnight for over 16 hours. DNA was extracted using GenElute™ (for sequencing and mRNA preparations) or GenElute™ High Purity (for transfection to HEK293 cells) Plasmid Miniprep Kits (Sigma-Aldrich) using the *Spin Method*, which is as follows:

2.2.6.1. Spin method protocol

Centrifuge speed was 16,000 g for all steps. The cultures were centrifuged for 1 min in 2 ml collection tubes, and the supernatant was discarded. The pellet was resuspended with 200 µl Resuspension buffer (contains RNase A) with a pipette. Lysis buffer (200 µl) was added and the tubes inverted 6-8 times. Neutralization buffer (350 µl) was added and the tubes inverted 6-8 times, followed by centrifugation for 10 min. The cleared lysate containing the plasmid DNA was transferred into GenElute™ spin columns and centrifuged for 1 min, and supernatant discarded. Wash solution was added to the column and spun for 1 min. When using the GenElute™ high-purity miniprep kit, two washes were used as follows. Wash solution 1 was added, centrifuged for 1 min and supernatant discarded. Wash solution 2 was added, centrifuged for 1 min and supernatant discarded. Spin columns were centrifuged to remove any excess ethanol, and then transferred to clean 1.5 ml Eppendorf tubes. DNA was eluted by adding PCR-grade H_2O to the spin column and centrifuged for 1 min.

2.2.6.2. DNA quantification and sequencing

DNA concentration was quantified using a NanoDrop™ 1000 spectrophotometer (Thermo Scientific). In accordance with the manufacturer's instructions, DNA samples were used if the 260/280 nm absorbance ratio was in the range of 1.8-2.0, and 260/230 nm

absorbance ratios were in the range of 2.0-2.2. Successful mutagenesis was verified by sequencing over the whole insert (Source Bioscience sequencing service).

2.2.7. mRNA transcription for *X. laevis* expression of *rSCN4A*/*rSCN1B*

Plasmid DNA was linearized using NheI (New England Biolabs) in a mix of 23 µl plasmid DNA, 3 µl BSA (10X), 3 µl 10X reaction buffer, 1 µl NheI enzyme and incubated for 2 hours at 37 °C and purified by QIAquick® PCR Purification Kit (Qiagen). The rat *SCN4A* and *SCN1B* clones were used to transcribe messenger RNA using an mMessage mMachine® T7 transcription kit (ambion®, Life Technologies™). Reagents were thawed on ice and mixed thoroughly. Each reaction contained 100 µl 2X NTP, 2 µl 10X reaction buffer, 6 µl linearized template DNA (>40 ng/µl), 2 µl enzyme mix. Each reaction was incubated at 37 °C for 2 hrs. After this 1 µl DNase was added to each reaction, and the reaction was incubated at 37 °C for further 15 minutes. To precipitate the RNA, water (30 µl) and LiCl (30 µl) was added, mixed, and left at -20 °C for >30 min. The RNA preparation was centrifuged at 16,000 g at 4 °C for >20 minutes, supernatant removed with pellet remaining, 750 µl -20°C 70% ethanol added and centrifuged for 10 min at 4 °C. The supernatant was removed, and left to air dry to remove any remaining ethanol. The RNA pellet was dissolved in RNase free water. The concentration was measured using a NanoDrop™ spectrophotometer (Thermo Fisher) and stored at -80 °C. Maximum concentration from the mRNA preparation, often >500 ng/µl, was injected to oocytes, to maximize expression to measure the small amplitude gating pore currents.

2.2.7.1. Agarose gel electrophoresis

In order to control for DNA integrity, agarose gel electrophoresis was performed. 1.0 g of agarose (Sigma-Aldrich) was dissolved by microwave heating in 100 ml 1X TAE solution (containing 40 mM Tris, 20 mM acetic acid, and 1 mM EDTA) to generate 1.0 % (w/v) agarose gels, appropriate for the expected band sizes of >1 kb. 1 µl 10,000X GelRed™ (BIOTIUM) nucleic acid gel stain was added to the solution. The DNA samples were

mixed with 2 µl 5X GelPilot® (Qiagen) DNA loading dye. Bands were separated by electrophoresis, and observed using a UV camera. The quality of the mutant mRNA preparations was confirmed by comparing the bands from mutant mRNA with that of wild type mRNA using 1 % agarose gel.

2.2.8. HEK293T cell culture and transfection

Human embryonic kidney 293 cells expressing the SV40 large T-antigen (HEK293T) cells were maintained in Gibco® Dulbecco's Modified Eagle Medium (DMEM, Life Technologies™) containing 4.5 g/l D-Glucose, L-glutamine (4.0 mM) and sodium pyruvate (1 mM) supplemented with 10 % fetal bovine serum (FBS, Life Technologies™). Cells were incubated at 37 °C with 5 % CO_2.

HEK293T cells grown in 1.9 cm^2 wells (Sigma-Aldrich) to 50-70 % confluency were transfected with 500 ng human *SCN4A* and 50 ng cop-GFP in 100 µl Opti-MEM® reduced serum medium (Life Technologies™) and 1.5 µl Lipofectamine® 2000 (Life Technologies™) and incubated overnight. Electrophysiological characterization by whole-cell voltage patch clamp of transfected cells was performed 48-72 hours after transfection.

Cells of similar morphology and fluorescence were consistently used for the electrophysiological recordings. On all days of recording wild-type constructs were recorded in parallel to mutant constructs confirm good expression, normal functional properties, and to allow accurate comparison of channel variants against wild-type constructs studied at the same time point and conditions. If on any day the wild-type data was significantly different from normal, these data, and any variant data recorded on the same day were excluded from data analysis.

Only isolated cells were patched. Cells of similar size were always recorded from, as judged by the whole-cell capacitance value (in pF) usually in region of 15-30 pF.

2.2.9. Preparation of *Xenopus laevis* oocytes

Xenopus laevis oocytes were provided by a central UCL facility. Individual oocytes were isolated with collagenase A (2 mg/ml) in oocyte Ringer's solution containing (in mM): NaCl 82.5, KCl 2, $MgCl_2$ 1, HEPES 5 (pH=7.5-7.6, NaOH) and stored in Modified Barth's Solution (in mM): NaCl 87.1, KCl 1, $MgSO_4$ 1.68, HEPES 10, $NaNO_3$ 0.94, $NaHCO_3$ 2.4, $CaCl_2$ 0.88 (pH=7.4, NaOH) supplemented with penicillin-streptomycin (0.5 mg/ml and 0.25 mg/ml, Sigma-Aldrich) and amikacin (0.1 mg/ml, Sigma-Aldrich).

2.2.10. Oocyte microinjection

Maximum concentration from the mRNA preparation, often >500 ng/µl, was injected to oocytes, to maximize expression to measure the small gating pore currents. Injection was performed in a total volume of 50 nl using a Nanoject I™ Auto-Nanoliter Injector (Drummond Scientific). Two-electrode voltage clamp recordings were performed 2-7 days post-injection to allow maximal Na_V channel expression. For alpha pore current measurements in oocytes, approximately 12.5 ng *SCN1B* mRNA and 12.5 ng *SCN4A* mRNA (1:1 ratio) was injected and recordings performed the following day.

2.3. Electrophysiology

2.3.1. HEK293T whole-cell voltage patch clamp

Recordings were performed using an Axopatch 200B amplifier (Axon Instruments), BNC-2090 (National Instruments) or Digidata 1550A analog-to-digital converter (Axon Instruments). Pipettes were pulled from borosilicate glass capillaries with filament (30-0056F, Harvard Apparatus) with a pipette resistance between 1.5-3 MΩ, connected to a CV-203BU headstage (Axon Instruments). Either an in-house programmed LabVIEW 2013 (National Instruments) interface (Kullmann, DM), or Clampex 10.5.0.9 (pCLAMP™, Molecular Devices) was used to generate voltage command protocols and acquire data.

Raw LabView data were exported as an ASCII file. All data were analyzed using pCLAMP™ (Molecular Devices), Excel (Microsoft) and Origin (OriginLab).

The extracellular solution contained (in mM): NaCl 145, KCl 4, $CaCl_2$ 1.8, $MgCl_2$ 1, HEPES 10 (pH=7.35, NaOH), osmolality 305 mOsm/kg). Intracellular solution contained (in mM): NaCl 5, CsCl 145, EGTA 10, HEPES 10 (pH=7.4, CsOH), osmolality 285-290 mOsm/kg). The liquid junction potential was calculated to be -4.4 mV using the built-in pCLAMP™ calculator and was not compensated for. Series resistance was compensated ≥60 % (but almost always ≥70 %). Prediction and compensation dials of the compensation were always set to the same value. Lag was 10 µs. Recordings with voltage error greater than 5 mV were discarded. This voltage error was calculated using:

V_error (in mV) = I x R_s((100-R_c)/100)/1000,

where I is the current (in pA), R_s is the series resistance in MΩ, R_c is the series resistance compensation in whole percent.

For all patch clamp recordings except the slow inactivation protocol, a –*P*/N leak subtraction protocol was used. This means that, an N number of subsweeps with 1/Nth of amplitude of the test voltage command are applied in an opposite direction of the voltage command protocol. The resulting currents are subtracted from current in response to test voltage command protocol so that any leak and capacitive currents arising from the given waveform stimulus are eliminated.

After attaining whole cell configuration, for every cell, the cell was allowed to stabilize while two “Activation” protocols with 10 s interpulse intervals were run. This procedure gives the cell approximately 10 minutes to stabilize while also being able to observe the stabilization of channel properties, before the test voltage protocols are run. In all data, the signal was 4-pole Bessel filtered at 5 kHz and sampled at 50 kHz except during the slow inactivation protocol, which was sampled at 100 Hz during the 10 s pre-pulse (see below for pulse protocols).

2.3.2. Two-electrode voltage clamp (TEVC) in *Xenopus laevis* oocytes

To study gating pore currents, constructed mutant rat *SCN4A* mRNA was co-injected with wild-type beta-1 rat (*SCN1B*) mRNA in *X. laevis* oocytes and studied by two-electrode voltage clamp (TEVC). *Xenopus laevis* oocytes are very large, thus allowing expression of a larger number of channels compared to other cell types, such as HEK293T. This generates macroscopic currents with a peak amplitude >15 μA, so that the low amplitude gating pore currents can be readily measured. Because the main pore current amplitude is very large, and the gating pore current amplitude ranges 0.1-1.0 % (or less) of the maximum main pore amplitude, tetrodotoxin (TTX) is added to fully block the main pore currents to separate the gating pore currents.

Data were acquired using a GeneClamp 500B amplifier (Axon Instruments), connected to Clampex 9.2 (Molecular Devices) via a DigiData 1200 analog-to-digital converter (Axon Instruments). Low-resistance pipettes (0.1-1.0 MΩ when filled with 3 M KCl) were pulled from thin-walled borosilicate glass capillaries (30-0068, Harvard Apparatus).

Extracellular sodium methanesulfonate (NaMeSO) solution contained (in mM): NaMeSO 120, $CaSO_4$ 1.8, HEPES 10 (pH=7.4, NaOH). During experiments where guanidinium replaces a fraction of sodium as the charge-carrying ion, a guanidine sulfate solution was used. Guanidinium has previously been used by the Isacoff and Catterall groups, who found that the conductance of guanidinium ions through the gating pore is higher than that of sodium ions (Sokolov et al., 2010; Tombola et al., 2005). The increased amplitude measured in the presence of guanidinium is likely due to the difference in structure of the ion and consequently hydration shell properties compared to sodium. Arginine side chains have a guanidinium moiety. Selectivity for larger guanidinium ion compared to smaller sodium ion is likely result of lower energy of dehydration of the guanidinium ion in a pore that normally permeates the arginine side chain. In other words, the gating pore would be predicted to provide a low-energy pathway for guanidinium ions present in the

extracellular space. Meanwhile, dehydration of smaller sodium ion is not optimized for the gating pore resulting in reduced permeation through the gating pore compared to the guanidinium ion.

Guanidine sulfate ($GnSO_4$) solution contained (in mM): $GnSO_4$ 120, $CaSO_4$ 1.8, HEPES 10 (pH=7.4, NaOH). NaMeSO and guanidine solutions were mixed to achieve the desired concentration ratio. These concentration ratios were either Na3:Gdn1 (90mM:30mM), Na1:Gdn1 (60mM:60mM), or Na1:Gdn3 (30mM:90mM). Unless otherwise stated the 1:1 ratio was mainly used. To measure the gating pore currents the oocytes were perfused with 1 µM tetrodotoxin (TTX) to block the main pore current. Signals were sampled at 5 kHz and 4-pole Bessel filtered at 1 kHz. No –*P*/4 leak subtraction was performed. The offline leak subtraction method is found in 2.5.2.

The alpha pore currents (in Chapter 4; Marisol Sampedro Castañeda) were studied only when the expression was low (<5 µA) to allow good voltage clamp. These experiments were performed in extracellular NaMeSO solution.

2.4. Analysis of HEK293T whole-cell patch clamp data

2.4.1. Voltage protocols of HEK293T whole-cell electrophysiology

The holding potential (V_h) for all recordings in HEK293T cells was -80 mV.

2.4.1.1. Voltage dependence of activation

Peak current in response to test voltages ranging from -150 mV to +70 mV in 10 mV increments was recorded and plotted against the test voltage. Data are reported in the range of -100 mV to +50 mV as there is no activation when voltages are more negative than -50 mV, and above +50 mV currents are very small as +60 and +70 mV test voltages are close to the sodium reversal potential. Peak conductance was calculated by dividing the peak current with ($V - E_{rev(Na^+)}$) where V is the voltage and $E_{rev(Na^+)}$ is the estimated reversal potential of Na^+. The $E_{rev(Na^+)}$ was estimated by fitting a straight line to current-voltage data in a range between +10 mV and +50 mV and extrapolating the fit to voltage where the current equals 0 pA.

2.4.1.2. Voltage dependence of fast inactivation

Pre-pulse potentials ranging from -150 mV to +70 mV were applied in 10 mV increments for 150 ms. Only data for pre-pulse between -150 mV and 0 mV are shown, as by -40 mV there is already full inactivation. After the pre-pulse a test voltage step to -10 mV was applied. The peak current at the test voltage was measured and plotted against the pre-pulse voltage.

2.4.1.3. Voltage dependence of slow inactivation

Pre-pulse potentials from -130 mV to +50 mV were applied in 10 mV increments for 10 s. After the prepulse, a 20 ms pulse to -100 mV was applied to allow the channels to recover from fast inactivation. Peak current amplitude was then measured in response to a test pulse to -10 mV and plotted against the pre-pulse voltage.

2.4.1.4. Time course of recovery from fast inactivation

Channels were inactivated during a 10 ms depolarizing step (P1) to 0 mV and then stepped to test voltage for an increasing duration of time. A second voltage step (P2) to 0 mV was then applied to see how much the channels had recovered from fast inactivation at the test voltage. The peak current amplitude during the second step (I_{P1}) was divided by the peak current amplitude during the first voltage step (I_{P2}) and plotted against the duration of the recovery period. The test voltage for the data presented in this thesis was -80 mV.

2.4.1.5. Time course of onset of open state fast inactivation

A double exponential function was fit to the current decay from current traces using the voltage protocol in 2.4.1.1. The time courses were measured in range -20 mV $\leq$ $V_{command}$ $\leq$ +20 mV. Only the time constant of the fast component that routinely carries >90% of the total amplitude was studied.

2.4.1.6. Fitting of Boltzmann and exponential functions to data

The voltage dependence of channel activation, fast- and slow inactivation was analyzed by fitting a Boltzmann equation to the data. The conductance and current data were fitted with Boltzmann equation: $G \text{ (or I)} = A + (B - A)/(1 + \exp((V-V_{1/2})/V_{slope}))$, where A and B are the minimum and maximum conductance (or current), $V_{1/2}$ is the voltage where conductance (or current) is (B+A)/ 2 and V_{slope} is the slope factor. For the graphs the data were the normalized to A and B (activation and fast inactivation), or dividing by B (slow inactivation).

Time courses of onset and recovery from inactivation were fitted with single or double exponential functions of form: $I = I_{ss} + \alpha_1\exp(-t/\tau_1) + \alpha_2\exp(-t/\tau_2)$, where I is current amplitude, I_{ss} is the plateau amplitude, α_1 and α_2 are the amplitudes for time constants τ_1 and τ_2, and t is time. For single exponential function $\alpha_2=0$. Single exponential fit was used

to study the time course of recovery from fast inactivation in HEK293T. A double exponential equation was used to study the time course of open state fast inactivation.

2.5. Analysis of *X. laevis* oocyte TEVC data

2.5.1. Voltage protocols for *Xenopus laevis* oocyte TEVC

Holding potential was -100 mV for all recordings described. Depolarizing pulses of 20 ms in 5 mV increments were applied to study main pore currents. Gating pore currents were measured by applying a 300 ms step to voltages ranging from -140 mV to +50 mV in 5 mV increments. The mean current during the last 200 ms of the test pulse is plotted against the voltage to analyze the voltage dependence of the gating pore currents. During solution changes (application of TTX, various concentration of guanidinium) and Hm-3 an "Application" protocol was run: from a holding potential of -100 mV, a 300 ms step to -20 mV was applied, followed by return to holding potential and a 150 ms step to +20 mV. The application protocol was used to assess when the current amplitude stabilized to a new steady state upon solution exchange.

2.5.2. Offline leak subtraction of gating pore current data after *X. laevis* oocytes TEVC recording

Linear leak conductance was estimated by fitting a straight line to the current-voltage data at a voltage range where the gating pore is assumed closed. The voltage range for the fit was routinely 0 mV to +20 mV for the data in chapter 4 and +10 mV to +30 mV for the data in chapter 4. Data with large linear leak conductance were discarded. For the data in the R222 chapter, in addition, cell with clear increments in leak currents at the voltage range of -10 mV to +20 mV were discarded. Using this method for p.R225G resulted in changes in current amplitude at all voltages suggesting that it does not have a clear

closed state where oocyte leak conductance could be analysed. Guanidinium specific current (I(Na:Gn)-I(Na)) is reported instead.

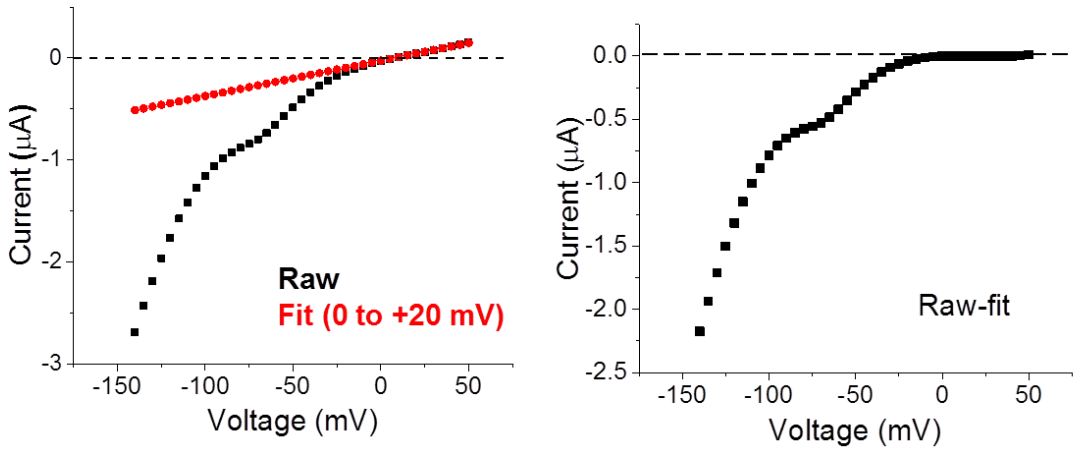

Figure 2.1. Current-voltage plot of leak-subtraction reveals the inwardly conducted gating pore current.

2.5.3. *Heriaeus melloteei* (Hm-3) toxin description and Hm-3 block

Hm-3 is a gating modifier toxin from the crab spider from *Heriaeus melloteei* previously found to modify gating of voltage-gated sodium channels (Berkut et al., 2014). Hm-3 is a 35 amino acid long amphiphilic molecule. On its surface it has a hydrophobic ridge, which is enriched in aromatic residues and surrounded by positive charges. It binds lipid vesicles that are either negatively charged or neutral. It was found by Berkut and colleagues to be a gating modifier, not a direct blocker, by shifting the voltage-dependence of activation to more depolarizing voltages (Berkut et al., 2014).

Block by Hm-3 was measured as I(compound)/I(Control). Dose-response curve to estimate IC50 was of form I/Icontrol = 1/(1+((Hm-3)/IC50)^h), where (Hm-3) is the Hm-3 concentration, IC50 is the Hm-3 concentration at which inhibition is half maximal, and h is the slope factor. For gating pore currents the dose-response curve was measured in

response to test pulse –100 mV. For the fit we assumed that the maximal block by Hm-3 would be 100% and h=1. The normalization of gating pore current pharmacology data was performed by dividing the current response by the current measured in response to voltage step to −140 mV in absence of Hm-3 for each cell.

For alpha pore currents, the block by Hm-3 was measured at -20 mV. Current amplitude in presence of the toxin is normalized to the current in absence of the toxin.

2.6. Statistical Analysis

Raw data were analyzed using pCLAMP™ 9.2 (Molecular Devices). Data analysis and graphical presentation was performed using OriginPro 64-bit (OriginLab®) and Excel 2010 (Microsoft® Windows™). Statistical analysis was performed using either Prism 4.0 (GraphPad Software, Inc) or SPSS (IBM Corporation). Normal distribution was first assessed using Shapiro-Wilk's normality test. Normally distributed data were compared against control using a one-way ANOVA with Bonferroni's multiple comparisons *post hoc* test. Equal variance was established using either Bartlett's test or Levene's test; if significantly different variance was established, a one-way ANOVA with Dunnett's *post hoc* test was performed. Non-normally distributed data were compared against the control condition using Kruskal-Wallis test with Dunn's multiple comparisons *post hoc* test. The test used is specified in each data set. The alpha level for all tests was 0.05.

3. Differing pathomechanisms and clinical presentations of mutations affecting the same S4 arginine in domain I of $Na_V1.4$

3.1. Background, aims, and hypothesis

SCN4A missense mutations that result in substitution of S4 arginine gating charge residues in $Na_V1.4$ have been shown to underlie either hypoPP type 2 or sodium-channel myotonia (Suetterlin et al., 2014). The prevailing pathomechanism in hypoPP type 2 is an aberrant leak current through the voltage-sensing domain, known as a gating pore current. Gating pore current causes depolarization of the muscle, in particular in hypokalemic conditions that reduce repolarizing potassium currents through Kir2.1 channels (Cannon, 2015). Depolarization results in $Na_V1.4$ channel inactivation, and flaccid paralysis. Myotonia is due to gain of function of $Na_V1.4$ due to attenuated fast inactivation or enhanced activation (Cannon, 2010; Matthews et al., 2010; Yang et al., 1996).

Characterizing the effects of genetic variants on channel function at the protein level is paramount to understand the underlying cause of disease. Typically the mutations affecting S4 arginines in domains I-III are associated with gating pore currents and periodic paralysis (Groome et al., 2014; Jurkat-Rott et al., 2012; Struyk et al., 2008) while mutations of S4 arginines in domain IV attenuate fast inactivation, resulting in gain of function and myotonia (Francis et al., 2011b).

An *SCN4A* mutation affecting an S4 arginine, p.R222Q, was found in a patient with paramyotonia congenita, while two other mutations affecting the same residue, p.R222W (Matthews et al., 2009) and p.R222G (Jurkat-Rott et al., 2012) were identified in patients with hypoPP type 2. Thus, curiously, different mutations affecting the same residue cause prevalently myotonic or paralytic phenotype depending on the nature of the substituting residue. My aim was to characterize the effects of the three substitution mutations on channel function and subsequently correlate the biophysical effects with the clinical phenotype.

I hypothesized that the identified mutations in the two individuals with hypoPP type 2 induce gating pore currents, while the myotonia caused resulted in gain of function of the main pore sodium current. This hypothesis was readily tested by expressing the *SCN4A* mutant clones in *Xenopus laevis* oocytes and HEK293T cells. *Xenopus* oocytes were be studied using two-electrode voltage clamp to detect putative gating pore currents, and the HEK293T cells are studied by whole-cell patch clamp, allowing characterization of fast main pore sodium current properties.

3.2. Results

3.2.1. Note on Results

Previous MRC CNMD PhD student Siobhan Durran identified the p.R222Q mutation, performed mutagenesis for p.R222Q and p.R222W mutants, and some TEVC recordings. The p.R222 mutant channels have been used for other projects by rotation students Louise King and Emma Wilson, post-doc Marisol Sampedro-Castañeda and my supervisor Roope Männikkö. Their data are included. Clinical description is by Karen Suetterlin and Emma Matthews.

3.2.2. Clinical details and genetic diagnosis

A 26 year old male from a consanguineous family presented at age 14 with severe myotonia and cold-precipitated muscle discomfort due to muscle stiffness, or the muscle seizing up. This is due to the persistent muscle contraction and the inability for the muscle to contract. The patient also had very rare episodes of weakness. Serum potassium levels were normal during the episodes. Distal myopathy with weakness of the hand was also found. Treatment with acetazolamide was ineffective, while mexiletine reduced symptoms. Clear myotonic events were measured using electromyography. The paternal aunt and maternal uncle are possibly also affected; however, no family members were available for investigation. The findings indicate a paramyotonia congenita diagnosis.

Genetic diagnosis revealed a heterozygous mutation c.665G>A in *SCN4A* leading to $Na_V1.4$ p.R222Q. A silent *CLCN1* mutation was also found (c.1650G>A). This was initially thought to be a polymorphism but during the course of this study the *CLCN1* variant was found to create a novel splice site in exon 15 and to be associated with recessive myotonia congenita (supplementary material of (Horga et al., 2013)). No muscle sample was available to confirm correct *CLCN1* splicing. Parental DNA was not available to confirm the inheritance pattern.

The p.R222W mutation (c.664C>T) has been found previously in two unrelated patients with hypoPP type 2 at the MRC Centre for Neuromuscular Diseases by Sanger sequencing (Matthews et al., 2009). As is typically the case, episodes of paralysis normally occurred at night or in the morning and low potassium was measured in the serum. Attacks first manifested in the second decade of the patient's life. It is unclear whether p.R222W is *de novo* or inherited due to lack of genetic information of parents. Similarly, the p.R222G mutation has been described previously in a patient with hypoPP type 2 (Jurkat-Rott et al., 2012). A detailed clinical report is however not available for this individual.

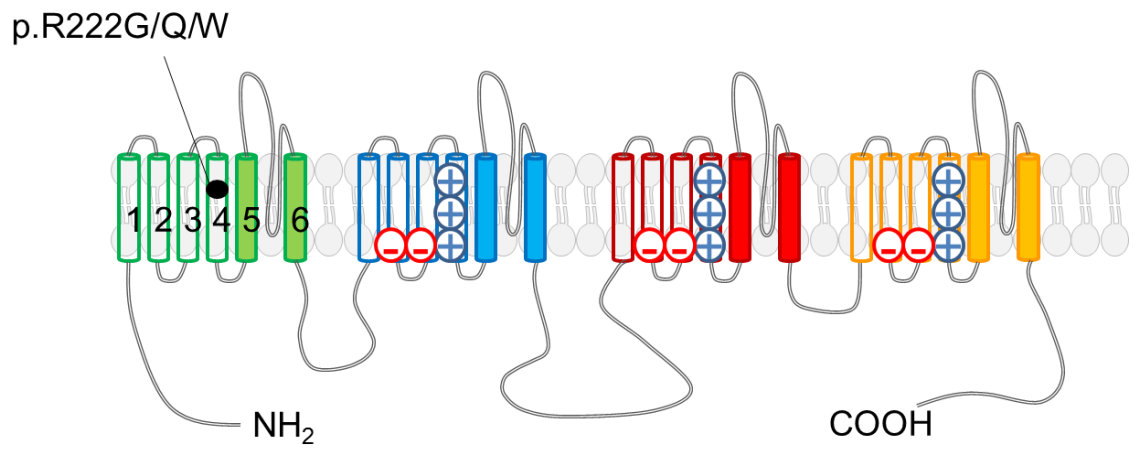

Figure 3.1. Location of R2-VSD I mutations p.R222G/Q/W mapped onto a schematic diagram of the NaV1.4 alpha subunit.

The location if the second arginine (R2) of voltage sensor domain (VSD) I p.R222 is illustrated by a filled black circle on a diagram of the voltage-gated sodium channel viewed from the side in the membrane plane if stretched out horizontally. Domains I-IV are color coded in green, blue, red, and yellow, respectively. The + signs indicate S4 helices that carry positively charged arginine, negative counter charges in S2 and S3 are indicated with - signs. These symbols are omitted from VSD-I for clarity.

3.2.3. Main pore current properties of VSD-I R2 mutants

3.2.3.1. Fast steady-state properties and current density

The effects of mutations on the functional main pore current properties were analyzed upon heterologous expression in HEK293T cells. P values in this text are uncorrected values from Bonferroni's *post hoc* test, or Games-Howell if the homogeneity of variance was found to be un-equal, using Levene's test for homoscedasticity. Homoscedasticity is another word for the homogeneous distribution of variance; the antonym heteroscedasticity conveys the opposite, i.e. where the variance is heterogeneously distributed. If a statistical test assuming homogenous variance is performed on a data set with heterogeneous variance, the statistical test may be invalidated. Testing for homogeneity of variance using Levene's test guides the selection of appropriate test. The Bonferroni threshold within-parameter comparisons is p=0.017 and p=0.0021 across all

eight parameters tested. The Levene's test was performed prior to the one-way ANOVA. Normal distribution of data was confirmed using Shapiro-Wilk's normality test. The n values are given in the table. Recordings of mutant variants were always performed with wild-type NaV1.4 in parallel. If wild-type deviated from normal parameters, the data were discarded.

The current density of p.R222W was severely reduced (Figure 3.2.; p.R222W: -46±5.8 pA/pF vs. WT: -117±14 pA/pF, p=0.00048, at 0 mV, uncorrected Games-Howell). The current density of p.R222Q was not significantly different from wild-type (p=0.422). In p.R222G a small difference was observed (p.R222G: -72±9.1 pA/pF vs. WT: 117±14 pA/pF, p=0.018, Games-Howell post hoc test). This is not statistically significant if we correct for the number of comparisons made, changing the Bonferroni threshold to p=0.05/3=0.0167.

The parameters of voltage dependence of activation and fast inactivation were derived from individual Boltzmann fits and averaged. Mean normalized conductance or current data were plotted against the test voltage (Figure 3.2). A marked hyperpolarizing shift in the voltage-dependence of activation of both p.R222Q and p.R222G channels was measured compared to wild-type (p.R222G: -28.2±0.6 mV, p=1.03E-7; p.R222Q: -29.3±1.4 mV, p=4.9E-7 vs WT: -19.9±0.8 mV; Figure 3.2; Table 3.1.). The voltage-dependence of activation of p.R222W channels was similar to wild-type (WT: -19.9±0.8 mV vs. p.R222W: -20.2±1.2 mV, p=1, Bonferroni *post hoc* test).

The slope of activation was wild-type like in p.R222G and p.R222Q (WT: 6.4±0.4 mV vs. p.R222Q: 7.5±0.3 mV, p=0.276; p.R222G: 6.5±0.2 mV; p=1; Bonferroni) and slightly less steep in p.R222W channels (p.R222W: 8.4±0.5 mV, p=0.0032, Bonferroni). This indicates reduced voltage sensitivity, consistent with removal of a voltage sensing arginine.

The voltage-dependence of fast inactivation was left-shifted in p.R222Q channels (p.R222Q: -72.0±2.1 mV vs. WT: -65.7±1.1 mV; p=0.032; uncorrected Bonferroni value),

meaning that the p.R222Q inactivates at more hyperpolarizing voltages, thereby reducing channel availability at physiological voltages; however was not reflected as reduced current density at -80 mV holding potential. A small shift was also measured in p.R222G and p.R222W clones, but this was not found to be statistically significant (p.R222G: -70.3±0.8 mV, p=0.075; p.R222W: -69.4±2.0 mV, p=0.423). Meanwhile, the slope factor of fast inactivation was similar across all channels (Table 3.2.).

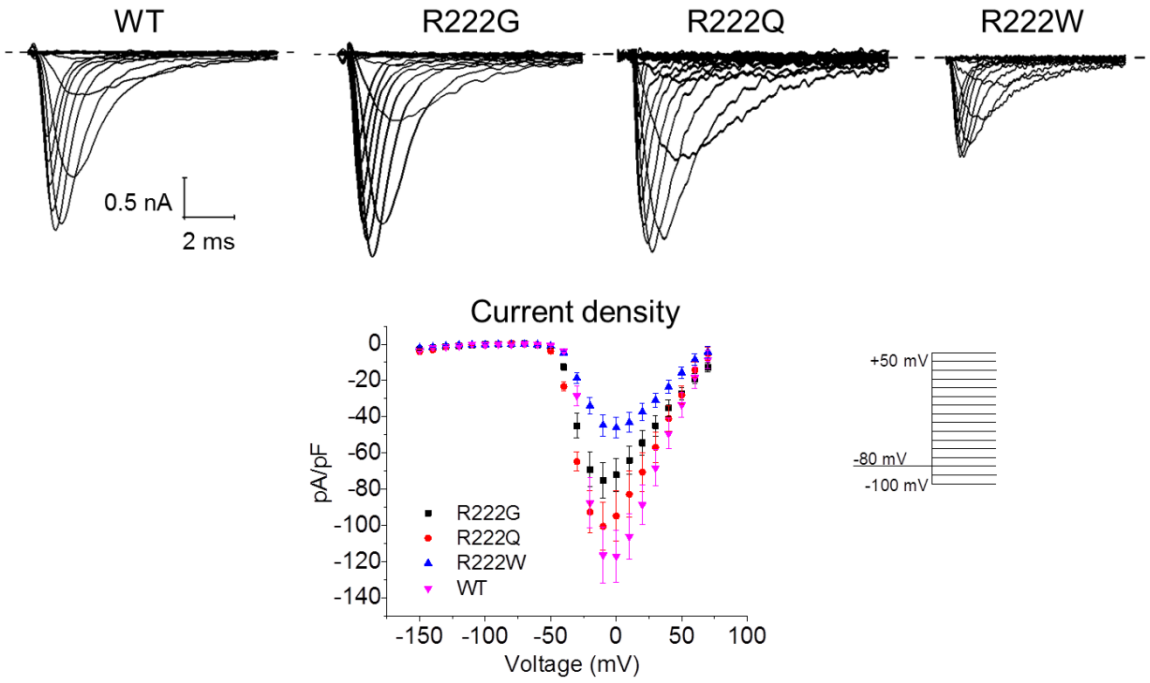

Figure 3.2. Current density of mutant R2 VSD-I channels.

Top: Representative central pore currents of human *SCN4A* wild-type, p.R222G, p.R222Q, and p.R222W channels in response to voltage steps between -150 mV to +40 mV in 10 mV increments. Voltage protocol in insert. Red trace: currents evoked by -30 mV voltage steps. **Bottom**: Mean current density using the protocol in A is plotted against the voltage. n(WT)=9; n(R222G)=7; n(R222Q)=11; and n(R222W)=9.

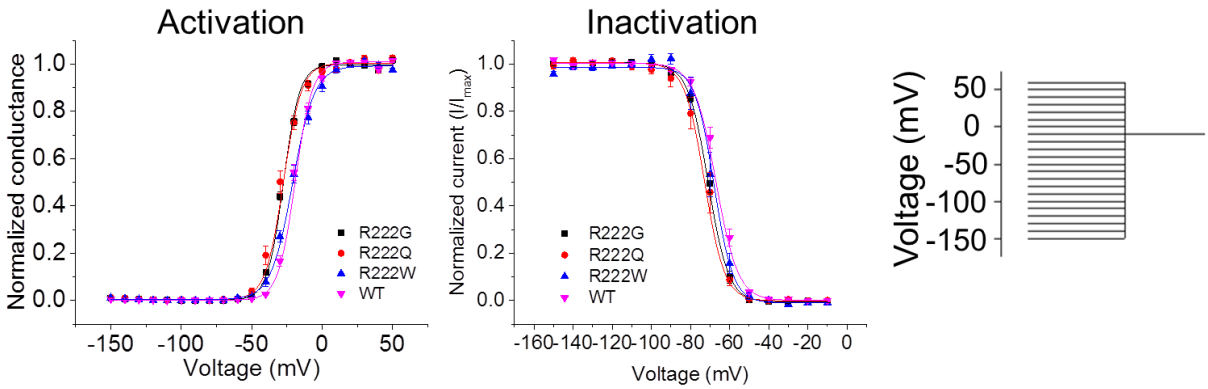

Figure 3.3. Voltage-dependence of activation and fast inactivation

oltage dependence of activation and fast inactivation. Plotted is the normalized conductance (C) or current (D) vs. the test (C) or the prepulse (D) potential in mV (x-axis). Mean data points are fitted with Boltzmann function. All data are represented as mean±SEM. Voltage protocol of fast inactivation is shown in insert of (D). Voltage protocol for activation as in Figure 3.2. n(WT)=9; n(R222G)=7; n(R222Q)=11; and n(R222W)=9.

3.2.3.2. Slow inactivation, rate of recovery from fast inactivation, and onset of open-state inactivation

A 15 mV hyperpolarizing shift voltage dependence of slow inactivation was measured in p.R222Q compared to wild-type (p.R222Q: -65.1±2.4 mV vs. WT: -50.3±1.3 mV, p=0.000043 uncorrected Bonferroni) and a -10 mV mV shift in p.R222G (-59.5±1.4, p=0.00153, uncorrected Bonferroni). Shift in the voltage dependence of slow activation of p.R222W channel did not reach significance. A summary of these data can be found in Table 3.2. No statistically significant difference was measured in the slope factor of slow inactivation derived from the Boltzmann fit to the normalized current data (Table 3.2, Figure 3.3B).

The rate of channel recovery from fast inactivation was also studied. No statistically significant difference in the tau of recovery from inactivation at -80 mV was measured. The largest mean difference across genotypes was wild-type compared to p.R222Q clones (p.R222Q: 9.0±0.7 ms vs. WT: 6.1±0.6 ms, p=0.0504, uncorrected p value). A high value of tau would represent slower recovery, consistent with enhanced fast inactivation (Table 3.2, Figure 3.3C).

The onset of open-state inactivation was also studied by fitting a second order exponential function to the decaying phase of the sodium current at 90 % of the peak to complete inactivation (Table 3.2, Figure 3.3A). A two-way repeated measures ANOVA followed by Bonferroni's post hoc test was performed to discern any differences between tau of each genotype at all five voltages. Both p.R222G and p.R222Q were similar to wild-type at all voltages, while p.R222W was slowed compared to wild-type at all voltages except 20 mV (-20 mV < Vm < 0 mV: $p<0.001$; 10 mV: $p<0.05$; Bonferroni *post hoc* test).

Table 3.1. Activation and fast inactivation.

Data are expressed as means ± standard error of the mean. Normal distribution was confirmed using Shapiro-Wilk's test. Means of mutant variants compared against wild-type channels was performed using a one-way ANOVA with Bonferroni's or Games-Howell *post hoc* test depending on whether the variance was found to be homogeneous or not using Levene's test for heteroscedasticity. * P <0.05; ** P <0.01; *** P <0.001 ($V_{1/2}$: mid-point voltage, Slope: slope factor)

Genotype		Activation			Fast inactivation	
	n	$V_{1/2}$(mV)	Slope (mV)	Current density at 0 mV (pA/pF)	$V_{1/2}$ (mV)	Slope (mV)
Wild-type	9	-19.1±0.8	6.4±0.4	-117±14	-65.7±1.0	5.1±0.1
p.R222Q	11	-29.3±1.4 ***	7.5±0.3	-94±14	-72.0±2.1*	5.1±0.4
p.R222G	7	-28.2±0.6 ***	6.5±0.2	-72±9.1	-70.3±0.8	4.8±0.2
p.R222W	9	-20.2±1.2	8.4±0.5**	-46±5.8***	-69.4±2.0	4.3±0.2

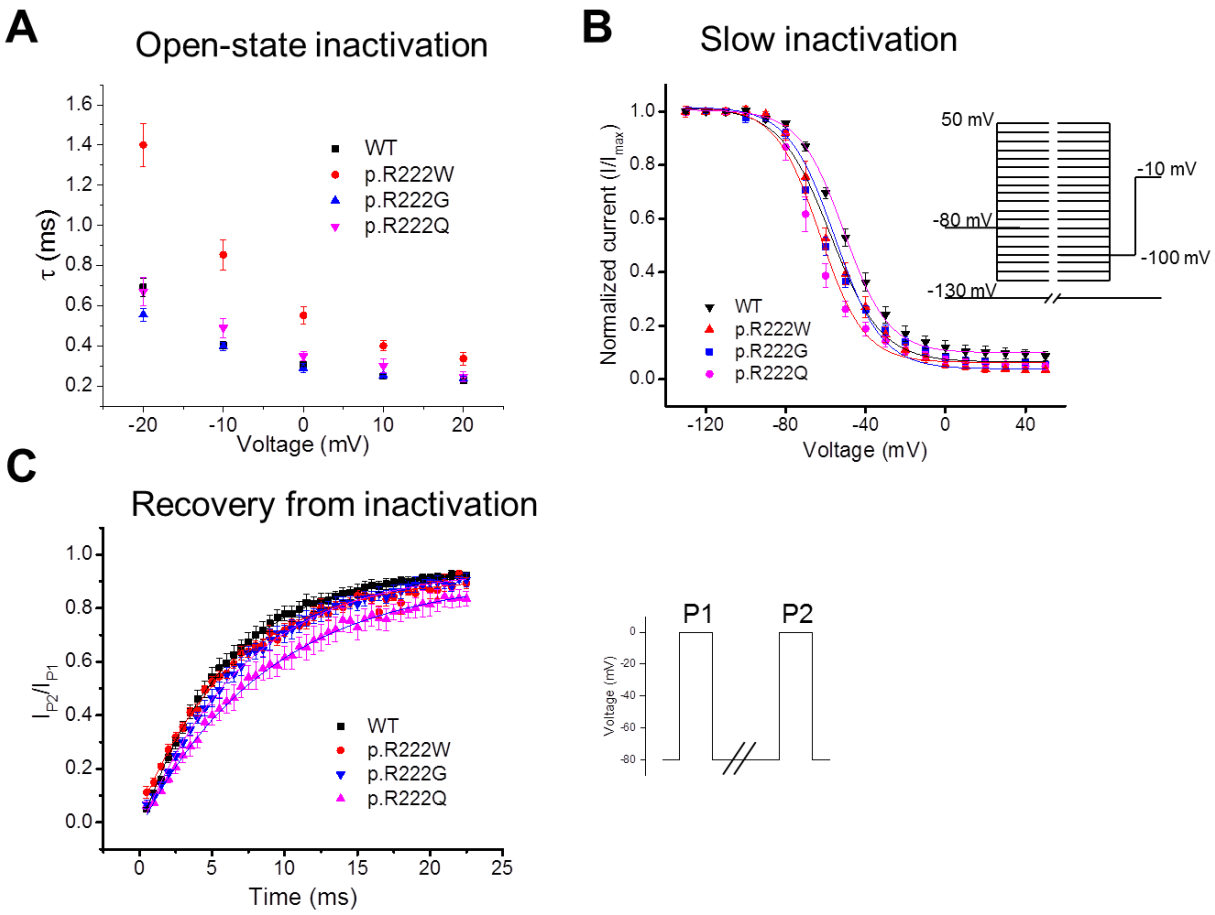

Figure 3.4. Onset of open-state inactivation, tau of recovery from inactivation, and slow inactivation properties in R2 VSD-I variants in HEK293T cells.

All data points are mean±SEM. (A) Time constant tau (ms) of the onset of open state fast inactivation plotted against the voltage in the range -20 < Vm < +20 mV. Two exponential curves were fit to the decaying phase of the sodium current (90% of peak). Only the fast component of the peak amplitude was analyzed. (B) Slow inactivation was determined by applying prepulse potentials from -130 mV to +50 mV in 10 mV increments for 10 s. A 20 ms pulse to -100 mV was applied to recover channels from fast inactivation, followed by a test pulse to -10 mV. The peak current measured at -10 mV was plotted against the prepulse voltage. Voltage protocol is shown in insert (C) Time course of recovery from fast inactivation at -80 mV. The peak current in response to second test pulse (I_{P2}) is measured following a recovery period of varying duration at hyperpolarized voltages. I_{P2} is divided by the peak current of a prepulse (I_{P1}) used to inactivate channels. Solid line shows a single exponential fit to the data. Voltage protocol is shown in insert.

Table 3.2. Recovery tau and slow inactivation

The peak current in response to second test pulse (I_{P2}) is measured following a recovery period of varying duration at hyperpolarized voltages. I_{P2} is divided by the peak current of the first pulse (I_{P1}) that inactivates channels. Solid line represents a single exponential fit to the mean data. Tabulated are mean values of single exponential fit to mean of individual cells from Figure 3.3. Means ± the standard error of means are shown. Statistical comparison: one-way ANOVA with Bonferroni's post hoc test against wild-type. **P* < 0.05, ***P* < 0.01, ****P* < 0.001.

Genotype	Recovery from fast inactivation		Slow inactivation		
	Tau of recovery @ -80 mV (ms)	*n*	$V_{1/2}$ (mV)	Slope (mV)	*n*
Wild-type	6.1±0.6	11	-50.3±1.3	11.9±0.8	8
p.R222Q	9.0±0.7	8	-65.1±2.4***	9.5±0.4	5
p.R222G	7.4±0.8	7	-59.5±1.4**	11.9±0.5	10
p.R222W	6.6+0.4	6	-56.6±2.5	12.0±0.8	5

3.2.4. Gating pore current properties of VSD-I R2 mutants

Chloride free extracellular solution (methanesulfonate was used as the anion) was used in order to minimize potential Cl^- carried endogenous currents occasionally present in the oocytes. Gating pore currents have not been reported previously using TEVC, as usually cut-open voltage clamp (COVC) is used. The COVC setup generates a lower data throughput but allows exchange of intracellular solution and better voltage clamp of a piece of an oocyte membrane. The benefit of TEVC is higher throughput that will enable larger scale pharmacological studies.

To improve the characterization of gating pore currents in TEVC we used guanidinium substitutions to confirm the presence of gating pore currents. A guanidinium moiety is present in the side chain of arginine and guanidinium substitution has been shown to increase the amplitude of gating pore currents (Sokolov et al., 2010). All the data included in this study are for oocytes where we have a recording in both NaMeSO and Na/Gn solutions. The gating pore current does not manifest if main pore currents are recorded, as the large amplitude of the hides the small-amplitude gating pore current. The gating pore current can be isolated when the main pore current is blocked using tetrodotoxin.

Additional exclusion criteria were applied (large increase in conductance in voltage range where linear leak was estimated or large non-specific leak conductance at voltage range where linear leak was estimated). The slope of the conductance of the linear leak current was the same for all the clones studied in this chapter in NaMeSO solution ($p<0.05$; one-way ANOVA followed by Bonferroni *post hoc* test). This suggests that there were no large differences in the leakiness of the oocytes between the clones, and that this voltage range is likely to represent the closed state of gating pore. Accordingly, the slope of the conductance of the linear leak current was the same for all the clones studied in Na/Gn solution ($p<0.05$, one-way ANOVA followed by Bonferroni *post hoc* test). Also, although difficult to accurately estimate in oocytes, the mean peak main pore current was the same

for all variants ($p<0.05$, one-way ANOVA followed by Bonferroni's *post hoc* test), suggesting that the mutations do not cause large changes in expression levels in *Xenopus* oocyte system.

Following leak subtraction oocytes expressing wild-type channels routinely show an outward current component in the physiological voltage range. It is unlikely that these currents are gating pore currents or currents due to endogenous channels in *Xenopus* oocytes. Rather, we assume that these are artifacts of the linear leak subtraction. Residual linear Na^+ current through the $Na_V1.4$ channel at the voltage range where leak is estimated could potentially help explain this artifact.

In NaMeSO all R222 mutants expressed currents that differ from WT gating pore currents, with clear downward deflections in the hyperpolarized voltage range (Figure 3.4). For R222Q and R222W channels a small inward deflection is observed at potentials negative to -50 mV. For R222G channels an inward gating pore current can be measured in Na1Gn1 solution. Leak subtracted current amplitudes at -100 mV were 0.07±0.02 µA, -0.28±0.04 µA, -0.03±0.02 µA, -0.04±0.01 µA for WT, R222G, R222Q and R222W channels, respectively. Thus, in NaMeSO there are clear indications that the R222 mutants carry gating pore currents. We aimed to confirm this by introducing guanidinium in the extracellular media.

For all mutant channels, substitution of extracellular NaMeSO by Na/Gn solution revealed a large inward current in the hyperpolarized voltage range. The gating pore current amplitude was largest for p.R222G channels (-2.8±0.3 µA at -100 mV), smaller for p.R222W channels (-1.2±0.2 µA), and smallest for p.R222Q (-0.5±0.1 µA) channels. Inward current component at physiological voltage was not detected for WT channels.

To determine if the amplitude of non-linear leak currents measured in mutants p.R222G/Q/W were larger compared to wild-type, a one-way ANOVA was performed on each voltage followed by pairwise comparisons of each mutant genotype versus wild-type

using the Games-Howell test (assuming non-equal variance). In total 38 comparisons were made, resulting in an adjusted alpha value of p=0.05/38=0.00132. This allowed ascertaining at which voltage gating pore currents were increased in mutants compared to wild-type.

In Na1:Gn1, p.R222G gating pore currents were significantly larger compared to wild-type at all voltages between -140 mV to -20 mV. In p.R222W gating pore current amplitudes were significantly larger between -140 mV and -90 mV, as well as between -70 mV to -15 mV; p.R222Q only between -115 mV and -100 mV, as well as between -75 mV and -35 mV.

The lack of significant difference between -95 mV and -75 mV in p.R222Q and p.R222W may be a result of the difficulty in leak-subtracting wild-type values, combined with a spread of variance in p.R222Q and p.R222W gating pore current amplitudes.

Wild-type channels showed a very small increase in inward currents, but the current at -100 mV was practically zero (-1.8±27.3 nA). This clearly indicates that the R222 mutant channels carry hyperpolarization activated gating pore currents.

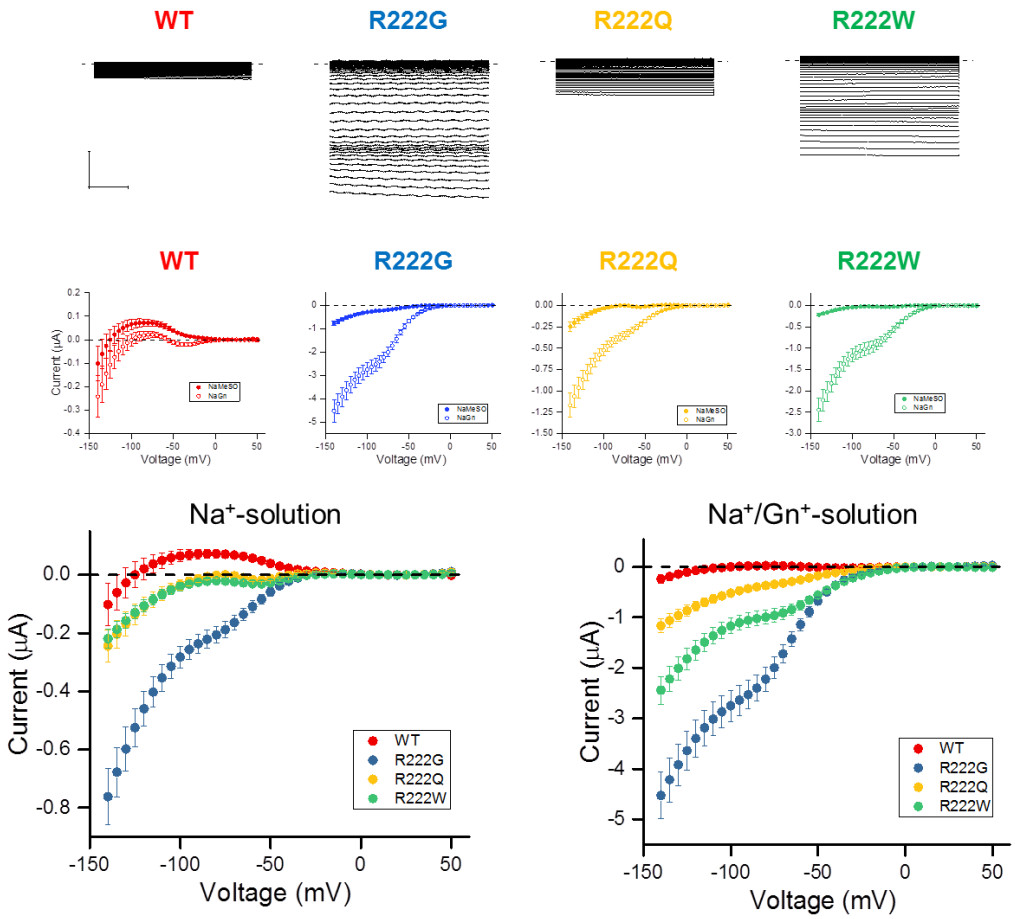

Figure 3.5. Gating pore currents in p.R222Q, p.R222W, and p.R222G mutant channels.

Top row: Raw leak currents in response to voltage steps between -140 mV to +50 mV in 5 mV increments after blocking the central pore current with TTX. Last 200 ms of 300 ms pulse are shown. Scale bar: y axis: 1 µA x axis: 50 ms **Middle row:** I-V plots of leak-subtracted gating pore current traces in different external solutions for wild-type (red), p.R222G (blue), p.R222Q (yellow), p.R222W (green), and gating pore currents in the presence of NaMeSO (solid symbols) or NaGn (open symbols) extracellular solutions. Data are mean±SEM. Sample sizes: WT: n=22, R222G: n=25, R222Q: n=24, R222W: n=22. **Bottom row:** I-V plots for all the clones in NaMeSO (left) and NaGn (right) solutions. Color coding is as above.

3.3. Discussion

The original aim of this project was to dissect the pathomechanism of mutations affecting the same residue affecting R2 of VSD-I causing distinct clinical phenotypes: PMC and HypoPP. This was achieved by analyzing the main pore current using a HEK293T expression system and by analyzing the gating pore currents using the *Xenopus laevis oocyte* system. Correlating channel properties with the clinical phenotype was complicated after the discovery that a silent mutation in *CLCN1* gene encoding ClC-1 chloride channel, instead of being a benign variant, was found to be associated with myotonia congenita (Horga et al., 2013). However, my data clearly show that, depending on their nature, different residues that substitute an S4 arginine can cause a range of alterations in both the main and gating pore current properties and consequently impact the clinical presentation of the patients carrying these variants.

3.3.1. Implications of main pore currents to clinical phenotype

Consistent with the notion that PMC is caused by gain of function mutations affecting the main pore of the $Na_V1.4$ channel (Matthews et al., 2010), we found that the activation of the PMC mutant (p.R222Q) was significantly enhanced. The resultant lowered activation threshold is consistent with increased muscle excitability and myotonia.

We also found that p.R222G channels found in a patient with HypoPP displayed a hyperpolarizing shift in the voltage dependence of activation. The consequence of this gain of function on clinical phenotype is not clear as the clinical report of the p.R222G patient does not mention myotonia to be present in the patient. I thus hypothesize that the large gating pore currents in this mutant channel underlie the predominant clinical phenotype in this patient, namely hypokalemic periodic paralysis.

The main pore properties of the hypoPP mutant p.R222W were not enhanced, but, in contrast, the current density was reduced. Similar loss of function properties have been

described in other HypoPP mutant channels with mutations in S4 arginines (Bendahhou et al., 2001; Jurkat-Rott et al., 2000; Struyk et al., 2000) potentially reflecting reduced stability of the mutant channel. The reduced current amplitude may contribute to reduced excitability in the muscle. However, it is not predicted to lead to muscle depolarization – a key hypoPP feature.

Also, as seen in the following chapters, adult carriers of heterozygous $Na_V1.4$ loss of function mutations do not have clinical presentations. In addition, in oocytes the current amplitude of R222W was not reduced. We do not know why one overexpression system more reliably expresses functional R222W channels. Finally, p.R222W mutant channels also showed slowed open state inactivation, causing increased sodium influx. Gain of function properties of $Na_V1.4$ such as slower inactivation have been associated with paramyotonia and hyperkalemic periodic paralysis, but not with HypoPP (Cannon, 2010; Suetterlin et al., 2014), suggesting that the slowed inactivation kinetics are not contributing to the hypoPP experienced by carriers.

The p.R222Q and p.R222G channels showed markedly enhanced slow inactivation. Attenuated slow inactivation has been suggested to be a pre-requisite for attack of hyperkalemic periodic paralysis in gain of function $Na_V1.4$ mutant channels (Hayward et al., 1997). According to this hypothesis attenuated slow inactivation is required to allow prolonged activation of gain of function $Na_V1.4$ variants at depolarized voltages. Enhanced slow inactivation, in contrast, would shut the depolarizing sodium current and preventing stabilization of the depolarized, paralyzed state of the muscle. Thus, despite enhanced activation, p.R222G and p.R222Q channels would not be able to sustain persistent depolarization due to enhanced slow inactivation. This is consistent with the absence of periodic paralysis associated with hyperkalemia in these patients. Depolarization of hypoPP muscle does not require sustained main pore currents as it is caused by a leak current through the VSD. Thus, while the enhanced slow inactivation of p.R222Q channels may prevent muscle depolarization by reducing the main pore currents,

enhanced slow inactivation of p.R222G is unable to prevent depolarizing leak current through the VSD. In contrast, it may contribute to reduced availability at depolarized voltages and thus contribute towards the pathogenicity.

The p.R222Q patient was treated successfully with use-dependent sodium channel blocker mexiletine. Mexiletine has been successfully used to treat myotonia caused by overactive $Na_V1.4$ channel. Thus, $Na_V1.4$ block in an overactive channel fits well with the functional characterization and myotonic phenotype.

3.3.2. Implications of gating pore currents to clinical phenotype

The three R222 mutant channels displayed gating pore currents. These current were small in NaMeSO, in particular p.R222Q and p.R222W, while guanidinium caused large increase in gating pore currents. These currents were active at physiological voltages. These data suggest that gating pore currents through p.R222W and p.R222G mutant channels underlie HypoPP in patients carrying these mutations.

The patient carrying the p.R222Q variant presented predominantly with myotonia. Occasional episodes of weakness may be present. It is possible that the smaller amplitude of the p.R222Q gating pore currents may contribute to the absence of reported episodes of hypokalemia-induced paralysis. However, due to the limitations of TEVC we cannot reliably normalize the gating pore current amplitude in the oocyte to the number of channels. To better compare the amplitude of the gating pore current between the clones it should be normalized to the amplitude of the gating current, which more accurately measures the number of channels expressed in the cell membrane.

Thus, it is possible that the reduced amplitude may be a result of reduced expression levels of this mutant channel in oocytes. However, we do not think this is the case as a) main pore current amplitudes were the same in all genotypes; b) the gating pore current amplitudes were consistently smaller in R222Q channels compared to R222G/W; and c)

the expression level was not compromised in HEK293 expression system. Thus our data suggest that the amplitude of the gating pore current contribute to the presentation of hypoPP. In this model, larger gating pore currents result in larger depolarization and increased probability of hypokalemia-induced depolarization.

Currently no correlation of gating pore current amplitude and clinical presentation exists. In fact, various estimates of gating pore current amplitude have been proposed ranging from 0.01% to 1% of the peak sodium current amplitude depending on the reporting laboratory (Sokolov et al., 2010; Struyk et al., 2008). Thus it is currently difficult to establish correlations between gating pore current amplitude and disease severity. However, thus far, all the hypoPP mutations in $Na_V1.4$ that have been functionally characterized show gating pore currents, and equally, mutant channels with gating pore currents are associated with hypoPP. However, it is conceivable that mutant channels with low amplitude gating pore currents have a smaller depolarizing effect on the muscle, and thus less likely to drive the muscle to a stable depolarized state. What seems clear is that the nature of the mutation affects the gating pore current properties. Further investigations are required to clarify the role of the gating pore current amplitude on the presentation of hypoPP.

Extrapolations of the effects of the gating pore current amplitude from our work are limited since mutations differentially affect the main pore current properties, and the p.R222Q patient carries an additional pathogenic *CLCN1* mutation. However, the main pore current properties of the p.R222Q mutation, associated predominantly with a myotonic phenotype, and p.R222G, associated with hypoPP, are identical. This suggests that the main pore current properties cannot explain the differing clinical phenotypes of p.R222G and p.R222Q patients. The potential role of reduced chloride currents in the p.R222Q patient is discussed below.

3.3.3. Implications of gating pore currents to channel function

Gating pore currents active at physiological voltages were detected for all p.R222 mutant channels (Figure 3.4.). In the depolarized state (positive to 0 mV), little or no gating pore currents are measured, suggesting that the gating pore (through which the ions are conducted) is occluded in the depolarized state. During depolarization the S4 segment is in an up state. The deep arginine residues occlude the gating pore. If this is indeed the case, then gating pore currents induced by mutations in deeper arginine residues should be active in the depolarized state. Conversely, mutations of the outermost arginine give rise to gating pore currents most prominently measured at the most hyperpolarized voltages. The voltage-dependence of gating pore currents of VSD-I arginines p.R219G (R1), p.R222G (R2), and p.R225G (R3) are shown in Figure 3.5. The voltage dependence of the gating pore currents in VSD-I is clearly consistent with the predicted up and down states of the S4 helix.

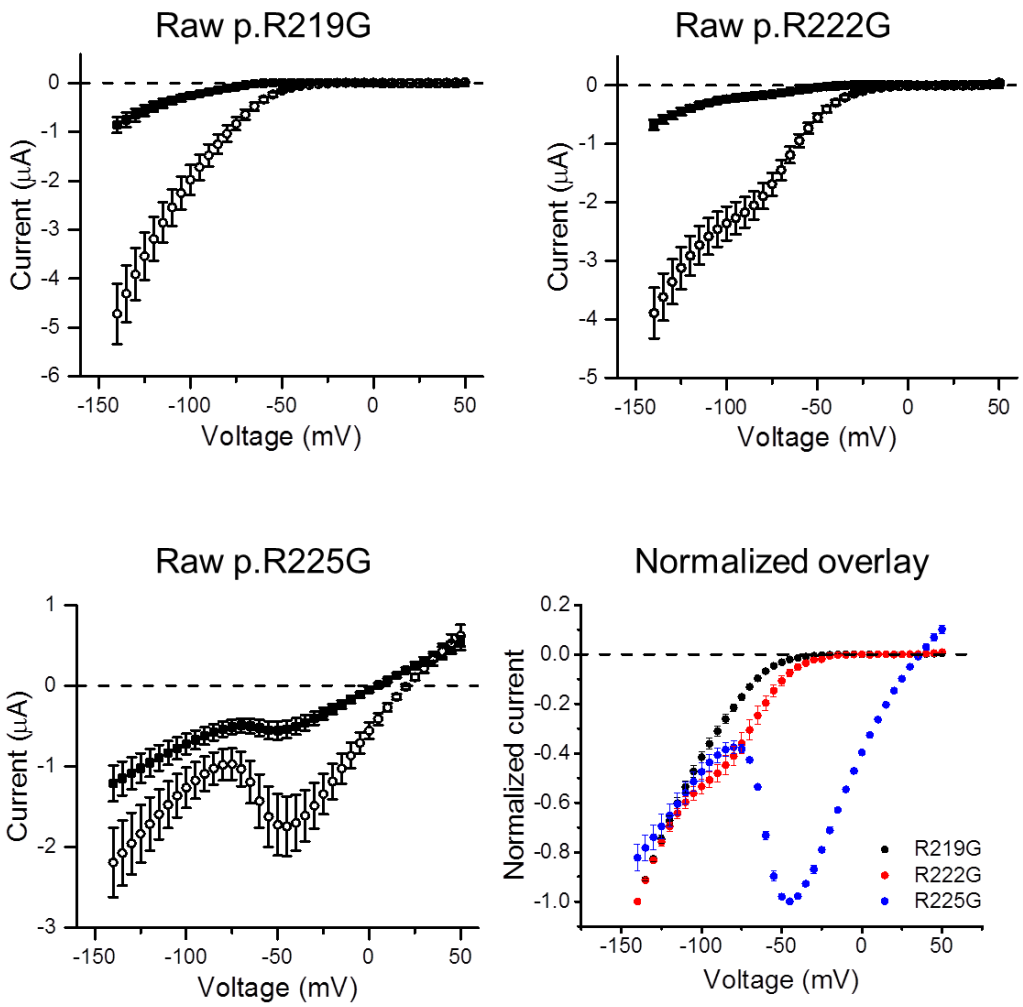

Figure 3.6. Differential behavior of gating pore currents induced by mutant VSD-I R1, R2, and R3. Current-voltage plots of gating pore currents in mutants p.R219G and p.R225G. Current for R219G channels is leak subtracted, for R225G channels the absolute currents are shown in NaMeSO (filled symbols) or NaGn (open symbols). In the overlay currents were normalized to the peak negative current of each cell. For R225G channels the guanidinium specific current is shown (I(NaGn)-I(NaMeSO)). Data are mean±SEM. Figure reproduced with permission from Roope Mannikko.

As predicted, at the most hyperpolarized voltages the gating pore current is active for the two most extracellular arginines, R219G and R222G. It seems that for R222G channels a larger depolarization than for R219G channels is required to close the gating pore, consistent with its location below R219. Neutralization of the third arginine (R225G) leads to depolarization-activated gating pore currents. Activation occurs approximately in voltages where the gating pore currents of R219G and R222G deactivate, suggesting that these events result in movement of the S4 voltage sensor. However, guanidinium increased the gating pore currents of R225G channels at all voltages, suggesting that the gating pore might not be fully closed at any voltage (R Mannikko, personal communication). Thus, no linear leak subtraction was performed for R225G channels. Instead, to minimize the effect of non-specific leak currents, only the guanidinium specific current is illustrated in Figure 3.6.

In all mutant channels, substitution of sodium with guanidinium in the extracellular solution increased the measured current amplitude of non-linear leak currents, confirming the presence of gating pore currents. This confirms that guanidinium is carried through the gating pore and with a higher conductance than sodium, at least in all the S4 arginine mutant channels in VSDs I-III of $Na_V1.4$ that conduct gating pore currents. This is in agreement with the work by Isacoff and Catterall groups (Sokolov et al., 2010; Tombola et al., 2005).

The increased amplitude measured in the presence of guanidinium is likely due to the difference in structure of the ion and consequently hydration shell properties compared to sodium, in a manner analogous to how potassium channels select for potassium over smaller sodium ion. Arginine residues have a guanidinium moiety and the gating pore current data suggest that the gating pore can easily dehydrate the guanidinium ion and provides a low-energy pathway for guanidinium ions. Meanwhile, the gating pore cannot dehydrate sodium as effectively due to the smaller size of sodium, potentially reducing the permeation rate of Na^+ ions.

It is unclear how the nature of the mutation affects the gating pore current amplitude. Large gating pore currents were carried when the arginine was substituted by the largest (W) and the smallest amino acid (G). Significantly smaller gating pore currents were conducted when the arginine was substituted by a polar glutamine (Q). Thus, it seems evident that the chemical properties of the substituting residue, not only the size, affect the gating pore current amplitude.

In addition, reduced gating pore current amplitude cannot be explained by reduced open probability. Voltage dependence of main pore current activation of R222Q channels did not differ from R222G channels and their gating pore currents are active at the same voltage range. This suggests that most likely, the voltage sensor spends a similar fraction of time in the down state for both these channels. Thus, the open probability of the gating pore, i.e. the time spent in the conducting down state, consequently cannot explain the difference in current amplitude.

Finally, the functional main pore properties of p.R222Q are recapitulated by the homologous $Na_V1.5$ (*SCN5A*) p.R222Q mutation (DIR2Q) found in a patient with ventricular ectopy and dilated cardiomyopathy (Mann et al., 2012). As in $Na_V1.4$ p.R222Q, the voltage-dependence of activation and slow inactivation of $Na_V1.5$ p.R222Q mutant channels were also significantly shifted in the hyperpolarizing direction. Gating pore currents have been measured in *SCN5A* mutants p.R219H, p.R222Q, and p.R225W (Gosselin-Badaroudine et al., 2012; Moreau et al., 2015). VSD-I R2 is predicted to stabilize the down state. When mutated, it is predicted that this down state is destabilized, by interrupting interactions with opposing countercharges in S2 and S3.

3.3.4. Implications of the silent *CLCN1* mutation for the clinical presentation of the p.R222Q patient

Unfortunately, drawing conclusions from the correlation of functional properties and clinical phenotype of the R222 mutations is complicated by concomitant mutation in the *CLCN1* gene in the patient carrying the p.R222Q mutation. Initially, this silent mutation was assumed to be a silent polymorphism. However, this mutation was later found associated with myotonia congenita (Horga et al., 2013), predicted to alter splicing of the channel mRNA, and likely results in non-functional ClC-1 channel, associated with recessive myotonia congenita. Given this sequencing information and verbal report of symptoms in the uncle and aunt, this is indicative that mutations are not *de novo*. It is possible that the mother and father each carried one variant, either the *CLCN1* or the *SCN4A* variant.

The *CLCN1* mutation (c.1650G>A) was previously described in recessive myotonia congenita (Horga et al., 2013). Two siblings were heterozygous and asymptomatic according to supplementary material of (Horga et al., 2013). Homozygous carriers of the c.1650G>A variant, as well as compound heterozygous carriers of this variant with another *CLCN1* myotonia congenita variant (p.Cys242X) displayed recessive myotonia congenita. The c.1650G>A variant segregated in our case with disease. This variant was predicted to alter channel splicing, but this has not been experimentally confirmed. A minigene assay could be used to study the effect of the mutation on splicing as no muscle biopsy was available to study the splicing in the muscle. The reduced chloride current may contribute to the more severe myotonic patient phenotype. In addition, reduced chloride current may also contribute to preventing periods of paralysis.

Other *CLCN1* variants have been shown to similarly modulate the phenotype of *SCN4A* variants (Furby et al., 2014). In this study, they examined the putative role of *CLCN1* variants in modulating *SCN4A* phenotypes. In all three cases, the electrophysiological

examination and clinical manifestations did not align with the *SCN4A* mutation identified. Sequencing of *CLCN1* found an additional heterozygous missense variant in all cases. In the first case, the p.G1306E *SCN4A* variant was identified, which is associated with a very severe case of myotonia, often presenting in infants (Caietta et al., 2013; Matthews et al., 2008; Mitrović et al., 1995). This residue is located in the DIII-DIV linker, thus disrupting the hinged lid mechanism for fast inactivation. Clinically the individual harboring this *CLCN1* variant had a much milder phenotype than previously reported in p.G1306E *SCN4A* cases. The p.M485V variant was found in *CLCN1*.

The short exercise test (SET) is a reliable biomarker distinguishing between *SCN4A* and *CLCN1* mutations. SET type II indicates myotonia congenita, while SCM or PMC are associated with type I or III. A type II pattern was found in the patient during SET, indicating that the p.M485V *CLCN1* variant modulates the p.G1306E *SCN4A* phenotype. In the second patient the p.T268M variant was identified in *CLCN1*, reported previously as either recessive or semi-dominant (Brugnoni et al., 1999). Together with the type II SET, it seems the *CLCN1* variant modified the concurrent p.R1337P *SCN4A* variant, because type II is contraindicated in SCM. This p.R1337P variant has not been functionally characterized previously, but is also located in the DIII-DIV cytoplasmic linker, suggesting it may disrupt fast inactivation.

In the third patient with mutant *SCN4A* p.I693M, no episodes of paralysis were reported. SET showed type III behavior. This was inconsistent with the clinical findings, because of warm-up improving muscle stiffness, prompting *CLCN1* sequencing. The variant p.R976X was found. The most important feature of the p.I693M mutant may be enhanced activation. Since no functional characterization was performed in any of the variants, it is unclear whether slow inactivation was affected. If this is the case in p.I693M, it may on its own cause a mixed myotonia/paralysis phenotype, and the reduced chloride current due to p.R976X *CLCN1* may prevent periodic paralysis. The mutant p.I693T causes both myotonia and paralysis (Mankodi et al., 2015).

There is (to my knowledge) a single case describing a *CLCN1* mutation where the patient presented with periodic paralysis. The individual carried variants p.F1290L (*SCN4A*) and p.E950K (*CLCN1*) (Kato et al., 2016). This patient presented with both myotonia and paralysis. The episodes of weakness were particularly severe and sometimes lasted for weeks. The p.F1290L variant resulted in markedly enhanced voltage-dependence of activation. The p.F1290L variant is located in the C-terminal end of S6 in domain III and thus is predicted to not conduct gating pore currents usually associated with periodic paralysis. This was however not tested.

It is unclear whether the p.E950K *CLCN1* variant is pathogenic as it was not studied. Preliminary data suggests it may be wild-type like (R. Mannikko, personal communication). However, the mother who harbored only this *CLCN1* variant had clear myotonia without paralysis. No mutations were identified in the father suggesting the *SCN4A* variant was *de novo*.

Evidence suggesting reduced chloride conductance may prevent episodes of paralysis is accumulating. It is known that ClC-1 mutations, despite reducing the repolarizing current, do not result in periods of paralysis. Pharmacologically reduced chloride conductance by bumetanide, a Na-K-2Cl transporter, has been shown to prevent paradoxical depolarization in wild-type mouse muscle and hypokalemia-induced muscle weakness in hypoPP $Na_V1.4$ mutant mouse models (Wu et al., 2013b). Further, 9-anthracene carboxylic acid (9-AC) blocks ClC-1 channels, thereby hyperpolarizing the depolarized muscle (Geukes Foppen et al., 2002). The authors found that this only occurred if 9-AC was added before extracellular potassium was reduced, not when 9-AC was given after extracellular potassium was reduced.

Prolonged depolarization may depolarize the reversal potential of chloride. Thus, large chloride conductance at the novel paralytic depolarized state may stabilize this state. Consequently, ClC-1 channel mutations that reduce muscle chloride conductance may

prevent the attacks of paralysis, as has been reported for 9-AC that blocks the ClC-1 channel and for bumetanide that hyperpolarizes chloride reversal. This supports the notion of beneficial effects of ClC-1 channel antagonists in hypoPP.

Taken together, these results point towards an intricate interplay between genetic variants in muscle that may have important implications for establishing genotype-phenotype relationships. It would be useful to systematically perform genetic screens for both *CLCN1* and *SCN4A* variants in patients to correlate with disease severity, allowing careful dissection of the potential modifying role of one variant on the other.

3.4. Summary

This chapter studied three variants affecting the same S4 arginine, R222. Two of these are found in individuals with hypoPP type 2 and one in an individual with paramyotonia congenita. All variants induce gating pore currents, although with different current amplitude. Enhanced activation of p.R222Q channel is consistent with myotonia while the prominent gating pore currents of p.R222W and p.R222G channels are consistent with hypoPP type 2.

Thus far mutations affecting the same S4 arginines have caused similar clinical and functional phenotypes (Matthews et al., 2009; Sokolov et al., 2007b). The results presented herein reveal interesting insights into the mechanisms of pathophysiology and structure-function, suggesting genetic data on S4 arginine mutations should be interpreted with caution. These results illustrate that a direct genotype-phenotype correlation is not likely based solely on genetic data. Where possible, functional analysis should be undertaken to support genetic analysis and provide insights into mechanisms of pathophysiology and improve therapeutic management.

4. Gating pore currents caused by hypoPP mutations p.R222G and p.R222W are blocked by the *Heriaeus melloteei* crab spider gating modifier toxin Hm-3

4.1. Background, aims, and hypothesis

The primary pathomechanism for hypokalemic periodic paralysis type 2 is the gating pore current through the voltage sensing domain. Currently no therapies directly targeting this aberrant leak current exists. Patients are counselled to avoid triggers such as carbohydrate rich meals. For the past half-century the carbonic anhydrase inhibitor acetazolamide has been the go-to drug for hypoPP type 2. Other carbonic anhydrase inhibitors such as diclofenamide have also been found effective. The mechanism of why acetazolamide reduces susceptibility to hypoPP episodes is unclear. It was first used in hyperPP and effective assumedly due its K^+ lowering effects (McArdle, 1962). Inadvertently it was used in patients with hypoPP and found effective in some cases. Blocking carbonic anhydrase is believed to affect pH regulation, and has also been shown to promote opening of calcium-activated potassium channels (Tricarico et al., 2000). It has also been found to induce a hyperpolarizing shift in the voltage-dependence of activation in ClC-1 channels expressed in HEK293T cells (Eguchi et al., 2006).

A limited number of individuals with hypoPP respond to acetazolamide, as little as 50 % (Matthews et al., 2011b). In individuals where acetazolamide was efficacious, the clinical outcome was a reduced frequency of attacks. However, the symptoms of a portion of individuals worsen with acetazolamide. As such, the development of alternative therapies is highly sought after, and targeting the disease mechanism directly would be the optimal scenario.

Toxins have previously been found to modify the function of voltage-gated ion channels by interacting with the VSDs (Catterall et al., 2007). These toxins are collectively known as gating modifier toxins. Gating modifiers that interact with VSD-II and VSD-IV of Na_V channels have been reported previously. For instance, beta-scorpion toxins were found to bind the extracellular end of S4 of VSD-II, thereby stabilizing the up state of the channel

(Catterall et al., 2007). This in turn enhanced channel activation, as seen by a hyperpolarizing shift in the voltage-dependence of activation.

Our collaborator in the Vassilevski lab in Moscow recently extracted a 35-amino acids long gating modifier toxin from the *Heriaeus melloteei* crab spider called Hm-3 (Berkut et al., 2014), which modified gating of $Na_V1.4$ and $Na_V1.5$, by shifting the voltage dependence of activation to more depolarized voltages. Hm-3 did not compete with TTX or other blockers that bind in channel pore. This suggests it acts as a gating modifier rather than direct pore blocker.

By using guanidinium in the extracellular solution we can magnify the amplitude of the gating pore currents and confirm that the currents we measure are indeed gating pore currents (chapter 3). Increased amplitude and pharmacological specificity of these currents allows us to study the pharmacology of gating pore currents.

We tested the hypothesis that Hm-3 may block the gating pore or otherwise modulate gating pore current properties of arginine mutant channels. This was tested by expressing the rat *SCN4A* clone in *Xenopus* oocytes and studying the effects of Hm-3 on the gating pore and main pore currents.

4.2. Results

4.2.1. Note on results

This chapter is a continuation of my work in the previous chapter on gating pore currents caused by mutations in the second S4 arginine residue of domain I (R2 VSD-I). Alexander Vassilevski and his group in Moscow produced the Hm-3 toxin. Initial oocyte recordings of Hm-3 on S4 arginine mutants were performed in collaboration with Louise King and Emma Wilson. Roope performed many recordings for Figure 4.3. My data was used to

further analyze the interaction between Hm-3 and $Na_V1.4$ channels. Zakhar O. Shenkarev and his group performed the NMR studies. These data are included in the discussion. Most oocyte recordings of the effect of Hm-3 on main pore currents in oocytes were performed by Marisol Sampedro-Castañeda. Frank Bosmans (Johns Hopkins University, Baltimore, US) performed experiments where *SCN4A* VSDs were substituted into $K_V2.1$ channels to test Hm-3 domain specificity.

4.2.2. Gating pore currents in VSD-I R2 mutants p.R222W and p.R222G

As shown in Chapter 3, robust gating pore currents can be measured in mutant p.R222G and p.R222W channels (Figure 4.1.). In both channels, after blocking the main pore with TTX a downward deflection can be seen in extracellular solution with sodium as extracellular monovalent cation at the most hyperpolarized holding potentials. No such current was seen for wild-type channels suggesting these do not carry gating pore currents. Substitution of half of the extracellular sodium with guanidinium markedly increased the non-linear current of p.R222W and p.R222G channels at hyperpolarized voltages, confirming the presence of gating pore currents in these mutants. Current amplitude of wild-type channels is minimally affected by substituting sodium with guanidinium in the extracellular solution (chapter 3). We used TEVC recordings in extracellular Na/Gn solution to study the pharmacology of gating pore currents.

4.2.3. Gating pore currents in p.R222W and p.R222G are blocked by the *Heriaeus melloteei* crab spider toxin Hm-3

We studied the effect of Hm-3 on gating pore currents through a set of S4 arginine mutations. Extracellular Na/Gn solution was used to confirm the presence of gating pore currents and to amplify the gating pore currents to an amplitude amenable for

pharmacological studies. The maximum Hm-3 test concentration was 10 µM. It was found that Hm-3 at this concentration blocked the gating pore currents in both p.R222G and p.R222W channels to similar levels. When measured at -80 mV the current amplitude in presence of 10 µM Hm-3 was reduced to 64±5 % (p.R222G, n=8) and 67±5 % (p.R222W, n=4) compared to the currents in its absence.

A concentration effect plot (Figure 4.2.; bottom; middle panel) for Hm-3 block of p.R222G channels was constructed using non-cumulative data (n=2-8 cells at each concentration) by dividing the current measured after addition of Hm-3 by the current measured in the absence of Hm-3 at various Hm-3 concentrations. The data were fit with a Hill equation. The IC_{50} for p.R222G channels measured from non-cumulative data was 5.4±0.8 µM at −80 mV.

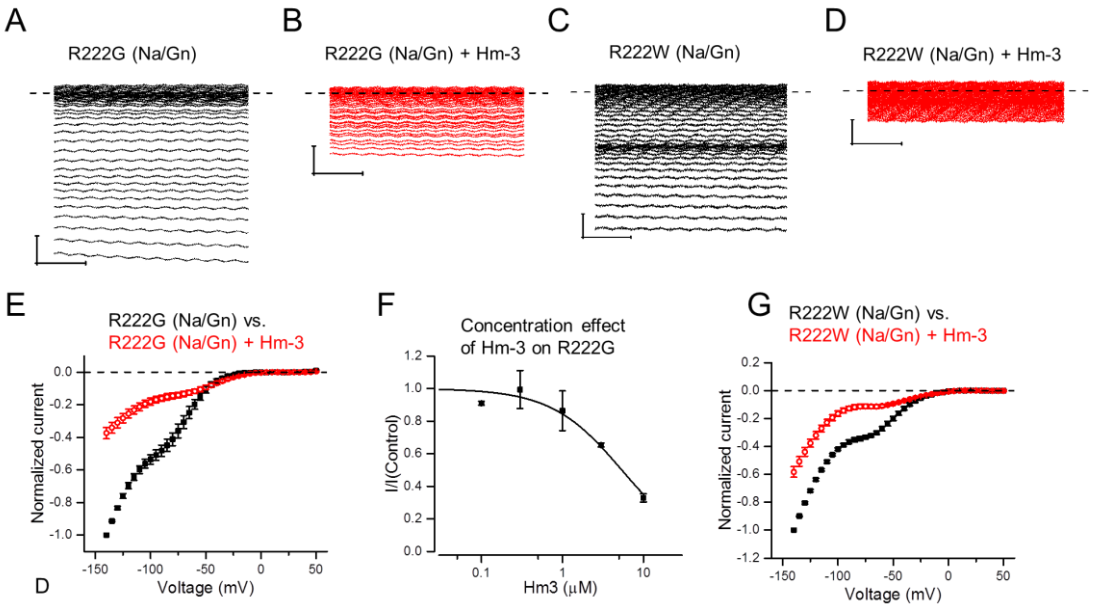

Figure 4.1. Hm-3 blocks gating pore currents of variants p.R222G and p.R222W

Top: Representative current traces of (A-B) p.R222G and (C-D) p.R222W mutant $Na_V1.4$ channels in Na1:Gn1 solution, before or after addition of 10 µM Hm-3. The last 200 ms of 300 ms voltage step to voltages ranging from -140 mV to +50 mV are shown. Scale bars: x=50 ms y=0.5 µA. **(E):** p.R222G (n=8 cells) gating pore current I-V plot either without (solid black squares) or with (open red circles) 10 µM Hm-3 added. Data

was normalized to current amplitude at -140 mV in absence of Hm-3 for each cell before averaging. (F)**:** dose-response curve of Hm-3 block in p.R222G mutant channels measured at -80 mV. The current amplitude measured in the presence of Hm-3 at each concentration was divided by the current in the absence of Hm-3. Dose-response function was fitted to the non-cumulative data (different cells). Extracellular solution was as previously Na1:Gn1. Sample size ranges from n=2 to n=8. **G:** p.R222W (n=4) in the absence (full circle) or presence (open circle) of 10 µM Hm-3. The currents for each cell were normalized as in E. Due to limited Hm-3 availability a concentration-effect curve was not performed in R222W.

4.2.4. Gating pore currents in arginine mutants of domain II and III

We wanted to test if the effect of Hm-3 was specific to VSD-I. Neutralization of gating charges in domain II and III also introduce gating pore currents (Sokolov et al., 2008; Struyk et al., 2008). Current-voltage plots of gating pore currents in p.R666G (R2, VSD-II) resemble those of p.R222G (Figure 4.3). Numbering R1/2/3 signifies which arginine is visualized (counting from the extracellular surface, e.g. R219 is R1, VSD-I. Both R2 of VSD-I and VSD-II activate at hyperpolarized voltages, though the shape of the current-voltage relationship differs slightly at the most hyperpolarized voltages. Meanwhile, neutralization of the third arginine p.R669G (R3, VSD-II) leads to clear depolarization-activated gating pore currents, analogous to p.R225G (R3, VSD-III) (Figure 4.3).

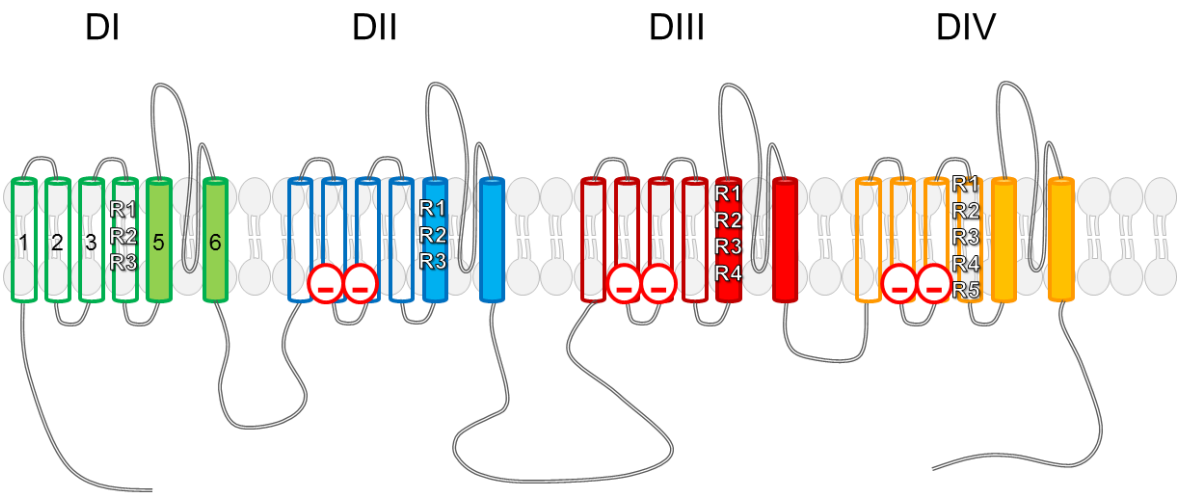

Domain	R1	R2	R3	R4	R5
DI	R219	R222	R225		
DII	R663	R666	R669		
DIII	R1122	R1125	R1128	R1131	
DIV	R1441	R1444	R1447	R1450	R1453

Figure 4.2. Position of gating charge arginines in the $Na_V1.4$ alpha pore subunit

Position of each arginine (R1-R5) localized to domains I to IV (DI-DIV). R1-R5 signify position of arginine counted from the extracellular side, with R1 being most extracellular, and R5 most intracellularly positioned. Rat NaV1.4 numbering.

In domain III, gating pore currents resulting from neutralization of the outermost arginine (R1) (human p.R1129) has not been detected (R1H: (Gosselin-badaroudine et al., 2012), and R1G: R Mannikko, personal communication). However, there is a report of a DIII-R1 mutation found in a patient with hypoPP (Hong et al., 2009, R1Q), suggesting a potential presence of gating pore currents. DIII-R2 mutations (p.R1125Q (Figure 4.3) and p.R1125G (not shown) introduce hyperpolarization-activated gating pore currents. Similarly, the IV plot of p.R1135C gating pore currents resembles those of p.R219G channels, showing hyperpolarization activated gating pore currents. Unlike VSD-I and –II, gating pore currents through both R2 and R3 are activated by hyperpolarization, suggesting that the arginines in these domains have non-equivalent roles. Our findings are in slight contrast with (Groome et al., 2014) who suggested that gating pore currents

through R1135C and R1135H channels activated at hyperpolarized voltages only following a depolarizing pre-pulse. In our experiments the holding voltage was -100 mV, and the hyperpolarization activated gating pore currents were readily detectable in NaMeSO and Na/Gn solutions (Figure 4.3).

Thus far no gating pore currents have been shown for mutations affecting arginines in S4 of VSD-IV in Na_V channels (Francis et al., 2011b; Habbout et al., 2016).

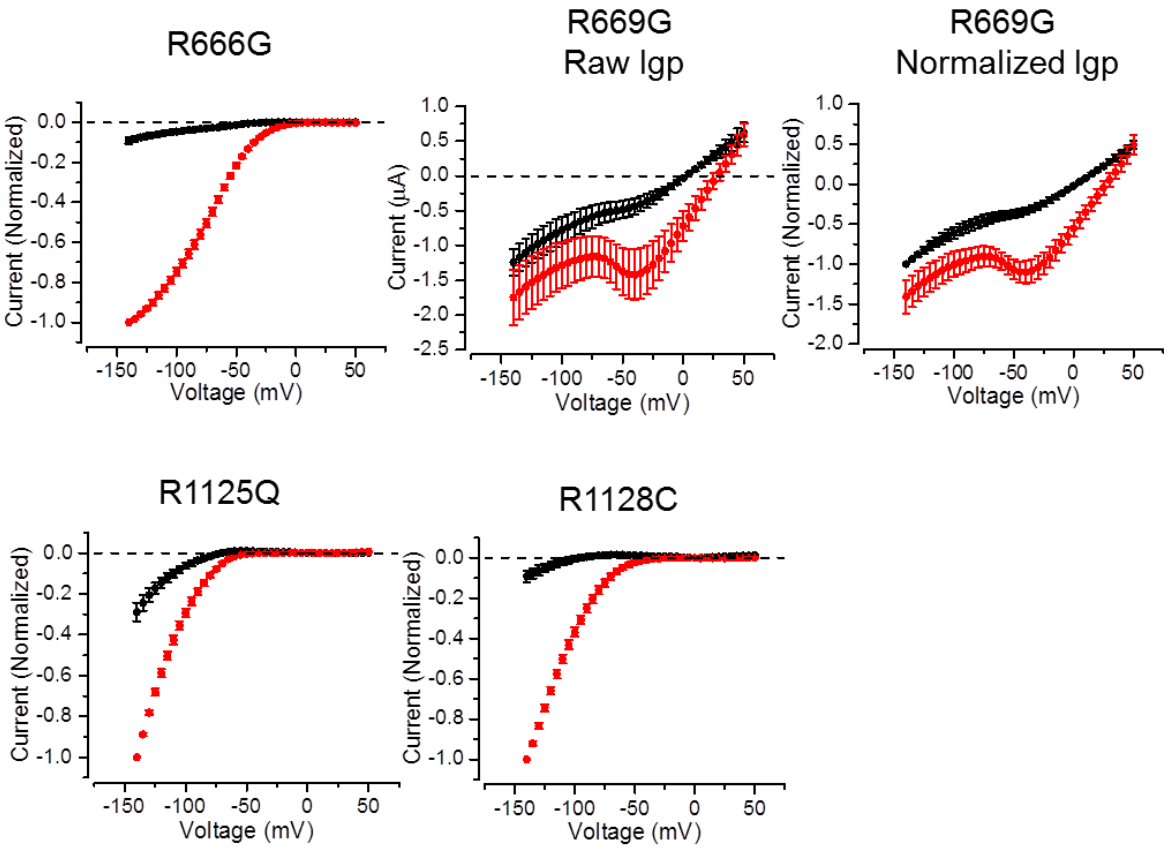

Figure 4.3. Gating pore currents induced by arginine substitution in VSD-II

Symbols are mean±SEM. A. Gating pore currents through R666G (VSD-II R2) channels in NaMeSO (black) and Na/Gn (red) solutions (n=11). Numbering refers to rat *SCN4A* clone. Data normalized to current amplitude at -140 mV in Na/Gn solution. B, C, Gating pore currents through R669G (VSD-II R3) in NaMeSO (black) and Na/Gn (red) solutions (n=3). B shows the raw currents; in C the currents are normalized to current amplitude at -140 in D & E. A Gating pore currents through R1125Q (D; VSD-III R2; n=9) and R1128C (E; VSD-III R2; n=13) channels in NaMeSO (black) and Na/Gn (red) solutions. Data normalized as in A.

4.2.5. Functional data show a VSD-I specific block by Hm-3

After establishing the presence of gating pore currents in various S4 arginine mutations we tested their sensitivity to Hm-3 block. We tested if 10 µM Hm-3 is able to block gating pore currents caused by neutralization of R1 and R3 of VSD-I (p.R219G and p.R225G) as well as R2 of VSD-II (p.R666G) and R2 VSD-III (p.R1125Q).The gating pore current amplitude remained unaffected in all these mutant channels by addition of Hm-3 into the bath solution (Figure 4.4.). This strongly suggests that this gating pore current block is not only specific to VSD-I, but to R2 in particular. The voltage dependence of gating pore currents of p.R225G channels showed potentially a small shift in the voltage dependence of activation.

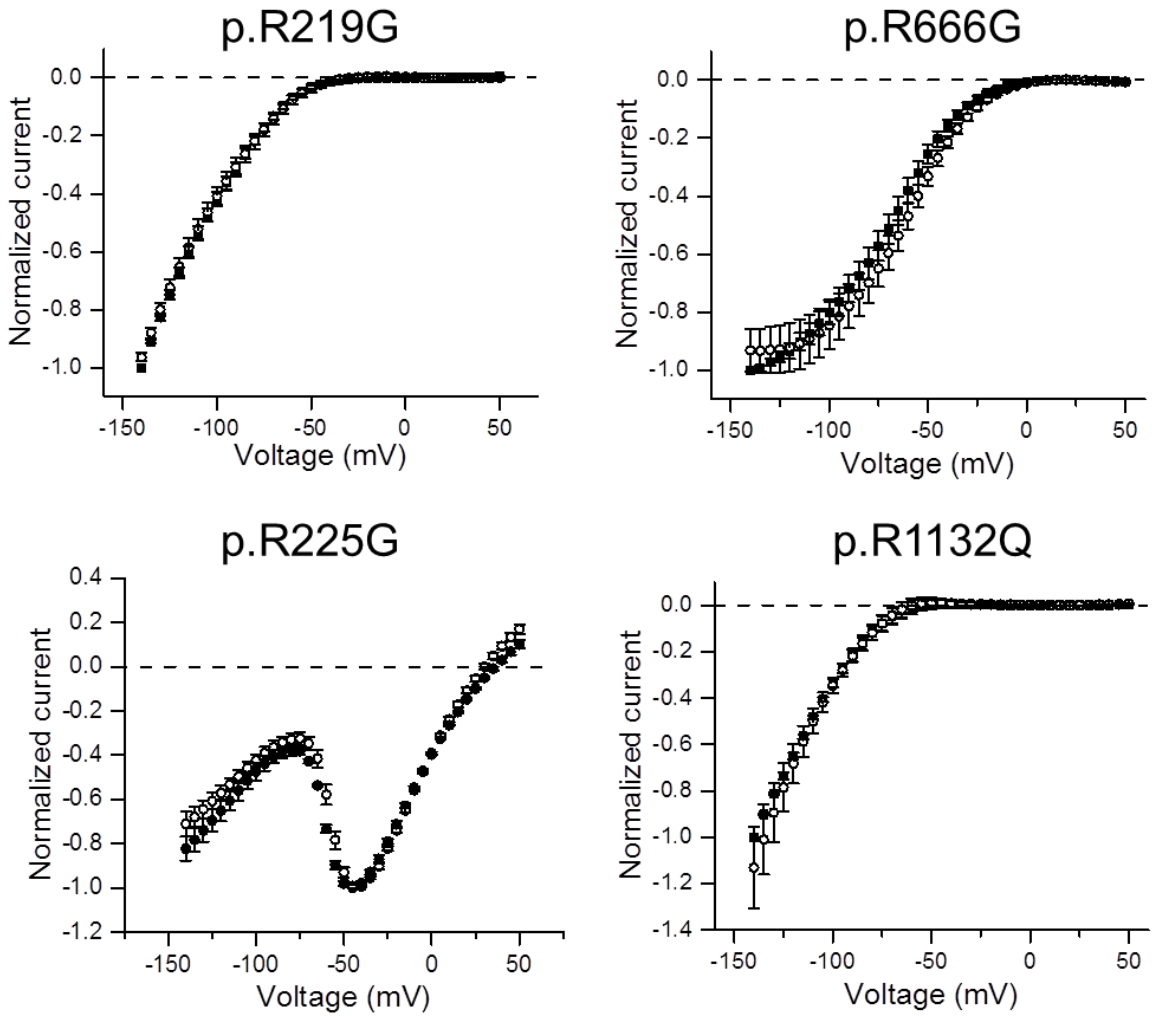

Figure 4.4. Hm-3 does not block gating pore currents caused by arginine mutations in domains II and III, or domain I R1, R3. Leak subtracted data are shown for all but R225G channels. The gating pore currents are shown in the absence (solid circles) and presence (open circles) of 10 µM Hm3 for the same channels (n=3 for each mutant). The currents for each cell were normalized by dividing the current measured at -140 mV in the absence of Hm-3 before averaging. Leak subtracted data were used for all but R225G channels. For R225G channels the current in NaMeSO was subtracted from the Na/Gn and Na/Gn & Hm-3 data. Data are mean±SEM.

4.3. Discussion

This chapter identified a novel gating modifier toxin capable of modulating gating pore currents in a manner that appears specific to the second arginine of the first voltage sensing domain (VSD-I). This is the first description of gating modifier toxin blocking the leak current underlying hypoPP, and suggests that gating modifier toxins are a useful source of identifying potentially therapeutically interesting gating pore current blockers. In addition, the data provide evidence that VSD-I is the main binding site of Hm-3. This is the first report of VSD-I being the specific target of gating modifier toxins that have previously been shown to bind to VSD-II or VSD-IV. In addition, our data suggest that using the TEVC method with guanidinium to specifically amplify the gating pore current amplitude may be used as screening platform for blockers of gating pore currents. The implications of my findings of Hm-3 binding to VSD-I were studied further by our collaborators.

4.3.1. Hm-3 specifically binds the first voltage sensor domain (VSD-I)

Gating pore currents in p.R222G and p.R222W were robustly blocked by Hm-3 at 10 µM. However, Hm-3 did not block omega currents in VSD-II mutant p.R666G or VSD-III mutant p.R1132Q. These data suggest that Hm-3 interacts only with VSD-I in a manner that allows inhibition of gating pore currents.

The specific binding to VSD-I was further studied by analyzing the effect of Hm-3 on main pore currents of wild-type and mutant channels expressed on *Xenopus* oocytes. To

ensure good voltage clamp the concentration of mRNA injected was 1/10th-1/100^{h} of the concentration injected to study gating pore currents and the currents were measured on the day following mRNA injection. The fraction of block by 1 µM Hm-3 was calculated by dividing the main pore current amplitude at -20 mV after Hm-3 block by the peak amplitude before Hm-3 addition. In wild-type channels a considerable fraction of main pore currents was blocked (approximately 60 %) at -20 mV by 1 µM Hm-3. However, the fraction of block in p.R219G and p.R222G main pore currents was markedly reduced compared to wild-type (n≥5 each clone, $P<0.01$; one-way ANOVA followed by Tukey's *post hoc* test; Figure 4.4). A small non-significant trend towards a reduced fraction block was observed in p.R222W channels (n=5). VSD-II R2 and VSD-III R3 mutant channels were blocked in a similar manner as wild-type. Thus, Hm-3 binding is affected by mutations in VSD-I, confirming that VSD-I forms a binding site for Hm-3. Intriguingly, although R219G gating pore currents were not blocked by Hm-3, the affinity of Hm-3 to $Na_V1.4$ is reduced due to the reduced block of p.R219G main pore channels.

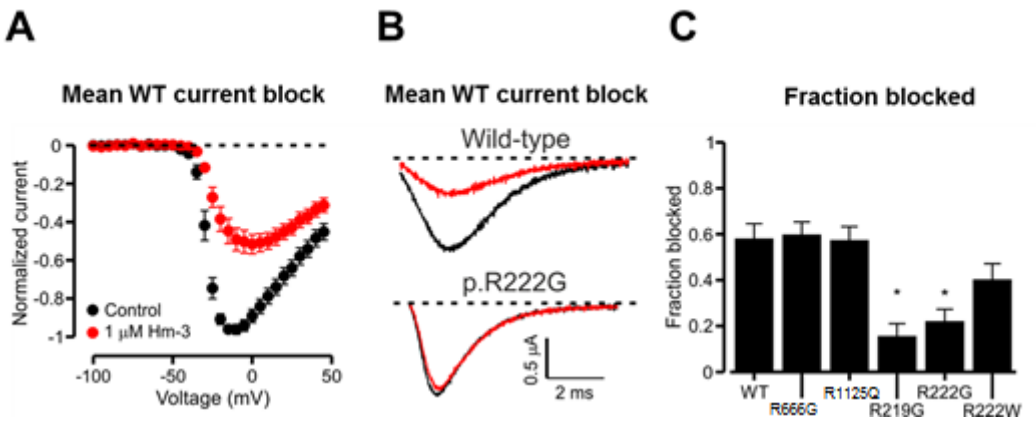

Figure 4.5. Hm-3 right-shifts the wild-type peak current and the fraction of main pore current block by Hm-3 is dependent on the channel genotype.

(**A**) Mean+SEM peak current amplitude in wild-type before and after 1 μM Hm-3 was added. Note the right-shift in the peak current after Hm-3 addition. Black symbols: before Hm-3; Red symbols: after 1 μM Hm-3 (**B**) Traces of WT and p.R222G mutant channels showing difference in block before (black trace) and after (red trace) Hm-3 addition. (**C**) Fraction of block of main pore currents of WT, DII mutant p.R666G, DIII mutant p.R1125Q, domain I R1 mutant p.R219G, and R2 mutants p.R222G and p.R222W. Asterisks indicate significant difference in mean (one-way ANOVA followed by Tukey's *post hoc* test). Significantly reduced fraction of block observed in p.R219G and p.R222G. Fraction of block was calculated by dividing main peak amplitude at -20 mV after Hm-3 vs. before Hm-3. Figure re-created with permission from Roope Mannikko and Marisol Sampredo-Castaneda. Marisol performed most of these recordings.

The gating and main pore current recordings strongly suggest that Hm-3 binds to VSD-I. This information was used by our collaborators who studied Hm-3 and its interaction with VSD-I by nuclear magnetic resonance (NMR) spectroscopy at different molar ratios. *In vitro* produced VSD-I of $Na_V1.4$ (L114-S246) were mixed with micelles, and Hm-3. NMR spectra of Hm-3 were first taken in the absence of VSD-I and the presence of the micelle to identify which regions of Hm-3 interact with the membrane. Labeled Hm-3 was studied in presence of the VSD-I and vice versa to identify regions forming the channel-toxin interaction.

Figure 4.6. illustrates in red the residues in VSD-I that show changes in NMR spectra upon addition of Hm-3 into the reaction mixture. The structure is based on a homology model of the VSD-I, also courtesy of the collaborators. Hm-3 interacts with VSD-I residues S199-T207 and L212-L215. No signal was available from residues 208-211. Because an Hm-3—VSD-I interaction was observed in L212 and L207, the adjacent (unassigned) glutamic (E208) and aspartic acids (D211) are assumed to form important interactions with positive residues in Hm-3. Both R1 (p.R219) and R2 (p.R222) were also unassigned, meaning it cannot be definitively concluded whether these residues interact with Hm-3 during block. There was no response measured in p.R225, suggesting it does not interact with Hm-3. Thus, NMR data confirmed our findings on interaction of VSD-I with Hm-3 and indicates that Hm-3 binds VSD-I by interacting with residues in extracellular end of S3 helix and in the S3-S4 loop.

To confirm the potential binding site collaborator Frank Bosman generated chimeric $K_V2.1$ / $Na_V1.4$ channels where the S3-S4 helix-loop-helix of each VSD of $Na_V1.4$ was implanted to the VSD of $K_V2.1$ channels, expressed in *Xenopus* oocytes and was functionally characterized by voltage clamp. Replacing the native motif of homotetrameric Kv2.1 channels by S3-S4 helix-loop-helix motifs of individual VSDs results in channels with four copies of the motif available for Hm-3 binding. Illustrated in the figure are conductance-voltage plots before (black symbols) and after (colored symbols) addition of 1.5 µM Hm-3. A depolarizing shift in the G-V curve is observed only when the motif of VSD-I is implanted (DI, top panel), indicating that only $K_V2.1$ channels expressing the S3-loop-S4 motif from domain I can be modulated by Hm-3. This further suggests Hm-3 interacts specifically with VSD-I and confirms its binding to the S3-S4 helix-loop-helix motif.

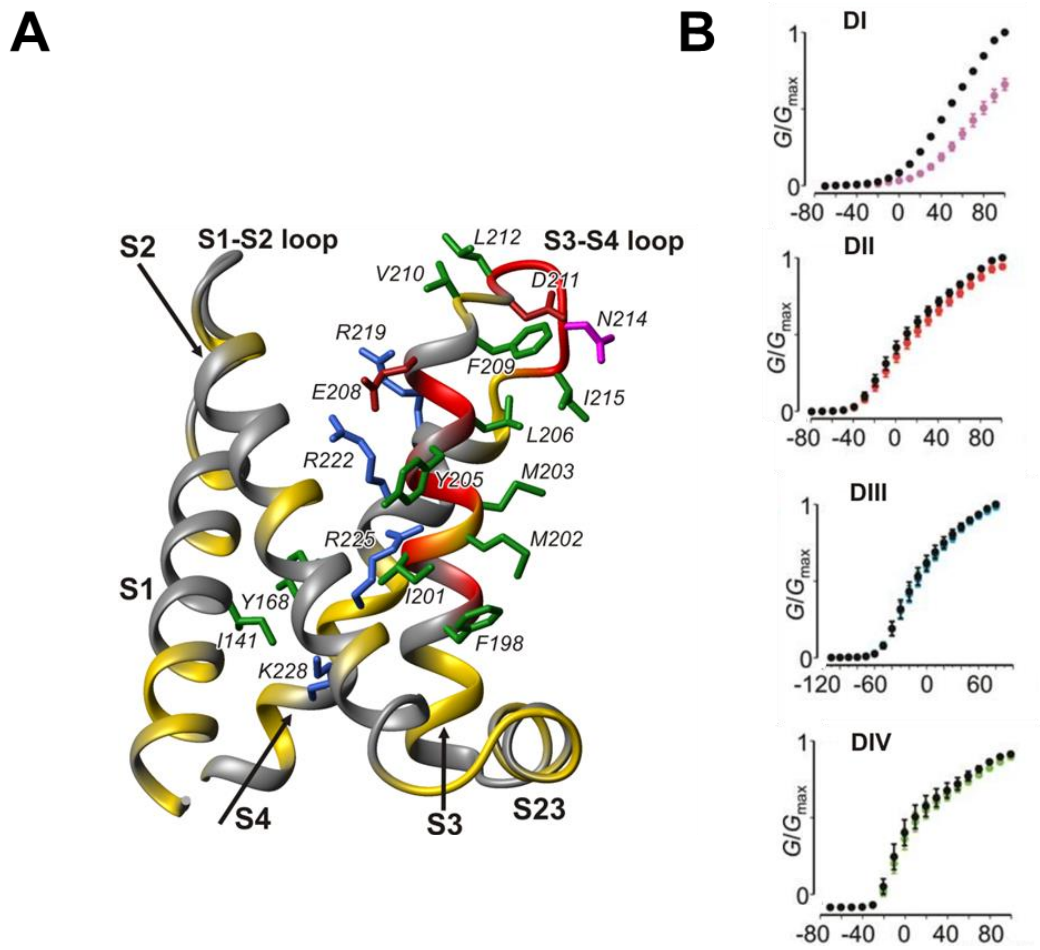

Figure 4.6. Specific binding of Hm-3 to VSD-I by NMR and functional experiments.

(**A**) NMR data of Hm-3 binding VSD-I at the S3-S4 loop. Red and yellow show the assigned residues; red residues showed interaction with Hm-3, yellow residues did not interact with Hm-3. Gray residues were unassigned. (**B**) $Na_V1.4$ VSDs I-IV (DI-DIV) were transplanted into Kv2.1 and 1.5 µM Hm-3 added to test the effect on conductance. Shown are normalized conductance-voltage plots (G/Gmax) in each of the domains inserted into Kv2.1 (n=3 each). Only change was observed in DI-transplanted channel after Hm-3 addition. Re-constructed with permission from Vassilevski group and Mannikko lab. NMR experiments by Zakhar O. Shenkarev lab. Kv2.1 data by Frank Bosmans' lab.

4.3.2. Implications for developing pharmacological therapy targeting the gating pore current directly

The ability of Hm-3 to block gating pore currents induced by p.R222G and p.R222W provides proof-of-principle evidence for the use of gating modifier toxin compounds

directly targeting the primary disease pathomechanism of hypoPP. This has not been shown previously. To our knowledge the only other blockers of gating pore currents associated with HypoPP is the guanidinium analog 1-(2,4-xylyl)guanidinium, albeit in the millimolar range (Sokolov et al., 2010). In addition, in structure-function studies, gating pore currents introduced by mutations of sequential multiple arginines, have been blocked by gating modifier toxins (Catterall et al., 2007). However, these mutations were not associated with hypoPP.

Because Hm-3 also modulates other human sodium channel isoforms including $Na_V1.5$, $Na_V1.2$, and $Na_V1.6$ (Berkut et al., 2014), it cannot in its natural form be used clinically due to predictably severe off-target effects. Also, since main pore currents are blocked by Hm-3 with higher affinity than the gating pore currents, this further suggests that Hm-3 is not clinically viable. More information is necessary to understand how Hm-3 interacts with VSD-I to potentially develop Hm-3-like substances to block gating pore currents caused by neutralization of gating charges in different domains. Interestingly, VSDs have recently been a target for development of Na_V isoform specific drugs for pain management (Ahuja et al., 2015). This suggests that targeting the VSDs may allow to improve Na_V isoform specificity of novel drugs.

Using a functional testing setup to screen for synthetic derivatives of Hm-3 like compounds, an optimal compound that only blocks the gating pore current (or only mild effect of main pore current), with no off-target effects may be found. The throughput of functional testing of gating pore currents could be enhanced by automated oocyte platforms such as HiClamp (MultiChannel Systems).

In addition, NMR spectroscopy of isolated VSDs is a useful tool for refining channel-toxin interactions. Combining NMR with functional characterization may be useful in improving the description of gating pore current blocking pharmacophores. NMR studies are however limited by their lack of electrical field (0 mV), which means that S4 segments of

voltage-gated channels will be in the up state. This currently narrows the usefulness of data derived from NMR studies when investigating the structural basis for hyperpolarization-activated gating pore current block.

4.3.3. The mechanism of Hm-3 block of main pore current and gating pore currents

The inhibition of hyperpolarization-activated gating pore currents and shift in the voltage dependence of activation to more depolarized voltages suggests that Hm-3 interacts with and stabilizes the VSD-I in the down state. However, the NMR data was gathered in micelles in the absence of voltage and with the VSD-I in the up state (0 mV). This limitation is similar for structural data available for voltage gated ion channels (Chakrapani et al., 2008). The NMR data indicate though that Hm-3 can interact with VSD-I in the up state. It has been suggested that some toxins function as cargos on VSDs of voltage gated ion channels, shuttling attached to, or within close proximity with the VSD as it moves between up and down states (Revell Phillips et al., 2005). This is consistent with our observations of Hm-3 interacting with VSD-I in both up and down states. However, in order to prevent normal channel activation, the affinity to the down state should be higher than to the up state.

Currently, the available VSD structures, including our NMR data are from the up state of the voltage sensor. Thus the down state of the VSD or the mechanism of gating pore current block by Hm-3 of the gating pore current active in the down state cannot be accurately modelled. However, it is likely that the relative localization of Hm-3 binding elements (S3 and S4 helices and the connecting loop) changes upon the down transition (Larsson et al., 1996; Tombola et al., 2005) and can underlie increased affinity of the Hm-3 to the down state. Our functional data shows that main pore inhibition by Hm-3 is reduced by mutations of R219 and R222 arginines, suggesting that Hm-3 interacts with

these residues in the down state. However, Hm-3 does not inhibit gating pore currents through p.R219G channels. The mechanism behind this discrepancy on gating pore current block remains to be established.

4.4. Summary

This chapter identified a gating modifier toxin, Hm-3, able to directly inhibit gating pore currents introduced by neutralization of VSD-I R2. This inhibition was specific to domain I, and in particular of gating pore currents of R2 mutations.

This provides the first proof-of-principle evidence that gating pore currents that underlie hypoPP can be blocked directly by gating modifier toxins, opening up a potential avenue for developing pharmacological agents that target the pathomechanism of hypoPP type 2 directly.

The use of guanidinium substitution can be used to detect and confirm the presence of gating pore currents in *SCN4A* mutants. Guanidinium appears to have a higher conductance through the pore compared to sodium. This should help throughput of confirming gating pore currents, and testing any putative gating pore blockers or synthetic derivatives.

5. Heteroallelic loss of function in the skeletal muscle sodium channel gene *SCN4A* cause congenital myopathy or fetal hypokinesia

5.1. Background, aims, and hypothesis

At the beginning of my PhD project only one report of recessive loss of function variants in $Na_V1.4$ associated with a clinical phenotype existed (Tsujino et al., 2003). The individual suffered from congenital myasthenic syndrome. Due to the single exceptional case, congenital myasthenia was often not included in the list of $Na_V1.4$ channelopathies. During my PhD, two additional congenital myasthenic syndrome cases due to recessive *SCN4A* mutations were described (Arnold et al. 2015; Habbout et al. 2016).

The study presented in this chapter identified compound heterozygous *SCN4A* variants in a patient with congenital myopathy. Myopathy is clinically distinct from myasthenia in the sense that the weakness experienced by the patient is fixed, whereas myasthenia is associated with increased fatigability. Curiously, one of the compound heterozygous mutations in the first myopathy case we studied affected an S4 arginine in VSD-III of $Na_V1.4$. This variant has been studied previously (Groome et al 2014). In addition to gating pore currents, the mutation enhances channel inactivation. Functional characterization of the second mutation revealed full absence of functional expression. This was the first time a null mutation of $Na_V1.4$ was found associated with disease.

From this we hypothesized that recessive loss-of-function *SCN4A* mutations may underlie congenital myopathy. This hypothesis was tested by functionally characterizing the identified variants in the index case and a further 10 individuals from five other kindreds in HEK293T cells by patch clamp. This allowed delineating the pathogenicity and mechanism of pathophysiology of these *SCN4A* variants.

5.2. Results

5.2.1. Note on results

The initial case was identified at UCL led by Professor Francesco Muntoni and team members Dr. Irina Zaharieva and Dr Emily Oates. The pathology team is led by Prof Caroline Sewry, Dr Rahul Phadke, Dr Lucy Feng. The work expanded as a result of an international collaboration across neuromuscular centers based in the United Kingdom, the Netherlands, Denmark, Norway, Australia, and Canada. Novel *SCN4A* mutations were detected in a patient cohort with congenital myopathy.

B.C. Children's & Women's Hospital, Canada team led by Dr Clara van Karnebeek and Professor Suzanne Lewis, Dr Hilary Vallance. The pathology team is led by Dr Glenda Hendson and the functional assessment of the mutations has been done by Dr Peter Ruben. Dr Erik-Jan Kamsteeg who has identified the *SCN4A* mutations in the Dutch-Sudanese family, the Danish family and the Norwegian family. Dr Eveline Blom who is the referring clinician for the Dutch-Sudanese family. Dr Magnhild Rasmussen, Consultant in child neurology, Oslo University Hospital who is the referring clinician for the Norwegian family. The Australian family was studied by collaborators at the Harry Perkins Institute of Medical Research, Centre for Medical Research, The University of Western Australia, Perth. The Danish family was identified by collaborators at the Copenhagen Neuromuscular Center and the Department of Clinical Neurophysiology at Rigshospitalet, University of Copenhagen, Denmark. Full affiliations list can be found at https://doi.org/10.1093/brain/awv352.

5.2.2. Identification of bi-allelic *SCN4A* mutations in patients with congenital myopathy or fetal akinesia

A young female with congenital myopathy was first identified at the UCL Institute of Child Health. Whole-exome sequencing revealed two mutations in *SCN4A* p.R104H and p.R1135C. The variant p.R104H was inherited from the mother and p.R1135C from the father, suggesting that the mutations are found in opposite alleles. Both parents were asymptomatic.

The p.R104 is located in the N-terminal domain, potentially important for channel trafficking (Clatot et al., 2012). p.R1135C is a positively charged arginine in S4 helix of VSD-III (Groome et al., 2014). The functional effects of this mutation have been previously reported (Groome et al., 2014). The novel p.R104H mutation was inserted into wild-type human *SCN4A* cDNA and transfected in HEK293T cells, allowing me to study the electrical properties of these channels by patch clamp.

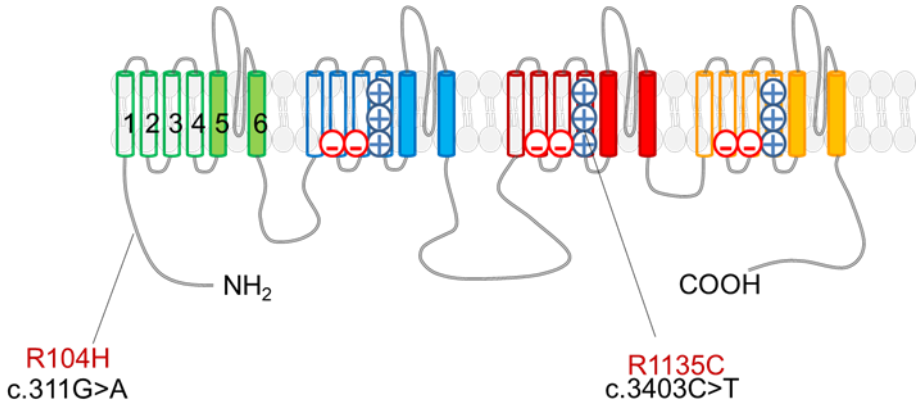

Figure 5.1. Location of mutations in the index case with congenital myopathy. Mutations located to the N-terminal domain (R104H) and S4 of domain III (R1135C, respectively).

I was unable to measure any currents in p.R104H mutant channels. The variant p.R1135C causes enhanced fast inactivation (Groome et al., 2014), resulting in reduced availability of $Na_V1.4$ channels in physiological voltages, thus constituting a loss of function. In addition, p.R1135H channels conduct gating pore currents, a finding that we confirmed by TEVC in *Xenopus laevis* oocytes (Figure 4.3). These findings led us to hypothesize that the combined effects of one full loss of function mutation and a partial loss of function mutation on opposite alleles give rise to congenital myopathy. The role of gating pore currents in myopathy is unknown.

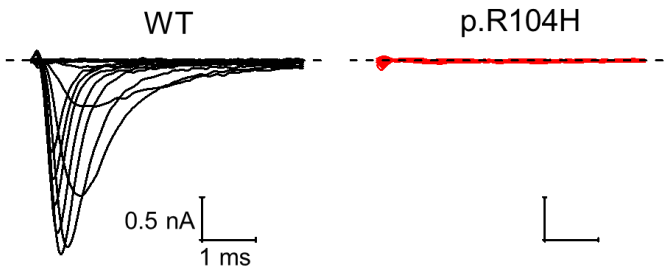

Figure 5.2. Functional expression of index case missense variant p.R104H reveals complete loss of function. Representative current traces for HEK293 cells expressing WT (left) and p.R104H (right) channels. Scale bars are 1 ms (x), 0.5 nA (y). Dashed lines show 0 current level.

5.2.3. Genetics of the myopathy cohort

Through a large European collaborative effort known as NeurOmics[1] ten additional cases with similar clinical manifestation were identified in five distinct kindreds by exome sequencing (Table 5.1; Figure 5.2.). All affected cases carried bi-allelic *SCN4A* mutations that segregated with disease. All 12 parents of the myopathy cohort and one unaffected

[1] NeurOmics is a research project funded by the European Commission bringing together important stakeholders in the field, from researchers, clinicians, bioinformaticians, patients, and ethics experts. More information here: RD-NeurOmics.eu

sibling were clinically unaffected carriers of a single *SCN4A* mutation. All but two mutations had not been described previously (Table 5.1), with p.R1135C described in a patient with hypoPP (Groome et al., 2014), and p.R225W in a patient with myotonia (Lee et al., 2009). No functional characterization of p.R225W is available. Three variants introduced premature stop codons (p.Q470X, p.A1049VfsX50, and p.Y1593X), predicted to produce polypeptides unable to form functional channels. p.A1049VfsX50 disrupts an essential splice site. Erroneous splicing was confirmed using reverse transcription PCR in the proband and the father.

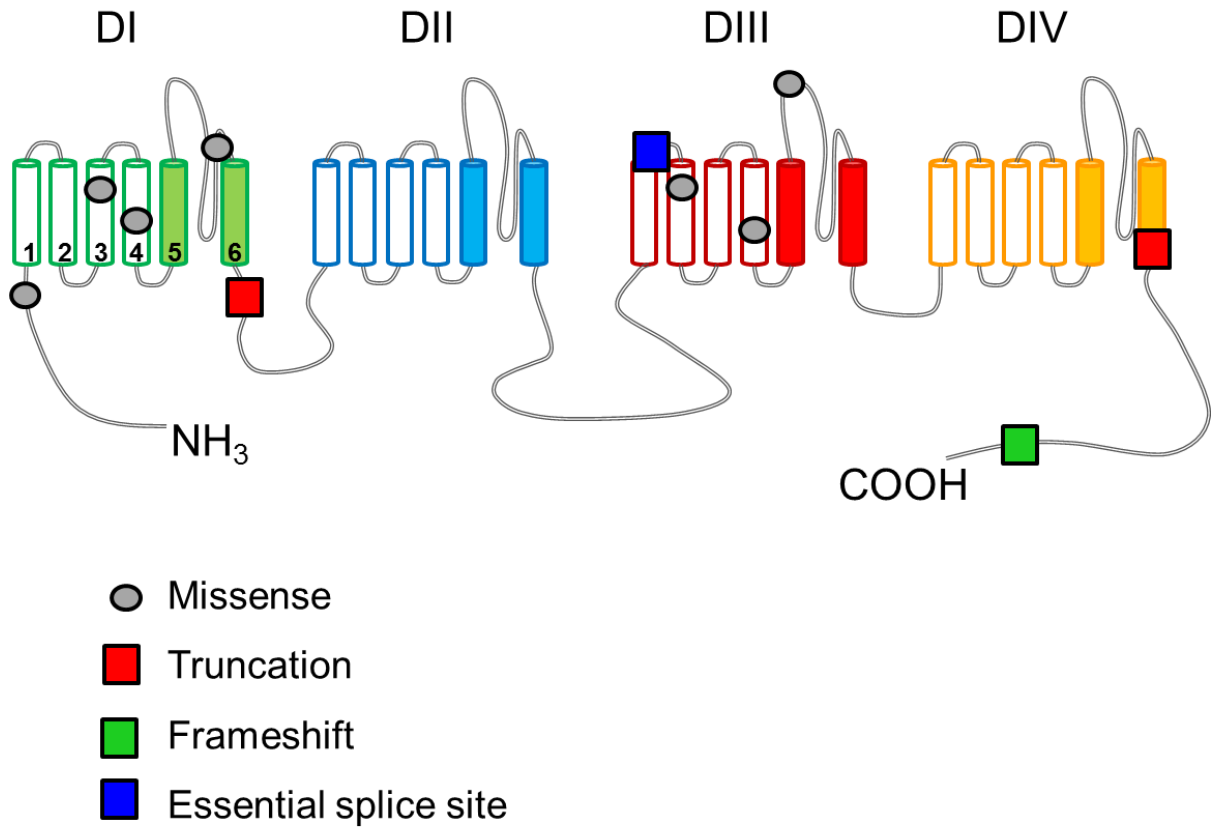

Figure 5.3. Location of all congenital myopathy variants.

Compound heterozygous mutations identified in the affected individuals from one family are presented with the same color. Domains DI-DIV color-coded in green, blue, red, and yellow, respectively. Symbols indicate type of mutation. Gray circle: missense; red square: truncation; green square: frameshift; blue square: essential splice site.

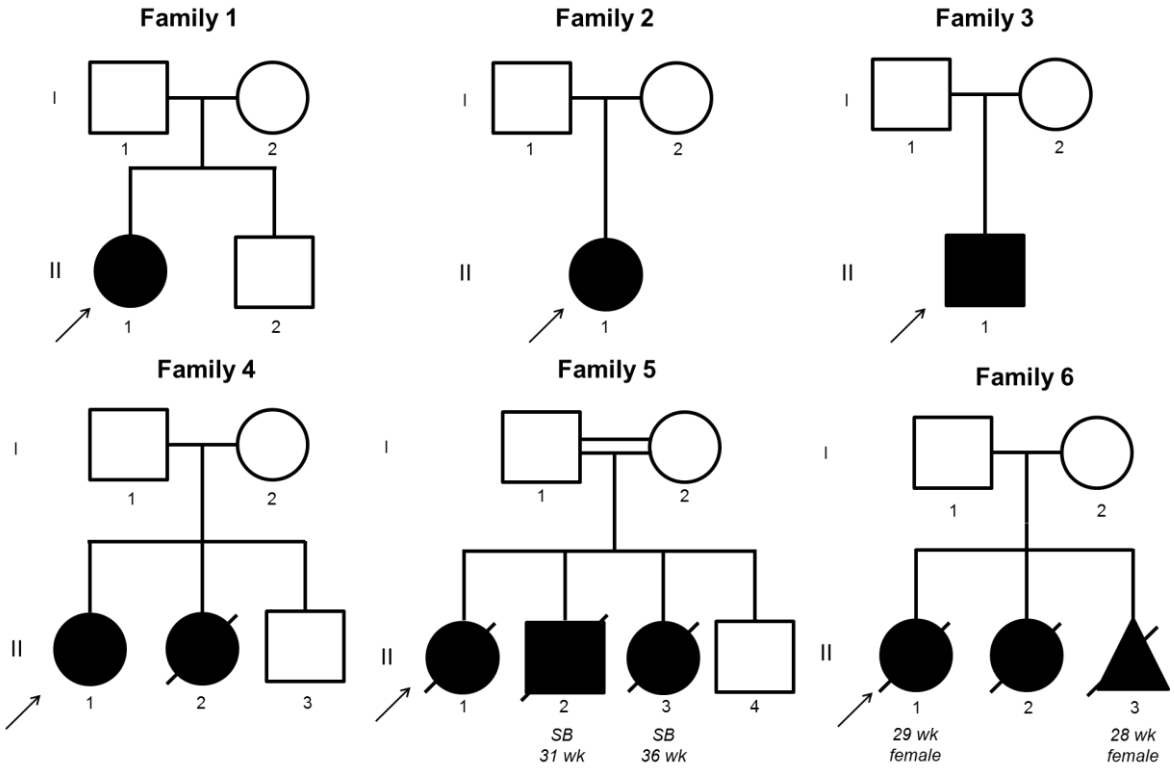

Figure 5.4. Family pedigrees of the six initial kindreds. Affected individuals represented by shaded symbols. Probands indicated with an arrow; age at stillbirth (SB) or pregnancy termination indicated below symbols. The remaining three individuals who died survived birth but died within hours of delivery.

Table 5.1. Overview of family genetics. Amino acid change, ExAC database frequency and association with reported sodium channelopathy. *MS: missense; FS: frameshift; ESS: essential splice site; hypoPP: hypokalemic periodic paralysis; NDM: non-dystrophic myotonia; -: not available; [1]Groome et al. (2014); [2]Lee et al. (2009).*

	Family 1		Family 2		Family 3		Family 4		Family 5	Family 6	
Amino acid change	p.R104H	p.R1135C	p.R225W	p.C1209F	p.Q470X	p.H1782Qfs65	p.D1069N	p.A1049VfsX50	p.P382T	p.M203K	p.Y1593X
Mutation type	MS	MS	MS	MS	NS	FS	MS	ESS	MS	MS	MS
ExAC allele frequency	-	-	-	0.000008	-	-	0.0000017	-	-	-	-
Reported previously	-	hypoPP[1]	NDM[2]	-	-	-	-	-	-	-	-

5.2.4. Major clinical findings

Patients presented with congenital myopathy on a spectrum of clinical severity. The majority of cases had *in utero* onset muscle weakness resulting in reduced fetal movements. Patients at the severe end of the clinical spectrum had severe fetal hypokinesia; seven died *in utero* or shortly after term. Autopsy showed marked muscle hypoplasia. The four surviving patients had generalized hypotonia and weakness at birth; neck- and mild to moderate facial muscle weakness without ptosis; and respiratory and feeding difficulties during infancy and early childhood. Respiratory complications were diverse. The proband from family 1 did not need respiratory aid until age 6, at which point a bi-level positive airway pressure (BiPAP) machine was used during sleep. The individual from family 2 had non-invasive respiratory support soon after birth and had cyanotic spells until 2 years of age. The proband in family 3 had respiratory difficulties which were helped using a BiPAP from 4 months of age, still ongoing (at 2.5 years), mostly used during sleep. The surviving individual in family 4 had to be resuscitated after birth, and was from then on intubated until 13 months of age. Until 2 years of age this individual was on BiPAP at night or during daytime periods of sleep.

5.2.5. Functional characterization of *SCN4A* variants

5.2.5.1. Main pore current properties in HEK293T cells

The proband in family 2 carries two missense variants C1209F and R225W. The R225W variant has previously been found in a patient with myotonia (Lee et al., 2009). Functional expression shows full absence of currents in C1209F channels (Figure 5.5). The voltage dependence of activation of R225W was shifted to more depolarized voltages and the

peak current density was reduced. Thus, the patient carries a full and a partial loss of function mutation, analogous to the index family.

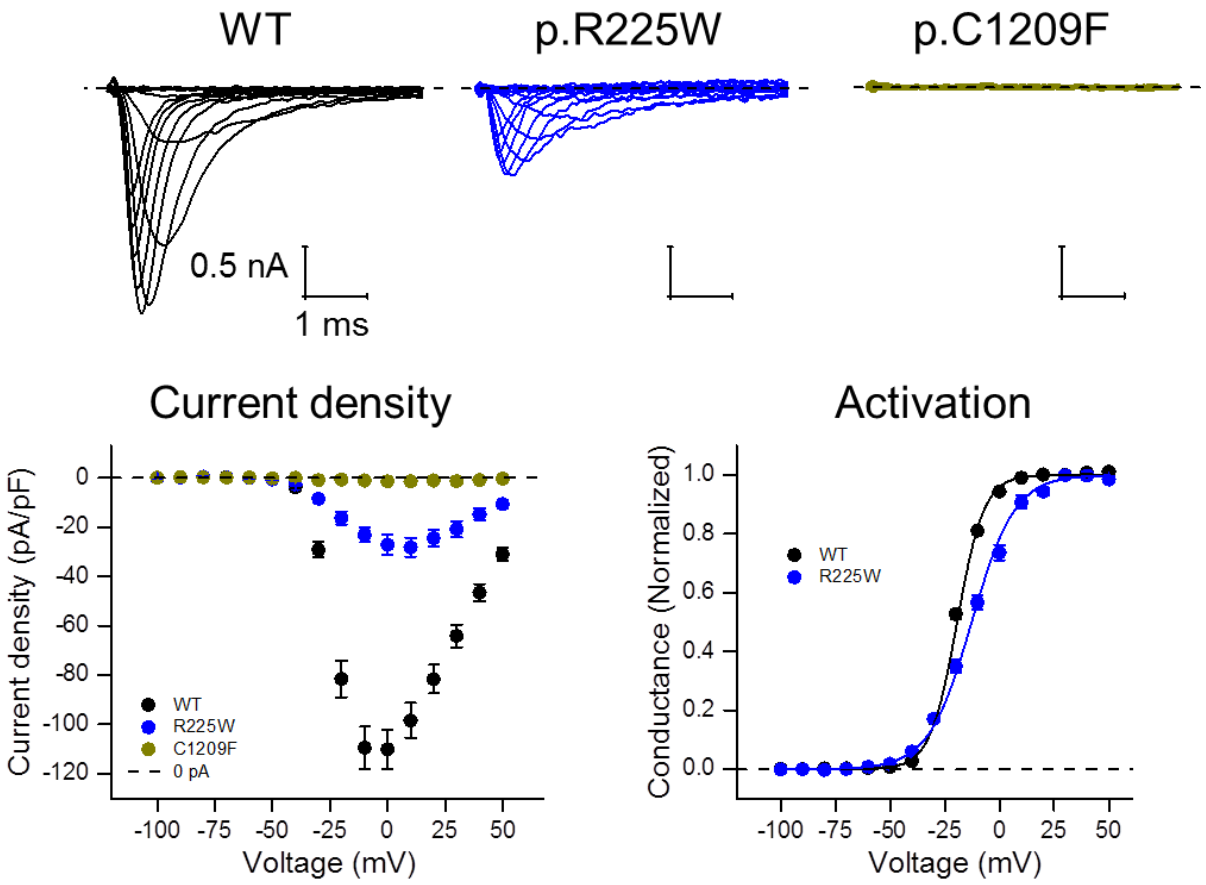

Figure 5.5. Family 2: Functional properties of variants p.R225W and p.C1209F. Top: Representative current traces for HEK293 cells expressing WT (left), R225W (center), and C1209F channels. Scale bars are 1 ms (x), 0.5 nA (y). Dashed lines show 0 current level. Bottom: Current density-voltage (left) and conductance-voltage (right) plots for WT (black), R225W (blue), and C1209F (dark yellow). Dashed lines show zero current or conductance levels. Solid lines show fits to mean conductance-voltage data.

The proband in family 3 carries nonsense variant p.Q470X and a frameshift variant p.H1782Qfs65. The truncation variant is predicted to produce polypeptides unable to form functional channels and was not studied in HEK293 cells. C-terminal frameshift variant p.H1782Qfs65 produced currents in HEK293 cells that were indistinguishable from WT

currents (Figure 5.6.). This variant was the only variant in which we could not detect changes in channel function.

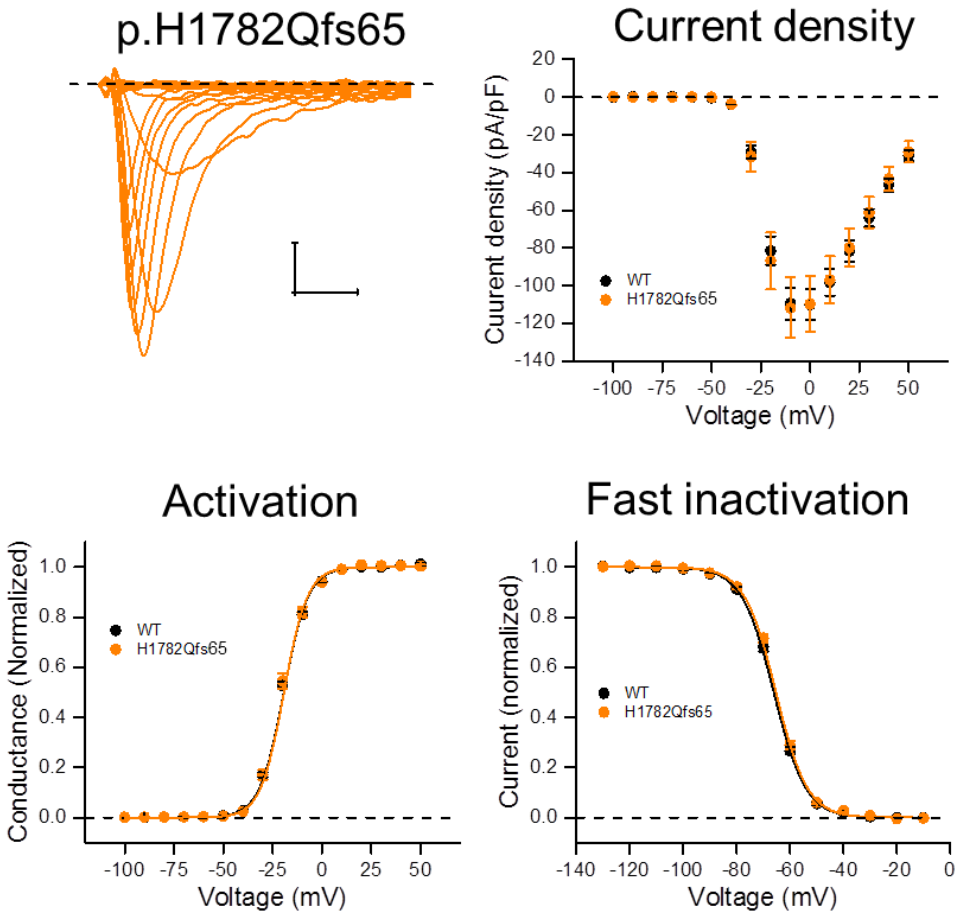

Figure 5.6. Family 3: Functional properties of H1782Qfs65 channels. Top, left: Representative current traces for HEK293 cells expressing H1782Qfs65 channels. Scale bars are 1 ms (x), 0.5 nA (y). Dashed lines show 0 current level. Top, right: Current density-voltage and plots for WT (black) and H1782Qfs65 (orange) channels. Bottom: Conductance-voltage (left) and current-voltage (right) plots used to assess the voltage dependence of channel activation and inactivation, respectively. Dashed lines show zero current or conductance levels. Solid lines show fits to mean conductance-voltage data.

The two affected individuals in family 4 carry p.D1069N missense and p.A1049VfsX50 frameshift variants. One of the two compound heterozygous carriers died, while the other presents with classic congenital myopathy. The frameshift variant leads to deletion of a splice site and truncation of the channel polypeptide. Thus this variant is predicted to produce polypeptides unable to form functional channels and was not studied in HEK293

cells. The p.D1069N variant produced currents with amplitudes similar to wild-type (Figure 5.7). The voltage dependence of both activation and fast inactivation were shifted to more depolarized voltages. The shift in voltage dependence of activation is a loss of function property, and thus both alleles of the carrier are loss of function variants.

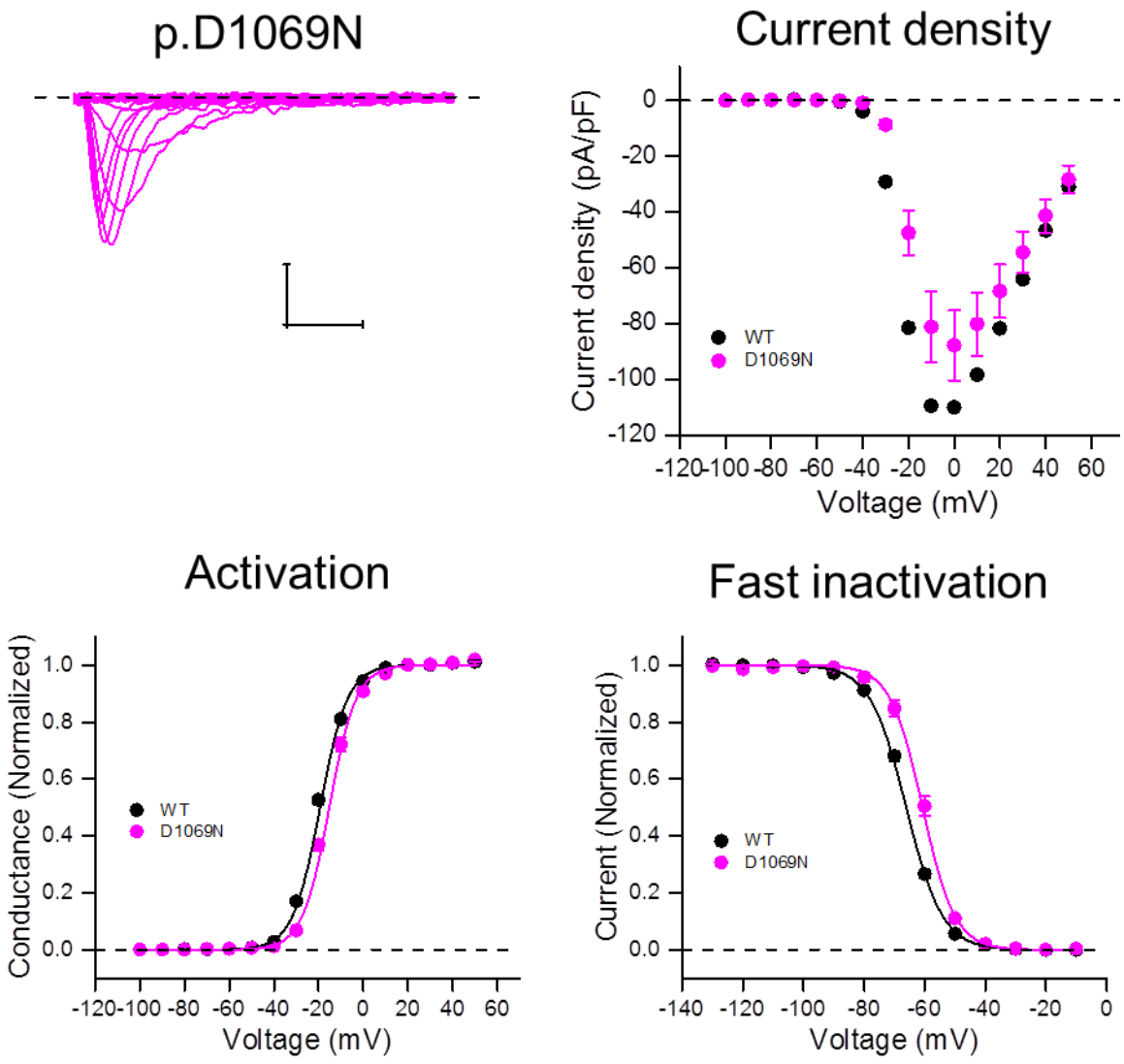

Figure 5.7. Family 4: Functional properties of p.D1069N mutant channels. Top, left: Representative current traces for HEK293 cells expressing D1069N channels. Scale bars are 1 ms (x), 0.5 nA (y). Dashed lines show 0 current level. Top, right: Current density-voltage plot for WT (black) and D1069N (magenta) channels. Bottom: Conductance-voltage (left) and current-voltage (right) plots used to assess the voltage dependence of channel activation and inactivation, respectively. Dashed lines show zero current or conductance levels. Solid lines show fits to mean conductance-voltage data.

The three affected members of Family 5 carried homozygous p.P382T missense variants. When expressed in HEK293 cells no sodium currents could be recorded, suggesting p.P382T is a null variant (Figure 5.8).

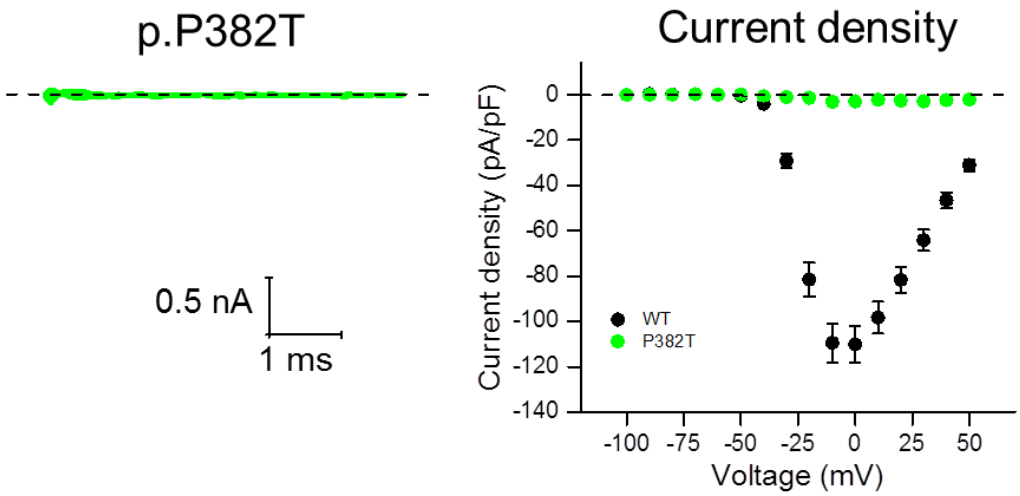

Figure 5.8. Family 5: Functional characterization of p.P382T mutant channels. Left: Representative current traces for HEK293 cells expressing P382T channels. Scale bars are 1 ms (x), 0.5 nA (y). Dashed lines show 0 current level. Right: Current density-voltage plot for WT (black) and P382T (green) channels.

The three affected individuals in family 6 carry p.M203K missense and p.Y1593X truncation variants. All compound heterozygous carries died *in utero*, at term, or the pregnancy was terminated. The truncation variant is predicted to produce polypeptides unable to form functional channels and was not studied in HEK293 cells. p.M203K variant produced currents with significantly reduced current amplitude (Figure 5.9.) and a shift in the voltage dependence of activation to more depolarized voltages. The shift in voltage dependence of activation is a loss of function property, and thus both alleles of the carrier are loss of function variants. The voltage dependence of fast inactivation was also shifted slightly (2.7 mV) but significantly to the depolarized voltages.

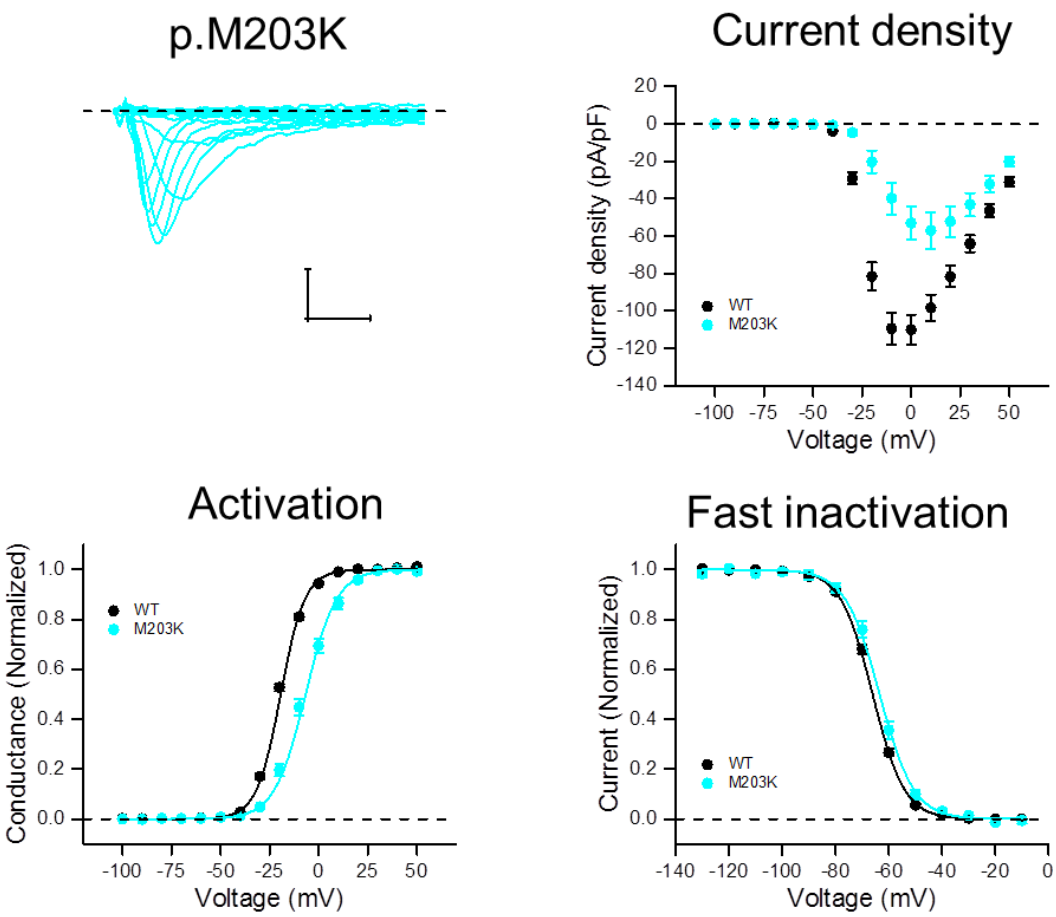

Figure 5.9. Family 6: Functional properties of p.M203K $Na_V1.4$ channels. Top, left: Representative current traces for HEK293 cells expressing p.M203K channels. Scale bars are 1 ms (x), 0.5 nA (y). Dashed lines show 0 current level. Top, right: Current density-voltage plot for WT (black) and M203K (cyan) channels. Bottom: Conductance-voltage (left) and current-voltage (right) plots used to assess the voltage dependence of channel activation and inactivation, respectively. Dashed black line shows zero current or conductance levels. Solid lines show fits to mean conductance-voltage data.

The mean parameters of voltage dependence of channel activation for the missense variants are given in Table 5.2. and for voltage dependence of fast inactivation in Table 5.3. We studied additional parameters of $Na_V1.4$ function that may influence the presentation of the cases. The voltage-dependence of slow inactivation was markedly enhanced in p.M203K channels, slightly enhanced in p.D1069N channels, and slowed in p.R225W channels (Figure 5.10.).

Table 5.2. Properties of channel activation. Data are expressed as means ± standard error of the mean. Statistical comparison of variants was performed using a one-way ANOVA with Bonferroni's *post hoc* test ($V_{1/2}$ and V_{slope} of activation) and Kruskal-Wallis with Dunn's *post hoc* test (I_{peak}). * *P* <0.05; ** *P* <0.01; *** *P* <0.001 ($V_{1/2}$: mid-point voltage, V_{slope}: slope factor, I_{peak}: peak current density at 0 mV).

Genotype	**Activation**			
	$V_{1/2}$ (mV)	V_{slope} (mV)	I_{peak} @ 0 mV) (pA/pF)	*n*
Wild-type	-20.0±0.4	6.4±0.12	-110.1±8.0	51
p.R104H	-	-	-	15
p.M203K	-7.0±1.2***	8.5±0.3***	-53.0±9.0**	12
p.R225W	-12.3±1.1***	10.7±0.34***	-27.1±4.1***	9
p.P382T	-	-	-	13
p.D1069N	-15.8±0.7***	6.2±0.3	-84.3±12.4	13
p.C1209F	-	-	-	11
p.H1782Qfs65	-20.2±0.8	6.1±0.2	-109.9±14.8	16

Table 5.3. Voltage dependence of channel fast inactivation. Data are expressed as means ± standard error of the mean. Statistical comparison of variants was performed using a one-way ANOVA with Bonferroni's *post hoc* test ($V_{1/2}$ of fast inactivation) and Kruskal-Wallis with Dunn's *post hoc* test (V_{slope} of fast inactivation). * *P* <0.05; ** *P* <0.01; *** *P* <0.001 ($V_{1/2}$: mid-point voltage, V_{slope}: slope factor, I_{peak}: peak current density at 0 mV)

Genotype	**Fast inactivation**		
	$V_{1/2}$ (mV)	V_{slope} (mV)	*n*
Wild-type	-65.8±0.4	5.6±0.1	52
p.M203K	**-63.1±0.9****	6.0±0.5	13
p.R225W	-66.0±0.6	5.2±0.3	13
p.D1069N	**-60.2±0.8*****	5.1±0.2	15
p.H1782Qfs65	-64.8±0.4	5.6±0.1	19

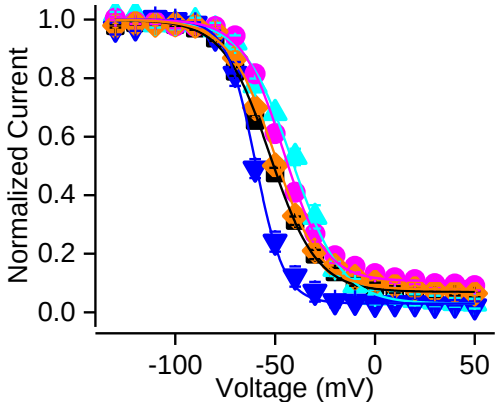

Genotype	Slow inactivation		
	$V_{1/2}$ (mV)	V_{slope} (mV)	*n*
Wild-type	-52.6±0.8	11.9±0.2	13
p.M203K	**-40.8±1.7*** **	12.6±0.4	4
p.R225W	**-59.8±1.0***	**7.7±0.8*** **	3
p.D1069N	**-46.5±0.9****	**10.3±0.3****	8
p.H1782Qfs65	-51.2±1.3	11.0±0.3	7

Figure 5.10. Slow inactivation properties. Slow inactivation determined from prepulse potentials from -130 mV to +50 mV in 10 mV increments for 10 s for WT (black), M203K (Cyan), R225W (blue), D1069N (magenta) and H1782Qfs65 (orange) channels. A 20 ms pulse to -100 mV was applied to recover channels from fast inactivation, followed by a test pulse to -10 mV. The peak current measured at -10 mV was plotted against the prepulse voltage. Solid lines represent Boltzmann fit to the mean data. All data points are mean±SEM. Mean values of fits of individual cells is given in the table. Data are expressed as means ± standard error of the mean. Statistical comparison was performed using a one-way ANOVA with Bonferroni's *post hoc* test. *P < 0.05, **P < 0.01, ***P < 0.001. ($V_{1/2}$: mid-point voltage, V_{slope}: slope factor, n/a: not available)

The time course of recovery from fast inactivation was wild-type like in all variants except p.D1069N, which recovered 1.7 times faster than wild-type channels (Figure 5.7.; Table 5.3.). No channel defects were measured in p.H1782Qfs65 channels. The p.R1135C channel was not expressed in HEK293T cells as it has been extensively studied previously, and found to left-shift the voltage-dependence of fast inactivation (Groome et al., 2014).

In order to study the onset of open-state inactivation, a double exponential curve was fit to the decaying phase of the sodium current trace at -20 mV $\leq V_{command} \leq$ 20 mV. Time constants of p.M203K and p.R225W channels were significantly slower compared to wild-type (Figure 5.11.).

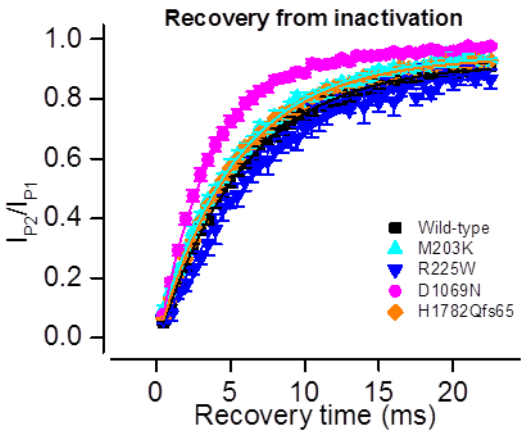

Genotype	Recovery from fast inactivation	
	$\tau_{recovery}$ (ms) @ -80 mV	*n*
Wild-type	5.85±0.29	24
p.M203K	5.49±0.23	12
p.R225W	6.84±0.67	3
p.D1069N	**3.54±0.22*** **	13
p.H1782Qfs65	5.39±0.29	10

Figure 5.11.Recovery from fast inactivation. Time course of recovery from fast inactivation at -80 mV for WT (black), M203K (Cyan), R225W (blue), D1069N (magenta) and H1782Qfs65 (orange) channels**.** The peak current in response to second test pulse (I_{P2}) is measured following a recovery period of varying duration at hyperpolarized voltages. I_{P2} is divided by the peak current of the first pulse (I_{P1}) that inactivates channels. Solid line represents a single exponential fit to the mean data. Mean values of fits of individual cells is given in the table. Means ± the standard error of means are shown. Statistical comparison: Kruskal-Wallis with Dunn's *post hoc* against wild-type. *P < 0.05, **P < 0.01, ***P < 0.001. (n/a: not available)

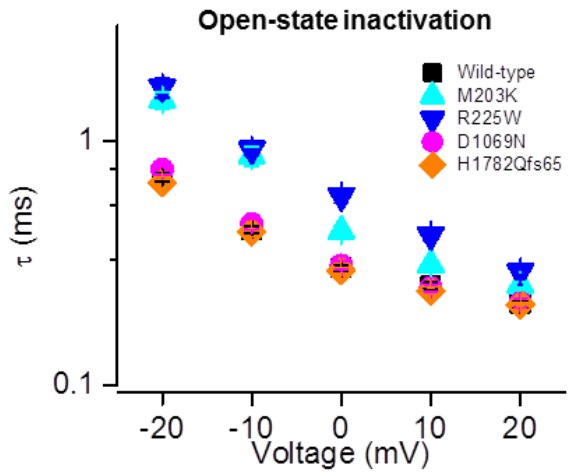

Genotype	Onset of open-state inactivation					
	Time constant (ms) at given voltage (mV)					
	-20	**-10**	**0**	**10**	**20**	*n*
Wild-type	0.73±0.03	0.44±0.01	0.31±0.01	0.26±0.01	0.22±0.01	49
p.M203K	**1.48±0.12*** **	**0.87±0.08*** **	**0.43±0.02***	0.31±0.01	0.27±0.01	12
p.R225W	**1.67±0.16*** **	**0.93±0.05*** **	**0.60±0.04*** **	**0.41±0.02****	0.29±0.01	9
p.D1069N	0.77±0.04	0.44±0.02	0.30±0.01	0.25±0.01	0.21±0.01	11
p.H1782Qfs65	0.68±0.04	0.43±0.02	0.30±0.01	0.24±0.01	0.21±0.01	16

Figure 5.12. Onset of open-state inactivation. Time constant (ms) of the onset of open state fast inactivation plotted against the voltage for WT (black), p.M203K (Cyan), p.R225W (blue), p.D1069N (magenta) and p.H1782Qfs65 (orange) channels. A double exponential curve was fit to the decaying phase of the sodium current (90% of peak). Only the fast component that carries majority of the amplitude (>90%) was analyzed. Data are expressed as means ± standard error of the mean. The mean values are shown in the table. Statistical comparison was performed using a two-way repeated measures (mixed factorial) ANOVA (voltage, genotype) with Bonferroni's *post hoc* test. *$P < 0.05$, **$P < 0.01$, ***$P < 0.001$.

5.2.5.2. Gating pore current properties in *Xenopus* oocytes

The p.R1135C has previously been studied, and shown to conduct gating pore currents. To verify this, we also expressed this variant. The data is shown in Figure 4.2. We found hyperpolarization-activated gating pore currents, as evidenced by an increased non-linear leak current in both NaMeSO and Na/Gn extracellular solutions.

Finally, the mutation p.R225W affects the same residue that when mutated to glycine conducts depolarization activated gating pore currents. However, so far we have not found any evidence of gating pore currents in this mutant channel. The change in current amplitude upon change of extracellular NaMeSO to Na/Gn is small and similar to WT channels. The large current increase in depolarized voltages that is evident in p.R225G channels is absent (n=7). Larger number of experiments will help confirm the absence of gating pore currents in p.R225W channels. Thus, the nature of the substituting residue at p.R225 seems to also have a significant effect on formation of gating pore currents.

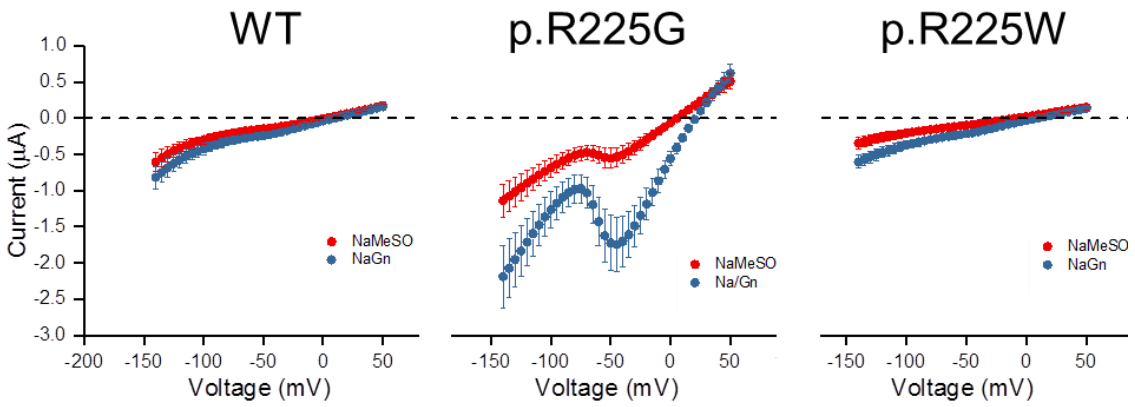

Figure 5.13. Gating pore currents in p.R225G, but not p.R225W channels. Mean raw currents in extracellular NaMeSO (red) and Na/Gn (blue) solutions for WT (left, n=22), p.R225G (middle, n=6) and R22GW (right, n=7) channels. Only WT data has gone through a rigorous quality control. However, the data clearly demonstrate a large increase in gating pore currents with a typical peak at -50 mV in Na/Gn solution for p.R225G that is absent in WT and p.R225W channels.

Table 5.4. Summary of biophysical effects and clinical effects

MS: missense; NS: nonsense; FS: frameshift; FADS: fetal akinesia deforma

Family number	*Amino acid change*	*Mutation type and location*	*Biophysical effect*	*Clinical effect*
1	p.R104H	MS, n-terminal domain	No currents	Congenital myopathy
	p.R1135C	MS, S4 arginine in VSD-III	Enhanced fast inactivation, gating pore currents	
2	p.R225W	MS, arginine in VSD-I	Reduced current	Congenital myopathy
	p.C1209F	MS, extracellular S5-S6 loop of DIII	No currents	
3	p.Q470X	NS, DI-DII cytoplasmic loop	No currents	Congenital myopathy (mild)
	p.H1782Qfs65	FS, c-terminal domain	No change in HEK293 cells; potentially muscle-specific defect	
4	p.D1069N	MS, S2 DII		One died, one congenital myopathy
	p.A1049VfsX50	FS, S1 DIII	No currents	
5	p.P382T	MS, extracellular S5-S6 loop DI	No currents	Three individuals with fetal akinesia
6	p.M203K	MS, S3 DI	Severely reduced current density	Two died in utero, one eight hours after delivery

5.3. Discussion

This is the first study describing *SCN4A* mutations in patients with congenital myopathy. Functional analysis was essential in confirming the pathogenicity and pathomechanism: recessive loss of function mutations in $Na_V1.4$—at least one of which is a full loss of function—cause congenital myopathy or fetal akinesia.

5.3.1. A new molecular pathomechanism associated with *SCN4A*

We found that all but one of the *SCN4A* variants in the myopathy cohort caused loss of function. Six of these result in full loss of function by truncating the channel protein or resulting in non-functional channels. Four additional variants resulted in partial loss of function. We propose that the combined effect of two loss of function mutant $Na_V1.4$ channels attenuates the action potential amplitude in skeletal muscle to a level insufficient to sustain normal muscle force.

All parents and one unaffected sibling were confirmed carriers of one *SCN4A* mutation but were unaffected clinically. This suggests that the loss of function in only one allele is insufficient to cause a clinical phenotype, indicating an autosomal recessive mechanism of inheritance. It appears that the coincidence of one full and one partial loss of function mutations is required for congenital myopathy, and two full (or near-complete) loss of function mutations are required for a fetal akinesia phenotype. This is in contrast to the classical autosomal dominant $Na_V1.4$ channelopathies myotonia and periodic paralysis where a single gain of function mutation is sufficient to cause a clinical phenotype.

Only three reports of loss of $Na_V1.4$ channel function with a clinical presentation exist (Arnold et al., 2015; Habbout et al., 2016; Tsujino et al., 2003). However, both the clinical presentation and the molecular pathomechanism differ from the congenital myopathy cohort. All three patients presented with myasthenia as the primary presentation. Functional analysis revealed in all three cases recessively inherited mutations causing

enhanced fast inactivation. Repetitive depolarizing pulses accumulate these channels in the inactive state more than wild-type channels, use-dependently reducing channel availability. Fatigable weakness of myasthenia is believed to be attributed to these defective inactivation properties of the channel (Habbout et al., 2016). In other words, this loss of function pathomechanism appears to be use-dependent; upon high frequency stimulation a larger fraction of mutant channels become unavailable compared to wild-type channels. In this study, however, we did not use any use-dependent protocols, as only one of the variants, p.R1135C, showed enhanced inactivation. This variant has been characterized by another laboratory and was not studied by me (Groome et al., 2014). As neither the voltage dependence of fast inactivation nor the rate of recovery from inactivation was compromised for any of the variants, we do not expect any of the variants in this study to display use-dependent changes in availability compared to wild-type channels.

The molecular pathomechanism is distinct in congenital myopathy and fetal akinesia. The net current is reduced to a larger extent as mutation in one of the alleles results in full loss of function. For only one variant, the loss of function was due to enhanced fast inactivation (p.R1135C). For other variants, the voltage dependence of activation and current density were attenuated. More severe loss of function reduces the voltage across the membrane to a level insufficient to sustain normal muscle contraction in baseline. In individuals with fetal akinesia—the most severe phenotype—the extent of sodium channel dysfunction was so severe that life could not be sustained. This occurred in several fetuses carrying homozygous null mutation and in two families with partial loss of function mutation that attenuated channel activation. In one family, one of the compound heterozygous carriers died while the other survived infancy, suggesting that the correlation between $Na_V1.4$ variants and clinical outcome is not linear.

In utero and in infancy the cardiac sodium channel isoform $Na_V1.5$ (*SCN5A*) is expressed in skeletal muscle, albeit at low levels. Over the first two years, the total *SCN4A* mRNA in

the human diaphragm increases from 30 % to approximately 40-45 % over 2-5 years of the mRNA levels found in adult muscle (Zhou and Hoffman, 1994). Meanwhile, *SCN5A* mRNA expression reduced from 10 % (of total adult level) in neonates to negligible levels at 5 years of age. In fetal skeletal muscle, the mean *SCN4A* expression was approximately 20-25 % of total expression of adults, compared to *SCN5A* which was approximately 5 % (4-5 fold lower than *SCN4A*). Due to the low expression of *SCN5A* in neonates, sodium currents are not large enough to compensate for bi-allelic complete $Na_V1.4$ loss of function variants, resulting in reduced firing and/or amplitude of action potentials.

Wu and colleagues developed a mouse model with a exon 12 deletion (*SCN4A* delta_Ex12), which deletes most of VSD-II (Wu et al., 2016). As in humans, Ex12/Ex12 (null) mice do not survive past the second day postnatally. Skeletal muscle preparations were used to record sodium current density. Peak sodium current density in +/delta_Ex12 mice was half of wild-type. To reveal any $Na_V1.5$-carrying currents, TTX was added to +/delta_Ex12 mice preparations. The previously recorded sodium current was completely ablated, suggesting that $Na_V1.5$ channels were absent of the muscle at the age of the recording (2-8 months) and that delta_Ex12 $Na_V1.4$ channels are unable to conduct sodium.

However, upon repeated stimulation (100 Hz) +/delta_Ex12 muscle force is reduced compared to wild-type. As all the $Na_V1.4$ channels expressed are WT, the voltage dependence of fast inactivation and rate of recovery are the same in both mice. This indicates that when the pool of available channels is reduced by KO, further reduction of channel availability has more severe consequences on muscle function. When fewer channels are available, repetitive stimulation may be particularly deleterious. For instance, in a heterozygous complete loss of function individual (+/null), only 50 % of channels are available in control conditions. If half of those channels are inactivated, only 25 % of total (compared to wild-type) channels are available. This is likely to explain why +/delta_Ex12

mice show reduced force upon repetitive simulation. Although the parents in the myopathy cohort (who are +/null *SCN4A* carriers) did not present any symptoms in the clinic or neurophysiological tests, these individuals may show decrements in muscle function during strenuous or lengthy exercise. Further investigation into this phenomenon is warranted. However, it is also possible that human muscle differs from mouse in the extent of sodium channel inactivation upon repetitive stimulation or in the minimum sodium channel availability required to sustain normal muscle force.

5.3.2. Intra- and interfamilial phenotype severity

The proband of Family 4 is currently in her early childhood, despite carrying the same channel variants as the sibling who died five hours after delivery. This suggests that the biophysical channel phenotype does not always directly correlate with the clinical outcome. The reason for the dramatically different phenotype is not clear. Genetic, epigenetic, or environmental factors may be at play. The death of the sibling who died occurred within a few hours of birth at term. It may also be that exposure to distinct external stressors might have caused different clinical outcome (see chapter 8). Other deaths in this cohort occurred at or before 36 weeks gestation.

It is not clear what genes may modify *SCN4A* function or compensate for the lack of functional sodium channels in some individuals. It is also not known whether fewer dysfunctional channels may be upregulated in some individuals thus reducing clinical phenotype severity. It is known that *SCN4A* variants can modify the clinical manifestation of myotonic dystrophy type 2 caused by expansion repeats in *CNBP* (Bugiardini et al., 2015). Conversely, the presentation of *SCN4A* myotonias can be modified by mutations in other genes, such as *CLCN1* as described in Chapter 3 and in (Furby et al., 2014).

Inter and intra-familial variability in clinical presentation has also been observed in other muscle condition, such as congenital myasthenic syndrome associated with mutations in the gene *CHRNG* (Vogt et al., 2012). Taken together, these studies strengthen the notion

that genetic variants in the same tissue may act in concert to modify the clinical phenotype. Characterization of further *SCN4A* myopathy cases will shed light to prevalence and mechanisms of intra- and inter-familiar variability.

5.3.3. Correlating channel defect with clinical presentation

Three mutations were predicted to encode non-functional channels by introducing premature stop codons (p.Q470X, p.A1049VfsX50, and p.Y1593X in Family 3, 4, and 6, respectively). No currents were measured in HEK293T cells transiently transfected with variants p.R104H, p.P382T, or p.C1209F on at least four separate occasions, with wild-type always expressed at the same time in parallel. Wild-type constructs consistently expressed good functional currents >1 nA. The p.P382T variant was homozygous and caused death *in utero* or shortly after term in three cases. The first infant died minutes after premature delivery (33/40). The second died prior to delivery (31/40) and the third died during delivery. This suggests that skeletal muscle without functional $Na_V1.4$ channels is unable to support life.

The remaining individuals were compound heterozygous with one mutation causing full loss of function and a second mutation causing partial loss of function *in trans*. Partial loss of function was measured in three out of four variants through attenuated channel activation (p.R225W, p.D1069N, and p.M203K); reduced current density (p.M203K and p.R225W); and enhanced slow inactivation (p.R225W). The reduced current density of p.R225W may be due to stabilized down state of S4, which reduces open probability. The voltage-dependence of activation is shifted in the depolarizing direction, i.e. more depolarization is required to open channels, hence a reduced sodium current measured at 0 mV. The p.R1135C mutation has previously been extensively characterized with enhanced fast inactivation constituting clear loss of function (Groome et al., 2014).

No loss of function was measured in p.H1782Qfs65 channels despite a similar clinical phenotype. The frameshift mutation is predicted to alter the last 65 C-terminal residues

and extend it by nine residues before a stop codon. It is possible that the frameshift mutation disrupts channel function in a tissue-specific manner, possibly disrupting signals responsible for channel trafficking or other muscle-specific interactions.

This child (family 3) has a similar clinical phenotype to cohort members in family 1 and 2. He was born following a pregnancy complicated by polyhydramnios (first noted at delivery), had marked neonatal-onset weakness and hypotonia associated with facial weakness, required significant feeding and respiratory support from birth, but continues to improve clinically. The frameshift mutation is predicted to alter the C-terminal of the protein and extends it by nine residues compared to the wild-type channel. Our analysis suggests that at least in HEK293T cells, the Nav1.4 channel C-terminus mutation has no detectable effects on the biophysical properties of the channel. This is in agreement with previous data showing that a deletion of the C-terminal 100 residues has no effect on channel gating (Herzog et al., 2003). However, it is possible that the frameshift mutation disrupts channel function in a tissue-specific manner, which cannot be detected in a heterologous expression system, or it might cause loss-of-function effect not elicited by the functional analyses undertaken in this study.

For example, the last five C-terminal amino acid residues play an important role in the interaction of Nav1.4 with the PDZ domain of syntrophins (Schultz et al., 1998), a scaffold protein that is a part of the dystrophin-associated protein complex integral to sustaining muscle integrity (Ehmsen et al., 2002). The p.H1782Qfs65 mutation is predicted to disrupt these residues. Alterations of the sequence of the C-terminus may also affect signals responsible for channel trafficking, targeting, activity, or stability. Additional studies are required to further investigate these possibilities.

The heterozygous p.R225W mutation has been reported in a patient with mild “pure” non-painful myotonia (Lee et al., 2009). In p.R225W channels the current density was severely reduced; the voltage-dependent activation attenuated; and the voltage-dependence of

slow inactivation enhanced. The changes in all these parameters result in loss of function. Open-state inactivation was also slowed in p.R225W, presenting as a gain of function effect. However, given the prevailing hypothesis that increased $Na_V1.4$ channel activity underlies myotonia (Cannon, 2015; Suetterlin et al., 2014; Trivedi et al., 2014), the functional properties of p.R225W channels presented here are inconsistent with the clinical presentation reported by Lee and colleagues, except for the slowed onset of open state inactivation. No myotonic features were described in either the patient or the heterozygous p.R225W carrier. Lending further support to our functional characterization of this mutation are studies of the homologous p.R225W mutation in cardiac $Na_V1.5$, showing markedly reduced current density (Bezzina et al., 2003); depolarizing shift in the voltage dependence of activation; and slowed fast inactivation (Moreau et al., 2015).

The compound heterozygous p.R1135C mutation has previously been described in recessive hypokalemic periodic paralysis (Groome et al., 2014). Consistent with periodic paralysis, gating pore currents were measured in these mutant channels (Figure 4.3.). The muscle weakness of the proband in our cohort was permanent – not periodic – suggesting the reduced channel availability by enhanced activation is the likely underlying molecular mechanism. Although recurrent brief episodes of increased muscle weakness have recently emerged in this patient, detailed neurophysiological examination revealed no signs indicative of periodic paralysis, myotonia, or neuromuscular junction abnormalities.

The enhanced slow inactivation measured in p.R225W results in loss of function and may contribute towards the reduced peak current density observed in HEK293T cells. In contrast, attenuated fast and slow inactivation in p.D1069N and p.M203K channels may result in increased sodium current amplitude following prolonged depolarization compared to WT channels. Recovery from fast inactivation was also enhanced in p.D1069N. These results recapitulate the previously studied p.D1069K substitution (negative to positive charge) in $Na_V1.4$, which also resulted in destabilized fast inactivation, enhanced

recovery, and displayed a depolarizing shift in the voltage-dependence of activation (Groome and Winston, 2013). Intriguingly, since no symptoms typically associated with gain of function mutations were reported in the carriers of these variants, this presents the interesting possibility that the loss of function effect of the same mutation may prevent the clinical presentation of the gain of function effects.

Thus, it is likely that the severity of the partial loss of function mutation determines the clinical outcome and additional properties of the main and gating pore currents may modify the clinical presentation. For example, the variant associated with death *in utero* was p.M203K, which showed the largest shift in the voltage dependence of activation. Identification of further cases will help to establish such correlations. However, as demonstrated by the siblings in family 4 with dramatically different clinical outcome. Two siblings were born, each carrying the same variants. One died five hours after birth, and the other survived birth and is currently 10 years old and symptom-free. With this in mind, it is difficult establishing genotype-phenotype correlations, as two *SCN4A* variants apparently do not create the same clinical presentation, even within the same family.

5.3.4. Implications for understanding $Na_V1.4$ structure-function relationships

Functional characterization of specific amino acid residue mutations gives crucial insights into the inner workings of voltage-gated ion channels.

The p.P382T variant is located in the S5-S6 loop of domain I, important for ion selectivity and permeation. It is likely that this residue impairs ion permeation completely, leading to the complete lack of currents measured in HEK293T cells expressing this variant. Equally, p.C1209F is located in the S5-S6 linker/pore loop and may be important for selective permeation or channel stability.

In contrast, because variants p.M203K, p.R225W, and p.R1135C are localized to the VSD, they are more likely to disrupt gating properties of the channel. This is also what we

see upon functional expression. All three variants show changes in voltage-dependent properties and/or gating kinetics.

The p.R104H disrupts an N-terminal residue likely important for channel trafficking. A previous study of the homologous residue in *SCN5A* found that p.R104W variants were retained in the ER when expressed in rat cardiomyocytes, suggesting this residue is important for trafficking of the channel to the membrane (Clatot et al., 2012). This hypothesis could be tested by $Na_V1.4$ immunostaining in muscle and in HEK293T cells.

5.3.5. Limitations to the study

Due to the low current amplitude recorded in p.R225W channels, the recovery from inactivation could only be studied in 3 cells (Table 5.3.; standard sample size is approximately *n*=10-13). This is also the case for slow inactivation analysis of p.R225W channels. As such these results should be interpreted with caution.

5.4. Summary

The work described in this chapter identifies a novel pathomechanisms of $Na_V1.4$ and describes congenital myopathy and fetal hypokinesia as novel disease associations with *SCN4A* dysfunction. It also illustrates the intriguing observation that carriers of a single null *SCN4A* allele do not have muscle presentations. These findings have important implications for genetic diagnostics and counselling of these conditions.

6. Identification of additional heteroallelic *SCN4A* loss of function mutations in fetal akinesia deformation sequence

6.1. Aims and hypothesis

Shortly after publishing the result presented in Chapter 5 (Zaharieva et al., 2016), our group was contacted by researchers with heteroallelic *SCN4A* mutations in cases with a clinical presentation of fetal akinesia deformation sequence (FADS). Fetal akinesia deformation sequence is a genetically and clinically heterogeneous disorder presenting during fetal development. Primary clinical manifestations include fetal akinesia (lack of movement *in utero*), developmental abnormalities, and arthrogryposis (joint contractures). This chapter aimed to extend the hypothesis that severe bi-allelic *SCN4A* loss of function causes fetal akinesia.

6.2. Results

6.2.1. Note on results

I have performed the functional characterization of the missense variants found in this cohort. Two of the cases carry frame-shift, splice-site or truncation, but no missense mutations. These were not functionally characterized but are included in this chapter to support the functional data and to amplify the cohort.

For Family 1, clinical assessment was performed by Professor Yuval Yaron at the Prenatal Genetic Diagnosis Unit, Tel Aviv Sourasky Medical Center, Tel Aviv, Israel.

For Family 2, clinical assessment, neuropathology, MRI, and genetics was performed by identified by Erik-Jan Kamsteeg, Gijs W. Santen, and Laura Donker Kaat. Santen and Donker Kaat are based at the Department of Clinical Genetics, Leiden University Medical Center, 2300 RC Leiden, the Netherlands. Erik-Jan Kamsteeg is based at Genome Diagnostics Nijmegen, Department of Human Genetics, Radboud University Medical Center, Nijmegen, The Netherlands.

For Family 3, clinical assessment, genetics, were performed by Mark Davis and his group at the Department of Diagnostic Genomics in Nedlands, WA, Australia.

For Family 4, clinical assessment and genetics was performed by Marjan M. Weiss at the Department of Clinical Genetics, VU University Medical Center, Amsterdam.

6.2.2. Genetics and major clinical findings

Thus far, eight individuals in four kindreds have been identified in the cohort with diagnosis of fetal akinesia deformation sequence, with genetic finding of biallelic *SCN4A* mutations. The cases in chapter 5 were diagnosed primarily with hypokinesia, whereas the eight fetuses in this work were akinetic: they displayed extensive lack of movement as well as arthrogryposis and polyhydramnios, leading to abortion or death at term. However, it is likely that the carriers of homozygous null mutation p.P382T in the fetal hypokinesia cohort would be largely akinetic.

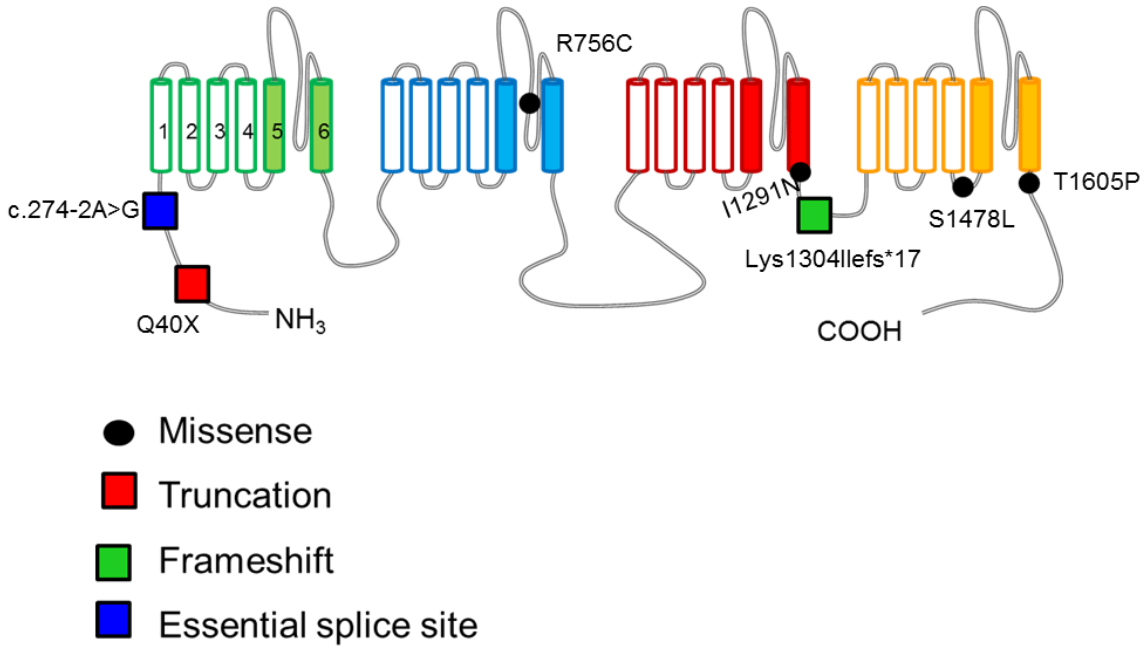

Figure 6.1. Location of FADS variants. Location of variants A: p.Q40X (N-terminal domain), B: splice variant c.274-2A>G (N-terminal domain), C: p.R756C (pore loop DII), D: p.I1291N (c-terminal end of DIII S6), E:

p.Lys1304Ilefs*17 (DIII-DIV cytoplasmic loop), F: p.S1478L (DIV S4-S5 linker), and G: p.T1605P (directly after S6 helix, DIV), mapped onto a schematic diagram of the $Na_V1.4$ alpha subunit viewed in the membrane plane.

6.2.1.1. Clinical and genetic findings of Family 1

In Family 1, genetic screening revealed a homozygous mutation (c.117_118delinsTT, p.Q40X) in two fetuses. This generates a transcript prematurely truncated at the N-terminal domain. Routine staining of the muscle revealed no clear abnormalities. Sonographies at age 20-24 weeks revealed arthrogryposis multiplex. Both heterozygous parents were declared fully healthy after extensive neurological examination (including EMG). Equally, two heterozygous siblings aged 7 and 15 displayed no symptoms.

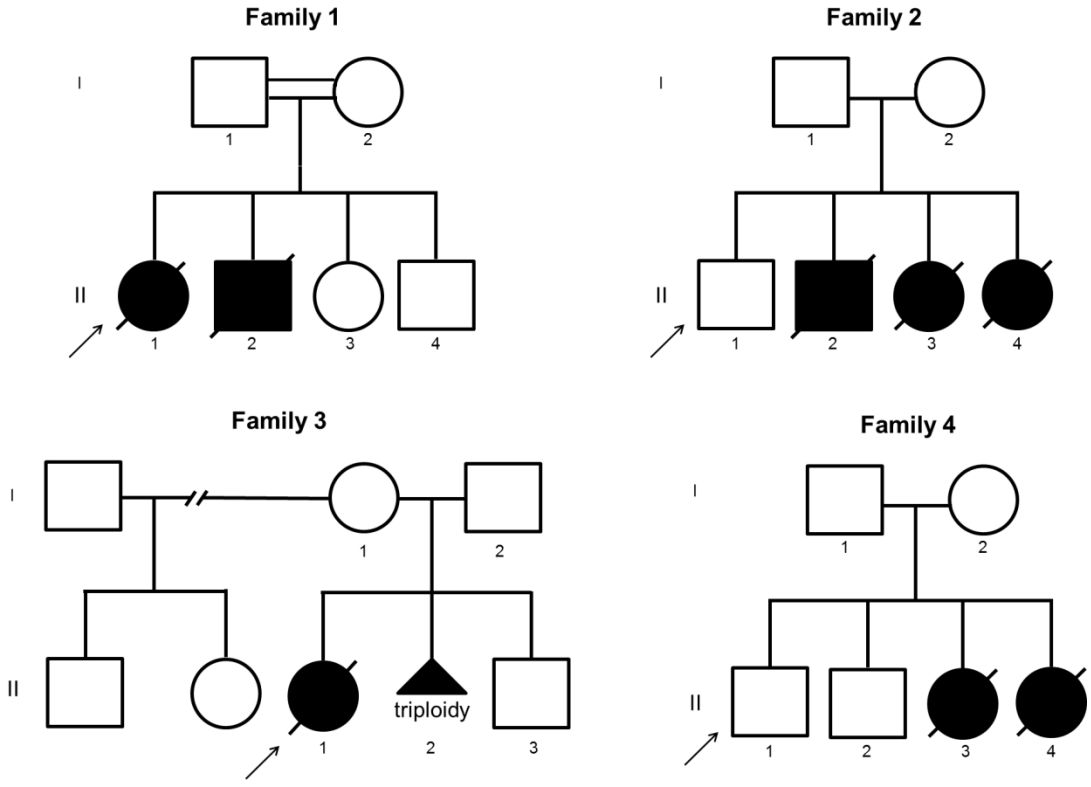

Figure 6.2. Family pedigrees of the four follow-up kindreds with FADS. Affected individuals represented by shaded symbols. Probands indicated with an arrow. Lines indicate death *in utero.*

Table 6.1. Newly identified cases with identical clinical presentation.

Amino acid change, ExAC database frequency and association with reported sodium channelopathy.

MS: missense; FS: frameshift; ESS: essential splice site-: not available

	Family 1	Family 2		Family 3		Family 4	
Amino acid change	p.Q40X (homozygous)	p.I1291N	p.T1605P	p.R756C	p.S1478L	p.Lys1304Ilefs*17	c.274-2A>G
Mutation type	Nonsense/ truncation	MS	MS	MS	MS	FS	ESS
ExAC allele frequency	-	-	-	-	-		
Reported previously	-	-	-	-	-		

6.2.1.2. Family 2

Four offspring descended from a healthy non-consanguineous couple from Kazakhstan. The mother was a heterozygous carrier of one of the variants. The family had no history of congenital malformations or hereditary disease. The first pregnancy resulted in a healthy heterozygous boy. The second, third, and fourth fetuses all carried heteroallelic mutations p.I1291N with p.T1605P in *trans*. The second pregnancy was aborted at 16 week's gestation after bilateral clubfoot and absence of fetal movement on ultrasound. In the third pregnancy, clubfoot was observed at week 16. Hypoplasia of the lungs without fetal movements, and development of hydrops in abdomen and thorax at 20 weeks led to terminated pregnancy. Genes previously associated with congenital myopathy (*CHRNA1*, *DOK7*, *CHRND*, *RAPSN*, *CHRNG*) were screened without positive results. The fourth fetus displayed clubfoot at 16 weeks. Pregnancy was terminated at week 18 due to absence of movement. Pathology revealed a myotubular morphology of the striated muscle. Functional characterization in HEK293T cells as outlined in chapters 3-5 revealed complete or near complete absence of sodium current in p.I1291N and p.T1605P variants,

respectively (Figure 6.3.). A current with small amplitude was measured in some cells expressing p.T1605P.

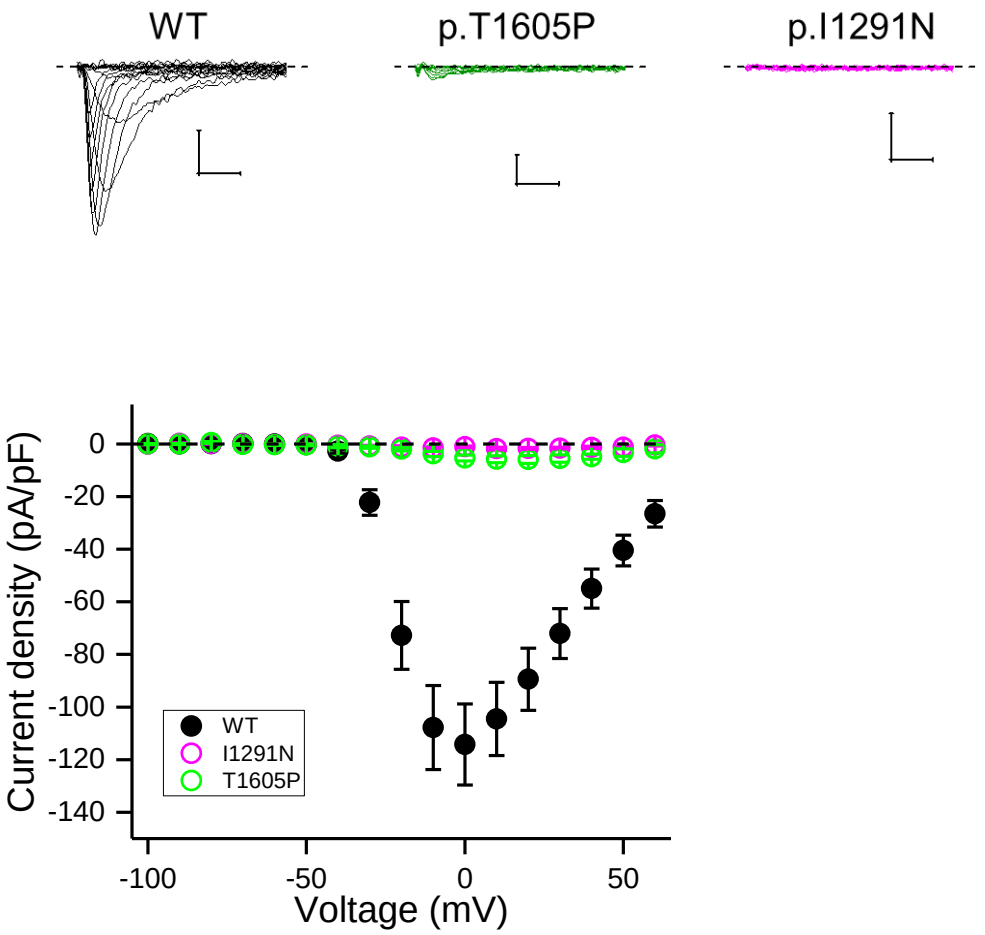

Figure 6.3. Family 2: functional characterization of missense variants by patch clamp. Top: representative current traces measured in wild-type and variants p.1291N, p.1605P, respectively. Scale bars: 1 ms (x-axis), 0.5 nA (y-axis). Dashed line: zero current. Bottom: Mean current density for WT (n=11), p.I1291N (n=13) and p.T1605P (n=15) channels.

6.2.1.3. Family 3

In family 3, two fetuses were terminated prematurely: one due to fetal akinesia, and the other due to triploidy. Parents were non-consanguineous. The mother was heterozygous for variant p.R756C and the variant p.S1478L was found *de novo* on the paternal allele. Both parents were asymptomatic. A third pregnancy is currently ongoing but the fetus is at the time of writing unaffected. Functional characterization by patch clamp in HEK293T

cells revealed complete or near complete absence of sodium current in p.R756C and p.S1478L variants (Figure 6.4.).

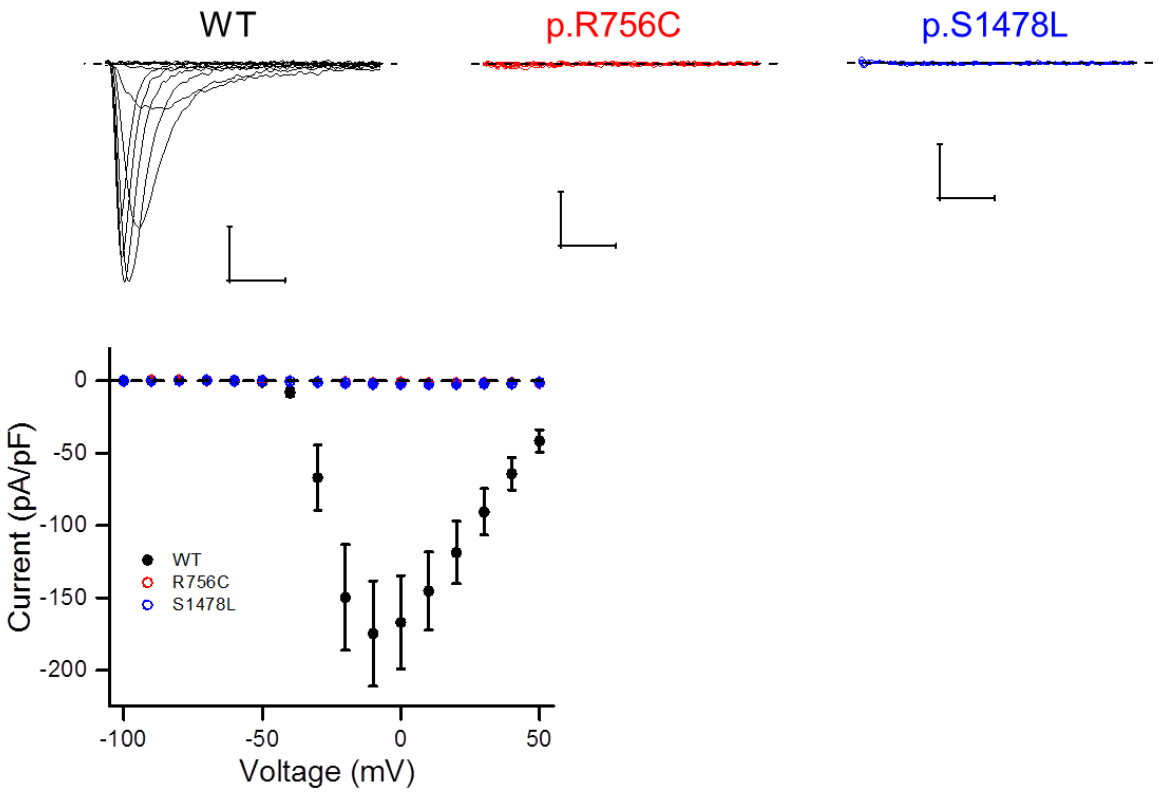

Figure 6.4. Functional characterization missense in family 3 variants by patch clamp. Top: representative current traces measured in wild-type (black), p.R756C (red) and p.S1478L (blue). Scale bars: 1 ms (x-axis), 1 nA (y-axis). Dashed line: 0 current. Bottom: Mean current density for WT (n=20) p.R756C (red, n=11), and p.S1478L (blue, n=12) channels.

6.2.1.4. Family 4

Two children died intrauterine. Both were compound heterozygous for a frameshift and a splice-site variant, c.3911_3912+1del and c.274-2A>G, respectively in *SCN4A*. Two healthy siblings were wild-type or heterozygous carrier. Both parents are heterozygous for one of the variants. The frameshift variant truncates the channel (p.Lys1304Ilefs*17). The splice site mutation is likely to result in defective splicing of intron 1 and both variants co-segregate with FADS in the family.

6.3. Discussion

The results presented in this chapter confirm the hypothesis stated in Chapter 5; namely that bi-allelic *SCN4A* mutations that result in complete or near-complete loss of function of $Na_V1.4$ underlie some cases of fetal akinesia deformation sequence. These findings reveal a wider prevalence of recessive *SCN4A* mutations associated with disease in general and in particular confirm it as a FADS gene. This expanding patient cohort with recessive *SCN4A* mutations improves correlation between the clinical phenotype and functional channel properties.

6.3.1. Severe *SCN4A* loss of function is incompatible with life

This chapter describes a series of novel compound heterozygous and homozygous *SCN4A* mutations in eight individuals from four kindreds with FADS. In line with the conclusions drawn from similarly affected individuals of family 5 in Chapter 5, the combined effect of two severe (or complete) loss of function mutant $Na_V1.4$ channels is likely to attenuate the action potential amplitude in skeletal muscle to a level insufficient to sustain any muscle force. The lack of clinical findings in confirmed carriers is in agreement with the previous conclusion that loss of function in a single allele is insufficient to cause clinical presentations, and further suggest an autosomal recessive mechanism of inheritance.

We also describe the first homozygous nonsense mutation in *SCN4A*, causing early truncation and full loss of function. Routine pathological examination did not reveal changes in this kindred, suggesting the akinesia is electrogenic in origin.

The functional properties of the missense variants in heterologous expression system could differ from those in expression systems. Functional expression should thus ideally be studied in the muscle to confirm our findings. However, the homozygous early truncation mutation definitively leads to lack of functional $Na_V1.4$ in the muscle, lending

further support for null *SCN4A* mutations underlying skeletal muscle presentations in the FADS cohort.

In contrast to FADS, carriers of compound heterozygous *SCN4A* variants with partial loss of function in one or both alleles may survive, manifesting instead a congenital myopathy or congenital myasthenic syndrome (Chapter 5). Consistent with role of *SCN4A* mutations in FADS, mice with exon 12 in *SCN4A* (Δ_Ex12) deleted, leading to *Scn4a* null/null mice, were always lethal (Wu et al., 2016). However, heterozygous null (+/null) mice displayed muscle subclinical fatigability. Wu and colleagues tabulate the spectrum of phenotypes associated with loss of function in *SCN4A* (Table 1, Wu et al. 2016). They report that +/LOF humans have fatigability with ptosis, and decrement on CMAP. However, this is incongruent with the findings in Zaharieva *et al.* (2016) which do not find any fatigability in complete (null) heterozygous carriers. What this may be instead based on is that Tsujino *et al*. (2003) considered the S246L variant to be a non-pathogenic variant, such that one of the alleles is incorrectly labeled WT (+).

In mice however, upon repetitive stimulation of muscle *ex vivo*, a decrement of the compound muscle action potential was seen. In haploinsufficient mice (heterozygous mice, +/Δ_Ex12) there was an approximately 50 % reduction in current density measured in muscle fibers. This is in agreement with our findings using heterologous expression in HEK293 cells. Further reduction in sodium current amplitude, for example by inactivation upon repetitive stimulation, may have more severe presentations in heterozygous loss-of-function mice that have 50% smaller channel availability than the wild-type mice.

At this time it is unclear if and how thoroughly the human heterozygous carriers were studied for subclinical details, such as fatigability. It is feasible to conceive that in conditions that severely reduce channel availability, such as repetitive high-frequency stimulation, the carriers of loss of function variants may be more susceptible to fatigability. The degree of reduction in sodium current amplitude in human heterozygous carriers

remains to be established, as do potential compensatory mechanisms that might differ in humans and mice. Further subclinical investigations targeting fatigability resistance in human heterozygous carriers may also be warranted.

Skeletal muscle $Na_V1.4$ channels may thus have large reserve that needs to be depleted before clinical (or subclinical) features can be detected. For other Na_V isoforms knock-down or loss of function of a single allele may cause symptoms. In *Scn5a* +/- mice halving of the net current density recorded in cardiomyocytes is detected (Papadatos et al., 2002). The voltage-dependence of activation or inactivation were both unaffected by the reduced current density. These mice display cardiac defects including ventricular tachycardia and impaired atrio-ventricular conduction. In addition, partial (heterozygous) loss of function mutations in $Na_V1.1$ (*SCN1A*) have been shown to cause febrile seizures. One missense variant, p.M145T, halved the current density compared to wild-type and right-shifted the voltage-dependence of activation (constituting another loss of function effect) (Mantegazza et al., 2005). However, loss of function mutations of $Na_V1.7$ in patients insensitive to pain are recessive (Cox et al., 2006). It may be that an abundance of $Na_V1.4$ channels in skeletal muscle are able to compensate for losing half of its channels, as observed in asymptomatic +/null human carriers.

6.2.2. Implications for genetic counseling and therapeutic options

The genetic and functional data presented herein implicates recessive *SCN4A* mutations as a monogenic cause of fetal akinesia. Evaluation of FADS cases should include genetic screening for and functional characterization of *SCN4A* variants.

All carriers of monoallelic complete loss of function mutations are fully healthy. As treatment for these disorders is currently unavailable, prevention should be considered. Pre-implantation genetic diagnosis (PGD) on human embryos can be used to establish whether a particular fertilized embryo is carrying mutations on one or two mutant *SCN4A* alleles. The oocytes identified to carry only a single mutation (or better yet—none) can

then be grown to the blastocyst stage, and selected for implantation using *in vitro* fertilization (IVF). If the pregnancy is successful, this should hopefully lead to an infant without skeletal muscle presentation. However, before PGD/IVF clinics are permitted to perform this procedure in the United Kingdom, the Human Fertilisation and Embryology Authority (HFEA) must consider and approve the condition. Although this disorder is very rare, PGD combined with *in vitro* fertilization may be a viable option for families facing this condition. A proposal to the HFEA to consider this condition for PGD is being discussed. Several other types of congenital myopathy are already on the list of approved disorders, so that the likelihood of such an application being accepted is high.

6.3.3. Implications for correlating function and structure of voltage-gated sodium channels

One of the mutations affects a novel site for the series of loss of function mutations, namely the p.S1478L located in the DIV S4-S5 linker. This mutation caused a severe reduction in the current density to none or almost zero in all cells recorded. It is widely postulated that the S4-S5 linker pulls S5 and S6 to open the pore domain (Payandeh et al., 2011a). It is possible that the p.S1478L variant disrupts the capability of the S4-S5 linker to serve the functional link. Alternatively, it may destabilize the channel structure and prevent its functional expression. The p.S1478C mutation has been shown functional (Lerche 1997). Mutations of rat $Na_V1.4$ at this residue (p.S1471D, p.S1471F, p.S1471K, and p.S1471M) result in non-functional channels, while mutations to alanine and threonine are tolerated and result in channels with WT-like inactivation (Filatov et al., 1998). Thus, it seems that small, polar (S, C, T) or small hydrophilic (A) residues at this location are tolerated, while introducing a charged or large hydrophobic residue, such as leucine at this location may destabilize the S4-S5 linker to a fully inactivated state. Studying surface expression of this variant should be able to dissect if the stability of channel protein is reduced. It is of note that the inactivation properties of mutations that do form functional channels are not altered compared to the WT.

The other variants affect pore loop (p.C756R), channel gate (p.I1291N) or are located directly after the S6 helix (p.T1605P). Introduction of proline changes into secondary structure suggesting that the secondary structure of region immediately following the intracellular gate of the channel is important for its function. Mutations in the pore loop or in the central pore where the channel gates lie may disrupt the selective permeation of sodium ions or stabilize the closed state of the channel gate. The p.I1291N mutation affects the intracellular end of S6, which has also been implicated as a binding site of the inactivation hinged lid. The molecular pathomechanism of all the variants remains to be established.

6.4. Summary

In this study, we establish that recessive *SCN4A* mutations that cause either a complete or near-complete loss of function on both alleles can cause fetal akinesia deformation sequence. These findings confirm *SCN4A* as a FADS gene, with important implications for the genetic diagnosis of patients with similar clinical phenotypes.

7. Bi-allelic *SCN4A* loss of function in congenital “corona” myopathy

7.1. Aims and hypothesis

Two brothers in a non-consanguineous family displayed a mild form of congenital myopathy. Although one sibling displayed normal motor development milestones, both had trouble walking and fell over often. Muscle biopsy revealed unusual changes in muscle structure with multiple internal nuclei arranged in a crown-like fashion. Heteroallelic *SCN4A* variants were identified in both siblings. Based on our findings in chapter 5 we hypothesized these variants may be underlying the congenital myopathy and that one of the variants would cause full and the other a partial loss of function.

7.2. Results

7.2.1. Note on results

In this chapter I performed functional characterization of additional *SCN4A* variants found in patients with congenital myopathy. The clinical case was from Grace Yoon's group in Toronto, Canada, who also performed the genetic analysis. Collaborators included Hernan Gonorazky, Christian R. Marshall, Maryam Al-Murshed, Lili-Naz Hazrati, Peter N. Ray, and Grace Yoon, all based at the Hospital Hospital for Sick Children in Toronto, Ontario, Canada.

7.2.2. Genetics and major clinical findings

Both siblings displayed similar clinical features with hypotonia was noted from birth. Both siblings fell over often and had trouble walking, although at least one of the siblings reached normal motor development milestones on time. Weakness impaired daily living and was observed in facial muscles, proximal leg muscles, arms, and shoulders. The patients both displayed mild ptosis.

Muscle MRI detected involvement same muscles as described in our original congenital myopathy cohort: gluteus maximus, sartorius, adductor magnus, and soleus muscles. Muscle pathology was distinct from Chapter 5, with necklace “corona” fibers in the younger brother. A comprehensive clinical description can be found in the reference Gonorazky *et al*. (2017). Two brothers were found to carry heteroallelic variants c.3425G>A (p.Arg1142Gln) and c.1123T>C (p.Cys375Arg) in *SCN4A*.

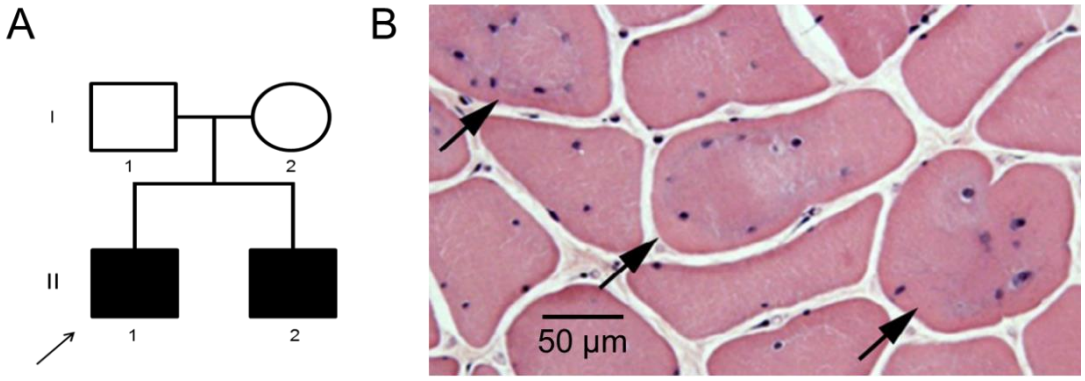

Figure 7.1. Pedigree and distinguishing muscle pathology of the mild congenital myopathy kindred. (A) Affected individuals represented by shaded symbols. Proband indicated with an arrow. (**B**) Muscle fibers (H&E stain) displaying nuclei arranged in a corona shaped fashion (arrows).

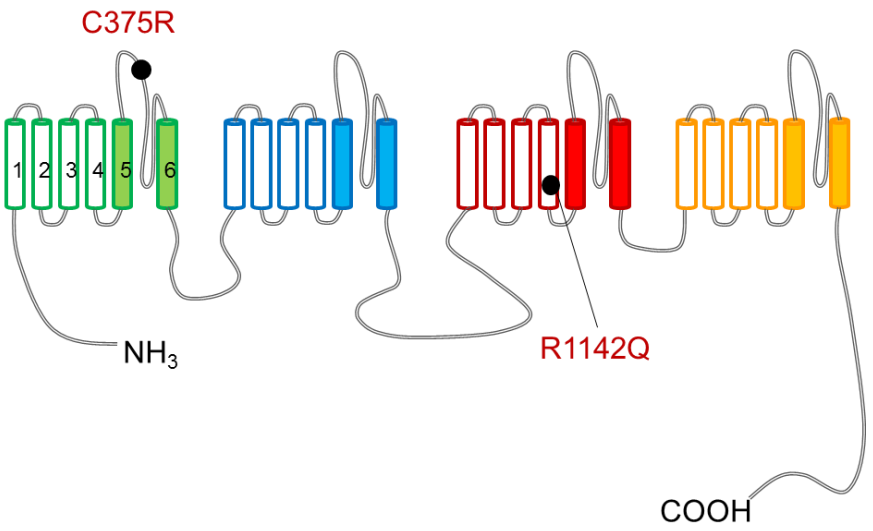

Figure 7.2. Location of mutations in both siblings with mild congenital myopathy. Mutations located to the S5-S6 loop (C375R) and S4 of domain III (R1142Q).

7.2.3. Functional characterization

Functional characterization of variants was performed by whole-cell patch clamp in HEK239T expressing p.C375R, p.R1142Q, and wild-type construct. No current was observed in p.C375R expressing cells (n=14; Figure 7.3.) over four separate transfections. Peak current density of p.R1142Q channels was also reduced although this did not reach significance. Voltage dependence of activation of the p.R1142Q channels showed a (+4 mV) depolarizing shift (p.R1142Q: −16.7 ± 0.7 mV, n=18 vs. WT: −20.4 ± 0.9 mV, n=15, p=0.008, Mann-Whitney *U* test). This constitutes a loss of function. No changes in the slope factor were measured (WT: 6.0 ± 0.3 mV vs. p.R1142Q: 6.6 ± 0.2 mV, $p<0.05$).

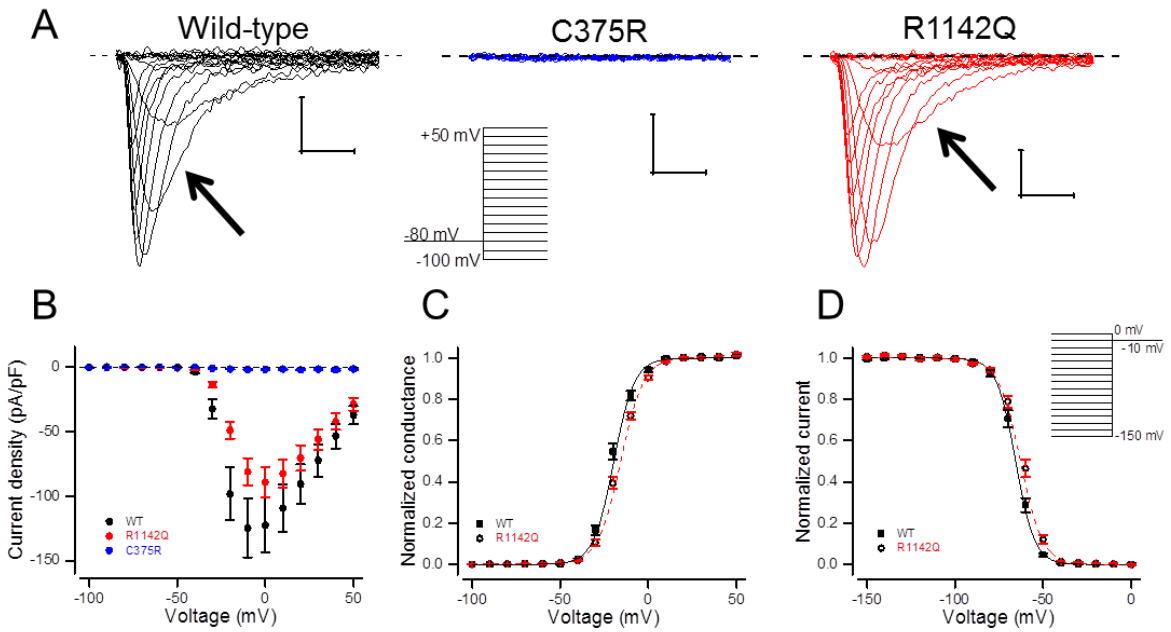

Figure 7.3. Functional properties of mutants p.C375R and p.R1142Q in HEK293T cells.

(**A**) Current traces for WT, p.C375R, and p.R1142Q, respectively. Scale bars are 0.5 ms (x-axis) and 0.5 nA (y-axis). *Insert:* voltage protocol: Voltage steps range from −100 mV to 50 mV in 10 mV increments from −80 mV holding voltage (**B**) Current density (current pA normalized to pF) of WT (black), R1142Q (red) and C375R (blue) channels, dashed line shows zero current level; (**C**) voltage-dependence of activation determined by voltage steps ranging from −100 mV to 50 mV in 10 mV increments from −80 mV holding voltage – conductance is plotted against test voltage step. Solid and dashed lines show fit of Boltzmann function to mean data; (**D**) voltage-dependence of fast inactivation. Insert shows voltage stimulating protocol. −150 mV to 0 mV pre-pulse voltage steps (150 ms) in 10 mV increments was followed by a test voltage step (−10 mV). Peak current recorded at -10 mV was normalized to the peak current and plotted against the pre-pulse voltage. Solid and dashed lines show fit of Boltzmann function to mean data.

The voltage-dependence of fast inactivation was slightly enhanced by 3.8 mV (R1142Q: −61.4 ± 1.0 mV, n = 18 vs. WT: −65.2 ± 1.0 mV, n = 15; p<0.01).This was accompanied with a small increase in the slope factor (p.R1142Q: 5.7 ± 0.2 mV vs. WT: 5.1 ± 0.1 mV, p<0.05).

Further, tau of recovery from inactivation was slightly enhanced (p.R1142Q: 4.3 ± 0.3 ms vs. WT: 6.4 ± 0.7 ms; p=0.008). No changes were measured in open-state inactivation

(Table 7.1; Figure 7.4.) or slow inactivation (WT: -49.0 ± 1.7 mV vs. p.R1142Q: -50.8 ± 1.5 mV).

Table 7.1. Tau of onset of open-state inactivation Data are expressed as means ± standard error of the mean. The mean values are shown in the table. Statistical comparison was performed using a two-way repeated measures (mixed factorial) ANOVA (voltage, genotype) with Bonferroni's *post hoc* test. ***P* < 0.01

	Onset of open-state inactivation (Time constant (ms) at given voltage (mV))	
Voltage	WT	p.R1142Q
-20	0.75 ± 0.05	0.92 ± 0.09**
-10	0.45 ± 0.02	0.50 ± 0.03
0	0.31 ± 0.01	0.36 ± 0.01
10	0.26 ± 0.01	0.29 ± 0.01
20	0.23 ± 0.01	0.26 ± 0.01

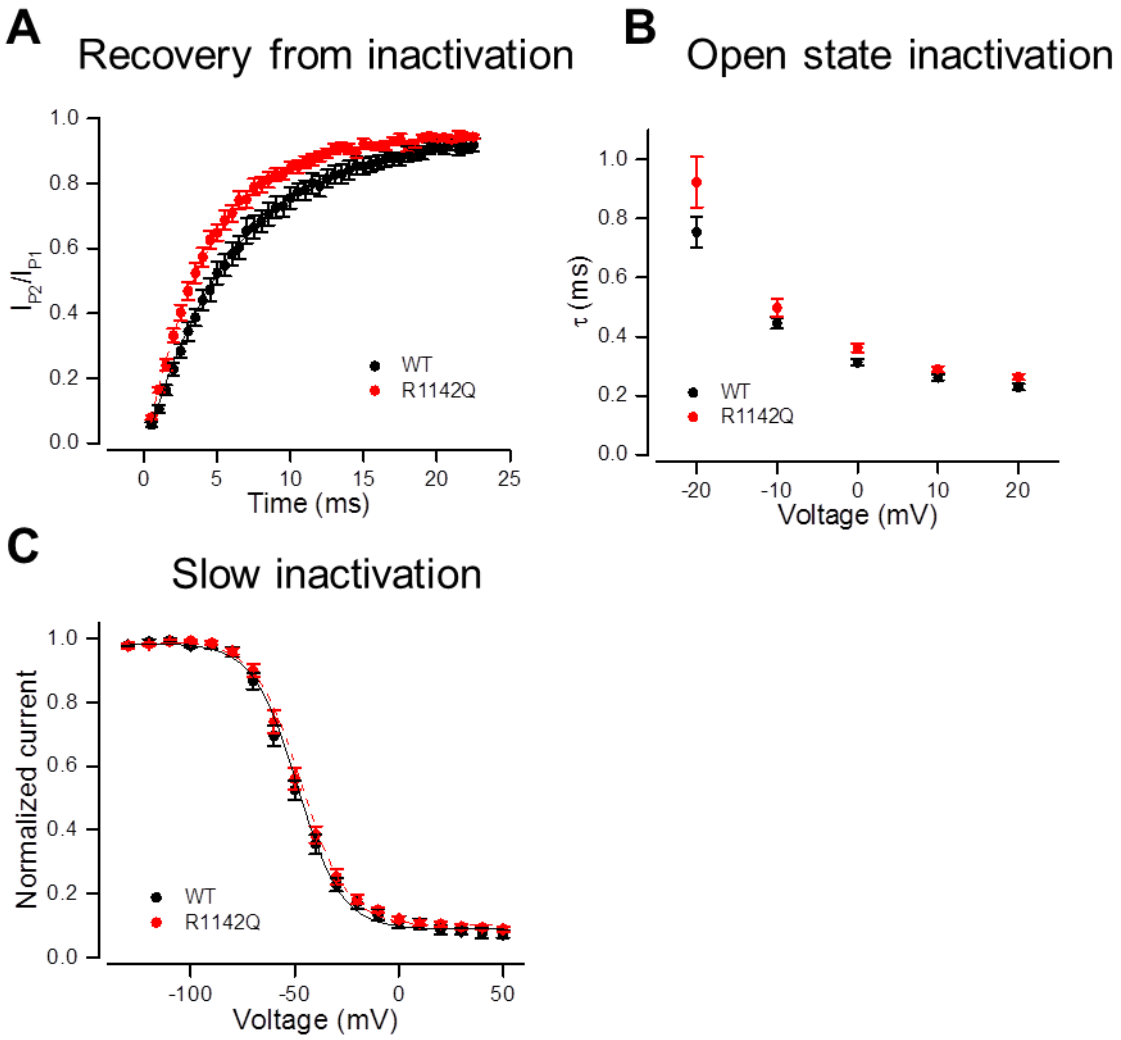

Figure 7.4. Inactivation properties for p.R1142Q vs. wild-type.

(A) Time course of recovery from fast inactivation. Peak current in response to second test pulse (I_{P2}) is measured following a recovery period of varying duration at -80 mV. I_{P2} is divided by the peak current of a prepulse (I_{P1}) that was also used to inactivate channels. Solid line shows a single exponential fit to the data. (B) Open state inactivation. Time constant (ms) of the onset of fast (open-state) inactivation plotted against the voltage. Two exponential curves were fit to the decaying phase of the sodium current (90% of peak). Only the fast component was analyzed, (C) Slow inactivation determined by applying 10 s prepulses ranging from -130 mV to +50 mV in 10 mV increments. A 20 ms pulse to -100 mV was applied to recover channels from fast inactivation, followed by a test pulse to -10 mV. The peak current in response to the -10 mV test step is plotted against the prepulse voltage. All data points are mean±SEM.

7.3. Discussion

This chapter describes a form of congenital myopathy associated with bi-allelic *SCN4A* loss of function mutations that is clinically milder compared to the four individuals who survived in Chapter 5. For example, while delay in early motor milestones was universal in the cases presented in chapter 5, one of the siblings in this chapter reached motor milestones in time – even if he had trouble walking and fell often. Both siblings carried the same two *SCN4A* variants. Functional characterization revealed a full loss of function on one allele, and a mild loss of function *in trans*. These data are striking, as they add further validity to the notion that the clinical phenotype is correlated with the severity of the channel dysfunction, i.e. the level of total sodium current availability reduction in the muscle.

7.3.1. Molecular pathomechanism and correlation with clinical phenotype

As in other *SCN4A* myopathy cases, no currents were measured in one of the variants (p.C375R). On the *trans* allele a mutation with loss of function with relatively small changes in channel function was found (p.R1142Q). The mild loss of function measured in p.R1142Q channels consists of a 4 mV depolarizing shift in the voltage-dependence of activation. In addition, the variant showed mildly attenuated fast inactivation and accelerated recovery from inactivation. Compared to the functional defects caused by the mutations in the four surviving cohort members of Chapter 5, the defects measured in p.R1142Q are very mild. The mildest in the Chapter 5 cohort is the individual carrying the p.D1069N. D1069N showed similar changes in channel function. It is possible that the less severe clinical phenotype is a direct function of the severity of the channel defect.

Clinical description and additional investigations are helping to identify features associated with *SCN4A* myopathies. The muscle pathology described in the two brothers is slightly different from surviving individuals in Chapter 5. The second sibling was found to have so

called necklace fibers—a pertinent finding—because this pathology type is usually associated with centronuclear myopathy. Muscle fibers with a pathological aberration in the form of a necklace in a ring around the edge of the fiber have been described previously (Bevilacqua et al., 2009). This is distinct from the older brother presented in this chapter, where the fibers instead form a crown-shaped structure, termed here corona fibers due to its resemblance of the corona shape seen at a solar eclipse (Gonorazky *et al*. 2017).

Despite distinctive muscle pathology we hypothesize that that the hypotonia present in the brothers is result of reduced sodium conductance in the muscle. It is unclear how a small amplitude $Na_V1.4$ loss of function would downstream result in a distinct muscle pathology. In general, the relation of $Na_V1.4$ disorders, including the dominant gain of function mutations, to changes muscle pathological features, remains to be established. The pathology described in this thesis appears very variable and non-specific, suggesting that drawing such correlations from the current data set alone would be ill-advised.

In addition, the MRI pattern of muscle involvement in the patients described in this chapter match well with muscle involvement described in the patient in chapter 5. We do not know the cause of specific muscle involvement. Investigation of MRI patterns of further *SCN4A* myopathy cases will help validate these findings and their diagnostic value.

7.3.2. Structure-function elucidation

The position of the mutant residues are important, with the p.C375R mutation located to the domain I S5-S6 extracellular loop and the p.R1142Q mutation is a domain III S4 gating charge (Figure 7.2.). These residues are conserved across channel isoforms. The p.R1142Q is the sixth (R6) and innermost gating charge of domain III. Only p.R1132 (R3) and p.R1135 (R4) have been implicated in disease. Mutations in both of these arginines have been found in patients with hypoPP, and have been shown to conduct gating pore currents (Francis et al., 2011a; Groome et al., 2014). There is a report of p.R1129 in

hypoPP in a single case but gating pore currents were not studied. Gating pore currents were not found when this arginine was mutated to histidine (Gosselin-Badaroudine et al., 2012). Equally, data from our lab suggest that mutation of p.R1138 does not carry gating pore currents (R. Mannikko, personal communication). In voltage-gated potassium channels, mutations of the first four arginines have been shown to result in gating pore currents (Starace and Bezanilla, 2001, 2004). In these channels, mutations of deeper arginines result in non-functional channels, suggesting that normally these arginines are essential for formation of stable VSD, or do not conduct gating pore currents (Starace and Bezanilla, 2001). As the p.R1142Q residue is so deep in the S4, it is unlikely to produce gating pore currents. Instead, in $Na_V1.4$ channels the mutation p.R1142Q seems to stabilize the down state of the VSD as more depolarized voltage is required to activate and inactivate the channel.

The p.C375R is located to the pore loop between segments S5 and S6 of domain I. A cysteine-to-arginine introduces a positive charge where a neutral amino acid (cysteine) was present previously. Another mutation causing full loss of function, p.P382T was identified in chapter 5, suggesting that the pore loops in general and that of domain I may form a hot spot for congenital myopathy mutations. This is consistent with the role of this region in setting the selective permeation.

7.4. Summary

Presented herein is a less severe form of congenital myopathy where on the second allele a mutation causes a loss of function less severe compared to those previously characterized in Chapter 5. In addition, a distinctive muscle pathology is observed in this case, thus expanding the range of phenotypes associated with heteroallelic *SCN4A* loss of function mutations.

8. *SCN4A* mutations associated with sudden infant death syndrome

8.1. Background, aims, and hypothesis

Sudden infant death syndrome (SIDS) is defined as the unexpected death of a seemingly healthy infant. It is the leading cause of infant death in developed countries. The pathogenesis of SIDS is not fully understood; however, current evidence implicates cardio- and respiratory dysfunction as important risk factors (Hakeem et al., 2015; Kinney and Thach, 2009). Co-smoking, co-sleeping, and a prone sleeping position are established common environmental risk factors, implicating the respiratory system as a key target.

Life-threatening laryngospasms and apneas have been described in carriers of $Na_V1.4$ gain of function mutations and in some cases are lethal. (Lion-François et al., 2010; Simkin et al., 2011). In addition, carriers of homozygous or compound heterozygous loss of function mutations have required respiratory aid the infancy (Zaharieva et al., 2015, Habbout et al., 2016), and Tsujino and colleagues (2003) also reported episodes of respiratory insufficiency since birth. Thus, dysfunction of $Na_V1.4$ in respiratory muscle can lead to life threatening respiratory complications in seemingly healthy infants. Based on the clinical presentation and the presence of *SCN4A* variants we hypothesized that respiratory complications may be due to *SCN4A* dysfunction, and could underlie some of the unexplained deaths by compromising the function of respiratory muscle controlling breathing. This chapter aims to test the hypothesis that some *SCN4A* variants identified in SIDS cases are pathogenic; that pathogenic *SCN4A* variants are over-represented in the SIDS cohort; and to delineate whether *SCN4A* mutations could constitute a novel risk factor for SIDS.

8.2. Results

8.2.1. A note on results

This project is in collaboration with St George's University and the Ackerman lab at the Mayo Clinic (Rochester, MN). Genetics was performed by Elijah Behr and colleagues at St. George's University Hospital (UK cohort), as well as the Ackerman lab (US cohort).

8.2.2. Genetics

In a cohort of 427 individuals who suffered sudden death, 28 different *SCN4A* variants were found in a total of 51 infants using next-generation sequencing. Of these, 332 SIDS cases were in the USA, and 95 SIDS cases in the UK. Six variants were novel, another five very rare (<1 in 20,000 in ExAC; Table 8.1.). Figure 8.1. illustrates the specific location of each variant found in the SIDS and control cohort. One of the novel variants, p.R1463S, was in UK skeletal muscle channelopathy database in a patient with myotonia.

A cohort of 729 individuals with European ancestry was used as control cohort. In the control cohort eight very rare or novel missense variants were found (Table 8.1.). In addition one intronic variant that was not predicted to alter splicing using the Human Splicing Finder tool was found in the control cohort (Desmet et al., 2009). The control cases have no history of cardiac, pulmonary, or neurological defects. The SIDS cohort was then refined to only include individuals of European ancestry. This controls for any inter-ethnic variance in the genetic profile of SIDS individuals, reducing the total number of SIDS cases to 278 with 6 rare *SCN4A* alleles (2.2%). The frequency of rare variants was not different compared to control cohort (1.2%, p=0.21, one tailed Fisher's exact test)

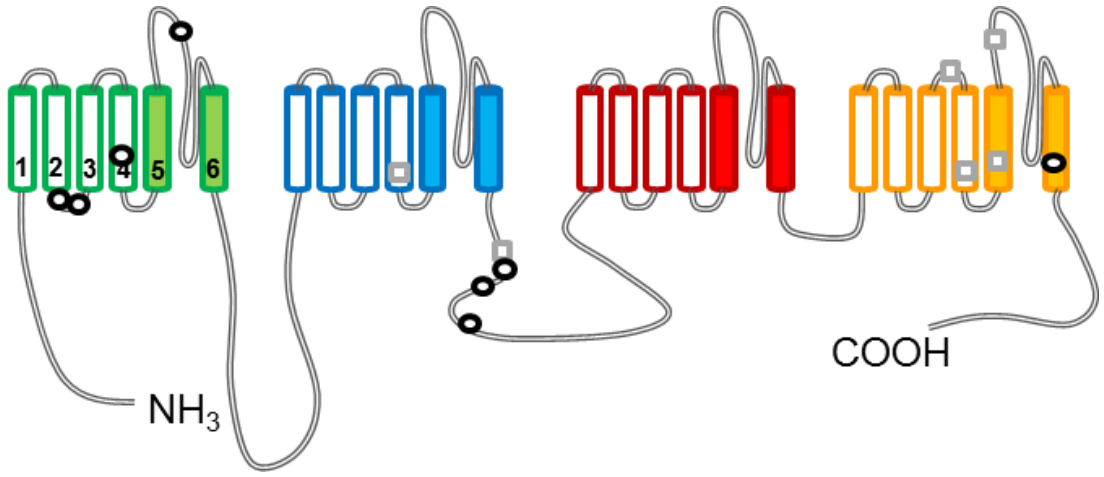

Figure 8.1. Location of *SCN4A* variants.

Schematic diagram of variants found in *SCN4A.* Gray squares constitute SIDS variants (p.S682W, p.G859R, p.V1442M, p.R1463S, p.M1493V, and p.E1520K). Control variants displayed as black circles (p.R179Q, p.R190W, p.L227F, p.D334N, p.G863R, p.A870T, p.M897K, and p.V1590I).

8.2.3. Clinical details of individuals in the SIDS cohort

This study used fully anonymized exome data such that further family information could not be identified. Apart from the data shown in Table 8.1., no clinical information or family history is available. Deaths occurred at ages 2-3 months. No increased risk of sleeping position, co-sleeping or smoke exposure was reported. In addition, no upper respiratory tract infections were reported. The criteria required to satisfy a diagnosis of sudden infant death are very stringent. When a seemingly healthy infant (in their first year of life) dies suddenly, it is classified as SIDS when autopsy as well and histopathology and microbiology rule out any other explanations. The investigations are performed by pediatrically trained medical examiner or experienced pathologist. These findings are then reviewed by a panel of several medical practitioners, who also review family history. A police investigation of the death scene is carried out, to rule out maltreatment or intentional harm to the child. In most cases (more than 90 %), this is ruled out, and medical examination and caring for the parents' welfare takes precedence (Fleming et al.,

2004). As soon as any crime is ruled out, it is imperative that the family is treated with the utmost care and that they are free from any accusation of crime.

Table 8.1. Genetic and clinical overview of *SCN4A* variant carriers in the SIDS cohort.

Allele frequency in databases ExAC (Exome Aggregation Consortium) or EVS (Exome Variant Server).

NK: not known; URTI: upper respiratory tract infection.

SCN4A Variant	Allele Frequency	Age (months)	Sex	Co-sleep	Evidence of URTI	Term	Sleep position	Exposure to cigarette smoke
c.2045C>G; **p.Ser682Trp**	0.00002626 (ExAC)	3	Male	yes	no	NK	prone	yes
c.2575G>A; **p.Gly859Arg**	0.00001756 (ExAC)	3	Female	yes	no	full	prone	NK
c.4324G>A; **p.Val1442Met**	0.00001025 (ExAC)	5	Male	no	no	pre-mature	supine	no
c.4387C>A; **p.Arg1463Ser**	NOVEL	3	Male	yes	no	full	side	yes
c.4477A>G; **p.Met1493Val**	NOVEL	3	Female	no	no	NK	prone	NK
c.4558G>A; **p.Glu1520Lys**	NOVEL	2	Male	NK	yes	NK	NK	NK

8.2.4. Functional expression of *SCN4A* variants in HEK293T cells

Mutations were inserted into human *SCN4A* cDNA by site-directed mutagenesis and expressed in HEK293T cells by transient transfection. The functional characteristics of all channel variants (both SIDS and control) were then studied using whole-cell patch clamp, and compared against wild-type parameters. As in all chapters, recordings were performed intertwined so as to minimize any data variability associated with batch effect errors. One intronic splice variant (c.393-1C>T) was identified in the control cohort, but was not studied functionally as it was predicted by the Human Splicing Tool to be non-pathogenic (Desmet et al., 2009).

Non-normal and kurtosed residuals from test for six out of seven parameters tested using Shapiro-Wilk's test (of residuals). Therefore we instead performed the non-parametric Kruskal-Wallis rank sum test. In addition, Levene's test for heteroscedasticity of variance was performed. Variance was found heteroscedastic in all groups except for the voltage-dependence ($V_{1/2}$) of fast inactivation. Thus, Kruskal-Wallis rank sum test was performed on all groups with Dunn's post hoc non-parametric pairwise multiple comparisons except the voltage-dependence $V_{1/2}$ of activation which was normally distributed, but with non-equal variance. On this parameter a one-way ANOVA was performed with the Games-Howell post hoc test for pairwise comparisons. P values presented are raw (un-corrected) p values before Bonferroni correction for multiple comparisons. For data transparency, and to include two levels of protection from false discovery rate, two levels of multiple correction were performed: either within-parameter, or across all parameters tested. The Bonferroni threshold for within-parameter comparison is p=0.003571429 (14 comparisons), while the threshold across all parameters is p=0.000510204 (98 comparisons). In this thesis the most conservative correction was used.

8.2.4.1. Voltage-dependent properties of activation and fast inactivation

Reduced current density was measured in two variants. In p.V1442M and p.E1520K the peak current density at 0 mV was 46±5 % and 39±4 % of the wild-type, respectively (Figure 8.2., Table 8.2.). The voltage-dependence of all variants was not significantly different from wild-type channels (Figure 8.2., Table 8.2.). In the control cohort the current densities as well as the voltage-dependence of activation were wild-type like for all variants (Figure 8.2., Table 8.2.).

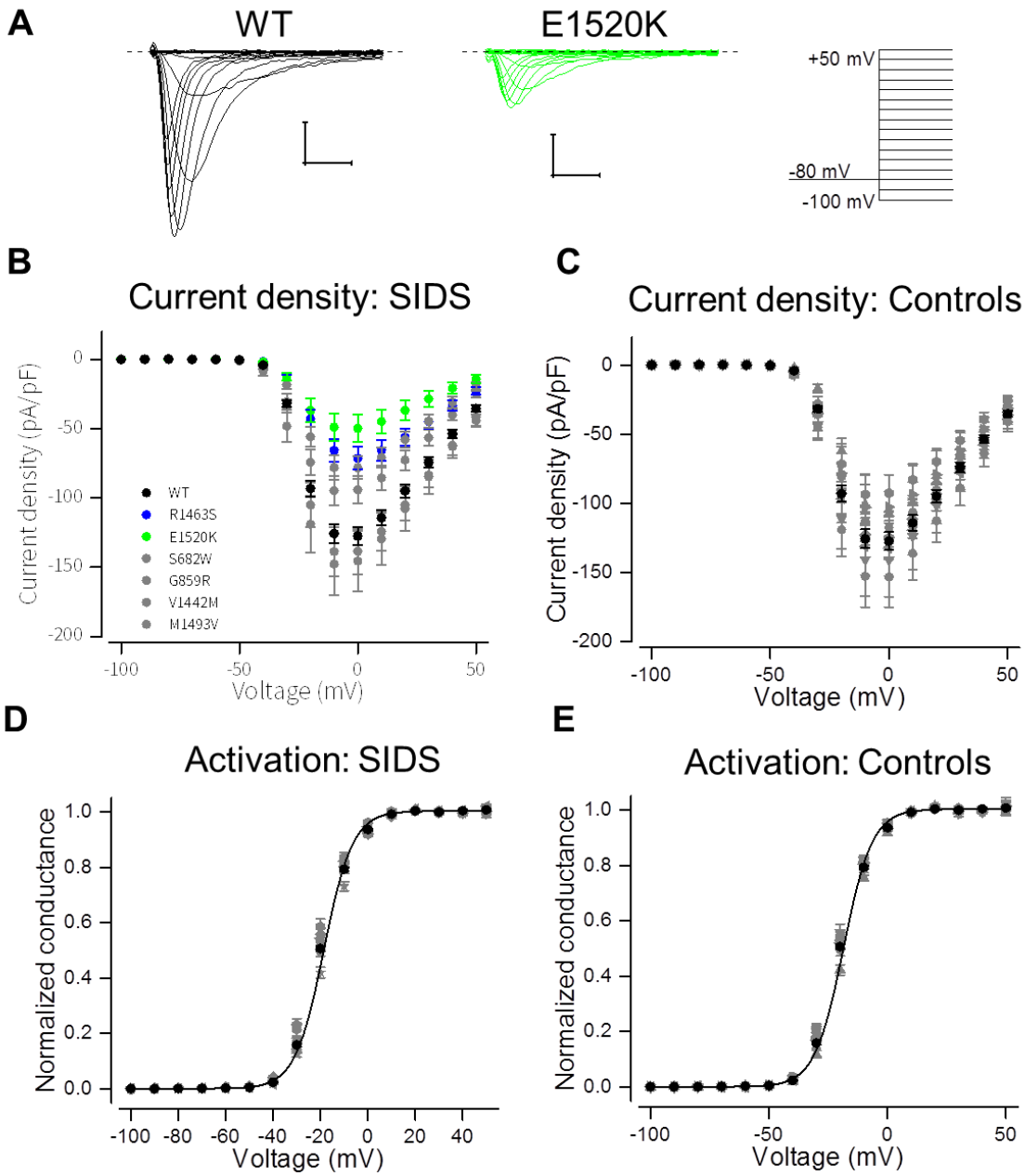

Figure 8.2. Current density and voltage-dependence of activation in SIDS and control variants.

(**A**). Representative current traces of wild-type and p.E1520K in response to test voltages ranging from -150 mV to +40 mV. Scale bars are 1 ms (x-axis), 0.5 nA (y-axis). Currents plotted to scale. Dashed lines indicate baseline current level at -80 mV holding voltage. (**B**) Peak current amplitude (mean±SEM) in response to test voltages ranging from -150 to +50 mV in 10 mV increments is plotted against the test voltage. (**C**) Normalized conductance ((Peak current/(Voltage - reversal voltage of the current)) is plotted (mean±SEM) against the test voltage. Mean data were normalized to maximum and minimum values of the Boltzmann fit and averaged. The solid lines represent the fit of Boltzmann equation to mean data from which the slope factor is calculated. Black: wild-type, blue: p.R1463S, gray: all variants with wild-type like properties.

The half-maximal voltage ($V_{1/2}$) of fast inactivation in p.R1463S was shifted 4.4 mV in the depolarizing direction compared to wild-type p.R1463S: -61.7+0.6 mV vs. WT: -65.3+0.3 mV, p=0.00002, un-corrected Dunn's value). This results in a gain of function similar to *SCN4A* variants associated with myotonia. Conversely, the voltage dependence of fast inactivation was shifted by -6.6 mV in the p.V1442M variant (p.V1442M: -71.9+1.0 mV vs. WT: -65.3+0.3 mV, p=2.5E-8; Table 8.2.). This results in loss of function by reduced channel availability, similar to *SCN4A* variants associated with recessive congenital myasthenia and in one case of congenital myopathy. No statistically significant changes to either the voltage of half-maximal inactivation or the slope factor of fast inactivation were found in any of the variants present in the control cohort (Figure 8.3.; Table 8.2.)

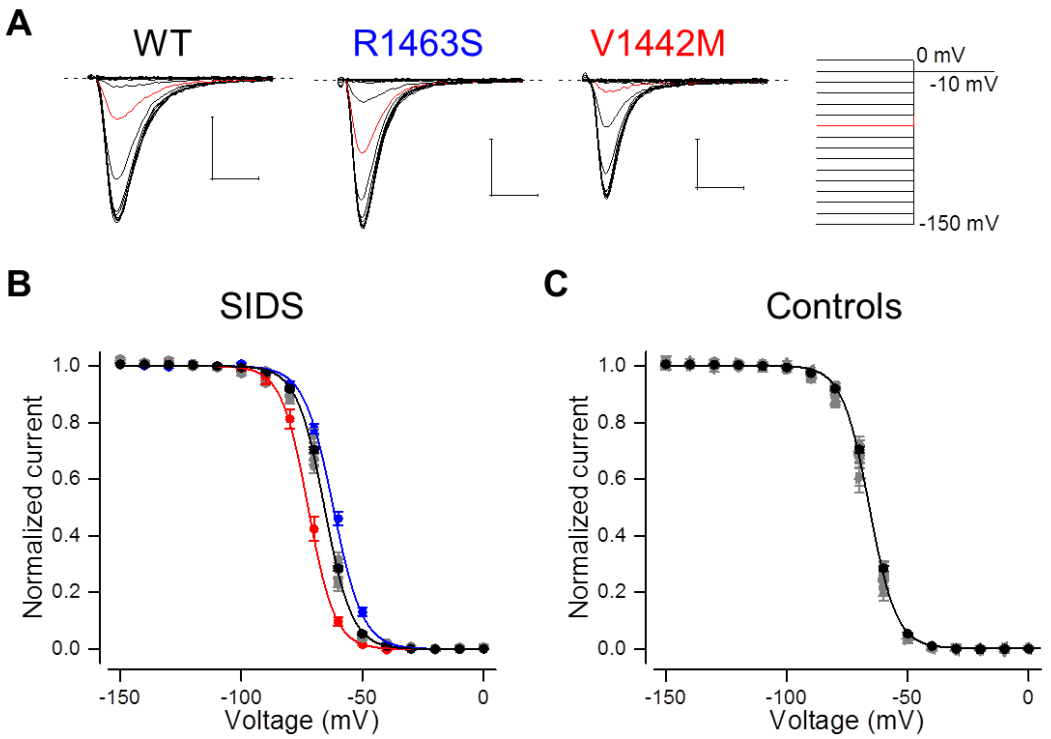

Figure 8.3. The voltage-dependence of fast inactivation in SIDS and control variants.

(**A**). Representative current traces in response to tail voltage step to -10 mV following 150 ms pre-pulse voltage steps ranging from -150 mV to +60 mV in 10 mV increments for wild type (WT), p.R1463S, and p.V1442M variants. First five milliseconds of the voltage step to -10 mV are shown. Scale bars are 1 ms (x-axis) and 1 nA (y-axis). Current response following pre-pulse voltage step to -60 mV is highlighted in red. The voltage protocol is shown to the right. Dashed lines indicate baseline current level at -80 mV holding voltage.

(**B, C**) The peak tail current amplitude plotted (mean±SEM) against pre-pulse voltage for SIDS (**B**) and Controls (**C**). Black: Wild-type, Blue: p.R1463S, Red: p.V1442M, Gray: all variants with wild-type like voltage dependence of fast inactivation. Individual data were normalized to maximum and minimum values of the Boltzmann fit and averaged. The solid lines represent the fit of Boltzmann equation to mean data.

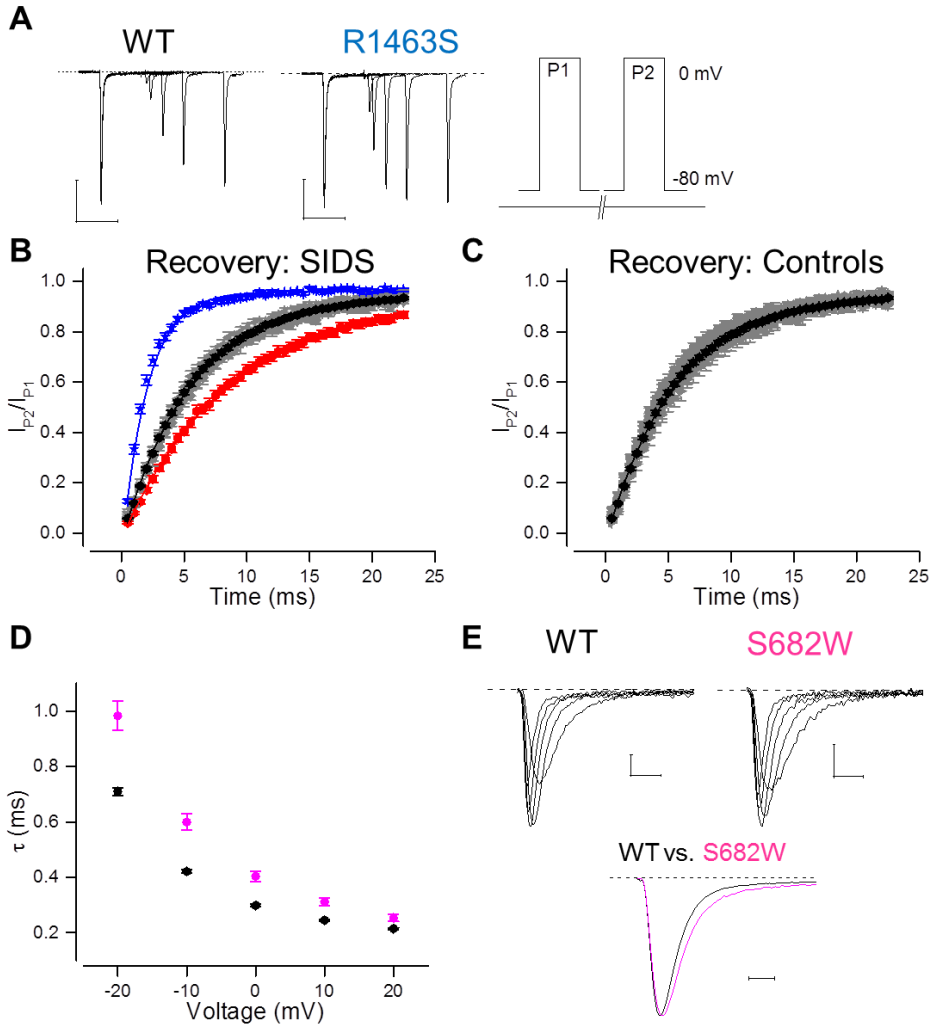

Figure 8.4. Recovery and time-course of open-state inactivation.

(**A**) Current traces for wild-type (WT) and p.R1463S channels using recovery from inactivation protocol. Only traces with 0, 1, 2, 5, 10, and 20 ms duration at recovery voltage of -80 mV shown. The voltage protocol applied displayed to the right. Channels were inactivated by a 10 ms voltage step to 0 mV and then stepped to recovery voltage of -80 mV for an increasing duration of time. A second voltage step to 0 mV was then applied to see how much the channels had recovered from fast inactivation. (**B**, **C**) Average recovery from inactivation in SIDS (**B**) and controls (**C**). The peak current amplitude during the second step (I_{P2}) is divided by the peak current amplitude during the first voltage step (I_{P1}) and plotted against the duration of the recovery period at -80 mV (mean±SEM). The solid lines represent fit of exponential function to the mean data. Black: wild-type, blue: p.R1463S, red: p.V1442M, gray, variants with wild-type like properties. (**D**, **E**) Time course of open state inactivation for wild-type (WT) and p.S682W channels. (**D**) The decay of activation from 90% of the peak

current was fitted with double exponential function. The time constant of the fast component that carries >90% of the amplitude is plotted against the test voltage. (**E**) Example current traces of a HEK293T cell expressing wild-type (black) and p.S682W (magenta) channels at voltage range -20 mV to + 20 mV (above). Mean current traces for wild-type (black) or p.S682W (magenta) channels in response to a voltage step to 0 mV. Individual traces were normalised to peak current amplitude.

Table 8.2. Summary of all biophysical properties of $Na_V1.4$ variants in SIDS and control cohorts with European ancestry. "Control" signifies *SCN4A* variants identified in a group of 729 individuals of European origin who did not show any neurological, cardiological, or skeletal muscle symptoms. These data control for the potential presence of NaV1.4 dysfunction in a fully healthy cohort. I_{Peak} column includes current amplitude of all the cells that expressed currents larger than 0.1 nA. Cells with I_{Peak} expressing currents larger than 0.5 nA were included in the analysis of the biophysical properties. Data represent mean±SEM. Voltage dependence of activation and fast inactivation, and time constant of open state fast inactivation were all analyzed in the recording for each cell.

Clone	**Activation**					**Fast Inactivation**				
	N	I_{Peak} @0 mV (pA/pF)	N	$V_{1/2}$ (mV)	V_{slope} (mV)	$V_{1/2}$ (mV)	V_{slope} (mV)	Tau (@0mV) (ms)	N	$T_{Recovery}$ (ms)
WT	149	-127.5±6.4	*146*	-19.5±0.2	6.4±0.1	-65.3±0.3	5.4±0.0	0.30±0.00	*105*	5.63±0.14
SIDS cohort										
S682W	19	-94.2±9.9	*17*	-21.2±0.7	**7.2±0.2**	-67.0±0.6	5.9±0.2	**0.40±0.02**	*17*	6.15±0.33
p		0.124294		1	0.00038	0.0168	0.00138	2.22E-07		0.168144
G859R	18	-138.5±16.4	*17*	-20.2±0.8	5.7±0.2	-64.2±0.6	5.1±0.1	0.31±0.01	*17*	5.20±0.30
P		0.400		1	0.013	0.184	0.0156	0.238		0.219
V1442M	14	-145.5±21.7	*14*	-21.7±0.8	6.3±0.2	**-71.9±1.0**	5.2±0.1	0.27±0.01	*13*	**8.51±0.46**
P		0.419		0.297	0.618	2.65E-08	0.173	0.069		0.000007
R1463S	27	**-71.3±8.3**	*25*	-17.4±0.5	6.7±0.2	**-61.7±0.6**	**6.3±0.1**	0.31±0.01	*19*	**1.95±0.09**
p		0.000054		1	0.177	2.23E-05	2.9E-08	0.077		1.98E-11
M1493V	17	-78.2±8.3	*17*	-19.2±0.5	6.7±0.3	-65.3±0.8	5.5±0.2	0.29±0.01	*7*	5.76±0.47
p		0.0068		1	0.727	0.929	0.456	0.997		0.611
E1520K	39	**-49.8±9.7**	*28*	-20.3±0.4	6.3±0.1	-66.3±0.5	5.4±0.2	0.33±0.01	*20*	5.63±0.29
p		2.1692E-14		1	0.305	0.052	0.880	0.0030		0.952

Control cohort

Clone			Activation				Inactivation		
	N	I_{Peak} @0 mV (pA/pF)	N	$V_{1/2}$ (mV)	V_{slope} (mV)	$V_{1/2}$ (mV)	V_{slope} (mV)	Tau (@0mV) (ms)	N	$T_{Recovery}$ (ms)
WT	149	-127.5±6.4	146	-19.5±0.2	6.4±0.1	-65.3±0.3	5.4±0.0	0.30±0.00	105	5.63±0.14
R179Q	11	-117.6±11.0	11	-19.3±0.6	6.5±0.2	-65.1±0.7	5.1±0.1	0.25±0.01	11	4.73±0.30
p		0.796		1	0.64	0.951	0.063	0.00167		0.063
R190W	14	-153.4±21.8	14	-20.7±0.5	6.4±0.2	-64.9±0.5	5.3±0.1	0.29±0.01	13	5.09±0.20
p		0.188		0.040	0.79	0.878	0.993	0.621		0.244
L227F	12	-107.7±16.1	12	-17.6±0.4	6.5±0.2	-67.8±0.8	5.6±0.1	0.33±0.02	10	5.33±0.30
p		0.543		1	0.827	0.005	0.186	0.043		0.604
D334N	10	-141.0±26.6	10	-21.0±0.9	6.4±0.2	-66.4±0.8	5.3±0.1	0.27±0.01	9	5.07±0.30
p		0.650		1	0.855	0.179	0.886	0.059		0.327
G863R	12	-124.6±15.8	12	-20.3±0.8	6.3±0.1	-66.1±0.7	5.2±0.2	0.29±0.01	10	5.71±0.21
p		0.649		1	0.435	0.258	0.410	0.801		0.634
A870T	16	-132.6±20.0	15	-20.0±0.6	6.4±0.1	-65.7±0.6	5.0±0.1	0.29±0.01	14	6.29±0.55
p		0.832		1	0.834	0.510	0.009	0.976		0.22
M897K	10	-102.8±23.3	9	-20.4±0.7	6.8±0.3	-67.7±1.3	5.5±0.2	0.31±0.02	7	6.21±0.54
p		0.263		1	0.311	0.065	0.485	0.911		0.286
V1590I	8	-92.8±13.2	8	-20.7±0.6	6.8±0.2	-65.8±0.9	5.4±0.2	0.30±0.02	7	5.73±0.61
p		0.288		1	0.199	0.417	0.703	0.962		0.683

Table 8.3. Summary of biophysical effects in *SCN4A* variants in SIDS cohort with channel dysfunction

MS: missense

Amino acid change	***Mutation type and location***	***Biophysical effect***
S682W	MS, intracellular end of S4 VSD-II	Slowed rate of open-state inactivation
V1442M	MS, S3-S4 linker of DIV	Negative shift in the voltage-dependence of fast inactivation and slowed recovery
R1463S	MS, S4 arginine of DIV	Positive shift in the voltage-dependence of fast inactivation and enhanced recovery
E1520K	MS, S5-S6 pore loop of DIV	Reduced current density

8.2.4.2. Recovery from fast inactivation and time-course of onset of open state inactivation.

To further delineate variant effects on channel function, the tau of recovery from fast inactivation and tau of onset of open-state inactivation were studied. Tau of recovery at -80 mV was markedly enhanced in p.R1463S mutant channels compared to wild-type (Table 8.2). The channel recovery at a faster rate from inactivation is a gain of function that allows better supports high frequency activity. Conversely, tau of recovery at -80 mV was markedly slowed in p.V1442M mutant channels (Table 8.2). This translates into considerably fewer channels available at the resting membrane potential. Faster and slower recovery rates of p.R1463S and p.V1442M channels are consistent with attenuated and enhanced voltage dependence of fast inactivation of these variants, respectively.

8.2.5. *SCN4A* variants causing channel dysfunction are over-represented in the SIDS cohort compared to controls

To first test if rare variants (<1 in 20,000 incidence) are over-represented in the SIDS cohort compared to the ethnically matched control cohort, a Fisher's exact test was performed. Six rare variants were found in the SIDS cohort (2.2 %; 6/278), and nine in the control cohort (1.2 %; 9/729); however, this rate was not significantly higher in the SIDS cohort (p=0.21).

Out of the 278 individuals in the SIDS cohort of European descent six variants were studied functionally. Out of these, four were found to cause either loss or gain of function. In the control cohort (729 ethnically matched controls without history of cardiopulmonary defects), no variants introduced a functional change in the mutant $Na_V1.4$ channel.

Fisher's exact test comparing the incidence of dysfunctional variants in either cohort (4/278 variants in SIDS cohort vs. 0/729 variants in the control cohort) found that variants causing channel dysfunction are over-represented in the SIDS cohort (p=0.0057). In the control cohort the intronic splicing variant was predicted as not pathogenic according to the Human Splicing Tool (Desmet, 2009). Even if this is incorrectly predicted, *SCN4A* variants that introduce $Na_V1.4$ dysfunction are still over-represented (p=0.02, Fisher's exact test).

8.3. Discussion

This chapter is the first description implicating *SCN4A* variants in sudden infant death syndrome. In a SIDS cohort restricted to only individuals from European descent, the *SCN4A* variants that elicited a channel dysfunction were over-represented in the SIDS cohort compared to ethnically matched controls. The channel defects were mixed, with both gain- and loss of function effects, similar to those seen in infants who have required respiratory support. Our data suggest that pathogenic *SCN4A* variants constitute a risk factor for SIDS.

Triple risk hypothesis of risk suggests that SIDS is most likely to occur when three risk factors are combined. These include 1) a vulnerable infant, 2) a critical development period and 3) external stressors. Our data suggest that pathogenic *SCN4A* mutations define a vulnerable infant. I will also discuss the potential implications of our findings on defining a critical development period when the infant is most susceptible to compromised *SCN4A* function.

8.3.1. Summary of effects of *SCN4A* variants from the SIDS cohort on channel function

A total of ten novel or very rare (<1 in 20,000) *SCN4A* variants were identified in a cohort of 427 individuals who suffered sudden death during infancy. Out of these, six were of European descent, while four were of non-European or mixed ancestry. Eight missense variants were found in a control cohort of 729 individuals. All the variants were expressed in HEK293T cells and functionally characterized by patch clamp. Two variants, p.R1463S and p.S682W displayed a gain of function consistent with other sodium channel myotonia genotypes. The p.R1463S variant enhanced recovery from fast inactivation and right-shifted the voltage-dependence of fast inactivation. Both these effects constitute a gain of function effect by increasing channel availability for high frequency firing. Similar to other

cases in (potassium-aggravated) myotonia, the p.S682W variant slowed the decay of sodium currents (Kubota et al., 2009). Three variants had clear loss of function.

The variant p.V1442M had a marked (-6.6 mV) shift in the voltage-dependence of fast inactivation, while the current density of cells expressing variant p.E1520K was more than halved compared to cells expressing wild-type channels. The variant p.V1442M also had slowed recovery from inactivation. These loss of function effects recapitulate that of p.V1442E channels studied by Tsujino and colleagues, albeit less severely (Tsujino et al., 2003). In both cases, this is predicted to reduce the number of channels available at resting membrane potential and to result in further reduction upon high frequency activity. As shown by Tsujino (2003) and Habbout (2016) during high-frequency this is likely underlying muscle fatigability observed in the patient. The loss of function observed in p.V1442M is predicted attenuate the muscle action potential amplitude and consequently muscle tone.

8.3.2. $Na_V1.4$ loss of function as a risk factor in sudden infant death syndrome

The suggestion of this work that heterozygous channel variants that cause loss of function may constitute a risk factor for SIDS seems to be in slight contrast to the data presented in Chapters 5-7, which show that adults carrying a single loss of function allele (even if null) have no clinical manifestations. However, infants carrying a single partial loss of function variant might be more vulnerable to dysfunction of (respiratory) muscle (See 8.3.4).

Reports of loss of function mutations in $Na_V1.4$ with clinical consequences are rare and show recessive inheritance (Habbout et al., 2016; Arnold et al., 2015; Tsujino et al., 2003). In these cases, reduced channel availability caused muscle weakness and fatigability leading to apnea and respiratory difficulties. However, reduction in total sodium current amplitude caused by mutation in only a single *SCN4A* allele may have only subclinical

effects on muscle action potential size, such as those seen in heterozygous $Na_V1.4$ loss of function mice (Wu et al., 2016). This effect may have more severe consequences in infants as discussed in section 8.3.4. Other forms of myasthenia have been associated with infant deaths and apneas previously (Ohno et al., 2001).

Bi-allelic $Na_V1.4$ loss of function mutations display severe respiratory complications in infancy. The presence of only a heterozygous loss of function in the SIDS cohort is likely to have less severe effects on the muscle tone of muscles controlling respiration an infant and is consistent with the child being seemingly healthy and not having been diagnosed with skeletal muscle or respiratory issues previously.

If the functional channel defects in this chapter are compared to chapters 5-7, where a completely null allele has no clinical presentation in adults, it may be that variants p.E1520K and p.V1442M are not pathogenic in heterozygosis. This is not the case. I would instead argue that, in a subset of cases, a loss of function mutation may position an infant at a larger risk of an adverse respiratory event compared to an infant without dysfunctional $Na_V1.4$ when combined with a critical time in muscle development when $Na_V1.4$ expression in respiratory muscle is low. This conclusion is in agreement with the prevailing consensus on SIDS pathogenesis referred to as the triple-risk model (Kinney and Thach, 2009). In this model, an accumulation of risk factors converge on a potentially life-threatening cardiopulmonary event when (A) an external stressor occurs in (B) an infant who is vulnerable and (C) in a critical state of development.

8.3.3. Gain of function mutations in *SCN4A* and SIDS risk

Gain of function mutations in *SCN4A* have in rare cases been associated with life-threatening respiratory compromise in infants with myotonia (Caietta et al., 2013; Desaphy et al., 2013; Lion-François et al., 2010; Portaro et al., 2016).) In neonates gain of function mutations may cause life-threatening apnea and hypoxia. Two fatalities have been reported in individuals carrying variants p.N1297K or p.A799S (Gay et al., 2008; Lion-

François et al., 2010). The p.A799S mutation had a hyperpolarizing shift in the voltage-dependence of activation and thus increased open probability (Simkin et al., 2011), while p.N1297K was not characterized *in vitro.* The p.N1297K variant is however located in the intracellular loop between DIII and DIV, and may compromise fast inactivation of the channel. The most common myotonic variant with presentation of severe apnea and laryngospasm is p.G1306E. This residue is also located in the intracellular DIII-DIV loop. It has been described in myotonia with SNEL onset. This glycine-to-glutamic acid substitution attenuated the rate of fast inactivation, as well as the voltage-dependence of fast inactivation (Mitrović et al., 1995). When sodium channels fail to inactivate, the muscle fiber is further depolarized, triggering myotonic discharges. In muscle fibers excised from patients with potassium-aggravated myotonia, depolarization was found to be enhanced secondary to excess serum potassium, which led to sustained sodium current influx which in turn increases sodium channel activation, further depolarizing the membrane (Lehmann-Horn et al., 1987).

The gain of function effects in p.R1463S and p.S682W mutant channels are commensurate with those described previously in patients with myotonia. Slowed rate of open state inactivation has been shown to be the pathomechanism of several other *SCN4A* variants associated with myotonia. Thus the effects of p.S682W mutation are qualitatively similar to known myotonic mutations. In addition to showing clearly attenuated fast inactivation, p.R1463S variant displayed mild loss of function caused by reduced current density. The pathogenicity of p.R1463S is further validated by its presence in an unrelated adult with sodium-channel myotonia at the MRC Centre for Neuromuscular Diseases, Queen Square, London, United Kingdom.

It is unclear why the infant did not present with myotonia but was seemingly healthy. The age of onset of *SCN4A* myotonia can range from neonatal onset to a milder presentation in the second decade of life (Matthews et al., 2010). For some infants the respiratory complications seems to be the first presentation of myotonia. It is currently unclear why

some infants do present with myotonia while for others the presentations start later in life. It is also possible that the loss of function properties of p.R1463S variant may have potentially dampened the presentation of the attenuated fast inactivation.

8.3.4. Changes in skeletal muscle channel expression profile during development may define a critical period

The presentations of classical skeletal muscle channelopathies show two important changes during development. Many channelopathies manifest only later in life, with no symptoms in infancy. On the other hand, the presentations affecting respiratory muscle are only detected in infants and in adults the respiratory symptoms alleviate.

The respiratory system including the musculature goes through a host of changes while adapting to life outside of the uterus. Two factors that may be crucial for the presentation of $Na_V1.4$ dysfunction are (1) the changes in the pattern of ion channel expression on the whole—and of Na_V channel isoforms in particular; and (2) the proportion of different muscle fiber types contributing to rapid breathing during hypoxia.

It has been shown that myoblasts (Weiss and Horn, 1986) and myofibers of newborn rats express TTX resistant Na_V channels (Harris and Marshall, 1973). This isoform is likely to be $Na_V1.5$. Its expression in the skeletal muscle has been shown using molecular biology techniques. Very few studies delineating $Na_V1.4$ and $Na_V1.5$ expression in skeletal muscle during development are currently available. One study using a technique called multiplex fluorescent PCR (QMF-PCR) studied the expression levels of the fetal/cardiac isoform $Na_V1.5$ and the adult/skeletal isoform $Na_V1.4$ in human fetal, neonatal, young child, and adult muscle tissue (Zhou and Hoffmann, 1994). Previous studies were limited by the use of cultured rat myogenic cells, but still conclude that the levels of *SCN4A* mRNA expression increase with time from a fetal/neonatal age. Extrapolating such findings across species should be used with caution considering the difference in overall muscle

type proportion in mice and rats compared to humans. Rodents have a higher rate of breathing and thus use fast twitch fibers more than humans (Polla et al., 2004).

In both the diaphragm and skeletal muscle of fetuses, the *SCN4A* mRNA expression is twice that of *SCN5A* Zhou and Hoffmann (1994). During development, *SCN4A* expression increases from 30 % in neonates to approximately 40-45 % at age of 2-5 years (where 100 % is the adult level). Conversely a decrease in *SCN5A* mRNA expression was measured over time, from approximately 10 % (of total adult level) in neonates reduced to negligible levels at 5 years of age. In skeletal muscle, the mean *SCN4A* expression in fetal samples was approximately 20-25 % of total mRNA expression measured in adult skeletal muscle extracts, compared to *SCN5A* which was approximately 5 % (i.e. 4-5 fold lower than total *SCN4A* mRNA expression). This may explain why onset of myotonia or hypoPP often occurs later in life, as the fetal isoform may in the first years of age be protective. The Zhou and Hoffman data set from human samples is however limited. The progression of $Na_V1.4$ expression at 5 years to adulthood is unclear, but believed to reach adult levels at or shortly after 10 years of age.

In addition to changes in Na_V channel expression, expression level of ClC-1 has been shown to increase with age resulting in enhanced repolarizing chloride currents that may alter the presentation of *SCN4A* dysfunction (Furby et al., 2014; Pierno et al., 1999).

When the rate of breathing is increased (e.g. during hypoxia) use of fast twitch muscle is more prevalent than of slow twitch muscle fibers (Polla et al., 2004). At the endplate border of fast twitch fibers the sodium channel density is four-fold higher than slow fibers (49-181 mA/cm^2 vs. 10-41 mA/cm^2) (Ruff and Whittlesey, 1993). This suggests that high sodium channel expression level is essential for the function of fast twitch fibers critical to combatting a hypoxic event. A loss of sodium current amplitude may thus have a higher impact on the function of fast twitch fibers, compared to slow twitch fibers that control calm breathing in the diaphragm (Meznaric and Cvetko, 2016).

In summary, we found that changes in ion channel properties may increase the vulnerability of a child, suggesting that the critical development period may include a period when the excitability properties of the muscle are undergoing crucial developmental changes. Changes in channel expression profiles and in fiber type may help define such a period. Further studies will be required to confirm these hypotheses.

8.3.5. Genetic analysis and implications for global SIDS risk

To test the hypothesis that pathogenic *SCN4A* variants are over-represented in individuals who suffered from SIDS compared to individuals without SIDS we compared the frequency of novel or rare variants (<1 in 20,000 in the ExAC database) in a SIDS and control cohort. Six rare variants were found in the SIDS cohort (2.2 %, 6/278) compared to nine in the larger control cohort (1.2 %, 9/729), though this was not significantly different (p=0.21, Fisher's exact test). The incidence of rare variants in the SIDS Exome sequencing analysis of our SIDS cohort was restricted to individuals of European descent as the control cohort was of European ancestry. This is important to reduce variability within the cohort potentially caused by different gene profiles that may have compensatory mechanisms.

Since the prevalence of rare variants was not significant, we hypothesized that the nature of the variant, i.e. whether or not it introduces $Na_V1.4$ channel dysfunction was what determined whether a specific variant increased the risk of SIDS or not. In the European disease and control cohorts, a total of 14 variants were studied functionally. Channel dysfunction was identified 4 out of 278 variants (1.4%) in the SIDS cohort compared to none of 729 controls. Using the Fisher's exact test, it was found that pathogenic *SCN4A* variants had significantly higher frequency in the SIDS cohort (p=0.0057) compared to controls.

Our control cohort also contained an intronic variant at the splice site. However, using the Human Splicing Finder, the intron splice variant c.393-1C>T found in one of the

individuals in the control cohort was predicted to not be pathogenic. However, if this variants were to be dysfunctional, *SCN4A* variants that cause channel dysfunction are still overrepresented in the SIDS cohort compared to controls (p=0.022, Fisher's exact test).

8.3.6. $Na_V1.4$ dysfunction and triple risk hypothesis of SIDS

An interplay of a series of factors are required for SIDS to occur. This is referred to as the triple-risk hypothesis (Filiano and Kinney, 1994; Kinney and Thach, 2009), where three factors coincide: (I) a vulnerable infant, (II) an external stressor, and (III) a critical period of development. Our study found that *SCN4A* variants that cause $Na_V1.4$ channel dysfunction are present more frequently in the SIDS cohort compared to the control population and thus are associated with more vulnerable infants.

With respect to the triple-risk hypothesis, our data suggest that the impaired $Na_V1.4$ function increases the value of the first risk factor, in other words, makes the infant more vulnerable. If we add to the triple-risk model a reduced sodium current entering the muscle and tone of muscles controlling respiration, the response of an infant in a critical development period may be less capable of combatting an event caused by external stressor, leading to an increased risk of life-threatening hypoxia. Although single-nucleotide polymorphisms in *SCN4A* may not be clinically pathogenic in an adult *per se*, in a situation where the triple risks coincide, a dysfunctional $Na_V1.4$ may increase the risk of sudden infant death.

Our findings also suggests that mutations in other genes that control skeletal muscle function, although not associated with clinical presentation, may increase the risk of a child being vulnerable to external stressors during the critical development period.

These findings are in line with the previously characterized cardiac *SCN5A* variants in two SIDS cohorts, and the frequency of variants with *SCN5A* variants in another SIDS cohort (2/96, 2.1%) (Ackerman et al., 2001). These two mutations were not found in a control

cohort of 400 individuals. The SIDS cohort size of the Ackerman study is however considerably smaller than ours. In a Norwegian cohort with 201 SIDS cases, eight *SCN5A* variants that caused $Na_V1.5$ channel dysfunction were identified (Wang et al., 2007). The prevalence of pathogenic *SCN5A* variants in the control cohort was not assessed in that study.

SCN4A is one of the first genes reported to have a higher prevalence of variants altering protein function in the SIDS cohort. Investigating further SIDS cohorts is important to confirm this finding. It is difficult to estimate in how many SIDS cases are actually related to dysfunctional $Na_V1.4$.

8.3.7. Correlating the biophysical impact of amino acid-residue specific variants with sodium channel structure and function

The p.E1520K variant is located in the pore loop between S5-S6 in DIV and may disrupt selective permeation or channel stability, similar to other mutations reported in chapters 5-7 that affect the pore loop.

The p.V1442M variant (DIV S3-S4 linker) inactivates at more hyperpolarized voltages, thus reducing channel availability at physiological voltages. The recovery rate from slow inactivation was reduced. These findings are consistent with the changes induced by p.V1442E in Tsujino et al. (2003), and further with Armstrong's predictions that domain IV plays an integral role in rate-limiting the onset of fast inactivation (Armstrong, 2006).

The p.R1463S variant affects S4 arginine in DIV and consistently reduced in compromised fast inactivation of the channel. Similar to other mutations affecting the S4 arginines the current amplitude was reduced, probably reflecting the reduced stability of the VSD caused by the neutralization of S4 arginine. Gating pore currents were assessed as the mutation has potential to lead to leak current though the VSD. A preliminary observation in *Xenopus* oocytes suggested that guanidinium did not increase steady state current amplitude (Marisol Sampedro-Castaneda and R. Mannikko, personal

communication). This is consistent with observation that other S4 arginine mutations in DIV do not lead to gating pore current (Gosselin-Badaroudine et al., 2012; Habbout et al., 2016).

The p.S682W mutation affects a residue in the intracellular end of S4 of VSD-II. This mutation affected the slope of channel activation and rate of open state inactivation. The change in slope of activation may suggest compromised movement of the VSD. As it has been suggested that open state inactivation is coupled to channel opening, it is possible that the reduced rate of open state inactivation reflects reduced rate of channel opening, consistent with the finding of defects in channel activation properties.

8.3.8. Outlook on genetic counseling and prevention options

Approaching SIDS prevention is not unequivocal. One glimmer of hope after the bereavement of a child is the ensuing minutious post-mortem examination and multidisciplinary clinical meeting to discuss each case. These data may provide clues for how to treat or prevent a potentially life-threatening hypoxic event in future cases. These data may include genetic analysis, and in case of ion channels the functional properties can be analyzed to confirm potential pathogenicity of the variant. If a $Na_V1.4$ gain of function mutation is found a sodium channel blocker used to treat myotonia may be useful. In previous cases of SNEL where infants suffered from life-threatening laryngospasms, either mexiletine or carbamazepine were well tolerated and had good therapeutic response (Caietta et al., 2013). In other cases, mexiletine was not well tolerated, and flecainide was used successfully in infants (Portaro et al., 2016) as well as adults (Desaphy et al., 2013). Genetic screen of healthy neonates is currently not feasible and ethically questionable. However, offspring of know carriers of pathogenic *SCN4A* may be observed and studied for signals of myotonia. Also, it would be possible to, if an infant dies, that genetic screening of a sibling could indicate whether this infant could benefit from for instance mexiletine as a prophylactic treatment.

If however a loss of function mutation is identified, means to *increase* excitability may be a possible approach. Acetazolamide has been used successfully in one case of congenital myasthenic syndrome (Tsujino et al., 2003), but not in another (Habbout et al., 2016). Another indirect treatment option is to use salbutamol, a beta-2 adrenergic receptor agonist. Salbutamol acts as a bronchodilator by targeting receptors in smooth muscle and has been used effectively in congenital myasthenic syndrome caused by mutations in *DOK7* (Burke et al., 2013). In these patients, salbutamol progressively improved muscle strength and was well tolerated. Also, regular salbutamol helped endurance strength in the index case of Chapter 5 (Zaharieva et al., 2016). A limitation to this approach is that individuals in this study were not infants, but children aged 6-14. Equally, the index case in Chapter 5 is currently 15 years old. Salbutamol has previously been efficaciously administered to infants with acute wheezing (Tal et al., 1983).

It should be recognized that SIDS is a tremendously traumatic event that has severe psychological and sociological impacts on the family, relatives, and friends. To this end, every measure should be made to disambiguate SIDS etiology. The ethical implications of retaining infant tissue are difficult as the parents may be undergoing tremendous stress after the event. Genetic evidence, or even a diagnosis, can have a positive impact on a family's psychological health.

8.3.9. Limitations to the study

Family genetic data are missing for this study. This is due to full anonymization of the data. Analysis of segregation and potential *de novo* mutations could add weight to the argument that the *SCN4A* mutations underlie cases of SIDS.

The whole exomes of SIDS cases were sequenced and it is possible that variants in other genes are present, which may also predispose to sudden death. Nevertheless, *SCN4A* variants that result in $Na_V1.4$ channel dysfunction are accumulated in our SIDS cohort, thus constituting a potential risk factor for SIDS regardless of genetic background. Full

genetic findings of the whole exome sequencing are beyond the scope of this thesis and will be followed up later.

8.4. Summary

This is the first description of $Na_V1.4$ dysfunction in sudden infant death syndrome. The data presented herein describe an over-representation of *SCN4A* variants causing channel dysfunction in the SIDS cohort compared to the control cohort. Changes in channel function were qualitatively similar to those described in infants with SNEL. With respect to the triple-risk model of SIDS, an infant with a dysfunctional $Na_V1.4$ channel is more vulnerable to external stressors during a critical development period. Analysis of the functional consequences of variants was essential to discover this accumulation as the frequency of rare and novel *SCN4A* variants did not significantly differ between the cohorts. Further analysis of SIDS cohorts will clarify the role of *SCN4A* variants as risk factor and may help define strategies in preventing this devastating syndrome.

9. Outlook

In addition to the discussion on the individual chapters on particular projects, my thesis has general implications that I will briefly discuss. I will discuss the importance of functional characterization in identification of novel channelopathies; the pathomechanistic spectra of $Na_V1.4$ loss of function mutations – for most of which my thesis provides the first characterization; and finally briefly overview the potential presence of gating pore currents in homologous sodium channels.

9.1. Functional genetics of ion channels

Due to the increase in whole-exome and next-generation sequencing data, *SCN4A* variants are increasingly present in a diverse group of disorders. One such example is rhabdomyolysis. Rhabdomyolysis is characterized by skeletal muscle damage, leading to leakage of broken down muscle tissue into the circulation. The resultant myoglobin accumulation in the circulation may be toxic, resulting in confusion, vomiting, and muscle pain. In severe cases acute kidney failure may ensue, which is potentially lethal.

Recently, *SCN4A* variants have been identified in rhabdomyolysis patients by internal (MRC Centre for Neuromuscular Diseases) and external collaborators. Many of the mutations are novel; the patients do not carry mutations in other known rhabdomyolysis genes; many of the mutations are predicted pathogenic; and homologous mutations in other Na_V channels have been associated with disease for some variants. To date, one case has been published describing an *SCN4A* mutation (p.M1592V) associated with rhabdomyolysis in a young girl with fixed weakness, episodic worsening of weakness and rhabdomyolysis (Lee and Chahin, 2013), but no functional characterization of the channel variant was carried out. This mutation has previously been associated with myotonia. One of the variants found in the current rhabdomyolysis cohort has also been previously found

in a patient with myotonia. Mechanistically, is unclear how *SCN4A* variants would cause or contribute to rhabdomyolysis. In some cases *RYR1* variants have been found in addition to *SCN4A* variants, but it is unclear how one might affect the other.

With this, it is important to recognize that functional expression of ion channel variants is essential to establish novel disease associations and to delineate disease pathomechanisms. This is still actual and well demonstrated in the chapters 5-8. With the increasing load of genetic data arising with the expansion of exome sequencing and next-generation sequencing, the role of functionally confirming the pathogenicity of genetic variants identified in disease cohorts is ever more important to establish genotype-phenotype correlations.

9.2. $Na_V1.4$ loss of function variants raising their ugly head

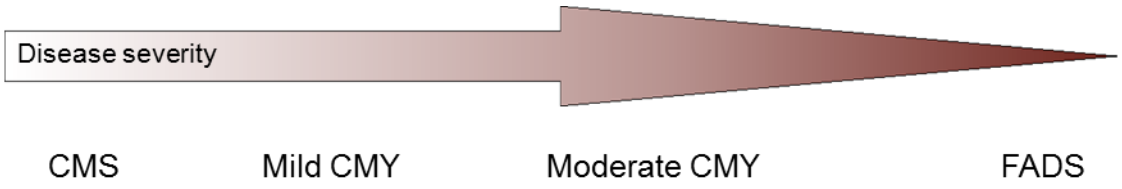

Figure 9.1. Increasing channel dysfunction severity correlates with increased clinical severity.
CMS: congenital myasthenic syndrome; CMY: congenital myopathy; FADS: fetal akinesia deformation sequence

I have characterized the function of several $Na_V1.4$ variants and demonstrated several novel mechanisms of pathophysiology and clinical associations. I have shown that neutralization of S4 arginine residues in domain I-III does not always result in hypoPP; revealed a novel pathophysiological mechanism of full loss of function in congenital myopathy and fetal akinesia – two phenotypes not previously associated with *SCN4A*; and

shown that *SCN4A* variants that cause sodium channel dysfunction are over-represented in a SIDS cohort.

Intriguingly, correlation between the severity of clinical presentation and of functional defects is emerging. The milder disorder congenital myasthenic syndrome is associated with bi-allelic enhanced fast inactivation; the mild congenital myopathy has a very mild loss of function combined with a full loss of function; the moderate-severe congenital myopathy has one moderate loss of function and one full loss of function mutation; and finally, fetal akinesia is associated with two complete or near-complete loss of function mutations (Figure 9.1). In biophysical terms there is a subtle difference between congenital myopathy described in Chapter 5 with FADS described in Chapter 6. Myopathy individuals always had a partial loss of function mutation on one of the alleles, e.g. in the form of reduced current density. In contrast, FADS individuals always had a full or near-full loss of function on both alleles. In other words, a partially functioning $Na_V1.4$ may be sufficient for life, but leads to myopathy, but if the extent of loss of function is sufficiently severe, FADS ensues.

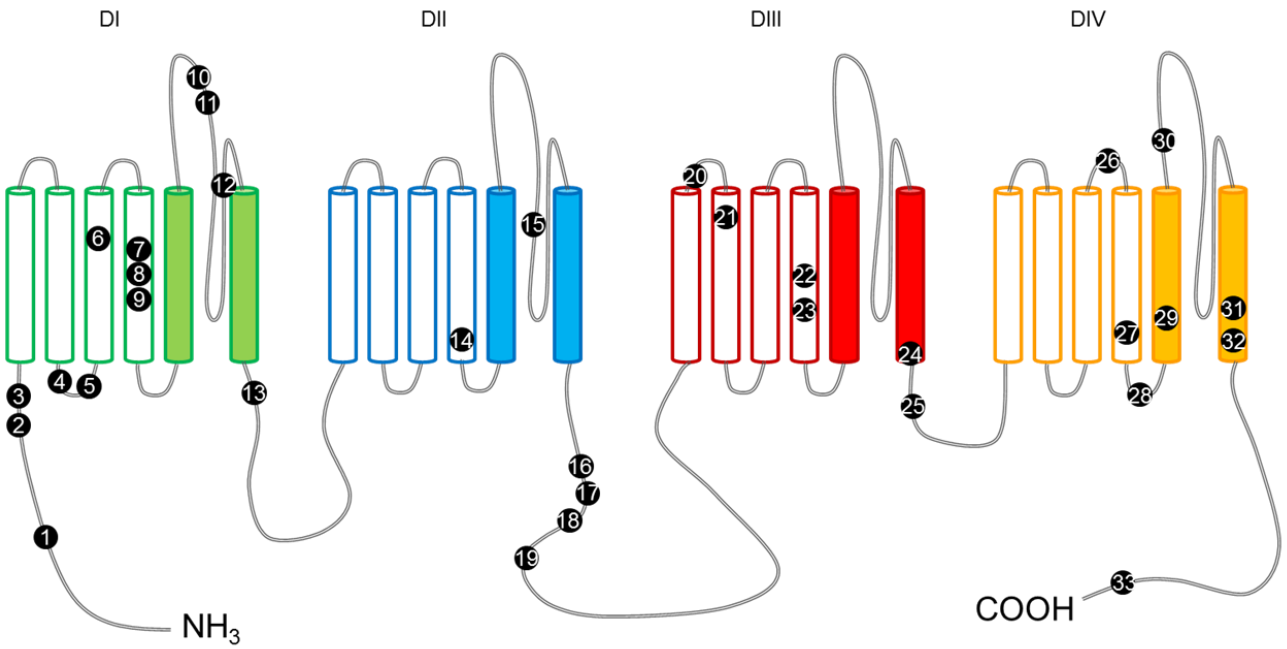

#	Mutation	Location	Effect
1	Q40X	NTD	Full LOF
2	c.274-2A>G	NTD	Full LOF
3	R104H	NTD	Full LOF
4	R179Q	S2-S3	WT-like
5	R190W	S2-S3	WT-like
6	M203K	S3	LOF; reduced current density
7a	R222G	R2 VSD-I	Igp
7b	R222Q	R2 VSD-I	Igp
7c	R222W	R2 VSD-I	Igp
8	R225W	R3 VSD-I	LOF; reduced current density
9	L227F	S4 VSD-I	WT-like
10	D334N	S5-S6 loop	WT-like
11	C375R	Pore loop DI	Full LOF
12	P382T	Pore loop DI	Full LOF
13	Q470X	DI-DII linker	Full LOF
14	S682W	S4 DII	Partial GOF
15	R756C	Pore loop DII	Full LOF
16	G859R	DII-DIII loop	WT-like
17	G863R	DII-DIII loop	WT-like
18	A870T	DII-DIII loop	WT-like
19	M897K	DII-DIII loop	WT-like
20	A1049VfsX50	S1-S2 DIII	Full LOF
21	D1069N	S2 DIII	LOF
22	R1135C	S4 DIII	LOF and Igp
23	C1209F	S4 DIII	Full LOF
24	I1291N	S6 DIII	Full/near-full LOF
25	K1304Ifs*17	DIII-DIV loop	Full LOF
26	V1442M	S3-S4 linker DIV	Partial LOF; enhanced inactivation slowed recovery
27	R1463S	S4 DIV	Partial LOF; enhanced recovery; slowed inactivation
28	S1478L	S4-S5 DIV	Full LOF
29	M1493V	S5 DIV	WT-like
30	E1520K	S5-S6 DIV	LOF; reduced current density
31	V1590I	S6 DIV	WT-like
32	Y1593X	S6 DIV	Full LOF
33	H1782Qfs65	CTD	Full LOF

Figure 9.2. Summary of *SCN4A* variants and their functional effects.

GOF: gain of function; LOF: Loss of function; CTD: C-terminal domain; NTD: n-terminal domain; WT-like: properties not significantly different from wild-type channels; S1-S6 denote segments 1-6; DI-DIV: domains I to IV; fs: frameshift; X: stop codon. For clarity residues R222G/Q/W are written as 7a-7c. VSD: voltage-sensing domain

9.2.1. Limitations to the studies of full loss of function mutations

As with any experiment, there are limitations to the conclusions drawn from chapters 5-7. The conclusion of loss of function is made based on the lack of currents measured despite expression in HEK293T cells. Immunocytochemistry analysis would show if mutant channels are retained in the endoplasmic reticulum, or whether channels are expressed at the membrane surface. For example, if a mutant channel is expressed at the membrane surface in a similar quantity as wild-type channels, it can be concluded that the lack of sodium current measured is due to a type of dysfunction in channel gating and/or conductance.

To control for $Na_V1.4$ protein expression we attempted immunocytochemistry but were struggling with diffuse background staining. Western blot was not performed, which is a limitation to the study. If a western blot were performed in conjunction with the HEK293 functional expression experiments it could be possible to see whether the protein is present in the transfected cells or not. If a protein band is observed, but no currents are recorded using patch clamp, this indicates that the protein is produced but it is non-functional or erroneously trafficked. Erroneous trafficking could for instance be the case of the N-terminal domain mutant p.R104H of Chapter 5, which is not seen to conduct any currents in patch clamp experiments. Further, if a channel were expressed at the membrane, but no main pore currents were measured, it could be possible to analyze instead the gating current. This may be possible, because the $Na_V1.4$ mutant channel is expressed at the membrane, bugt becomes problematic if a mutation causes defective voltage sensing domain movement, and the lack of gating current becomes a flawed readout of the experiment.

The conclusions in chapters 5-7 are instead based on the data at hand – the position of the mutation, and the effect measured in the heterologous expression system. Importantly, the findings correlate well and explain the clinical findings.

9.3. Implications for other channels and channelopathies

The idea that gating pore currents could be present in other diseases has been raised previously (Catterall, 2010). Several mutations in other channelopathies such as Dravet syndrome (*SCN1A, SCN8A*) and familial hemiplegic migraine (*CACNA1A*) affect S4 arginine residues; however, no gating pore current has yet been shown in these channels. Gating pore currents were not found in $Na_V1.2a$ when a single arginine was mutated (Sokolov et al., 2005). $Na_V1.2a$ required substitution of both R1 and R2 to Q of domain II (R850Q and R853Q) to observe a substantial gating pore current in the resting state (Sokolov et al., 2005).

Catterall (2010) and (Jurkat-Rott et al., 2012) have extensively reviewed the pathophysiological role of the gating pore current. Gating pore currents have been described in sodium channels $Na_V1.4$ and $Na_V1.5$. The first gating pore current was discovered in *Drosophila Shaker* potassium channels by substituting the first S4 arginine with a histidine (R1H), generating an inward hyperpolarization-activated proton current (Starace and Bezanilla, 2004). However, as suggested by the data in chapter 3, the nature of the substituting residue may also affect the presentation of gating pore currents with R222Q mutant channel showing several fold smaller gating pore currents than R222G mutant channels. It has been suggested that this process may be dependent on the nature of the adjacent residues. In *Shaker*, alanine residues at position “R0” are favorable. However, this is likely to be different across channel types and requires further investigation.

10. Conclusions

The aim of my project was to elucidate further detail into pathomechanisms of the classical $Na_V1.4$ channelopathies, and to assess the potential association and pathomechanisms of *SCN4A* variants detected in patients with conditions previously not associated with *SCN4A* mutations. This project combined molecular biology and electrophysiological techniques to study in detail the pathogenicity and mechanisms of mutations in *SCN4A*.

My data have helped elucidate the pathomechanisms of three different mutations affecting the same voltage sensing S4 arginine residue found in patients with either myotonia or hypoPP. The data is consistent with the prevailing understanding of the pathomechanisms of the classical $Na_V1.4$ channelopathies. In addition, my data on gating pore currents of these variants allowed identifying a novel blocker of gating pore currents and led to a detailed functional and molecular characterization of a novel toxin-channel interaction. Further analysis of gating modifier toxins may help characterize pharmacological hits that block gating pore currents and that may have clinical or research applications.

My PhD project also provided the first description of recessive $Na_V1.4$ loss of function mutations underlying fetal akinesia deformation sequence and congenital myopathy. These findings have important implications for genetic diagnostics of these conditions. Deciphering the pathomechanism of these conditions may open research avenues to find ways to correct the defect in channel function. In the absence of intervention, pre-implantation genetic diagnosis may be useful in families where recessive $Na_V1.4$ loss of function mutations underlie fetal akinesia deformation sequence.

My data provide evidence that *SCN4A* variants that cause subclinical alterations in channel function predispose infants to sudden death. These findings should be confirmed in a larger SIDS cohort to clarify the extent of *SCN4A* association with SIDS to allow a discussion to make genetic screening and interventions a possibility.

11. References

Ackerman, M.J., Siu, B.L., Sturner, W.Q., Tester, D.J., Valdivia, C.R., Makielski, J.C., and Towbin, J. a (2001). Postmortem molecular analysis of SCN5A defects in sudden infant death syndrome. JAMA *286*, 2264–2269.

Ahuja, S., Mukund, S., Deng, L., Khakh, K., Chang, E., Ho, H., Shriver, S., Young, C., Lin, S., Johnson, J.P., et al. (2015). Structural basis of Nav1.7 inhibition by an isoform-selective small-molecule antagonist. Science (80-.). *350*.

Albuquerque, E.X., Pereira, E.F.R., Alkondon, M., and Rogers, S.W. (2009). Mammalian nicotinic acetylcholine receptors: from structure to function. Physiol. Rev. *89*, 73–120.

Alexander, S.P.H., Benson, H.E., Faccenda, E., Pawson, A.J., Sharman, J.L., Catterall, W.A., Spedding, M., Peters, J.A., and Harmar, A.J. (2013). The Concise Guide to PHARMACOLOGY 2013/14: ion channels. Br. J. Pharmacol. *170*, 1607–1651.

Amenta, F., and Tayebati, S. (2008). Pathways of Acetylcholine Synthesis, Transport and Release as Targets for Treatment of Adult-Onset Cognitive Dysfunction. Curr. Med. Chem. *15*, 488–498.

Armstrong, C.M. (2006). Na channel inactivation from open and closed states. Proc. Natl. Acad. Sci. U. S. A. *103*, 17991–17996.

Arnold, W.D., Feldman, D.H., Ramirez, S., He, L., Kassar, D., Quick, A., Klassen, T.L., Lara, M., Nguyen, J., Kissel, J.T., et al. (2015). Defective fast inactivation recovery of Nav1.4 in congenital myasthenic syndrome. Ann. Neurol. *77*, 840–850.

Ashcroft, F.M. (2006). From molecule to malady. Nature *440*, 440–447.

Backx, P.H., Yue, D.T., Lawrence, J.H., Marban, E., and Tomaselli, G.F. (1992). Molecular localization of an ion-binding site within the pore of mammalian sodium channels. Science *257*, 248–251.

Ben-Johny, M., Yang, P.S., Niu, J., Yang, W., Joshi-Mukherjee, R., and Yue, D.T. (2014). Conservation of Ca2+/calmodulin regulation across Na and Ca2+ channels. Cell *157*, 1657–1670.

Bendahhou, S., Cummins, T.R., Griggs, R.C., Fu, Y.H., and Ptáek, L.J. (2001). Sodium channel inactivation defects are associated with acetazolamide-exacerbated hypokalemic periodic paralysis. Ann. Neurol. *50*, 417–420.

Berkut, A. a, Peigneur, S., Myshkin, M.Y., Paramonov, A.S., Lyukmanova, E.N., Arseniev, A.S., Grishin, E. V, Tytgat, J., Shenkarev, Z.O., and Vassilevski, A. a (2014). Structure of Membrane-Active Toxin from Crab Spider Heriaeus melloteei Suggests Parallel Evolution of Sodium Channel Gating Modifiers in Araneomorphae and Mygalomorphae. J. Biol. Chem. 0–26.

Bevilacqua, J.A., Bitoun, M., Biancalana, V., Oldfors, A., Stoltenburg, G., Claeys, K.G., Lacène, E., Brochier, G., Manéré, L., Laforêt, P., et al. (2009). “Necklace” fibers, a new histological marker of late-onset MTM1- related centronuclear myopathy. Acta Neuropathol. *117*, 283–291.

Bezzina, C.R., Rook, M.B., Groenewegen, W.A., Herfst, L.J., Van der Wal, A.C., Lam, J., Jongsma, H.J., Wilde, A. a M., and Mannens, M.M. a M. (2003). Compound heterozygosity for mutations (W156X and R225W) in SCN5A associated with severe cardiac conduction disturbances and degenerative changes in the conduction system. Circ. Res. *92*, 159–168.

Black, J.A., Frézel, N., Dib-Hajj, S.D., and Waxman, S.G. (2012). Expression of Nav1.7 in DRG Neurons Extends from Peripheral Terminals in the Skin to Central Preterminal Branches and Terminals in the Dorsal Horn. Mol. Pain *8*, 1744-8069-8–82.

Böhm, S.K., Grady, E.F., and Bunnett, N.W. (1997). Regulatory mechanisms that modulate signalling by G-protein-coupled receptors. Biochem. J. *322 (Pt 1)*, 1–18.

Boiko, T., Rasband, M.N., Levinson, S.R., Caldwell, J.H., Mandel, G., Trimmer, J.S., and Matthews, G. (2001). Compact myelin dictates the differential targeting of two sodium channel isoforms in the same axon. Neuron *30*, 91–104.

Boiko, T., Van Wart, A., Caldwell, J.H., Levinson, S.R., Trimmer, J.S., and Matthews, G. (2003). Functional specialization of the axon initial segment by isoform-specific sodium channel targeting. J. Neurosci. *23*, 2306–2313.

Bolz, F., Kasper, S., Bufe, B., Zufall, F., and Pyrski, M. (2017). Organization and Plasticity of Sodium Channel Expression in the Mouse Olfactory and Vomeronasal Epithelia. Front. Neuroanat. *11*, 28.

Bouzat, C., Bren, N., and Sine, S.M. (1994). Structural basis of the different gating kinetics of fetal and adult acetylcholine receptors. Neuron *13*, 1395–1402.

Brackenbury, W.J., and Isom, L.L. (2011). Na Channel β Subunits: Overachievers of the Ion Channel Family. Front. Pharmacol. *2*, 53.

Brackenbury, W.J., Davis, T.H., Chen, C., Slat, E.A., Detrow, M.J., Dickendesher, T.L., Ranscht, B., and Isom, L.L. (2008). Voltage-Gated Na+ Channel 1 Subunit-Mediated Neurite Outgrowth Requires Fyn Kinase and Contributes to Postnatal CNS Development In Vivo. J. Neurosci. *28*, 3246–3256.

Brackenbury, W.J., Calhoun, J.D., Chen, C., Miyazaki, H., Nukina, N., Oyama, F., Ranscht, B., and Isom, L.L. (2010). Functional reciprocity between Na+ channel Nav1.6 and 1 subunits in the coordinated regulation of excitability and neurite outgrowth. Proc. Natl. Acad. Sci. *107*, 2283–2288.

Brackenbury, W.J., Yuan, Y., O'Malley, H.A., Parent, J.M., and Isom, L.L. (2013). Abnormal neuronal patterning occurs during early postnatal brain development of Scn1b-null mice and precedes hyperexcitability. Proc. Natl. Acad. Sci. *110*, 1089–1094.

Brose, N., Petrenko, A.G., Südhof, T.C., and Jahn, R. (1992). Synaptotagmin: a calcium sensor on the synaptic vesicle surface. Science *256*, 1021–1025.

Brugnoni, R., Galantini, S., Confalonieri, P., Balestrini, M.R., Cornelio, F., and Mantegazza, R. (1999). Identification of three novel mutations in the major human skeletal muscle chloride channel gene (CLCN1), causing myotonia congenita. Hum. Mutat. *14*, 447.

Bryant, S.H., and Morales-Aguilera, A. (1971). Chloride conductance in normal and myotonic muscle fibres and the action of monocarboxylic aromatic acids. *219*, 367–383.

Bugiardini, E., Rivolta, I., Binda, A., Soriano Caminero, A., Cirillo, F., Cinti, A., Giovannoni, R., Botta, A., Cardani, R., Wicklund, M.P., et al. (2015). SCN4A mutation as modifying

factor of Myotonic Dystrophy Type 2 phenotype. Neuromuscul. Disord. *25*, 301–307.

Burke, G., Hiscock, A., Klein, A., Niks, E.H., Main, M., Manzur, A.Y., Ng, J., de Vile, C., Muntoni, F., Beeson, D., et al. (2013). Salbutamol benefits children with congenital myasthenic syndrome due to DOK7 mutations. Neuromuscul. Disord. *23*, 170–175.

Caietta, E., Milh, M., Sternberg, D., Lépine, A., Boulay, C., McGonigal, A., and Chabrol, B. (2013). Diagnosis and outcome of SCN4A-related severe neonatal episodic laryngospasm (SNEL): 2 new cases. Pediatrics *132*, e784-7.

Calhoun, J.D., and Isom, L.L. (2014). The Role of Non-pore-Forming β Subunits in Physiology and Pathophysiology of Voltage-Gated Sodium Channels. In Handbook of Experimental Pharmacology, pp. 51–89.

Cannon, S.C. (2000). Spectrum of sodium channel disturbances in the nondystrophic myotonias and periodic paralyses. Kidney Int. *57*, 772–779.

Cannon, S.C. (2010). Voltage-sensor mutations in channelopathies of skeletal muscle. J. Physiol. *588*, 1887–1895.

Cannon, S.C. (2015). Channelpathies of skeletal muscle excitability. Compr. Physiol. *5*, 761–790.

Capes, D.L., Goldschen-Ohm, M.P., Arcisio-Miranda, M., Bezanilla, F., and Chanda, B. (2013). Domain IV voltage-sensor movement is both sufficient and rate limiting for fast inactivation in sodium channels. J. Gen. Physiol. *142*, 101–112.

Cartaud, A., Strochlic, L., Guerra, M., Blanchard, B., Lambergeon, M., Krejci, E., Cartaud, J., and Legay, C. (2004). MuSK is required for anchoring acetylcholinesterase at the neuromuscular junction. J. Cell Biol. *165*, 505–515.

Catterall, W. a (2000). From ionic currents to molecular mechanisms: the structure and function of voltage-gated sodium channels. Neuron *26*, 13–25.

Catterall, W. a (2010). Ion channel voltage sensors: structure, function, and pathophysiology. Neuron *67*, 915–928.

Catterall, W.A. (1986). Voltage-dependent gating of sodium channels: correlating structure and function. Trends Neurosci. *9*, 7–10.

Catterall, W.A. (2014). Structure and function of voltage-gated sodium channels at atomic resolution. Exp. Physiol. *99*, 35–51.

Catterall, W.A., Goldin, A.L., and Waxman, S.G. (2005). International Union of Pharmacology. XLVII. Nomenclature and structure-function relationships of voltage-gated sodium channels. Pharmacol. Rev. *57*, 397–409.

Catterall, W.A., Cest??le, S., Yarov-Yarovoy, V., Yu, F.H., Konoki, K., and Scheuer, T. (2007). Voltage-gated ion channels and gating modifier toxins. Toxicon *49*, 124–141.

Chahine, M., Bennett, P.B., George, A.L., and Horn, R. (1994). Functional expression and properties of the human skeletal muscle sodium channel. Pflugers Arch - Eur J Physiol *427*, 136–142.

Chakrapani, S., Cuello, L.G., Cortes, D.M., and Perozo, E. (2008). Structural Dynamics of an Isolated Voltage-Sensor Domain in a Lipid Bilayer. Structure *16*, 398–409.

Cheah, C.S., Yu, F.H., Westenbroek, R.E., Kalume, F.K., Oakley, J.C., Potter, G.B.,

Rubenstein, J.L., and Catterall, W.A. (2012). Specific deletion of NaV1.1 sodium channels in inhibitory interneurons causes seizures and premature death in a mouse model of Dravet syndrome. Proc. Natl. Acad. Sci. *109*, 14646–14651.

Chen, C., Bharucha, V., Chen, Y., Westenbroek, R.E., Brown, A., Malhotra, J.D., Jones, D., Avery, C., Gillespie, P.J., Kazen-Gillespie, K.A., et al. (2002). Reduced sodium channel density, altered voltage dependence of inactivation, and increased susceptibility to seizures in mice lacking sodium channel 2-subunits. Proc. Natl. Acad. Sci. *99*, 17072–17077.

Chen, C., Calhoun, J.D., Zhang, Y., Lopez-Santiago, L., Zhou, N., Davis, T.H., Salzer, J.L., and Isom, L.L. (2012). Identification of the cysteine residue responsible for disulfide linkage of Na+ channel α and β2 subunits. J. Biol. Chem. *287*, 39061–39069.

Clatot, J., Ziyadeh-Isleem, A., Maugenre, S., Denjoy, I., Liu, H., Dilanian, G., Hatem, S.N., Deschênes, I., Coulombe, A., Guicheney, P., et al. (2012). Dominant-negative effect of SCN5A N-terminal mutations through the interaction of Nav1.5 α-subunits. Cardiovasc. Res. *96*, 53–63.

Colding-Jørgensen, E. (2005). Phenotypic variability in myotonia congenita. Muscle and Nerve *32*, 19–34.

Corrochano, S., Männikkö, R., Joyce, P.I., McGoldrick, P., Wettstein, J., Lassi, G., Raja Rayan, D.L., Blanco, G., Quinn, C., Liavas, A., et al. (2014). Novel mutations in human and mouse SCN4A implicate AMPK in myotonia and periodic paralysis. Brain *137*, 3171–3185.

Cox, J.J., Reimann, F., Nicholas, A.K., Thornton, G., Roberts, E., Springell, K., Karbani, G., Jafri, H., Mannan, J., Raashid, Y., et al. (2006). An SCN9A channelopathy causes congenital inability to experience pain. Nature *444*, 894–898.

Cummins, T.R., Sheets, P.L., and Waxman, S.G. (2007). The roles of sodium channels in nociception: Implications for mechanisms of pain. Pain *131*, 243–257.

Davies, N.P., Imbrici, P., Fialho, D., Herd, C., Bilsland, L.G., Weber, A., Mueller, R., Hilton-Jones, D., Ealing, J., Boothman, B.R., et al. (2005). Andersen-Tawil syndrome: new potassium channel mutations and possible phenotypic variation. Neurology *65*, 1083–1089.

Desaphy, J.F., Modoni, A., Lomonaco, M., and Camerino, D.C. (2013). Dramatic improvement of myotonia permanens with flecainide: A two-case report of a possible bench-to-bedside pharmacogenetics strategy. Eur. J. Clin. Pharmacol. *69*, 1037–1039.

Desaphy, J.F., Carbonara, R., D'Amico, A., Modoni, A., Roussel, J., Imbrici, P., Pagliarani, S., Lucchiari, S., Monaco, M. Lo, and Camerino, D.C. (2016). Translational approach to address therapy in myotonia permanens due to a new SCN4A mutation. Neurology *86*, 2100–2108.

Desmet, F.O., Hamroun, D., Lalande, M., Collod-Bëroud, G., Claustres, M., and Béroud, C. (2009). Human Splicing Finder: An online bioinformatics tool to predict splicing signals. Nucleic Acids Res. *37*, 1–14.

Djouhri, L., Newton, R., Levinson, S.R., Berry, C.M., Carruthers, B., and Lawson, S.N. (2003). Sensory and electrophysiological properties of guinea-pig sensory neurones expressing Nav1.7 (PN1) Na+channel α subunit protein. J. Physiol. *546*, 565–576.

Doyle, D.A., Morais Cabral, J., Pfuetzner, R.A., Kuo, A., Gulbis, J.M., Cohen, S.L., Chait,

B.T., and MacKinnon, R. (1998). The structure of the potassium channel: molecular basis of K+ conduction and selectivity. Science *280*, 69–77.

Duflocq, A., Le Bras, B., Bullier, E., Couraud, F., and Davenne, M. (2008). Nav1.1 is predominantly expressed in nodes of Ranvier and axon initial segments. Mol. Cell. Neurosci. *39*, 180–192.

Dumbacher, J.P., Spande, T.F., and Daly, J.W. (2000). Batrachotoxin alkaloids from passerine birds: a second toxic bird genus (Ifrita kowaldi) from New Guinea. Proc. Natl. Acad. Sci. U. S. A. *97*, 12970–12975.

Eguchi, H., Tsujino, A., Kaibara, M., Hayashi, H., Shirabe, S., Taniyama, K., and Eguchi, K. (2006). Acetazolamide acts directly on the human skeletal muscle chloride channel. Muscle Nerve *34*, 292–297.

Ehmsen, J., Poon, E., and Davies, K. (2002). The dystrophin- complex The Dystrophin-Associated Protein Complex. J. Cell Sci. *2002*, 2801–2803.

El-Bizri, N., Kahlig, K.M., Shyrock, J.C., George, A.L., Belardinelli, L., and Rajamani, S. (2011). Ranolazine block of human Na v 1.4 sodium channels and paramyotonia congenita mutants. Channels (Austin). *5*, 161–172.

Engel, A.G., Ohno, K., and Sine, S.M. (2003). Congenital myasthenic syndromes: A diverse array of molecular targets. J. Neurocytol. *32*, 1017–1037.

Fan, C., Lehmann-Horn, F., Weber, M.-A., Bednarz, M., Groome, J.R., Jonsson, M.K.B., and Jurkat-Rott, K. (2013). Transient compartment-like syndrome and normokalaemic periodic paralysis due to a Cav1.1 mutation. Brain *136*, 3775–3786.

Filatov, G.N., Nguyen, T.P., Kraner, S.D., and Barchi, R.L. (1998). Inactivation and Secondary Structure in the D4/S4-5 Region of the SkM1 Sodium Channel. J. Gen. Physiol. *111*, 703–715.

Filiano, J.J., and Kinney, H.C. (1994). A perspective on neuropathologic findings in victims of the sudden infant death syndrome: the triple-risk model. Biol. Neonate *65*, 194–197.

Fleming, P.J., Blair, P.S., Sidebotham, P., and Hayler, T. (2004). Clinical review. Br. Med. J. *328*, 331–334.

Flucher, B.E., and Tuluc, P. (2017). How and why are calcium currents curtailed in the skeletal muscle voltage-gated calcium channels? J. Physiol. *595*, 1451–1463.

Francis, D.G., Rybalchenko, V., Struyk, A., and Cannon, S.C. (2011a). Leaky sodium channels from voltage sensor mutations in periodic paralysis, but not paramyotonia. Neurology *76*, 1635–1641.

Francis, D.G., Rybalchenko, V., Struyk, A., and Cannon, S.C. (2011b). Leaky sodium channels from voltage sensor mutations in periodic paralysis, but not paramyotonia. Neurology *76*, 1635–1641.

Fredj, S., Sampson, K.J., Liu, H., and Kass, R.S. (2009). Molecular basis of ranolazine block of LQT-3 mutant sodium channels: evidence for site of action. Br. J. Pharmacol. *148*, 16–24.

Furby, A., Vicart, S., Camdessanché, J.P., Fournier, E., Chabrier, S., Lagrue, E., Paricio, C., Blondy, P., Touraine, R., Sternberg, D., et al. (2014). Heterozygous CLCN1 mutations can modulate phenotype in sodium channel myotonia. Neuromuscul. Disord. *24*, 953–959.

Gamal El-Din, T.M., Martinez, G.Q., Payandeh, J., Scheuer, T., and Catterall, W.A. (2013). A gating charge interaction required for late slow inactivation of the bacterial sodium channel NavAb. J. Gen. Physiol. *142*, 181–190.

Gautron, L., Sakata, I., Udit, S., Zigman, J.M., Wood, J.N., and Elmquist, J.K. (2011). Genetic tracing of Nav1.8-expressing vagal afferents in the mouse. J. Comp. Neurol. *519*, 3085–3101.

Gay, S., Dupuis, D., Faivre, L., Masurel-Paulet, A., Labenne, M., Colombani, M., Soichot, P., Huet, F., Hainque, B., Sternberg, D., et al. (2008). Severe neonatal non-dystrophic myotonia secondary to a novel mutation of the voltage-gated sodium channel (SCN4A) gene. Am. J. Med. Genet. A *146A*, 380–383.

Geukes Foppen, R.J., van Mil, H.G.J., and van Heukelom, J.S. (2002). Effects of chloride transport on bistable behaviour of the membrane potential in mouse skeletal muscle. J. Physiol. *542*, 181–191.

Gilchrist, J., Das, S., Van Petegem, F., and Bosmans, F. (2013). Crystallographic insights into sodium-channel modulation by the 4 subunit. Proc. Natl. Acad. Sci. *110*, E5016–E5024.

Goldin, A.L. (2003). Mechanisms of sodium channel inactivation. Curr. Opin. Neurobiol. *13*, 284–290.

Goldin, A.L., Barchi, R.L., Caldwell, J.H., Hofmann, F., Howe, J.R., Hunter, J.C., Kallen, R.G., Mandel, G., Meisler, M.H., Netter, Y.B., et al. (2000). Nomenclature of Voltage-Gated Sodium Channels. Neuron *28*, 365–368.

Gong, B., Rhodes, K.J., Bekele-Arcuri, Z., and Trimmer, J.S. (1999). Type I and type II Na(+) channel alpha-subunit polypeptides exhibit distinct spatial and temporal patterning, and association with auxiliary subunits in rat brain. J. Comp. Neurol. *412*, 342–352.

Gonorazky, H.D., Marshall, C.R., Al-Murshed, M., Hazrati, L.-N., Thor, M.G., Hanna, M.G., Männikkö, R., Ray, P.N., and Yoon, G. (2017). Congenital myopathy with “corona” fibres, selective muscle atrophy, and craniosynostosis associated with novel recessive mutations in SCN4A. Neuromuscul. Disord. *27*, 574–580.

Gosselin-badaroudine, P., Delemotte, L., Moreau, A., Klein, M.L., and Chahine, M. (2012). Gating pore currents and the resting state of Na v 1 . 4 voltage sensor domains. Proc. Natl. Acad. Sci. U. S. A. *109*, 19250–19255.

Gosselin-Badaroudine, P., Delemotte, L., Moreau, A., Klein, M.L., and Chahine, M. (2012). Gating pore currents and the resting state of Nav1.4 voltage sensor domains. Proc. Natl. Acad. Sci. U. S. A. *109*, 1–6.

Groome, J.R., and Winston, V. (2013). S1-S3 counter charges in the voltage sensor module of a mammalian sodium channel regulate fast inactivation. J. Gen. Physiol. *141*, 601–618.

Groome, J.R., Lehmann-Horn, F., Fan, C., Wolf, M., Winston, V., Merlini, L., and Jurkat-Rott, K. (2014). NaV1.4 mutations cause hypokalaemic periodic paralysis by disrupting IIIS4 movement during recovery. Brain *137*, 998–1008.

Habbout, K., Poulin, H., Rivier, F., Giuliano, S., Sternberg, D., Fontaine, B., Eymard, B., Morales, R.J., Echenne, B., King, L., et al. (2016). A recessive Nav1.4 mutation underlies congenital myasthenic syndrome with periodic paralysis. Neurology *86*, 161–169.

Hakeem, G.F., Oddy, L., Holcroft, C. a., and Abenhaim, H. a. (2015). Incidence and

determinants of sudden infant death syndrome: a population-based study on 37 million births. World J. Pediatr. *11*, 41–47.

Harper, A.A., and Lawson, S.N. (1985). Electrical properties of rat dorsal root ganglion neurones with different peripheral nerve conduction velocities. J. Physiol. *359*, 47–63.

Harris, J.B., and Marshall, M.W. (1973). Tetrodotoxin-resistant action potentials in newborn rat muscle. Nat. New Biol. *243*, 191–192.

Hayward, L.J., Brown, R.H., and Cannon, S.C. (1997). Slow inactivation differs among mutant Na channels associated with myotonia and periodic paralysis. Biophys. J. *72*, 1204–1219.

Hayward, L.J., Sandoval, G.M., and Cannon, S.C. (1999). Defective slow inactivation of sodium channels contributes to familial periodic paralysis. Neurology *52*, 1447–1447.

Heinemann, S.H., Terlau, H., Stühmer, W., Imoto, K., and Numa, S. (1992). Calcium channel characteristics conferred on the sodium channel by single mutations. Nature *356*, 441–443.

Herzog, R.I., Liu, C., Waxman, S.G., and Cummins, T.R. (2003). Calmodulin binds to the C terminus of sodium channels Nav1.4 and Nav1.6 and differentially modulates their functional properties. J. Neurosci. *23*, 8261–8270.

Hille, B. (1975). BRIEF COMMUNICATIONS THE RECEPTOR FOR TETRODOTOXIN AND SAXITOXIN A STRUCTURAL HYPOTHESIS. Biophys J *15*, 615–619.

Horga, A., Rayan, D.L.R., Matthews, E., Sud, R., Fialho, D., Durran, S.C.M., Burge, J. a., Portaro, S., Davis, M.B., Haworth, A., et al. (2013). Prevalence study of genetically defined skeletal muscle channelopathies in England. Neurology *80*, 1472–1475.

Hsu, E.J., Zhu, W., Schubert, A.R., Voelker, T., Varga, Z., and Silva, J.R. (2017). Regulation of Na(+) channel inactivation by the DIII and DIV voltage-sensing domains. J. Gen. Physiol. *149*, 389–403.

Islas, A. a, Sánchez-Solano, A., Scior, T., Millan-PerezPeña, L., and Salinas-Stefanon, E.M. (2013). Identification of Navβ1 residues involved in the modulation of the sodium channel Nav1.4. PLoS One *8*, e81995.

Isom, L.L., and Catterall, W.A. (1996). Na+channel subunits and Ig domains. Nature *383*, 307–308.

Isom, L.L., De Jongh, K.S., Patton, D.E., Reber, B.F., Offord, J., Charbonneau, H., Walsh, K., Goldin, A.L., and Catterall, W.A. (1992). Primary structure and functional expression of the beta 1 subunit of the rat brain sodium channel. Science *256*, 839–842.

Isom, L.L., Ragsdale, D.S., De Jongh, K.S., Westenbroek, R.E., Reber, B.F.X., Scheuer, T., and Catterall, W.A. (1995). Structure and function of the β2 subunit of brain sodium channels, a transmembrane glycoprotein with a CAM motif. Cell *83*, 433–442.

Jurkat-Rott, K., and Lehmann-Horn, F. (2006). Paroxysmal muscle weakness - The familial periodic paralyses. J. Neurol. *253*, 1391–1398.

Jurkat-Rott, K., Mitrovic, N., Hang, C., Kouzmenkine, A., Iaizzo, P., Herzog, J., Lerche, H., Nicole, S., Vale-Santos, J., Chauveau, D., et al. (2000). Voltage-sensor sodium channel mutations cause hypokalemic periodic paralysis type 2 by enhanced inactivation and reduced current. Proc. Natl. Acad. Sci. *97*, 9549–9554.

Jurkat-Rott, K., Groome, J., and Lehmann-Horn, F. (2012). Pathophysiological role of omega pore current in channelopathies. Front. Pharmacol. *3*, 112.

Kallen, R.G., Sheng, Z.H., Yang, J., Chen, L.Q., Rogart, R.B., and Barchi, R.L. (1990). Primary structure and expression of a sodium channel characteristic of denervated and immature rat skeletal muscle. Neuron *4*, 233–242.

Kato, H., Kokunai, Y., Dalle, C., Kubota, T., Madokoro, Y., Yuasa, H., Uchida, Y., Ikeda, T., Mochizuki, H., Nicole, S., et al. (2016). A case of non-dystrophic myotonia with concomitant mutations in the SCN4A and CLCN1 genes. J. Neurol. Sci. *369*, 254–258.

Kaufmann, S.G., Westenbroek, R.E., Maass, A.H., Lange, V., Renner, A., Wischmeyer, E., Bonz, A., Muck, J., Ertl, G., Catterall, W.A., et al. (2013). Distribution and function of sodium channel subtypes in human atrial myocardium. J. Mol. Cell. Cardiol. *61*, 133–141.

Kawakami, Y., Ito, M., Hirayama, M., Sahashi, K., Ohkawara, B., Masuda, A., Nishida, H., Mabuchi, N., Engel, A.G., and Ohno, K. (2011). Anti-MuSK autoantibodies block binding of collagen Q to MuSK. Neurology *77*, 1819–1826.

Kazarinova-Noyes, K., Malhotra, J.D., McEwen, D.P., Mattei, L.N., Berglund, E.O., Ranscht, B., Levinson, S.R., Schachner, M., Shrager, P., Isom, L.L., et al. (2001). Contactin associates with Na+ channels and increases their functional expression. J. Neurosci. *21*, 7517–7525.

Kinney, H.C., and Thach, B.T. (2009). The sudden infant death syndrome. N. Engl. J. Med. *361*, 795–805.

Kubota, T., Kinoshita, M., Sasaki, R., Aoike, F., Takahashi, M.P., Sakoda, S., and Hirose, K. (2009). New mutation of the Na channel in the severe form of potassium-aggravated myotonia. Muscle and Nerve *39*, 666–673.

Kuo, C.C., and Bean, B.P. (1994). Na+ channels must deactivate to recover from inactivation. Neuron *12*, 819–829.

Lacroix, J.J., Campos, F. V, Frezza, L., and Bezanilla, F. (2013). Molecular bases for the asynchronous activation of sodium and potassium channels required for nerve impulse generation. Neuron *79*, 651–657.

Larsson, H.P., Baker, O.S., Dhillon, D.S., and Isacoff, E.Y. (1996). Transmembrane movement of the shaker K+ channel S4. Neuron *16*, 387–397.

Lee-Kwon, W., Goo, J.H., Zhang, Z., Silldorff, E.P., and Pallone, T.L. (2007). Vasa recta voltage-gated Na+ channel Nav1.3 is regulated by calmodulin. Am J Physiol Ren. Physiol *292*, F404-14.

Lee, E., and Chahin, N. (2013). A patient with mutation in the SCN4A p.M1592v presenting with fixed weakness, rhabdomyolysis, and episodic worsening of weakness. Muscle Nerve *48*, 306–307.

Lee, A., Fakler, B., Kaczmarek, L.K., and Isom, L.L. (2014). More Than a Pore: Ion Channel Signaling Complexes. J. Neurosci. *34*, 15159–15169.

Lee, S.-C., Kim, H.-S., Park, Y.-E., Choi, Y.-C., Park, K.-H., and Kim, D.-S. (2009). Clinical Diversity of SCN4A-Mutation-Associated Skeletal Muscle Sodium Channelopathy. J. Clin. Neurol. *5*, 186–191.

Lehman, W., Hatch, V., Korman, V., Rosol, M., Thomas, L., Maytum, R., Geeves, M.A., Van Eyk, J.E., Tobacman, L.S., and Craig, R. (2000). Tropomyosin and actin isoforms

modulate the localization of tropomyosin strands on actin filaments. J. Mol. Biol. *302*, 593–606.

Lehmann-Horn, F., Kuther, G., Ricker, K., Grafe, P., Ballanyi, K., and Rudel, R. (1987). ADYNAMIA EPlSODlCA HEREDITARIA SODIUM CURRENT AND THE EFFECT OF EXTRACELLULAR pH WITH MYOTONIA: A NON-INACTIVATING. Muscle Nerve 10–363.

Leiter, J.C., and Böhm, I. (2007). Mechanisms of pathogenesis in the Sudden Infant Death Syndrome. Respir. Physiol. Neurobiol. *159*, 127–138.

Lerche, H., Heine, R., Pika, U., George, A.L., Mitrovic, N., Browatzki, M., Weiss, T., Rivet-Bastide, M., Franke, C., and Lomonaco, M. (1993). Human sodium channel myotonia: slowed channel inactivation due to substitutions for a glycine within the III-IV linker. J. Physiol. *470*, 13–22.

Leterrier, C. (2018). The axon initial segment: an updated viewpoint. J. Neurosci. 1922–17.

Li, C., Ullrich, B., Zhang, J.Z., Anderson, R.G.W., Brose, N., and Südhof, T.C. (1995). Ca2+-dependent and -independent activities of neural and non-neural synaptotagmins. Nature *375*, 594–599.

Linford, N.J., Cantrell, A.R., Qu, Y., Scheuer, T., and Catterall, W.A. (1998). Interaction of batrachotoxin with the local anesthetic receptor site in transmembrane segment IVS6 of the voltage-gated sodium channel. Proc. Natl. Acad. Sci. *95*, 13947–13952.

Lion-François, L., Mignot, C., Vicart, S., Manel, V., Sternberg, D., Landrieu, P., Lesca, G., Broussolle, E., Billette De Villemeur, T., Napuri, S., et al. (2010). Severe neonatal episodic laryngospasm due to de novo SCN4A mutations: A new treatable disorder. Neurology *75*, 641–645.

Liu, C.J., Dib-Hajj, S.D., Black, J.A., Greenwood, J., Lian, Z., and Waxman, S.G. (2001). Direct Interaction with Contactin Targets Voltage-gated Sodium Channel Nav1.9/NaN to the Cell Membrane. J. Biol. Chem. *276*, 46553–46561.

Malhotra, J.D., Koopmann, M.C., Kazen-Gillespie, K.A., Fettman, N., Hortsch, M., and Isom, L.L. (2002). Structural Requirements for Interaction of Sodium Channel β1 Subunits with Ankyrin. J. Biol. Chem. *277*, 26681–26688.

Mankodi, A., Grunseich, C., Skov, M., Cook, L., Aue, G., Purev, E., Bakar, D., Lehky, T., Jurkat-Rott, K., Pedersen, T.H., et al. (2015). Divalent cation-responsive myotonia and muscle paralysis in skeletal muscle sodium channelopathy. Neuromuscul. Disord. *25*, 908–912.

Mann, S. a., Castro, M.L., Ohanian, M., Guo, G., Zodgekar, P., Sheu, A., Stockhammer, K., Thompson, T., Playford, D., Subbiah, R., et al. (2012). R222Q SCN5A mutation is associated with reversible ventricular ectopy and dilated cardiomyopathy. J. Am. Coll. Cardiol. *60*, 1566–1573.

Männikkö, R., Elinder, F., and Larsson, H.P. (2002). Voltage-sensing mechanism is conserved among ion channels gated by opposite voltages. Nature *419*, 837–841.

Mantegazza, M., Yu, F.H., Catterall, W. a, and Scheuer, T. (2001). Role of the C-terminal domain in inactivation of brain and cardiac sodium channels. Proc. Natl. Acad. Sci. U. S. A. *98*, 15348–15353.

Mantegazza, M., Gambardella, A., Rusconi, R., Schiavon, E., Annesi, F., Cassulini, R.R.,

Labate, A., Carrideo, S., Chifari, R., Canevini, M.P., et al. (2005). Identification of an Nav1.1 sodium channel (SCN1A) loss-of-function mutation associated with familial simple febrile seizures. Proc. Natl. Acad. Sci. U. S. A. *102*, 18177–18182.

Matthews, E., Tan, S. V, Fialho, D., Sweeney, M.G., Sud, R., Haworth, a, Stanley, E., Cea, G., Davis, M.B., and Hanna, M.G. (2008). What causes paramyotonia in the United Kingdom? Common and new SCN4A mutations revealed. Neurology *70*, 50–53.

Matthews, E., Labrum, R., Sweeney, M.G., Sud, R., Haworth, A., Chinnery, P.F., Meola, G., Schorge, S., Kullmann, D.M., Davis, M.B., et al. (2009). Voltage sensor charge loss accounts for most cases of hypokalemic periodic paralysis. Neurology *72*, 1544–1547.

Matthews, E., Fialho, D., Tan, S. V., Venance, S.L., Cannon, S.C., Sternberg, D., Fontaine, B., Amato, a. a., Barohn, R.J., Griggs, R.C., et al. (2010). The non-dystrophic myotonias: Molecular pathogenesis, diagnosis and treatment. Brain *133*, 9–22.

Matthews, E., Manzur, A.Y., Sud, R., Muntoni, F., and Hanna, M.G. (2011a). Stridor as a neonatal presentation of skeletal muscle sodium channelopathy. Arch. Neurol. *68*, 127–129.

Matthews, E., Portaro, S., Ke, Q., Sud, R., Haworth, A., Davis, M.B., Griggs, R.C., and Hanna, M.G. (2011b). Acetazolamide efficacy in hypokalemic periodic paralysis and the predictive role of genotype. Neurology *77*, 1960–1964.

McArdle, B. (1962). ADYNAMIA EPISODICA HEREDITARIA AND ITS TREATMENT. Brain *85*, 121–148.

McClatchey, a I., Cannon, S.C., Slaugenhaupt, S. a, and Gusella, J.F. (1993). The cloning and expression of a sodium channel beta 1-subunit cDNA from human brain. Hum. Mol. Genet. *2*, 745–749.

McClatchey, A.I., Van den Bergh, P., Pericak-Vance, M.A., Raskind, W., Verellen, C., McKenna-Yasek, D., Rao, K., Haines, J.L., Bird, T., and Brown, R.H. (1992). Temperature-sensitive mutations in the III-IV cytoplasmic loop region of the skeletal muscle sodium channel gene in paramyotonia congenita. Cell *68*, 769–774.

McCusker, E.C., Bagnéris, C., Naylor, C.E., Cole, A.R., D'Avanzo, N., Nichols, C.G., and Wallace, B.A. (2012). Structure of a bacterial voltage-gated sodium channel pore reveals mechanisms of opening and closing. Nat. Commun. *3*, 1102.

McEwen, D.P., Meadows, L.S., Chen, C., Thyagarajan, V., and Isom, L.L. (2004). Sodium Channel β1 Subunit-mediated Modulation of $Na_v1.2$ Currents and Cell Surface Density Is Dependent on Interactions with Contactin and Ankyrin. J. Biol. Chem. *279*, 16044–16049.

McKillop, D.F., and Geeves, M.A. (1993). Regulation of the interaction between actin and myosin subfragment 1: evidence for three states of the thin filament. Biophys. J. *65*, 693–701.

Meznaric, M., and Cvetko, E. (2016). Size and Proportions of Slow-Twitch and Fast-Twitch Muscle Fibers in Human Costal Diaphragm. Biomed Res. Int. *2016*, 1–6.

van Mil, H.G., Geukes Foppen, R.J., and Siegenbeek van Heukelom, J. (1997). The influence of bumetanide on the membrane potential of mouse skeletal muscle cells in isotonic and hypertonic media. Br. J. Pharmacol. *120*, 39–44.

Minett, M.S., Nassar, M.A., Clark, A.K., Passmore, G., Dickenson, A.H., Wang, F., Malcangio, M., and Wood, J.N. (2012). Distinct Nav1.7-dependent pain sensations require different sets of sensory and sympathetic neurons. Nat. Commun. *3*, 791.

Mitrovic, N., George, a L., and Horn, R. (2000). Role of domain 4 in sodium channel slow inactivation. J. Gen. Physiol. *115*, 707–718.

Mitrović, N., George, a L., Lerche, H., Wagner, S., Fahlke, C., and Lehmann-Horn, F. (1995). Different effects on gating of three myotonia-causing mutations in the inactivation gate of the human muscle sodium channel. J. Physiol. *487 (Pt 1*, 107–114.

Moon, R.Y., Horne, R.S.C., and Hauck, F.R. (2007). Sudden infant death syndrome. Lancet *370*, 1578–1587.

Moreau, a., Gosselin-Badaroudine, P., Delemotte, L., Klein, M.L., and Chahine, M. (2015). Gating pore currents are defects in common with two Nav1.5 mutations in patients with mixed arrhythmias and dilated cardiomyopathy. J. Gen. Physiol. *145*, 93–106.

Moreau, A., Gosselin-Badaroudine, P., and Chahine, M. (2014). Biophysics, pathophysiology, and pharmacology of ion channel gating pores. Front. Pharmacol. *5*, 53.

Namadurai, S., Balasuriya, D., Rajappa, R., Wiemhöfer, M., Stott, K., Klingauf, J., Edwardson, J.M., Chirgadze, D.Y., and Jackson, A.P. (2014). Crystal Structure and Molecular Imaging of the Na v Channel β3 Subunit Indicates a Trimeric Assembly. J. Biol. Chem. *289*, 10797–10811.

Namadurai, S., Yereddi, N.R., Cusdin, F.S., Huang, C.L., Chirgadze, D.Y., Jackson, A.P., and Jackson, A.P. (2015). A new look at sodium channel b subunits.

Narahashi, T. (1974). Chemicals as tools in the study of excitable membranes. Physiol. Rev. *54*, 813–889.

Noda, M., Suzuki, H., Numa, S., and Stühmer, W. (1989). A single point mutation confers tetrodotoxin and saxitoxin insensitivity on the sodium channel II. FEBS Lett. *259*, 213–216.

North, K.N., Wang, C.H., Clarke, N., Jungbluth, H., Vainzof, M., Dowling, J.J., Amburgey, K., Quijano-Roy, S., Beggs, A.H., Sewry, C., et al. (2014). Approach to the diagnosis of congenital myopathies. Neuromuscul. Disord. *24*, 97–116.

O'Malley, H. a., and Isom, L.L. (2015). Sodium Channel β Subunits: Emerging Targets in Channelopathies. Annu. Rev. Physiol. *77*, 481–504.

Ogiwara, I., Iwasato, T., Miyamoto, H., Iwata, R., Yamagata, T., Mazaki, E., Yanagawa, Y., Tamamaki, N., Hensch, T.K., Itohara, S., et al. (2013). Nav1.1 haploinsufficiency in excitatory neurons ameliorates seizure-associated sudden death in a mouse model of Dravet syndrome. Hum. Mol. Genet. *22*, 4784–4804.

Ogiwara, I., Miyamoto, H., Tatsukawa, T., Yamagata, T., Nakayama, T., Atapour, N., Miura, E., Mazaki, E., Ernst, S.J., Cao, D., et al. (2018). Nav1.2 haplodeficiency in excitatory neurons causes absence-like seizures in mice. Commun. Biol. *1*, 96.

Ohno, K., Tsujino, A., Brengman, J.M., Harper, C.M., Bajzer, Z., Udd, B., Beyring, R., Robb, S., Kirkham, F.J., and Engel, A.G. (2001). Choline acetyltransferase mutations cause myasthenic syndrome associated with episodic apnea in humans. Proc. Natl. Acad. Sci. U. S. A. *98*, 2017–2022.

Papadatos, G.A., Wallerstein, P.M.R., Head, C.E.G., Ratcliff, R., Brady, P.A., Benndorf, K., Saumarez, R.C., Trezise, A.E.O., Huang, C.L.-H., Vandenberg, J.I., et al. (2002). Slowed conduction and ventricular tachycardia after targeted disruption of the cardiac sodium channel gene Scn5a. Proc. Natl. Acad. Sci. *99*, 6210–6215.

Patino, G., and Isom, L. (2010). Electrophysiology and beyond: Multiple roles of Na+ channel β subunits in development and disease. Neurosci. Lett. *486*, 53–59.

Payandeh, J., and Minor, D.L. (2015). Bacterial Voltage-Gated Sodium Channels (BacNaVs) from the Soil, Sea, and Salt Lakes Enlighten Molecular Mechanisms of Electrical Signaling and Pharmacology in the Brain and Heart. J. Mol. Biol. *427*, 3–30.

Payandeh, J., Scheuer, T., Zheng, N., and Catterall, W.A. (2011a). The crystal structure of a voltage-gated sodium channel. Nature *475*, 353–358.

Payandeh, J., Scheuer, T., Zheng, N., and Catterall, W. a (2011b). The crystal structure of a voltage-gated sodium channel. Nature *475*, 353–358.

Payne, C.E., Brown, A.R., Theile, J.W., Loucif, A.J.C., Alexandrou, A.J., Fuller, M.D., Mahoney, J.H., Antonio, B.M., Gerlach, A.C., Printzenhoff, D.M., et al. (2015). A novel selective and orally bioavailable Na_v 1.8 channel blocker, PF-01247324, attenuates nociception and sensory neuron excitability. Br. J. Pharmacol. *172*, 2654–2670.

Van Petegem, F., Lobo, P. a., and Ahern, C. a. (2012). Seeing the forest through the trees: Towards a unified view on physiological calcium regulation of voltage-gated sodium channels. Biophys. J. *103*, 2243–2251.

Pierno, S., De Luca, A., Beck, C.L., George, A.L., and Conte Camerino, D. (1999). Aging-associated down-regulation of ClC-1 expression in skeletal muscle: phenotypic-independent relation to the decrease of chloride conductance. FEBS Lett. *449*, 12–16.

Plaster, N.M., Tawil, R., Tristani-Firouzi, M., Canún, S., Bendahhou, S., Tsunoda, A., Donaldson, M.R., Iannaccone, S.T., Brunt, E., Barohn, R., et al. (2001). Mutations in Kir2.1 cause the developmental and episodic electrical phenotypes of Andersen's syndrome. Cell *105*, 511–519.

Polla, B., D'Antona, G., Bottinelli, R., and Reggiani, C. (2004). Respiratory muscle fibres: specialisation and plasticity. Thorax *59*, 808–817.

Portaro, S., Rodolico, C., Sinicropi, S., Musumeci, O., Valenzise, M., and Toscano, A. (2016). Flecainide-Responsive Myotonia Permanens With SNEL Onset: A New Case and Literature Review. Pediatrics *137*, e20153289–e20153289.

Priest, B.T., Murphy, B.A., Lindia, J.A., Diaz, C., Abbadie, C., Ritter, A.M., Liberator, P., Iyer, L.M., Kash, S.F., Kohler, M.G., et al. (2005). Contribution of the tetrodotoxin-resistant voltage-gated sodium channel NaV1.9 to sensory transmission and nociceptive behavior. Proc. Natl. Acad. Sci. *102*, 9382–9387.

Ptácek, L.J., George, a L., Griggs, R.C., Tawil, R., Kallen, R.G., Barchi, R.L., Robertson, M., and Leppert, M.F. (1991). Identification of a mutation in the gene causing hyperkalemic periodic paralysis. Cell *67*, 1021–1027.

Ptácek, L.J., George, a L., Barchi, R.L., Griggs, R.C., Riggs, J.E., Robertson, M., and Leppert, M.F. (1992). Mutations in an S4 segment of the adult skeletal muscle sodium channel cause paramyotonia congenita. Neuron *8*, 891–897.

Ptáček, L.J. (2015). Episodic disorders: channelopathies and beyond. Annu. Rev. Physiol. *77*, 475–479.

Pusch, M. (2002). Myotonia caused by mutations in the muscle chloride channel gene CLCN1. Hum. Mutat. *19*, 423–434.

Qu, Y., Rogers, J., Tanada, T., Scheuer, T., and Catterall, W.A. (1995). Molecular

determinants of drug access to the receptor site for antiarrhythmic drugs in the cardiac Na+ channel. Proc. Natl. Acad. Sci. U. S. A. *92*, 11839–11843.

Ragsdale, D.S., McPhee, J.C., Scheuer, T., and Catterall, W. a (1994). Molecular determinants of state-dependent block of Na+ channels by local anesthetics. Science *265*, 1724–1728.

Ragsdale, D.S., McPhee, J.C., Scheuer, T., and Catterall, W.A. (1996). Common molecular determinants of local anesthetic, antiarrhythmic, and anticonvulsant block of voltage-gated Na+ channels. Proc. Natl. Acad. Sci. U. S. A. *93*, 9270–9275.

Ramachandra, R., McGrew, S.Y., Baxter, J.C., Howard, J.R., and Elmslie, K.S. (2013). NaV1.8 channels are expressed in large, as well as small, diameter sensory afferent neurons. Channels *7*, 1–4.

Ravenscroft, G., Laing, N.G., and Bonnemann, C.G. (2014). Pathophysiological concepts in the congenital myopathies: blurring the boundaries, sharpening the focus. Brain *138*, 246–268.

Renganathan, M., Gelderblom, M., Black, J.A., and Waxman, S.G. (2003). Expression of Nav1.8 sodium channels perturbs the firing patterns of cerebellar purkinje cells. Brain Res. *959*, 235–242.

Revell Phillips, L., Milescu, M., Li-Smerin, Y., Mindell, J.A., Kim, J. Il, and Swartz, K.J. (2005). Voltage-sensor activation with a tarantula toxin as cargo. Nature *436*, 857–860.

Rook, M.B., Evers, M.M., Vos, M.A., and Bierhuizen, M.F.A. (2012). Biology of cardiac sodium channel Nav1.5 expression. Cardiovasc. Res. *93*, 12–23.

Ruff, R.L., and Whittlesey, D. (1993). Na+ currents near and away from endplates on human fast and slow twitch muscle fibers. Muscle Nerve *16*, 922–929.

Rusconi, R., Scalmani, P., Cassulini, R.R., Giunti, G., Gambardella, A., Franceschetti, S., Annesi, G., Wanke, E., and Mantegazza, M. (2007). Modulatory proteins can rescue a trafficking defective epileptogenic Nav1.1 Na+ channel mutant. J. Neurosci. *27*, 11037–11046.

Saleh, S., Yeung, S.Y.M., Prestwich, S., Pucovský, V., and Greenwood, I. (2005). Electrophysiological and molecular identification of voltage-gated sodium channels in murine vascular myocytes. J. Physiol. *568*, 155–169.

Sansone, V.A., Burge, J., McDermott, M.P., Smith, P.C., Herr, B., Tawil, R., Pandya, S., Kissel, J., Ciafaloni, E., Shieh, P., et al. (2016). Randomized, placebo-controlled trials of dichlorphenamide in periodic paralysis. Neurology *86*, 1408–1416.

Satin, J., Kyle, J.W., Chen, M., Bell, P., Cribbs, L.L., Fozzard, H. a, and Rogart, R.B. (1992). A mutant of TTX-resistant cardiac sodium channels with TTX-sensitive properties. Science *256*, 1202–1205.

Schantz, E.J. (1986). Chemistry and Biology of Saxitoxin and Related Toxins. Ann. N. Y. Acad. Sci. *479*, 15–23.

Schultz, J., Hoffmuüller, U., Krause, G., Ashurst, J., Macias, M.J., Schmieder, P., Schneider-Mergener, J., and Oschkinat, H. (1998). Specific interactions between the syntrophin PDZ domain and voltage-gated sodium channels. Nat. Struct. Biol. *5*, 19–24.

Seoh, S.A., Sigg, D., Papazian, D.M., and Bezanilla, F. (1996). Voltage-sensing residues in the S2 and S4 segments of the Shaker K+ channel. Neuron *16*, 1159–1167.

Sharkey, L.M., Cheng, X., Drews, V., Buchner, D. a, Jones, J.M., Justice, M.J., Waxman, S.G., Dib-Hajj, S.D., and Meisler, M.H. (2009). The ataxia3 mutation in the N-terminal cytoplasmic domain of sodium channel Na(v)1.6 disrupts intracellular trafficking. J. Neurosci. *29*, 2733–2741.

Shen, H., Zhou, Q., Pan, X., Li, Z., Wu, J., and Yan, N. (2017). Structure of a eukaryotic voltage-gated sodium channel at near-atomic resolution. Science (80-.). *355*, eaal4326.

Shields, S.D., Butt, R.P., Dib-Hajj, S.D., and Waxman, S.G. (2015). Oral administration of PF-01247324, a subtype-selective Nav1.8 blocker, reverses cerebellar deficits in a mouse model of multiple sclerosis. PLoS One *10*, e0119067.

Simkin, D., and Bendahhou, S. (2011). Skeletal muscle Na+ channel disorders. Front. Pharmacol. *OCT*.

Simkin, D., Léna, I., Landrieu, P., Lion-François, L., Sternberg, D., Fontaine, B., and Bendahhou, S. (2011). Mechanisms underlying a life-threatening skeletal muscle Na^+ channel disorder. J. Physiol. *589*, 3115–3124.

Singh, R.R., Tan, S.V., Hanna, M.G., Robb, S.A., Clarke, A., and Jungbluth, H. (2014). Mutations in SCN4A: a rare but treatable cause of recurrent life-threatening laryngospasm. Pediatrics *134*, e1447-50.

Smith, P.L., Baukrowitz, T., and Yellen, G. (1996). The inward rectification mechanism of the HERG cardiac potassium channel. Nature *379*, 833–836.

Sokolov, S., Scheuer, T., and Catterall, W. a. (2005). Ion permeation through a voltage-sensitive gating pore in brain sodium channels having voltage sensor mutations. Neuron *47*, 183–189.

Sokolov, S., Scheuer, T., and Catterall, W.A. (2007). Gating pore current in an inherited ion channelopathy. Nature *446*, 76–78.

Sokolov, S., Scheuer, T., and Catterall, W. a (2008). Depolarization-activated gating pore current conducted by mutant sodium channels in potassium-sensitive normokalemic periodic paralysis. Proc. Natl. Acad. Sci. U. S. A. *105*, 19980–19985.

Sokolov, S., Scheuer, T., and Catterall, W.A. (2010). Ion permeation and block of the gating pore in the voltage sensor of NaV1.4 channels with hypokalemic periodic paralysis mutations. J. Gen. Physiol. *136*, 225–236.

Squire, J.M., and Morris, E.P. (1998). A new look at thin filament regulation in vertebrate skeletal muscle. FASEB J. *12*, 761–771.

Starace, D.M., and Bezanilla, F. (2001). Histidine scanning mutagenesis of basic residues of the S4 segment of the shaker k+ channel. J. Gen. Physiol. *117*, 469–490.

Starace, D.M., and Bezanilla, F. (2004). A proton pore in a potassium channel voltage sensor reveals a focused electric field. Nature *427*, 548–553.

Statland, J.M., Bundy, B.N., Wang, Y., Rayan, D.R., Trivedi, J.R., Sansone, V. a, Salajegheh, M.K., Venance, S.L., Ciafaloni, E., Matthews, E., et al. (2012). Mexiletine for symptoms and signs of myotonia in nondystrophic myotonia: a randomized controlled trial. JAMA *308*, 1357–1365.

Struyk, A.F., and Cannon, S.C. (2007a). A Na^+ Channel Mutation Linked to Hypokalemic Periodic Paralysis Exposes a Proton-selective Gating Pore. J. Gen. Physiol. *130*, 11–20.

Struyk, A.F., and Cannon, S.C. (2007b). A Na+ channel mutation linked to hypokalemic periodic paralysis exposes a proton-selective gating pore. J. Gen. Physiol. *130*, 11–20.

Struyk, A.F., and Cannon, S.C. (2008). Paradoxical depolarization of BA2+- treated muscle exposed to low extracellular K+: Insights into resting potential abnormalities in hypokalemic paralysis. Muscle Nerve *37*, 326–337.

Struyk, a F., Scoggan, K. a, Bulman, D.E., and Cannon, S.C. (2000). The human skeletal muscle Na channel mutation R669H associated with hypokalemic periodic paralysis enhances slow inactivation. J. Neurosci. *20*, 8610–8617.

Struyk, A.F., Markin, V.S., Francis, D., and Cannon, S.C. (2008). Gating pore currents in DIIS4 mutations of NaV1.4 associated with periodic paralysis: saturation of ion flux and implications for disease pathogenesis. J. Gen. Physiol. *132*, 447–464.

Stühmer, W., Conti, F., Suzuki, H., Wang, X.D., Noda, M., Yahagi, N., Kubo, H., and Numa, S. (1989). Structural parts involved in activation and inactivation of the sodium channel. Nature *339*, 597–603.

Südhof, T.C. (2013). A molecular machine for neurotransmitter release: synaptotagmin and beyond. Nat. Med. *19*, 1227–1231.

Südhof, T.C., and Rizo, J. (2011). Synaptic vesicle exocytosis. Cold Spring Harb. Perspect. Biol. *3*, 1–14.

Suetterlin, K., Männikkö, R., and Hanna, M.G. (2014). Muscle channelopathies: recent advances in genetics, pathophysiology and therapy. Curr. Opin. Neurol. *27*, 583–590.

Suetterlin, K.J., Bugiardini, E., Kaski, J.P., Morrow, J.M., Matthews, E., Hanna, M.G., and Fialho, D. (2015). Long-term Safety and Efficacy of Mexiletine for Patients With Skeletal Muscle Channelopathies. JAMA Neurol. *72*, 1531.

Tal, A., Bavilski, C., Yohai, D., Bearman, J.E., Gorodischer, R., and Moses, S.W. (1983). Dexamethasone and salbutamol in the treatment of acute wheezing in infants. Pediatrics *71*, 13–18.

Tammaro, P., Conti, F., and Moran, O. (2002). Modulation of sodium current in mammalian cells by an epilepsy-correlated beta 1-subunit mutation. Biochem. Biophys. Res. Commun. *291*, 1095–1101.

Tawil, R., Ptacek, L.J., Pavlakis, S.G., DeVivo, D.C., Penn, a S., Ozdemir, C., and Griggs, R.C. (1994). Andersen's syndrome: potassium-sensitive periodic paralysis, ventricular ectopy, and dysmorphic features. Ann. Neurol. *35*, 326–330.

Teramoto, N., Zhu, H.L., Yotsu-Yamashita, M., Inai, T., and Cunnane, T.C. (2012). Resurgent-like currents in mouse vas deferens myocytes are mediated by NaV1.6 voltage-gated sodium channels. Pflugers Arch. Eur. J. Physiol. *464*, 493–502.

Terlau, H., Heinemann, S.H., Stühmer, W., Pusch, M., Conti, F., Imoto, K., and Numa, S. (1991). Mapping the site of block by tetrodotoxin and saxitoxin of sodium channel II. FEBS Lett. *293*, 93–96.

Tombola, F., Pathak, M.M., and Isacoff, E.Y. (2005). Voltage-Sensing Arginines in a Potassium Channel Permeate and Occlude Cation-Selective Pores. Neuron *45*, 379–388.

Tricarico, D., Barbieri, M., and Camerino, D.C. (2000). Acetazolamide opens the muscular KCa2+ channel: a novel mechanism of action that may explain the therapeutic effect of the drug in hypokalemic periodic paralysis. Ann. Neurol. *48*, 304–312.

Trimmer, J.S., and Rhodes, K.J. (2004). Localization of voltage-gated ion channels in mammalian brain. Annu. Rev. Physiol. *66*, 477–519.

Tristani-Firouzi, M., Jensen, J.L., Donaldson, M.R., Sansone, V., Meola, G., Hahn, A., Bendahhou, S., Kwiecinski, H., Fidzianska, A., Plaster, N., et al. (2002). Functional and clinical characterization of KCNJ2 mutations associated with LQT7 (Andersen syndrome). J. Clin. Invest. *110*, 381–388.

Trivedi, J.R., Cannon, S.C., and Griggs, R.C. (2014). Nondystrophic myotonia: challenges and future directions. Exp. Neurol. *253*, 28–30.

Tsujino, A., Maertens, C., Ohno, K., Shen, X.-M., Fukuda, T., Harper, C.M., Cannon, S.C., and Engel, A.G. (2003). Myasthenic syndrome caused by mutation of the SCN4A sodium channel. Proc. Natl. Acad. Sci. U. S. A. *100*, 7377–7382.

Ulbricht, W. (1998). Effects of veratridine on sodium currents and fluxes. Rev. Physiol. Biochem. Pharmacol. *133*, 1–54.

Ursu, S.-F., Alekov, A., Mao, N.-H., and Jurkat-Rott, K. (2012). ClC1 chloride channel in myotonic dystrophy type 2 and ClC1 splicing in vitro. Acta Myol. Myopathies Cardiomyopathies Off. J. Mediterr. Soc. Myol. *31*, 144–153.

Vassilev, P., Scheuer, T., and Catterall, W. a (1989). Inhibition of inactivation of single sodium channels by a site-directed antibody. Proc. Natl. Acad. Sci. U. S. A. *86*, 8147–8151.

Vassilev, P.M., Scheuer, T., and Catterall, W. a (1988). Identification of an intracellular peptide segment involved in sodium channel inactivation. Science *241*, 1658–1661.

Vogt, J., Morgan, N. V, Rehal, P., Faivre, L., Brueton, L. a, Becker, K., Fryns, J.-P., Holder, S., Islam, L., Kivuva, E., et al. (2012). CHRNG genotype-phenotype correlations in the multiple pterygium syndromes. J. Med. Genet. *49*, 21–26.

Wallace, R.H., Wang, D.W., Singh, R., Scheffer, I.E., George, a L., Phillips, H. a, Saar, K., Reis, a, Johnson, E.W., Sutherland, G.R., et al. (1998). Febrile seizures and generalized epilepsy associated with a mutation in the Na+-channel beta1 subunit gene SCN1B. Nat. Genet. *19*, 366–370.

Wang, S.Y., and Wang, G.K. (1998). Point mutations in segment I-S6 render voltage-gated Na+ channels resistant to batrachotoxin. Proc. Natl. Acad. Sci. U. S. A. *95*, 2653–2658.

Wang, D.W., Desai, R.R., Crotti, L., Arnestad, M., Insolia, R., Pedrazzini, M., Ferrandi, C., Vege, A., Rognum, T., Schwartz, P.J., et al. (2007). Cardiac sodium channel dysfunction in sudden infant death syndrome. Circulation *115*, 368–376.

Wang, G.K., Calderon, J., and Wang, S.-Y. (2008). State- and use-dependent block of muscle Nav1.4 and neuronal Nav1.7 voltage-gated Na+ channel isoforms by ranolazine. Mol. Pharmacol. *73*, 940–948.

Wang, S.-Y., Nau, C., and Wang, G.K. (2000). Residues in Na+ Channel D3-S6 Segment Modulate both Batrachotoxin and Local Anesthetic Affinities. Biophys. J. *79*, 1379–1387.

Van Wart, A., Trimmer, J.S., and Matthews, G. (2007). Polarized distribution of ion channels within microdomains of the axon initial segment. J. Comp. Neurol. *500*, 339–352.

Webb, J., Wu, F.F., and Cannon, S.C. (2009). Slow inactivation of the NaV1.4 sodium

channel in mammalian cells is impeded by co-expression of the β1 subunit. Pflugers Arch. Eur. J. Physiol. *457*, 1253–1263.

Weiss, R., and Horn, R. (1986). Functional differences between two classes of sodium channels in developing rat skeletal muscle. Science (80-.). *233*, 361–364.

Wong, L.C.H., and Behr, E.R. (2014). Sudden unexplained death in infants and children: the role of undiagnosed inherited cardiac conditions. Europace 1–8.

Wood, J.N., Boorman, J.P., Okuse, K., and Baker, M.D. (2004). Voltage-gated sodium channels and pain pathways. J. Neurobiol. *61*, 55–71.

Wu, F., Mi, W., and Cannon, S.C. (2013a). Beneficial effects of bumetanide in a CaV1.1-R528H mouse model of hypokalaemic periodic paralysis. Brain *136*, 3766–3774.

Wu, F., Mi, W., and Cannon, S.C. (2013b). Bumetanide prevents transient decreases in muscle force in murine hypokalemic periodic paralysis. Neurology *80*, 1110–1116.

Wu, F., Mi, W., Fu, Y., Struyk, A., and Cannon, S.C. (2016). Mice with an NaV1.4 sodium channel null allele have latent myasthenia, without susceptibility to periodic paralysis. Brain *139*, 1688–1699.

Wu, F., Quinonez, M., DiFranco, M., and Cannon, S.C. (2018). Stac3 enhances expression of human $Ca_V1.1$ in *Xenopus* oocytes and reveals gating pore currents in HypoPP mutant channels. J. Gen. Physiol. *150*, 475–489.

Wu, F.F., Gordon, E., Hoffman, E.P., and Cannon, S.C. (2005). A C-terminal skeletal muscle sodium channel mutation associated with myotonia disrupts fast inactivation. J. Physiol. *565*, 371–380.

Wu, L., Nishiyama, K., Hollyfield, J.G., and Wang, Q. (2002). Localization of Nav1.5 sodium channel protein in the mouse brain. Neuroreport *13*, 2547–2551.

Yan, Z., Zhou, Q., Wang, L., Wu, J., Zhao, Y., Huang, G., Peng, W., Shen, H., Lei, J., and Yan, N. (2017). Structure of the Na v 1.4-β1 Complex from Electric Eel. Cell *170*, 470–475.e11.

Yang, N., George, a L., and Horn, R. (1996). Molecular basis of charge movement in voltage-gated sodium channels. Neuron *16*, 113–122.

Yarov-Yarovoy, V., Brown, J., Sharp, E.M., Clare, J.J., Scheuer, T., and Catterall, W.A. (2001). Molecular Determinants of Voltage-dependent Gating and Binding of Pore-blocking Drugs in Transmembrane Segment IIIS6 of the Na^+ Channel α Subunit. J. Biol. Chem. *276*, 20–27.

Yoshinaga, H., Sakoda, S., Good, J.-M., Takahashi, M.P., Kubota, T., Arikawa-Hirasawa, E., Nakata, T., Ohno, K., Kitamura, T., Kobayashi, K., et al. (2012). A novel mutation in SCN4A causes severe myotonia and school-age-onset paralytic episodes. J. Neurol. Sci. *315*, 15–19.

Yu, F.H., and Catterall, W.A. (2004). The VGL-Chanome : A Protein Superfamily Specialized for Electrical Signaling and Ionic Homeostasis. 1–18.

Zaharieva, I.T., Thor, M.G., Oates, E.C., Karnebeek, C. Van, Hendson, G., Blom, E., Witting, N., Rasmussen, M., Gabbett, M.T., Ravenscroft, G., et al. (2016). Loss-of-function mutations in SCN4A cause severe foetal hypokinesia or 'classical' congenital myopathy. Brain *139*, 674–691.

Zhang, K., and Wang, X. (2013). Maternal smoking and increased risk of sudden infant death syndrome: A meta-analysis. Leg. Med. *15*, 115–121.

Zhou, J., and Hoffman, E.P. (1994). Pathophysiology of sodium channelopathies. Studies of sodium channel expression by quantitative multiplex fluorescence polymerase chain reaction. J. Biol. Chem. *269*, 18563–18571.